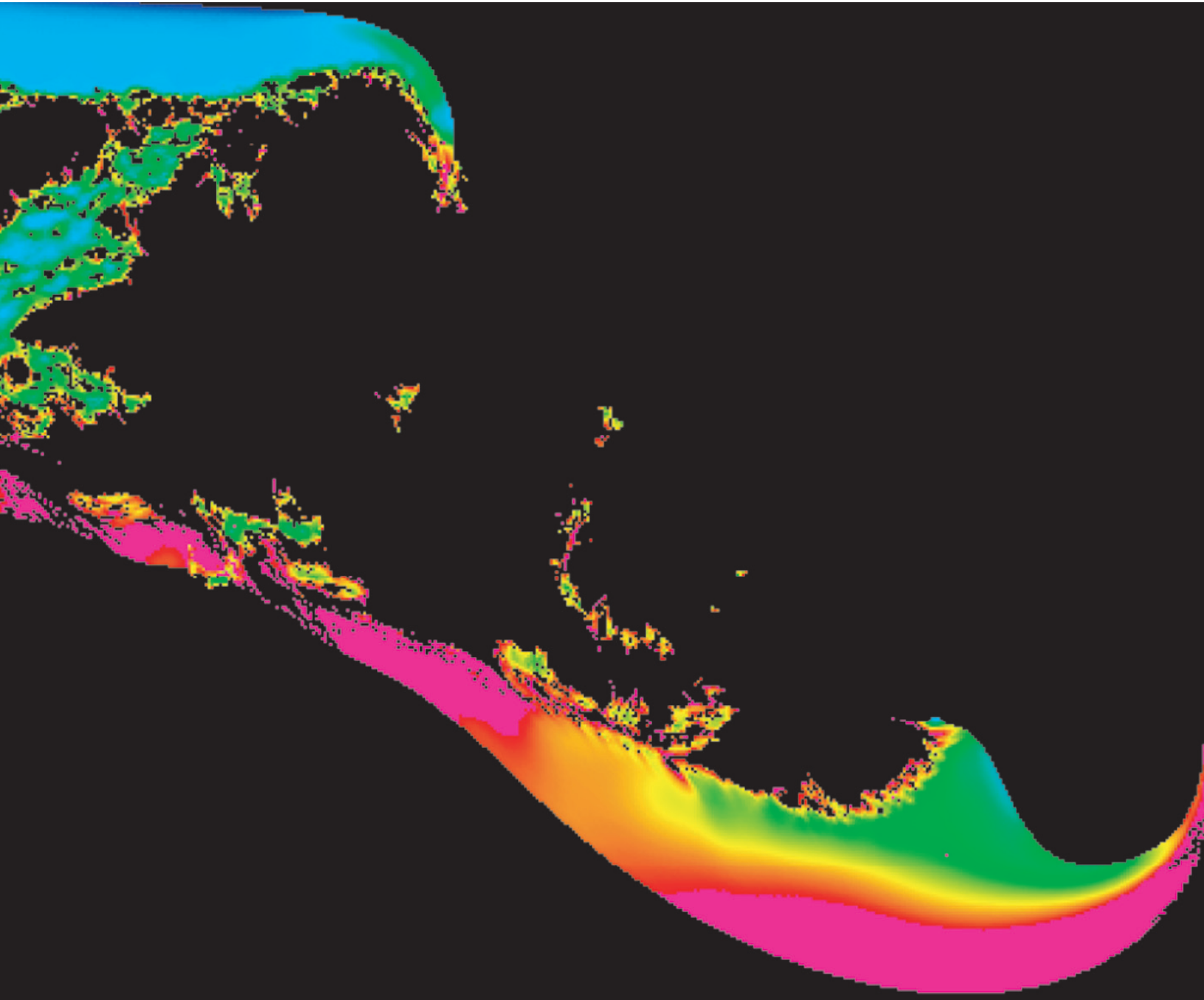
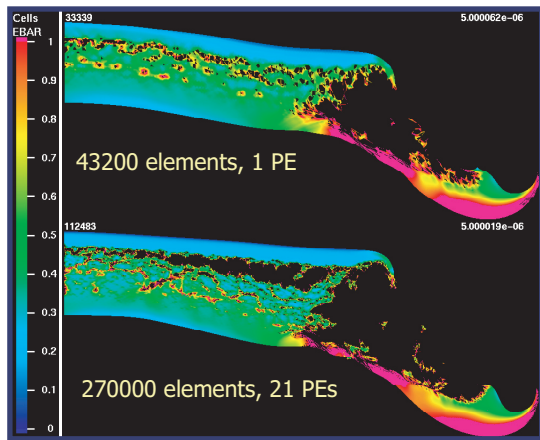


THEORETICAL DIVISION

NUCLEAR WEAPONS PROGRAM HIGHLIGHTS

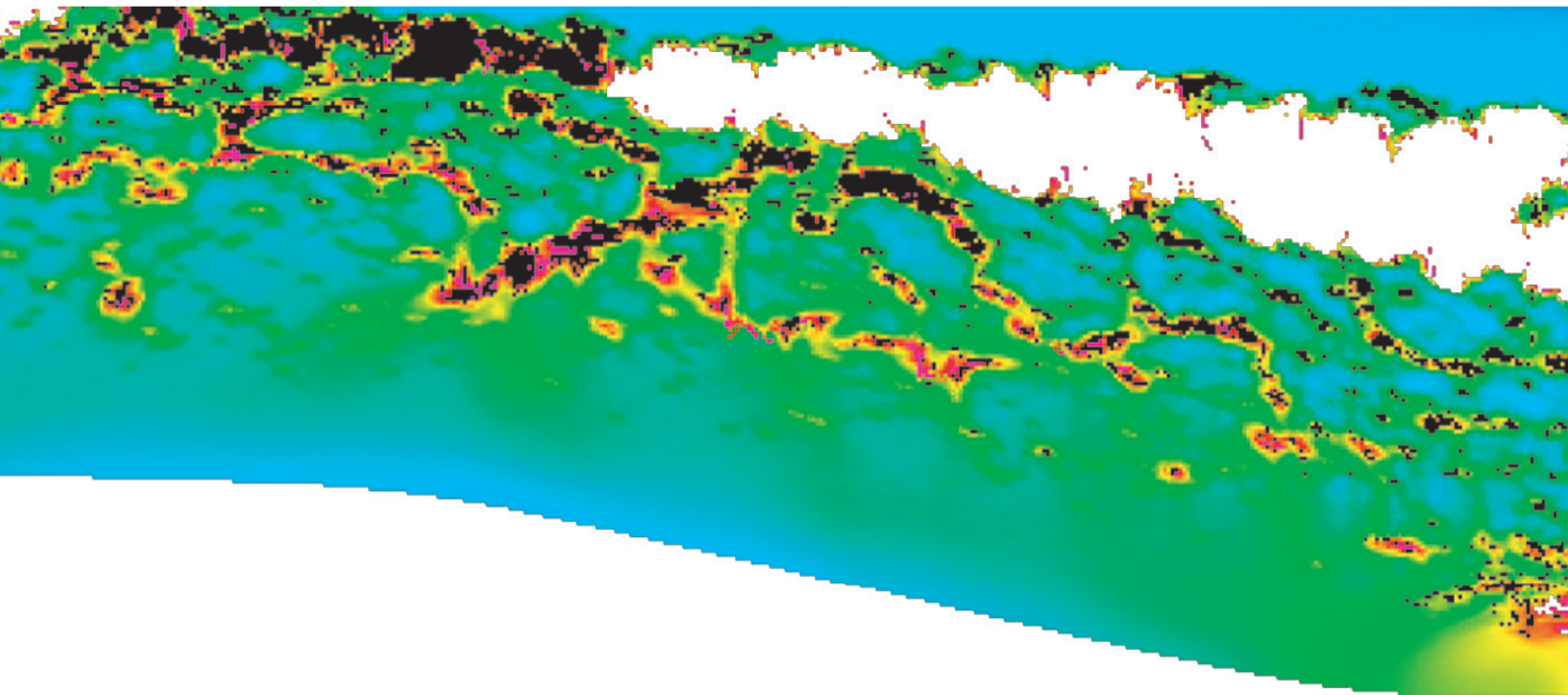
2004–2005





About the Cover

The image on the front cover is taken from Epic simulations of a miniature-detonator experiment conducted at Los Alamos National Laboratory (a tantalum cylinder driven by a cylinder of PETN high-explosive detonated at the center of the outside surface) using a single processor and 21 processors on SGI Origin 2000. (Both calculations are shown at the left on this page.) The 21-processor calculation has much higher mesh resolution, but the two calculations show about the same results indicating that the lower-resolution single-processor calculation is fully converged. See the full paper "Parallel Epic Porting, Simulations, and Performance," by Manjit S. Sahota, Eric N. Harstad, and Paul J. Maudlin (T-3); Thomas A. Mason (MST-8); and Eric M. Mas (T-1) on page X in this volume.



THEORETICAL DIVISION NUCLEAR WEAPONS PROGRAM HIGHLIGHTS 2004–2005

Issued June 2005

Division Leader

Alan R. Bishop

Deputy Division Leader

Paul J. Dotson

Editor

Denise Sessions

Publication Designer

Shirley Veenis

Electronic Publication Specialist

E. Katherine Valdez

Printing Coordinator

Guadalupe D. Archuleta

We gratefully acknowledge the authors who contributed to this publication.

Address mail to

Los Alamos National Laboratory

Theoretical Division Office

P.O. Box 1663, Mailstop B210

Los Alamos NM 87545

http://www.lanl.gov/organization/profiles/t_profile.shtml

Tel: 505.667.4401, Fax: 505.665.4055

≈ **Unclassified** ≈

THEORETICAL DIVISION NUCLEAR WEAPONS PROGRAM HIGHLIGHTS 2004–2005

Preface

Theoretical (T) Division plays an important role in the Nuclear Weapons Program at Los Alamos, providing a significant amount of the underlying theoretical and modeling capability in the areas of dynamic materials response and equation of state, nuclear and atomic physics, plasma physics, fluid mechanics, and computational methods for the Laboratory. These capabilities are brought to bear, in collaboration with our colleagues elsewhere in the Laboratory, on the increasingly challenging problems arising from the Stockpile Stewardship Program. In order to validate a truly predictive simulation capability, the fidelity of the underlying physics descriptions must continue to improve, and this requires the development and implementation of more sophisticated physics models into the simulation codes in a close partnership with our experimental, modeling, and simulation capabilities.

Researchers in T Division work with theoretical colleagues in other divisions and with coworkers in experimental divisions to produce models of physical behavior. These models ultimately are expressed in continuum form but draw from subscale modeling and theory to best capture those macroscopic effects that are driven by phenomena at atomic or mesoscales. These models are validated by fundamental scientific data, parameterized, and implemented into codes, to be further tested against evermore complex integral experiments. The improved capability resulting from these newer-generation physics models is making significant differences in our ability to fulfill our stockpile stewardship responsibilities.

Paul J. Dotson
Deputy Division Leader, Theoretical Division

TABLE OF CONTENTS

Preface

| | |
|----------------------------------------------|-----|
| Paul J. Dotson, Deputy Division Leader | iii |
|----------------------------------------------|-----|

Equation of State

| | |
|--------------------------------------------------------------------------------------------------------------------------------------------------------------------------------------------------------------------------------------------|----|
| Equation of State Developments in T-1 | 2 |
| <i>Nicolas Bock, Eric Chisolm, Scott Crockett, Giulia De Lorenzi-Venneri, Denise George, Carl Greeff, J. D. Johnson, Sven Rudin, and Duane Wallace (T-1)</i> | |
| Modeling Dynamic Phase Changes in Zr—EOS and Kinetics | 4 |
| <i>Carl Greeff and Sven Rudin (T-1), Frank Addressio and Eric Harstad (T-3), Paulo Rigg and Rob Hixson (DX-2), G.T. Gray, III (MST-8), Yusheng Zhao and Jianzhong Zhang (LANSCE-12), and Marcus Knudson (Sandia National Laboratories)</i> | |
| Adiabatic and Non-Adiabatic Contributions to the Free Energy from the Electron-Phonon Interaction for Na, K, Al, and Pb | 6 |
| <i>Nicolas Bock and Duane C. Wallace (T-1), D. Coffey (Buffalo State College)</i> | |
| Unified Model of the Grüneisen Parameter, Melting Temperature, and Shear Modulus for a Compound | 8 |
| <i>Leonid Burakovsky (T-1) and Dean L. Preston (P-22)</i> | |
| Extending the CCW EOS: Extending the Nuclear Contribution to High Temperatures | 10 |
| <i>Eric D. Chisolm, Scott D. Crockett, and Duane C. Wallace (T-1)</i> | |
| Dynamic Response of Simple Liquids from Vibration-Transit Theory | 12 |
| <i>Giulia De Lorenzi-Venneri and Duane Wallace (T-1)</i> | |
| Direct Numerical Simulations of PBX 9501 with Reaction Chemistry | 14 |
| <i>Eric M. Mas, Brad E. Clements, and Denise C. George (T-1)</i> | |
| Calculations to Refine Beryllium's Equation of State | 16 |
| <i>Sven P. Rudin and J. D. Johnson (T-1)</i> | |

Condensed Matter, Materials Science, and Chemistry

| | |
|--------------------------------------------------------------------------------------------------------------------------------------------------------------------------------|----|
| Nonspherical Void Growth Theories | 20 |
| <i>Brad E. Clements and Eric M. Mas (T-1), and Paul J. Maudlin (T-3)</i> | |
| Large-Scale Dislocation Dynamics Simulation of Bulk Deformation | 22 |
| <i>Richard LeSar (T-12), and Nasr Ghoniem and Zhiqiang Wang (University of California at Los Angeles)</i> | |
| N-Scaling Materials Response by Density Matrix Perturbation Theory | 24 |
| <i>Anders M.N. Niklasson (T-1), Matt Challacombe (T-12), and Valéry Weber (T-12 and University of Fribourg, Switzerland)</i> | |
| A Model for Heterogeneous Materials Including Phase Transformations | 26 |
| <i>Frank L. Addessio and Todd O. Williams (T-3), and Brad E. Clements and Eric M. Mas (T-1)</i> | |
| An Implicit Thermomechanical Composite Model of PBX 9501 | 28 |
| <i>Curt A. Bronkhorst and Todd O. Williams (T-3), Darla G. Thompson (DX-2), and Cheng Liu (MST-8)</i> | |
| Modeling Phase Transformations with Strength in Zirconium | 30 |
| <i>Eric N. Harstad, Francis L. Addessio, Q. Ken Zuo, and Todd O. Williams (T-3); and Carl W. Greeff (T-1)</i> | |
| Direct Numerical Simulation of Polycrystal | 32 |
| <i>Manjit S. Sahota, Rick M. Rauenzahn, Frank L. Addessio, and Francis H. Harlow (T-3)</i> | |
| Damage Surface Based on the Critical Crack Orientation | 34 |
| <i>Q. Ken Zuo and Frank L. Addessio (T-3), John K. Dienes (T-14)</i> | |
| Numerical Simulation of Realistic Foam Microstructures | 36 |
| <i>Andrew Brydon and Scott Bardenhagen (T-14)</i> | |
| Strain-Induced Phase Transformations in Shape Memory Alloys | 38 |
| <i>Rajeev Ahluwalia, Turab Lookman, and Avadh Saxena (T-11)</i> | |
| Mesoscale Simulations of Crack Propagation | 40 |
| <i>V. Dwivedi [University of California at Santa Barbara (UCSB)/T-11]; Rajeev Ahluwalia, Turab Lookman, and Avadh Saxena (T-11); and S. Bannerjee (UCSB)</i> | |
| Viscoelastic Behavior of Polymers | 42 |
| <i>David Hall and Turab Lookman (T-11), and Edward Kober (T-14)</i> | |
| Impurities Block the α to ω Martensitic Transformation in Titanium | 44 |
| <i>Richard G. Hennig, Dallas R. Trinkle, and John W. Wilkins (Ohio State University); Johann Bouchet and Robert C. Albers (T-11); and Srivilliputhur G. Srinivasan (MST-8)</i> | |
| Towards Modeling Elastic Properties of Estane® | 46 |
| <i>Kim Ø. Rasmussen and Turab Lookman (T-11), Panagiotis Maniadis (CNLS/T-11), and Edward M. Kober (T-14)</i> | |

| | |
|----------------------------------------------------------------------------------------------------|-----------|
| World Record: Large-Scale Molecular-Dynamics Simulation of 19 Billion Particles | 48 |
| <i>Kai Kadau (T-14), Timothy C. Germann (X-7), and Peter S. Lomdahl (T-11)</i> | |
| Thermal Decomposition of Nitromethane using Reactive Molecular Dynamics | 50 |
| <i>Si-ping Han (T-14 and California Institute of Technology) and Alejandro Strachan (T-14)</i> | |
| Micromechanical Modeling of the Binder Material of PBX 9501 | 52 |
| <i>David Hanson (T-12)</i> | |
| Quantum Molecular Dynamics Simulations of Liquid Plutonium and Hydrogen/Metal Mixtures..... | 54 |
| <i>Joel D. Kress (T-12) and Lee A. Collins (T-4)</i> | |
| Energy Exchange between Mesoparticles and Their Internal Degrees of Freedom | 56 |
| <i>Brad Lee Holian (T-12) and Alejandro Strachan (T-14)</i> | |
| Decomposition of Nitroplasticizer in Plastic-Bonded Explosive PBX 9501 | 58 |
| <i>Denise K. Pauler (T-12 and Cornell University) and Joel D. Kress (T-12)</i> | |

Shock and Detonation Physics

| | |
|-----------------------------------------------------------------------------------------------------------------------------------------------------------------------------------------------------|-----------|
| Design of a Fragment Generator | 62 |
| <i>Eric M. Mas (T-1), Paul Maudlin (T-3), and Jon Mace (DX-2)</i> | |
| Shock Passage Over an Interface | 64 |
| <i>Rick Rauenzahn, Manjit Sahota, and Francis Harlow (T-3); Robert Gore (X-2); Michael Steinkamp (X-3); and Jon Weisheit (T-15)</i> | |
| Numerical Simulation of Plastic-Bonded Explosives | 66 |
| <i>Scott Bardenhagen and Andrew Brydon (T-14)</i> | |
| The Nexus between Reactive MD Simulations of RDX and the Reactive Euler Equations..... | 68 |
| <i>Shirish M. Chitanvis (T-14)</i> | |
| Atomistic Studies of PBX 9501 Constituents and Interactions Among Them..... | 70 |
| <i>Eugenio Jaramillo and Thomas D. Sewell (T-14); Chee Kwan Gan and Matt Challacombe (T-12); and Hemali Davande, Dmitry Bedrov, Oleg Borodin, and Grant D. Smith (University of Utah)</i> | |
| Large-Scale Simulations of Shock-Induced Transformations in Gallium, on the Way to Plutonium..... | 72 |
| <i>Kai Kadau (T-14), Timothy C. Germann (X-7), Peter S. Lomdahl (T-11), Brad L. Holian (T-12), Ramon J. Ravelo (University of Texas/X-7), Frank J. Cherne (DX-2), and Michael I. Baskes (MST-8)</i> | |
| Atomistic Investigations into the Dependence of Detonation Properties on Material Parameters using Molecular Dynamics | 74 |
| <i>Edward Kober and Andrew J. Heim (T-14)</i> | |
| Detonation Products Equation of State | 76 |
| <i>M. Sam Shaw and C. J. Tymczak (T-14)</i> | |

| | |
|-------------------------------------------------------------------------------------------------|----|
| Anisotropic Plasticity of NiAl under Dynamical Loading | 78 |
| <i>Alejandro Strachan (T-14) and Sheng-Nian Luo (P-24)</i> | |
| Mesodynamical Simulations with Quantum Mechanical Description of the Thermal | 80 |
| <i>Alejandro Strachan (T-14) and Brad Lee Holian (T-12)</i> | |
| Influence of Elastic Shear Stiffness on Richtmyer-Meshkov Instability | 82 |
| <i>JeeYeon N. Plohr (T-1) and Bradley J. Plohr (T-13)</i> | |
| Modeling Plastic Instability and Strain Localization in Explosively Driven U6 Hemi | 84 |
| <i>Q. Ken Zuo and Paul J. Maudlin (T-3), and Lawrence M. Hull (DX-3)</i> | |

Fluid Dynamics

| | |
|------------------------------------------------------------------------------------------------------------------------------------------------------------------------------------------------------------------------------------------------------|-----|
| Flux Calculations in the Heat Transfer Component of TELLURIDE | 88 |
| <i>Travis Austin, Markus Berndt, J. David Moulton, and Mikhail Shashkov (T-7)</i> | |
| Shear Localization in Tantalum Top Hat Samples | 90 |
| <i>Curt A. Bronkhorst and Paul J. Maudlin (T-3), and Ellen K. Cerreta, Thomas A. Mason, and George T. Gray III (MST-8)</i> | |
| Compressible Particle Model for Turbulent Mix Calculations | 92 |
| <i>Michael C. Cline, Manjit S. Sahota, Peter J. O'Rourke, and David J. Torres (T-3), and Margaret S. Hubbard (X-3)</i> | |
| Phase Separation Simulations using Annular Centrifugal Contactors | 94 |
| <i>Nely T. Padial-Collins, W. Brian VanderHeyden, Qisu Zou, and Duan Z. Zhang (T-3), and Scott Sportsman (NMT-2)</i> | |
| The Effect of Initial Conditions on the Turbulent Rayleigh-Taylor Flow | 96 |
| <i>Praveen Ramaprabhu (CNLS), Guy Dimonte (X-4), and M.J. Andrews (Texas A&M University)</i> | |
| Nuclear Weapons Effects: Agent Defeat Simulations | 98 |
| <i>Manjit S. Sahota, Rick M. Rauenzahn, and W. Brian VanderHeyden (T-3), and Merri M. Wood-Schultz (X-2)</i> | |
| Parallel Epic Porting, Simulations, and Performance | 100 |
| <i>Manjit S. Sahota, Eric N. Harstad, and Paul J. Maudlin (T-3); Thomas A. Mason (MST-8); and Eric M. Mas (T-1)</i> | |
| High-Explosive Safety Study Update | 102 |
| <i>Qisu Zou, Duan Z. Zhang, W. Brian VanderHeyden, and Nely Padial-Collins (T-3)</i> | |
| Nanohydrodynamics Simulations: An Atomistic View of the Raleigh-Taylor Instability | 104 |
| <i>Kai Kadau (T-14), Timothy C. Germann (X-7), Peter S. Lomdahl (T-11), Brad L. Holian (T-12), Guy Dimonte (X-4), Nicolas G. Hadjiconstantinou (Massachusetts Institute of Technology), and Berni Alder (Lawrence Livermore National Laboratory)</i> | |

Computational Sciences

| | |
|----------------------------------------------------------------------------------------------------------------|-----|
| Accelerated Inexact Newton Method for Casting Simulations | 108 |
| <i>Andrew P. Kuprat (T-1)</i> | |
| A Memory Efficient Parallel Tridiagonal Solver | 110 |
| <i>Travis M. Austin, Markus Berndt, and J. David Moulton (T-7)</i> | |
| Efficient Smoothing of Unstructured Grids | 112 |
| <i>Markus Berndt and J. David Moulton (T-7)</i> | |
| Interface Reconstruction on General Polygonal Meshes | 114 |
| <i>Rao V. Garimella, Mikhail J. Shashkov, and Blair K. Swartz (T-7)</i> | |
| Mimetic Discretizations of Diffusion Equation on Polygonal Meshes | 116 |
| <i>Konstantin Lipnikov and Mikhail Shashkov (T-7), and Yuri Kuznetsov (University of Houston)</i> | |
| An Arbitrary-Lagrangian-Eulerian Code for Polygonal Mesh: ALE INC(ubator) | 118 |
| <i>Raphaël Loubère and Mikhail Shashkov (T-7)</i> | |
| A Subcell Remapping Method on Staggered Polygonal Grids for Arbitrary-Lagrangian-Eulerian Methods | 120 |
| <i>Raphaël Loubère and Mikhail Shashkov (T-7)</i> | |
| The Repair Paradigm: New Algorithms and Applications to Compressible Flow | 122 |
| <i>Raphaël Loubère, Martin Staley, and Burton Wendroff (T-7)</i> | |
| CORE: Conservative Remapper | 124 |
| <i>Martin Staley and Mikhail Shashkov (T-7)</i> | |

Nuclear Physics

| | |
|-------------------------------------------------------------------------------------------------------------------------------------------------------------------------------|-----|
| Attribution for Nuclear Devices Based on Reactor Grade Fuel | 128 |
| <i>Anna C. Hayes, Patrick Goda, Jack Hills, and Gerard Jungman (T-6); and John Richter (X-4)</i> | |
| Implications of the Uncertainties in the n + Li Cross Sections | 130 |
| <i>Anna C. Hayes (T-6), Gerald Hale (T-16), Steven Howe (LANSCE-DO), Andrew S. Johnson (X-2), Britton A. Girard (X-4), Thomas J. Gorman (X-3), and Robert C. Little (X-5)</i> | |
| New Antineutrino Spectra for Plutonium and Uranium | 132 |
| <i>Anna C. Hayes and Corinne M. Teeter (T-6), William B. Wilson (T-16), and Michael Martin Nieto (T-8)</i> | |
| Nuclear Isomers | 134 |
| <i>Anna C. Hayes and Gerard Jungman (T-6), Eric Lynn (T-16), and Britt Girard (X-4)</i> | |
| Radiochemical Detectors Probe Physical Processes | 136 |
| <i>Gerard Jungman and Anna C. Hayes (T-6)</i> | |

| | |
|-----------------------------------------------------------------------------------------------------------------------------------------------------------------------|------------|
| Prompt Beta Spectroscopy as a Diagnostic for Mix in Ignited NIF Capsules..... | 138 |
| <i>Anna C. Hayes and Gerard Jungman (T-6), Johndale C. Solem (T-DO), Paul A. Bradley (X-2), and Robert S. Rundberg (C-INC)</i> | |
| Intrinsic Decay of Quantum Many-Body Systems..... | 140 |
| <i>George E. Cragg and Arthur K. Kerman (Massachusetts Institute of Technology)</i> | |
| Neutron Cross Sections for Reactions on ^6Li and ^9Be | 142 |
| <i>Gerald M. Hale (T-16)</i> | |
| Combining Differential and Integral Cross Sections to Improve Nuclear Data for Fission Applications..... | 144 |
| <i>Toshihiko Kawano (T-16), Kenneth M. Hanson (CCS-2/T-16), Stephanie C. Frankle (X-5), Patrick Talou and Mark B. Chadwick (T-16), and Robert C. Little (X-5)</i> | |
| Correlated Neutron Emission in Fission..... | 146 |
| <i>Sebastien Lemaire, Patrick Talou, Toshihiko Kawano, Mark B. Chadwick, and David G. Madland (T-16)</i> | |
| Importance of Proton-Nucleus Strong Interaction to Proton-Radiography Simulation..... | 148 |
| <i>Lon-Chang Liu (T-16)</i> | |
| Critical Assembly Data Testing for Nuclear Cross Sections..... | 150 |
| <i>Robert E. MacFarlane and Mark B. Chadwick (T-16), Michael MacInnes (X-2), and Robert C. Little (X-5)</i> | |
| Global Calculation of Nuclear Shape Isomers..... | 152 |
| <i>Peter Möller (T-16), Ragnar Bengtsson and Peter Olivius (Lund University, Sweden)</i> | |
| Testing the Predictive Power of Nuclear-Structure Models Against New Experimental Data.. | 154 |
| <i>Peter Möller (T-16)</i> | |
| Detection of Antineutrinos for Nonproliferation..... | 156 |
| <i>Michael Martin Nieto (T-8), Anna C. Hayes and Corinne M. Teeter (T-6), William B. Wilson (T-16), and William D. Stanbro (N-4)</i> | |
| ^8Be Nuclear Data Evaluation..... | 158 |
| <i>Philip R. Page and Gerald M. Hale (T-16)</i> | |
| The Nuclear Reaction Code McGNASH..... | 160 |
| <i>Patrick Talou, Mark B. Chadwick, Phillip G. Young, and Toshihiko Kawano (T-16)</i> | |
| Neutron Emission Spectra from Actinides..... | 162 |
| <i>Phillip G. Young and Robert E. MacFarlane (T-16), Mark B. Chadwick (PADNWP), and Stephanie C. Frankle (X-5)</i> | |

Atomic Physics

| | |
|---------------------------------------------------------------------------------------------------------------------------------|-----|
| Line-Edge Blending in ATOMIC | 166 |
| <i>Joseph Abdallah, Jr., Peter Hakel, David P. Kilcrease, Norman H. Magee, Jr., Stephane Mazevet, and Manolo Sherrill (T-4)</i> | |
| New Methods for Spectral Generation in ATOMIC | 168 |
| <i>Joseph Abdallah, Jr., Manolo Sherrill, Stephane Mazevet, Norman H. Magee, Jr., David P. Kilcrease, and Peter Hakel (T-4)</i> | |
| Parallel Rate Matrix Solvers in the ATOMIC Code | 170 |
| <i>James Colgan and Joseph Abdallah (T-4), Christopher J. Fontes and H. L. Zhang (X-5)</i> | |
| Time-Dependent Studies of Photoionization of Light Systems: Beyond Two-Electron Systems | 172 |
| <i>James Colgan (T-4)</i> | |
| The ATOMIC Equation of State | 174 |
| <i>Stephane Mazevet, Joseph Abdallah, Peter Hakel, David P. Kilcrease, Norman H. Magee, Jr., and Manolo Sherrill (T-4)</i> | |

Plasma Physics

| | |
|-----------------------------------------------------------------------------------------------------------|-----|
| Recent Developments in High Energy-Density Plasma Physics | 178 |
| <i>Michael S. Murillo and Jon Weisheit (T-15)</i> | |
| Electromagnetic Excitation Rates for Nuclear Isomers in a Hot Dense Plasma | 180 |
| <i>Thomas C. Luu and Anna C. Hayes (T-6), and James L. Friar (T-16)</i> | |
| Self-Focusing of Plasma Waves and the Control of Laser-Plasma-Instability | 182 |
| <i>Harvey A. Rose (T-13)</i> | |
| Extended Thomas-Fermi Models for Equations of State of Dense, High Energy-Density Matter | 184 |
| <i>George Csanak (T-4), Jérôme Daligault and Michael S. Murillo (T-15)</i> | |

Astrophysics

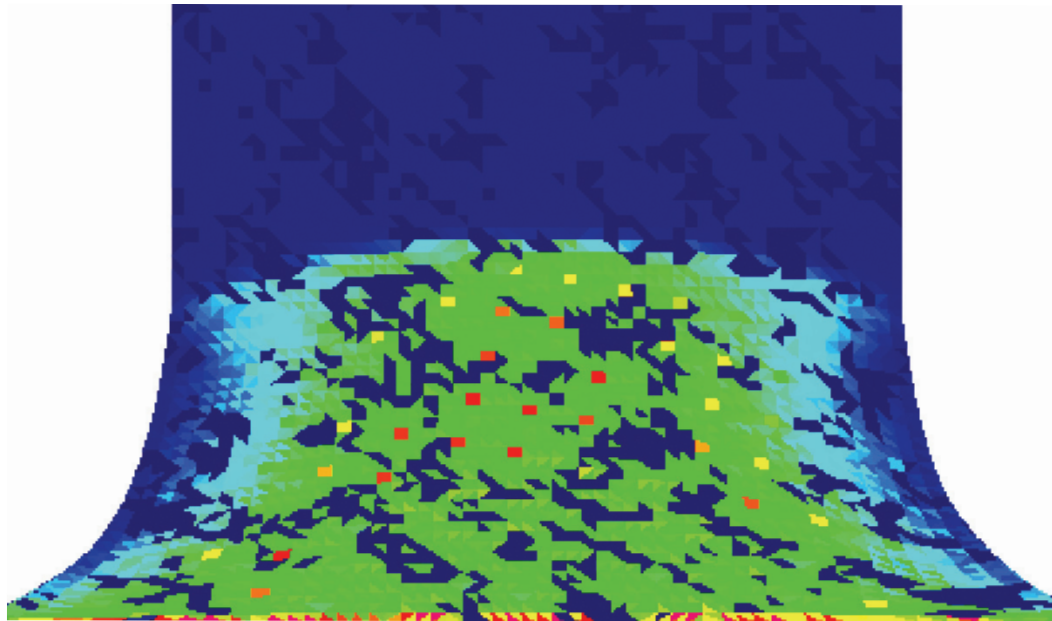
| | |
|-------------------------------------------------------------------------------------------------------------------------|------------|
| Theoretical Prediction of an Observed Solar g-Mode | 188 |
| <i>Arthur N. Cox (T-6) and Joyce A. Guzik (X-2)</i> | |
| Modeling Supernova Explosions | 190 |
| <i>Chris Fryer and Gabe Rockefeller (T-6), Kim New (X-2), and Aimee Hungerford (CCS-4)</i> | |
| Stellar Burning and Mixing | 192 |
| <i>Falk Herwig, Alexander Heger, and Frank Timmes (T-6); and Rob Hueckstaedt and Rob Coker (X-2)</i> | |
| Fission Neutron Multiplicity Functions for Preinitiation Calculations | 194 |
| <i>Thomas C. Luu, Jack Hills, Gerard Jungman, and Anna C. Hayes (T-6)</i> | |
| On Variations in the Peak Luminosity of Type Ia Supernovae | 196 |
| <i>Frank X. Timmes (T-6), Edward F. Brown (Michigan State University), and J. W. Truran (University of Chicago)</i> | |
| Physical Properties of White Dwarf Atmospheres | 198 |
| <i>Stephane Mazevet (T-4), Piotr Kowalski and Didier Saumon (X-7)</i> | |

Predictive Science and Uncertainty Quantification

| | |
|--------------------------------------------------------------------------------------------------|------------|
| The Use of Smoothing Splines to Assess Uncertainties in Alpha Curves | 202 |
| <i>Timothy C. Wallstrom (T-13)</i> | |
| Physics Package Confidence: “ONE” vs “1.0” | 204 |
| <i>David H. Sharp (T-13 and X-DO), Timothy C. Wallstrom (T-13), and Merri Wood-Schultz (X-2)</i> | |

| | |
|----------------------------------|------------|
| <i>Author Index</i> | 206 |
|----------------------------------|------------|

EQUATION OF STATE



Equation of State Developments in T-1

Nicolas Bock, Eric Chisolm, Scott Crockett, Giulia De Lorenzi-Venneri, Denise George, Carl Greeff, J. D. Johnson, Sven Rudin, and Duane Wallace (T-1)

The latest release of the SESAME library was performed on April 7, 2004. The release contains new tables for the following materials: copper, aluminum, deuterium, butane, hexane, propane, He-3, and two d-He-3 50/50 mixtures. The new tables for these materials introduce eleven new material numbers. In addition, 72 new subtables were added. The release was verified and validated under Los Alamos National Laboratory (LANL) guidelines.

The new deuterium Equation of State (EOS) in the library is a retrofit done to match the diamond anvil room temperature isotherm and the Hugoniot obtained by the Sandia National Laboratories effort on the Z machine.

Analysis of the High Explosive EOS created by Sam Shaw (T-14) was performed to study the viability of extending the EOS over the standard SESAME temperature and density range while preserving his work to machine accuracy. After performing the analysis, we then completed two different extensions of these various EOS.

We produced five different EOS mixes to assist the work of the WBWG, which includes members from the Thermonuclear Applications Group (X-2) and the Primary Design and Assessment Group (X-4) in the Applied Physics Division.

We have assessed the EOS of various isotopes of LiH. This work was stimulated by questions raised by one of our users who noted that we have several such EOS and that the quality of most of them is questionable.

(For example, some do not approach the ideal gas limit correctly.) We have compared diamond anvil data and shock data to all previous EOS and have produced a new EOS. This work was completed in Quarter 1 of FY 2005.

An important direction in EOS research has been to improve the treatment of materials undergoing phase transitions. Work in T-1 has improved the microscopic theory, as well as algorithms for data analysis and dynamic simulations for such materials. A recent collaboration with experimentalists in other LANL divisions and Sandia has elucidated the EOS, phase diagram, and kinetics of Zr. A single EOS and kinetic model is able to accurately simulate the phase transition under shock wave and isentropic compression loading.

The current EOS for Be was called into question with the finding in the open literature of electronic structure results and diamond anvil data. To clarify this situation, we are performing density functional theory (DFT) calculations aimed at refining the EOS. Our preliminary results for the average phonon frequency led to a Grüneisen parameter in good agreement with our current EOS, but the results point to some improvements. If the minor differences between our DFT results and the earlier value remain with higher-accuracy calculations, they will be incorporated into a more accurate EOS.

The EOS experimental data set for Sn is fairly extensive, including information from efforts at Los Alamos and elsewhere on the melting curve and temperatures for release isentropes. To evaluate this data and provide direction to these experimental efforts, we have reexamined with care our current EOS for Sn and found it satisfactory but at odds with this data. We are now doing more detailed calculations to firm up our opinion. It is important to determine if there are problems with the experiments.

We have continued our work to extend the CCW methods for constructing EOS to the entire temperature and density range required for SESAME tables. We have determined how to extend the nuclear contribution to

the free energy to very high temperatures, well beyond the liquid regime, and we have argued that the electron excitation-nuclear motion contribution, usually neglected at low temperatures, is also negligible at very high temperatures ($T \geq 100 T_m$).

We calculated the adiabatic and non-adiabatic contributions to the free energy of metals due to the electron-phonon interaction at temperatures between 0 and 1.5 times the melting temperature. We considered different metals and found the zero temperature value of the non-adiabatic contribution for each, which had not been calculated previously. We also determined the crossover temperature between the adiabatic and non-adiabatic contribution for each metal and found that it is at rather high temperatures but below melting.

The Vibration-Transit Theory recently developed in our group has been applied to the study of the dynamic response of liquids, as experimentally observed in inelastic neutron scattering and inelastic x-ray scattering. We have calculated the dynamic structure factor for sodium from the theory and from molecular dynamics simulation for a simple monatomic liquid, a model for sodium. Once more we have found support for the validity of the theory. We have been able to establish the fundamental role of atomic vibrations in single random configurations in determining the essential character of the Brillouin peak in the dynamic structure factor. Further developments of the theory regarding the role of transits are underway.

We have worked on validation and verification of the T-1 EOS computer codes GRIZZLY and OpenSesame by: (1) developing test suites for both GRIZZLY and OpenSesame and comparing the results generated by running on several platforms, (2) analyzing the causes of the different results generated by running on different platform and improving the numeric methods in OpenSesame to minimize

these differences, (To this end, the rational interpolator and the method of finding zeros of a function were changed. Also, iterative calls to the root finder replaced an unstable double binary/double Newton's method.), (3) improving code documentation (<http://opensesame.lanl.gov>), (4) placing all code, test suites, and documentation under version control, and (5) modernizing GRIZZLY so that it ports easily to new platforms.

We have improved the capabilities of OpenSesame by: (1) adding an isobar plotting capability, and (2) adding melt models, shear modulus models, the Morse models, the Virial match model, and the Rose models.

We have made periodic releases to the user community of OpenSesame and GRIZZLY.

We participated in the Isentropic Compression Experiments (ICE) workshop at Sandia and provided theoretical support. The group is continually working on establishing a stronger collaboration effort with the Z machine and gas gun efforts at Sandia.

For more information, contact Eric Chisolm (echisolm@lanl.gov).

Acknowledgements

We would like to acknowledge NNSA's Advanced Simulation and Computing (ASC), Materials and Physics Program for financial support.

Modeling Dynamic Phase Changes in Zr—EOS and Kinetics

Carl Greeff and Sven Rudin (T-1),
Frank Addessio and Eric Harstad (T-3),
Paulo Rigg and Rob Hixson (DX-2),
G.T. Gray, III (MST-8), Yusheng Zhao
and Jianzhong Zhang (LANSCE-12),
and Marcus Knudson (Sandia National
Laboratories)

Theoretical Division, in partnership with the Los Alamos National Laboratory's nuclear weapons programs, has historically been the home of advanced research in high-pressure equations of state (EOS) and shock physics. An important direction in this research at present is to improve our predictive capabilities for materials undergoing solid-solid phase changes. An interdivisional and multilaboratory collaboration is shedding new light on phase transitions elemental zirconium (Zr). Recent work has led to new understanding of the phase diagram and EOS of this element and has revealed information on transformation kinetics and impurity effects. Ongoing work aims to improve the microscopic basis for the EOS and the description of the mechanical response.

A basic element of this work is the development of a high accuracy EOS, in the form of free energy functions for the individual phases. The resulting EOS is sufficiently accurate to allow us to make inferences about kinetics by comparing simulations with time-resolved data from dynamic compression experiments. Figure 1 shows the Hugoniot of Zr, which exhibits two distinct phase transitions. By correlating the Hugoniot with static compression and thermodynamic data, and electronic structure theory, we can associate the branches of the Hugoniot with definite crystal structures. The α -phase is hcp, the ω -phase is hexagonal with 3 atoms per unit cell, and β is bcc. The lower Hugoniot data lie along the metastable extension of the α -phase branch. This nonequilibrium behavior reflects the finite transformation rate.

A model for the kinetics of the α - ω phase transition has been proposed and applied to simulate dynamic experiments [1]. The model is successful in capturing the main features of wave profiles under various loading conditions. Figure 2 gives an illustration. The experimental VISAR profile was obtained in DX-2. The experiment consists of a sapphire impactor striking a Zr sample with a sapphire window. These investigations have shown a strong role of impurities in reducing the transformation rate. This is manifested in Fig. 2 through the higher transition threshold and broader wave in the lower purity sample. This same EOS and kinetic model was also successfully used to model isentropic compression experiments on the Sandia National Laboratories' Z-machine.

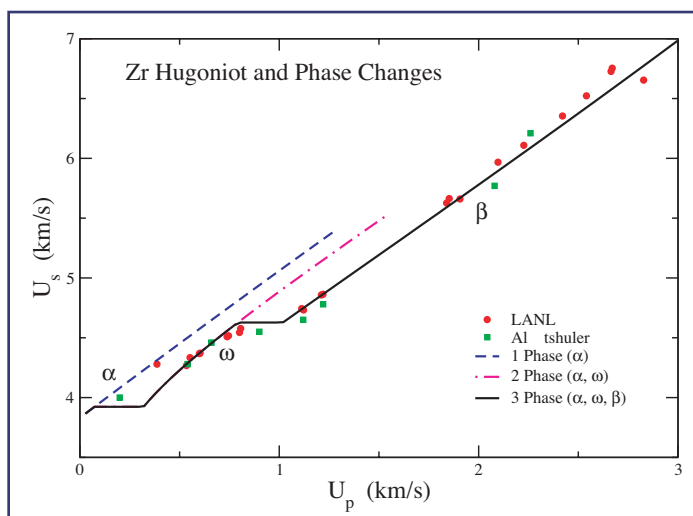


Figure 1—
Hugoniot of Zr. Solid
curve is equilibrium.
Dashed curves
are metastable
extensions. Points
are experimental data.

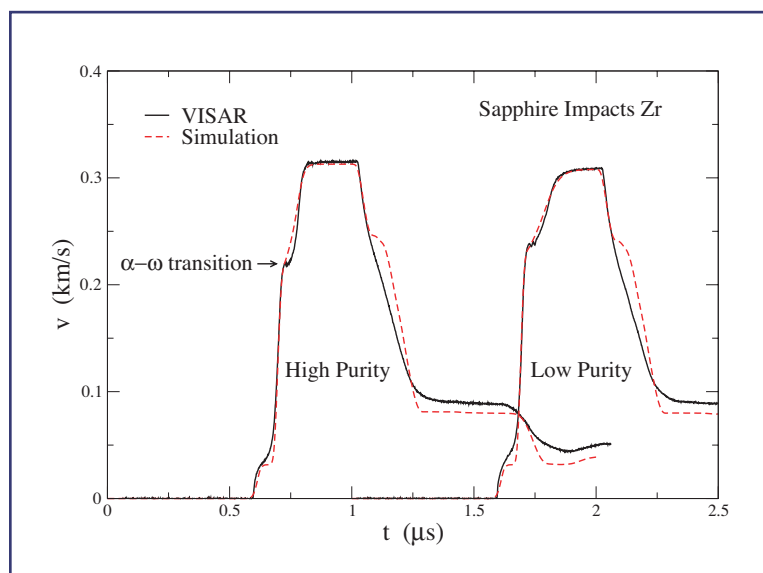


Figure 2—
Time-resolved
observation of α - ω
transition in Zr.
Solid black curves
are experimental
VISAR. Dashed red
curves are simula-
tion. Rate effects
are represented in
both the position of
the break and the
slope of the subse-
quent rise.

We are working to improve the EOS with lattice vibrational frequencies from electronic structure theory. These calculations tie into mechanical modeling by providing elastic moduli at high pressure, where they are difficult to measure. A complication that arises in Zr is significant anharmonicity. This is illustrated in Fig. 3, which shows the energy change associated with some high symmetry phonon displacements for Cu, Zr, and U. For a linear restoring force, the curves would be flat. In contrast to Cu, both Zr and U show substantial nonlinearity. Experimentally, this leads to strong temperature dependence of the corresponding frequency.

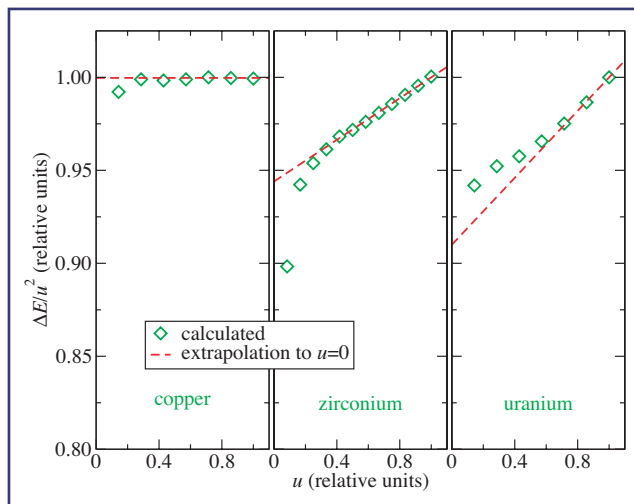


Figure 3—
Energy vs displace-
ment for high symmetry
phonon modes of Cu,
Zr, and U. For a linear
restoring force, the curve
is constant, as for Cu.

The shock-wave simulations discussed earlier in this paper use a simple elastic, perfectly plastic constitutive model, which leads, for example, to the difference with experiment in the shape of the release wave. Ongoing modeling efforts aim to improve the constitutive modeling and also to address the coupling of shear stress to the phase transition [2].

[1] C.W. Greeff, P.A. Rigg, M.D. Knudson, R.S. Hixson, and G.T. Gray, III, "Shock Compression of Condensed Matter-2003," in *AIP Conference Proceedings* 706, M.D. Furnish and Y.M. Gupta, Eds. (AIP Conference Proceedings, Melville, NY, 2004).

[2] E. Harstad et al., "Modeling Phase Transformations with Strength in Zirconium," contribution on p. 30 in this volume.

For more information, contact Carl Greeff (greeff@lanl.gov).

Acknowledgements

We would like to acknowledge NNSA's Advanced Simulation and Computing (ASC), Materials and Physics Program for financial support.

Adiabatic and Non-Adiabatic Contributions to the Free Energy from the Electron-Phonon Interaction for Na, K, Al, and Pb

Nicolas Bock and Duane C. Wallace (T-1),
D. Coffey (Buffalo State College)

The electron-phonon interaction is known to affect measurably a number of quantities. The low-temperature specific heat of metals for example is linear in temperature,

$$C = (\Gamma_{bs} + \Gamma_{ep})T = \Gamma_{bs}(1 + \lambda)T$$

and consists of contributions from band structure (Γ_{bs}) and electron-phonon interaction (Γ_{ep}). λ depends on the material and is generally quite small for nearly free electron metals and of order 0.1. For transition metals or strongly correlated materials λ can be as large as 1.2–2 and become very important for our theoretical understanding of those materials. For instance, one can calculate the electronic

density of states at the chemical potential from the coefficient Γ_{bs} of the specific heat, which is an important quantity in theoretical models. Without accurate knowledge of the size of the effect of the electron-phonon interaction, λ , an accurate density of states cannot be extracted from experiment. A better understanding of the electron-phonon interaction is also important for other phenomena. The effect of superconductivity for example is caused by the effective interaction between electrons mediated by their interactions with phonons in a number of metals.

In this work we calculated the electron-phonon contribution to the free energy within the pseudopotential formalism up to second order in the interaction. The phonon spectrum was calculated from a Born-von Kármán force constant model and the pseudopotential from Harrison and Ashcroft pseudopotential models. We used appropriate parameters for four different metals, Na, K, Al, and Pb. We divided the free energy into an adiabatic and a non-adiabatic contribution. We calculated these separately for the four materials for temperatures between 0 and roughly 1.5 times the melting temperature. Previous authors have not calculated the electron-phonon contribution to the free energy in such detail. By looking at only limited ranges of temperature (Grimvall) or calculating the contribution to the entropy instead of the free energy (Allen), previous authors missed important details.

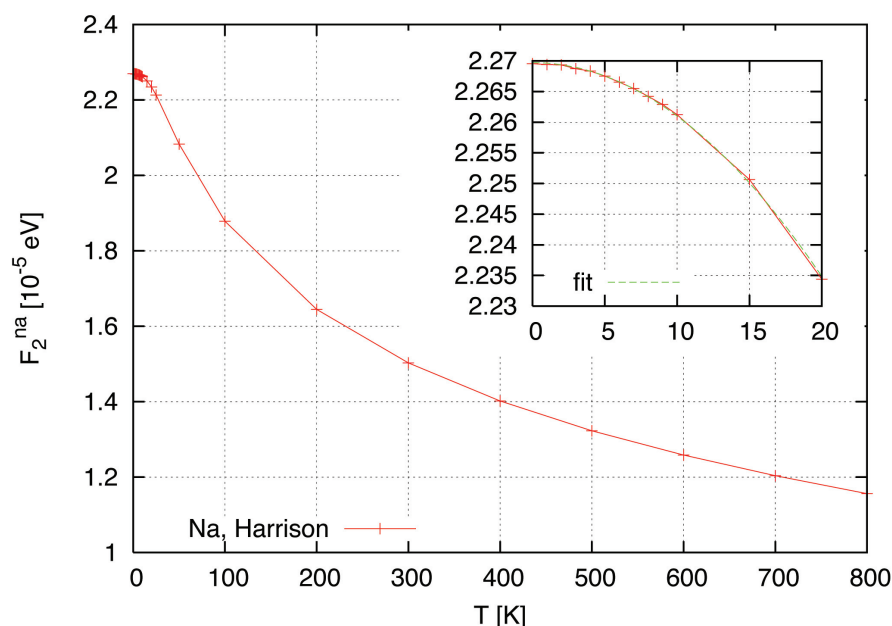


Figure 1—
The non-adiabatic contribution for Na using a Harrison pseudopotential model. Shown in the inset is a fit to the function $C_2 + A_2 T^2$.

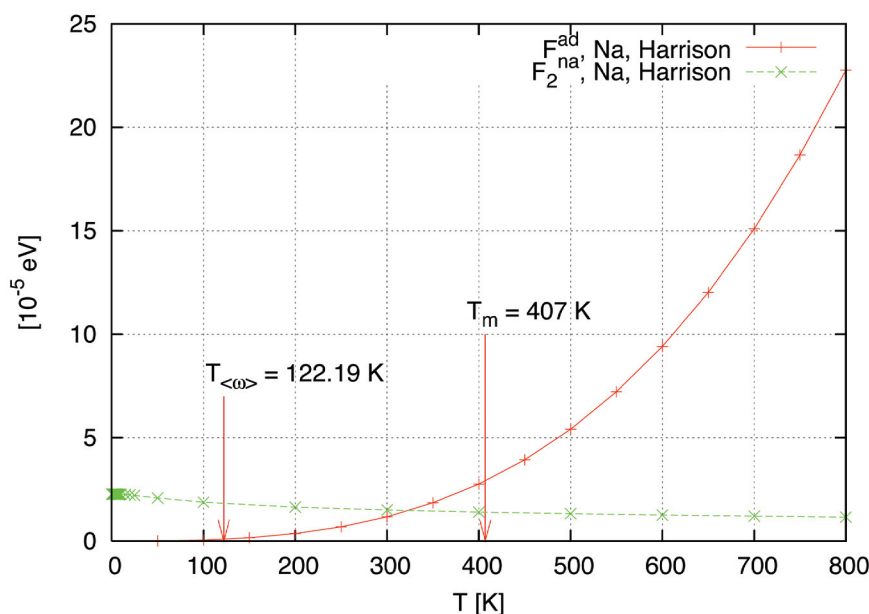


Figure 2—
Adiabatic and non-adiabatic contributions for Na in one graph. Melting temperature and temperature of the average phonon frequency are shown.

Figure 1 shows our result for the non-adiabatic contribution to the free energy for Na. From a Sommerfeld expansion at low temperatures we expect this contribution to go as $C_2 + A_2 T^2$ and the fit shown in the inset shows very good agreement with this form. We are able to extract the curvature A_2 and the zero temperature value C_2 . C_2 has not been calculated previously because previous authors calculated only the entropy.

Figure 2 shows the adiabatic and the non-adiabatic contributions for Na. The adiabatic contribution exhibits quadratic temperature dependence at low temperatures and cubic dependence at high temperatures. Since the adiabatic approximation is equivalent to the classical limit for the ion motion, it should work well at high temperatures and it is therefore not surprising that it dominates the free energy at $T > 300\text{K}$. The non-adiabatic contribution, which can be understood as the quantum corrections to the classical behavior becomes more important for low temperatures and dominates in that regime. For reference we included the melting temperature of Na and the temperature of the average phonon frequency in the graph.

The crossover between the adiabatic and the non-adiabatic contribution is at about 80% of the melting temperature and well above the average phonon frequency temperature.

Our results for K, Al, and Pb will be published elsewhere. Just as in Na, we find that the crossover happens between the melting temperature and the temperature of the average phonon frequency.

From our results it is evident that care has to be taken when calculating the free energy or derived quantities. Because the crossover is at such high temperatures a typical phonon frequency in a metal cannot be used reliably to decide whether one is dealing with a high- or low-temperature regime. Our calculations suggest that for temperatures above the average phonon frequency to up to the melting temperature both the adiabatic and the non-adiabatic contributions to the free energy need to be evaluated, whereas at low temperatures the adiabatic contribution can be safely neglected.

For more information, contact Nicolas Bock (nbock@lanl.gov).

Acknowledgements

We would like to acknowledge NNSA's Advanced Simulation and Computing (ASC), Materials and Physics Program for financial support.

Unified Model of the Grüneisen Parameter, Melting Temperature, and Shear Modulus for a Compound

*Leonid Burakovsky (T-1) and
Dean L. Preston (P-22)*

A reliable model of the adiabatic (isentropic) shear modulus of a polycrystalline solid at temperatures up to the melting temperature, and up to megabar pressures is needed for many applications. It is generally assumed that the ratio of the plastic flow stress (shear stress necessary to induce plastic deformation at a given strain rate) to the shear modulus is approximately independent of pressure. In other words, the predominant pressure dependence of the plastic flow stress is contained in the shear modulus. An accurate, simple analytic (for fast evaluation) model of the shear modulus is therefore essential for numerical simulations of material deformation over extremes of pressure and temperature.

We have developed a new unified analytic model of the Grüneisen parameter, melting temperature, and shear modulus. It allows one to construct all three—the Grüneisen gamma, melting curve, and shear modulus—in terms of a common set of input parameters, thus providing independent tests for its validity, by comparing each of the three to the corresponding data.

Initially, the model was developed for simple elemental solids. Its reliability was proven by means of good-to-excellent agreement of the predicted melting curves and shear moduli to available experimental data and theoretical calculations on over a third of the elements in the periodic table.

More recently, the model has been generalized on compounds, that is, complex substances having two or more elemental constituents. The generalized model has been used to construct new SESAME melting curve and shear modulus tables for a number of compounds. In Fig. 1, a new SESAME melting curve for lithium fluoride (solid curve) is compared to the existing SESAME table (small points) and experimental data (large points). In Fig. 2, a new SESAME shear modulus for magnesium orthosilicate is compared to the experimental data on three solid phases of this compound (shown by points of different sizes).

**For more information, contact
Leonid Burakovsky (burakov@lanl.gov).**

Acknowledgements

We would like to acknowledge NNSA's Advanced Simulation and Computing (ASC), Materials and Physics Program for financial support.

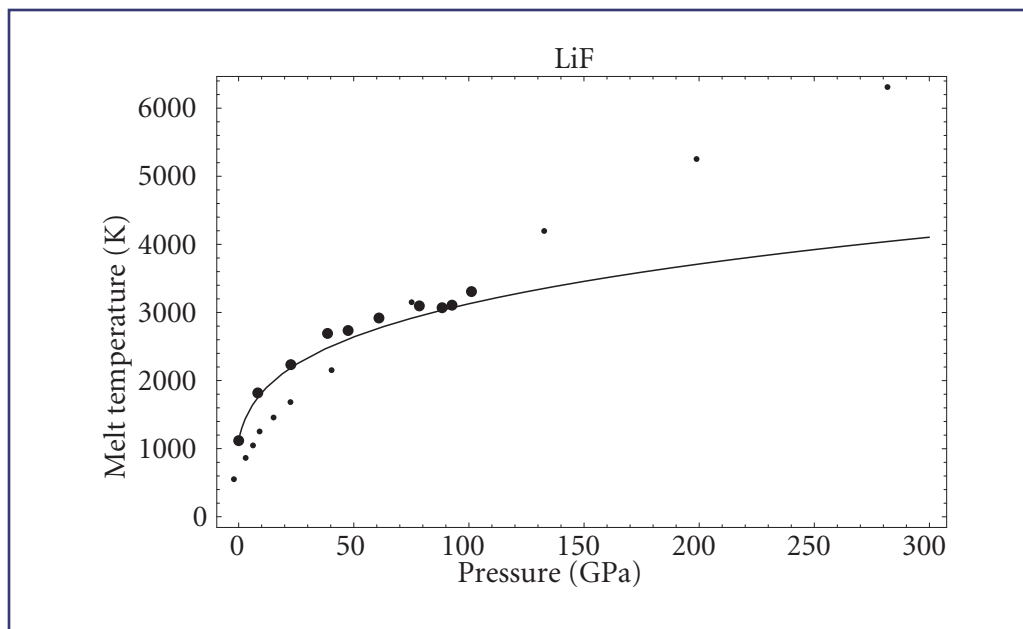


Figure 1—
A new SESAME melting curve for lithium fluoride (solid curve) is compared to the existing SESAME table (small points) and experimental data (large points).

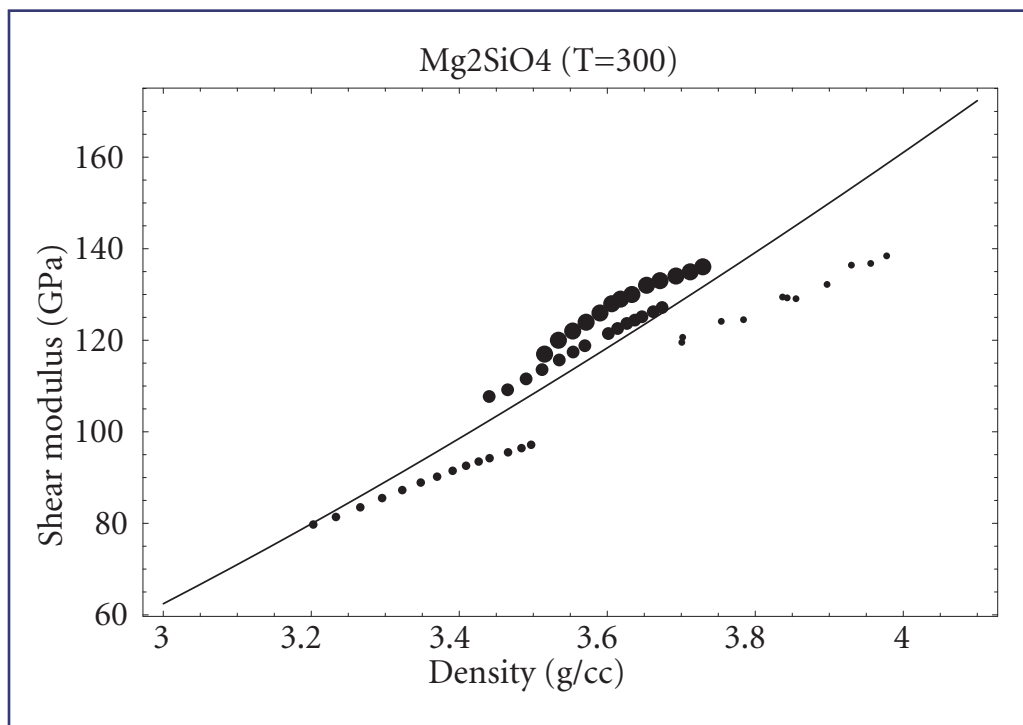


Figure 2—
A new SESAME shear modulus for magnesium orthosilicate is compared to the experimental data on three solid phases of this compound (shown by points of different sizes).

Extending the CCW EOS: Extending the Nuclear Contribution to High Temperatures

Eric D. Chisolm, Scott D. Crockett, and Duane C. Wallace (T-1)

This is a progress report on our efforts to apply the results summarized in [1] to make new equations of state (EOS) and to generate new tables for the SESAME database. In our initial work, reported in [2] and last year's volume, we described a theory that is applicable at all densities above ρ_{ref} and at all temperatures below roughly five times the melting temperature, at which point the nuclear motion becomes gaslike and renders our liquid theory inapplicable. Since a typical SESAME EOS [3] covers compressions from 10^{-4} to 10^4 and temperatures up to 10^5 eV, to construct SESAME EOS using this theory we must consider how to extend its range of validity substantially. This requires meeting two challenges: (1) extend the EOS to higher densities, where density functional theory (DFT) and experimental results are not available but the theory is still sound, and (2) extend the theory itself to high temperatures, where the nuclear motion becomes gaslike, and to densities below ρ_{ref} .

Last year we solved most of the first problem, providing techniques to extend the melt curve, solid and liquid cold curves, and solid and liquid nuclear contributions to arbitrary density. Here we report our progress on the second challenge, extending the theory; we will also summarize the problems that remain.

Our underlying strategy remains the same as in [2]: relying on basic condensed matter theory and observed trends in low-compression material behavior, we concluded that a generic material under extreme conditions will be a structureless metal crystal that melts normally to a metal liquid;

we then develop interpolations between our original EOS and this high-compression and high-temperature state. By doing so, we incorporate the best physics in each region of temperature and compression.

Before extending the nuclear theory to high temperatures, we decided to incorporate into the low-temperature liquid theory [4] a phenomenological treatment of the "boundary term" in the free energy, the term that accounts for the fact that the potential valleys in which the system moves in the liquid state have boundaries that the liquid probes in its motion. While we do not have a detailed theory for this term, its effects on the free energy of a liquid are considerable. Experimental results for C_v of nine liquid metals at atmospheric pressure and temperatures up to five times melting are well fit by the expression

$$C_{ph}^l = 3k \left[\frac{T}{T_m} \right]^{-\alpha} \quad (1)$$

where k is Boltzmann's constant, T_m is the melting temperature, and $\alpha = 0.17$ best fits the data. (See Fig. 1.) We determined the free energy that produces this specific heat and that equals the no-boundary-term liquid free energy at melt, and we used it as our low-temperature free energy for the liquid.

To determine the nuclear free energy at high temperature, we used the expression from pseudopotential perturbation theory,

$$F_{nuc}^g(\rho, T) = \Omega(\rho) + kT \left[\ln \left(\frac{\rho \Lambda^3}{M} \right) - 1 \right] + \frac{1}{2} \langle \varphi \rangle, \quad (2)$$

where the Ω term is responsible for metallic binding, φ is the interatomic potential, M is the atomic mass, and Λ is the thermal de Broglie wavelength. By examining the relative sizes of the terms in Eq. 2, we were able to argue that the middle term was by far the largest, so only it needed to be retained in our theory.

Just as at low temperatures, the high-temperature theory contains a term we have neglected up to this point: the effect of interactions between the motion of the

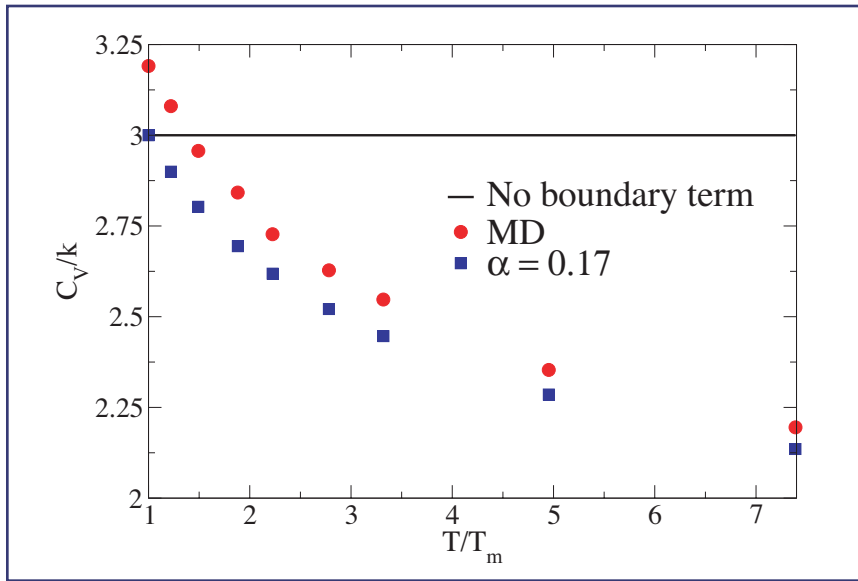


Figure 1—
The nuclear contribution to C_v for pseudo-potential sodium at $\rho = 1.0063 \text{ g/cm}^3$ as a function of T/T_m . The solid line is $C_v = 3k$, the prediction of the liquid theory without any boundary term. The circles are molecular dynamics (MD) results, and the squares are values from Eq. 1 with $\alpha = 0.17$ evaluated at the same points. The difference between the MD and Eq. 1 is due to anharmonicity, which is present in the MD and slowly approaches zero as T increases.

nuclei and thermal excitation of the electrons. At low temperatures, it can be shown that this term is much smaller than the electronic contribution, but at high temperatures that argument fails. However, we were able to argue that at high temperatures this term is much smaller than the nuclear contribution we considered in the previous paragraph, so it remains negligible at high temperatures, just as at low temperatures, but for a different reason.

Finally, we constructed interpolation formulas between the low- and high-temperature forms for the nuclear free energy as follows. We defined the nuclear free energy to be

$$F_{nuc} = \chi F_{ph}^l + (1 - \chi) F_{nuc}^g \quad (3)$$

where F_{ph}^l is the liquid free energy including boundary effects constructed at the beginning, F_{nuc}^g is the high-temperature nuclear term we just considered, and the function χ monotonically decreases from 1 at $T = T_m$ to zero as T goes to infinity, with the first two temperature derivatives vanishing at T_m . This guarantees that the new F_{nuc} reproduces the old liquid free energy and thermodynamic functions at T_m while approaching the high-temperature free energy as T increases.

The only remaining tasks are (a) to extend the electronic contribution to high compressions and temperatures, and (b) to extend the full theory to densities below ρ_{ref} .

Details of this work can be found in [5].

[1] D.C. Wallace, *Statistical Physics of Crystals and Liquids* (World Scientific, Singapore, 2002).

[2] E.D. Chisolm, S.D. Crockett, and D.C. Wallace, "Extending the CCW EOS I: Extending the Cold and Nuclear Contributions to High Compression," Los Alamos National Laboratory report LA-UR-03-7344 (Oct. 2003).

[3] S.P. Lyon and J.D. Johnson, "T-1 Handbook-Sesame Equation of State Library Volumes 1 and 2 (Public Version)," Los Alamos National Laboratory report, LA-UR-99-3900 (July 1999).

[4] E.D. Chisolm and D.C. Wallace, *J. Phys.: Condens. Matter* **13**, R739 (2001).

[5] E.D. Chisolm and D.C. Wallace, "Extending the CCS EOS II: Extending the Nuclear Contribution to High Temperatures," Los Alamos National Laboratory report LA-UR-04-3948 (June 2004).

For more information, contact Eric Chisolm (echisolm@lanl.gov).

Acknowledgements

We would like to acknowledge NNSA's Advanced Simulation and Computing (ASC), Materials and Physics Program for financial support.

Dynamic Response of Simple Liquids from Vibration-Transit Theory

Giulia De Lorenzi-Venneri and
Duane Wallace (T-1)

The Vibration-Transit (V-T) theory for liquid dynamics [1], recently developed in our group, is a new fundamental tool to evaluate accurate equations of state but also it gives a new insight in the physics of liquids. In this work we applied V-T theory to study the dynamic response of a simple liquid. We found not only support for the theory, through comparison with molecular dynamics (MD) simulation, but also we were able to contribute to the understanding of the microscopic origin of the Brillouin peak of inelastic scattering experiments.

Vibration-Transit theory is based on the idea that the many-body potential energy surface underlying the motion of the liquid system consists of an enormous number of valleys, the overwhelming majority of which correspond to random configurations of the atoms in the system. All these random valleys have the same energy and the same macroscopic properties. The barriers between valleys are sharp and the time spent by the system in the transitions from one valley to another is almost instantaneous.

The random valleys are quasiharmonic and they all have the same distribution of normal mode frequencies. The entire motion in the monatomic liquid is then comprised of two elements: vibrations in the random valleys and transits between them. Both experimental results and MD simulations support this view.

One interesting probe of the dynamic response of liquids is the dynamical structure factor, $S(q, \omega)$, which is the power spectrum of the time dependent density-density correlation function, and therefore a direct test of the microscopic dynamics. On the other hand $S(q, \omega)$ enters in an explicit formula for the cross sections in inelastic scattering experiments and can therefore be actually measured.

A typical behavior of $S(q, \omega)$ from MD simulation is shown in Fig. 1. Our system is a simple monatomic liquid, sodium at the density of the melt, with 500 particles with periodic boundary conditions, at a temperature just above melting, $T = 395\text{K}$. We explore a range of small q , close and up to the maximum of $S(q)$, the static structure factor. The Brillouin peak is clearly dominant. As q increases, its maximum shifts from small ω to larger ones and eventually it turns around. At $q = 1.1050 \text{ bohr}^{-1}$, almost at the maximum of $S(q)$, the Brillouin peak disappears, while the Rayleigh peak becomes dominant.

If the liquid is rapidly quenched, it falls in one of the random valleys and a low temperature trajectory remains trapped inside that valley for a very long time. $S(q, \omega)$ in this supercooled liquid, shown in Fig. 2, exhibits a very similar behavior to the liquid, but the Rayleigh peak has disappeared and the Brillouin peak is sharper.

For this supercooled liquid, V-T theory gives an explicit expression for $S(q, \omega)$ in terms of only the positions of the atoms in a random configuration (at the bottom of the valley) and its normal mode frequencies and eigenvectors (there are no transits). A comparison of the V-T theory prediction and MD evaluation for one typical q is shown in Fig. 3. The agreement is perfect, showing that the approximations used in the theory (harmonic one-phonon) are highly accurate.

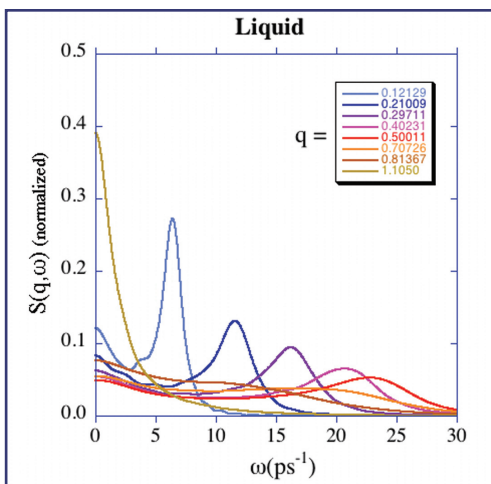
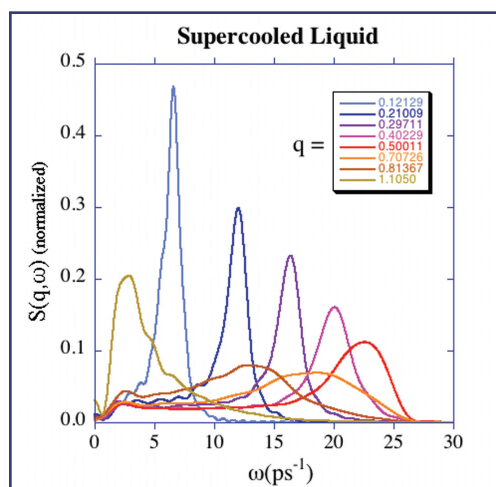
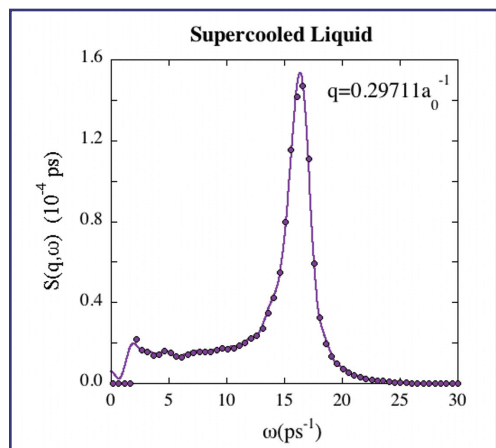


Figure 1—
Dynamic Structure Factor for sodium at $T = 395\text{K}$ from molecular dynamics simulation for eight different values of q (in units of bohr^{-1}). In this case the system wanders among many different random valleys; there is ample diffusion.



But furthermore we learned an important fact about the nature of the Brillouin peak. From the theory, $S(q, \omega)$ is the sum of statistically independent cross sections for a set of noninteracting vibrational modes. This means that the width of the Brillouin peak in Fig. 2 and Fig. 3 is the *natural width*. No relaxation process is involved.



For the liquid system, we can still separately evaluate from V-T theory the contribution of only the vibrational motion in one typical single random valley at $T = 395\text{K}$. The comparison with a complete MD evaluation of $S(q, \omega)$ is shown in Fig. 4. The striking result is that the position of the Brillouin peak, evaluated from the vibrational motion in a single random valley (V-T theory) and from a MD trajectory that transits among numerous valleys, is the same in both, and we see that the natural width is about half of the width in the liquid. This result is valid for the

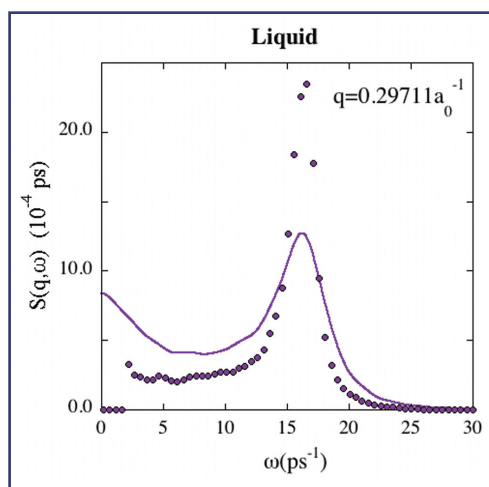


Figure 2—
As in Fig. 1, but at $T = 24\text{K}$. In this case the system is trapped in a single random valley; there is no diffusion.

whole range of q for which a Brillouin peak is present, as depicted in Fig. 5. The figure proves that this dispersion curve for the liquid (which is in agreement also with experiments) can be completely evaluated from only the independent vibrational modes in a single valley, without the need to invoke coupling between the modes and relaxation

Figure 3—
Comparison between molecular dynamics and V-T theory for one of the cases shown in Fig. 2 at $T = 24\text{K}$.

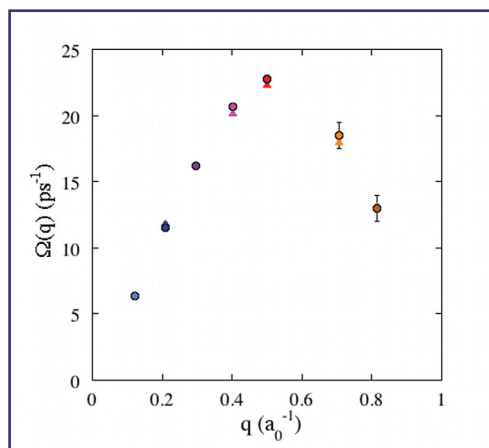


Figure 4—
Comparison between molecular dynamics and V-T theory for one of the cases shown in Fig. 1 at $T = 395\text{K}$.

Figure 5—
Position of the Brillouin peak maximum as a function of q , in the liquid. Molecular dynamics results (circles) and V-T theory (triangles) almost coincide.

times, a notion in contrast to previous interpretation.

Work to study the role of transits and how to incorporate them in explicit evaluations within V-T theory is presently underway.

[1] D.C. Wallace, *Phys. Rev. E* **56**, 4179 (1997).

For more information, contact Giulia De Lorenzi-Venneri (gvenneri@lanl.gov).

Acknowledgements

We would like to acknowledge NNSA's Advanced Simulation and Computing (ASC), Materials and Physics Program for financial support.

Direct Numerical Simulations of PBX 9501 with Reaction Chemistry

*Eric M. Mas, Brad E. Clements, and
Denise C. George (T-1)*

This is the continuation of last year's report on direct numerical simulations (DNSs) of the high explosive PBX 9501 [1]. Last year we described how we were representing individual high-explosive grains in the composite high explosive PBX 9501. PBX 9501 has a very complicated microstructure, consisting of high-melting explosive (HMX) grains (95 wt%) embedded in a plasticized Estane® polymer matrix (5 wt%). The HMX grains range in size from several hundred micrometers to submicrometer diameters. In last year's report we described how we generated a 1-million-element three-dimensional (3D) mesh of PBX 9501 using an experimental particle size distribution of HMX crystals. We also described how we applied a load to this virtual sample of PBX 9501 similar to the load the material would experience in a Split Hopkinson Pressure Bar experiment. We showed that the mechanical response was similar to that observed in the experiment. We also showed that the microstructure had dramatic effects on the distribution of all tracked observables within the sample including stress and pressure. Finally, we described why these simulations were of great interest to scientists in Chemistry Division. Since we observed broad peaks in the pressure distribution, and not a spike at the average pressure as would be predicted by a homogeneous model, these simulations suggest that even during high compression rate experiments, such as plate impact experiments, regions of relatively low pressure persist. This would allow pores which are known to exist in the high explosive to remain while those in the high pressure regions are squeezed out. These pores are thought to be integral in maintaining the high explosives shock sensitivity; without them, it is believed,

the material becomes insensitive to shock initiation. But, the experimentalists are not observing this type of behavior, and they believe that our simulations may explain why they do not. In this report we describe how we have extended our model by incorporating reaction chemistry into the model.

For the HMX grains that are explicitly represented in the 3D mesh of PBX 9501 we incorporated a two-phase reaction chemistry model into the simulations. We represented the solid phase with a linear $U_s - U_p$ form of the equation of state with constant specific heat. A gamma law also with a constant specific heat described the gas phase of the HMX. The mixture of the unreacted and reacted material was solved assuming common pressure and temperature by using Newton's method. The finite element analysis coupled with the material response of the HMX provides us everything we need except the relative amount of solid and gas which we attained from a single Arrhenius relationship experimentally determined and found in Gibbs and Popolato (Los Alamos Scientific Laboratory Explosive Property Data). This is the same kinetics used in the JTF model for PBX 9501 except in that model the temperature is an effective hot spot temperature which was parameterized to fit experimental data. In the present case the temperature is the one predicted by our mechanical response and two-phase mixture of gas and solid.

We conducted two high-rate simulations on our virtual sample of PBX 9501; one that mimicked a Taylor impact test and one that mimicked a plate impact test. In the Taylor test the PBX 9501 sample impacts a rigid steel anvil. We approximate this in the simulation by applying velocity boundary condition to the bottom of the sample moving up at a rate similar to those used in these experiments. There are no constraints on the virtual sample for any of the other nodes, and the nodes that are forced into the sample are allowed to move laterally relative to the direction of applied load. The plate-impact experiment is similar to the Taylor simulation except that the nodes on the surface of the virtual sample on the four lateral surfaces must remain on those surfaces. This more closely approximates a uniaxial strain experiment that is produced in a real plate-impact test.

Figure 1 shows the temperature 0.34 microseconds into the simulation of the Taylor test. Figures 1 and 2 are of a slice through the middle of the 3D virtual sample of PBX 9501. We can see the wave traveling up the sample and the lateral surfaces expanding in response to the load. The temperature plot shows a region of heightened temperature. The “dirty-binder,” discussed in last year’s report, is represented by the purple color and does not enter the calculations for temperature because currently we are only allowing the large HMX crystals to change phases. This is helpful in that it allows us to determine where within the large HMX crystals we are predicting reaction. We note here that these simulations are meant to be proof-of-principle calculations. We realize that observing temperature spikes in a single element is endemic of under-resolution of the grid; however, we believe that we can still draw qualitative information from these simulations and can determine if further research is warranted. As can be seen, the temperature spikes seem to occur within the HMX grains and on their surface with equal likelihood. This is in qualitative contrast with the plate impact simulation in Fig. 2 where the temperature spikes are preferentially on the surface of the large grains, specifically, at what appear to be bridging points.

Figure 2 shows the temperature distribution in the virtual PBX 9501 sample 0.5 microseconds into the simulation. As mentioned above, the distribution is qualitatively different from the Taylor simulation. We also note that in this case the temperature spikes are distributed over several elements, which may indicate that we are at an adequate spatial resolution for these simulations.

In summary, these are preliminary simulations and represent a proof-of-principle calculation. Our kinetics equation uses single-step kinetics and is an oversimplification of the true reaction dynamics of HMX. Mechanisms such as frictional heating between grains, frictional heating across crack surfaces, and pore

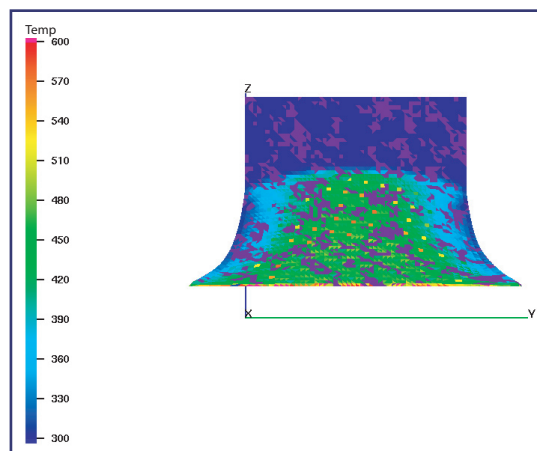


Figure 1—
Snapshot of the temperature distribution in the Taylor impact simulation after 0.34 microseconds.

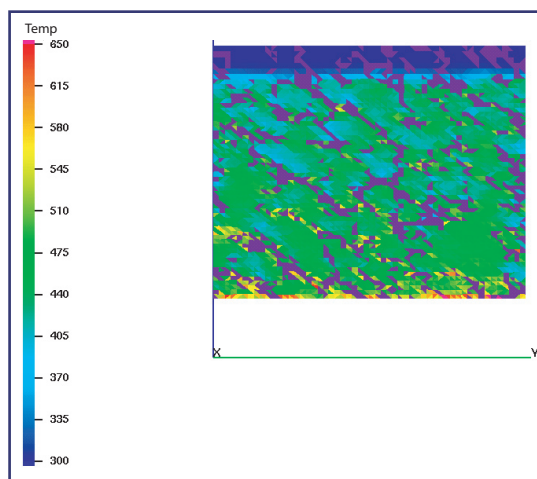


Figure 2—
Snapshot of the temperature distribution in the plate impact simulation after 0.5 microseconds.

collapse are absent from our calculations.

We are looking at a single mechanism for the formation of hot spots, namely, focusing of deformation due to plasticity and microcracking from the heterogeneity of the microstructure of PBX 9501. While we do not believe that this is the only mechanism for hot-spot generation, we believe that this study strongly indicates that it cannot be ignored as a contributing factor.

[1] E.M. Mas, B.E. Clements, D.C. George, “Theoretical Division Activities in Support of the Nuclear Weapons Program,” Los Alamos National Laboratory report LA-UR-04-0916 (Feb. 2004), p. 110.

For more information, contact Eric M. Mas
(mas@lanl.gov).

Acknowledgements

We would like to acknowledge NNSA’s Advanced Simulation and Computing (ASC), Materials and Physics Program, and the Joint DoD/DOE Munitions Technology Development Program for financial support.

Calculations to Refine Beryllium's Equation of State

Sven P. Rudin and J. D. Johnson (T-1)

Our current equation of state (EOS) for beryllium is based on experimental data and empirical models. This construction does not fully constrain the resulting EOS, and recently uncovered experimental results in the literature show slight disagreement with the established EOS of Be. Is this due to the original construction of the EOS, or are the original and newer experiments incompatible with each other? To help resolve this question, we turn to the third underpinning of a successful EOS, density functional theory (DFT) (see Fig. 1).

Figure 2 shows the calculated average phonon frequency θ_0 for Be in the hexagonal close packed (hcp) structure as a function of volume. This average phonon frequency provides a measure for how much thermal energy Be can absorb. How this measure changes with volume determines the thermal EOS and is quantified in the Grüneisen parameter Γ . The Grüneisen parameter is given by the (logarithmic) derivative of θ_0 with respect to the volume, which we obtain by first fitting our calculated θ_0 as a function of V .

Figure 3 compares the calculated Grüneisen parameter with that of the original EOS model. While the differences are reasonably small, a slight change in the model improves the agreement without destroying the good agreement obtained for other variables such as the cold curve (see Fig. 4).



Figure 1—
The three components that contribute complementary data to an EOS—experiment, empirical models, and DFT calculations.

The average phonon frequencies shown here are from preliminary calculations using DFT. These calculations are now being systematically improved, the end goal being an EOS for Be that is consistent with all data available to us.

*For more information, contact
Sven P. Rudin (srudin@lanl.gov).*

Acknowledgements

We would like to acknowledge NNSA's Advanced Simulation and Computing (ASC), Materials and Physics Program for financial support.

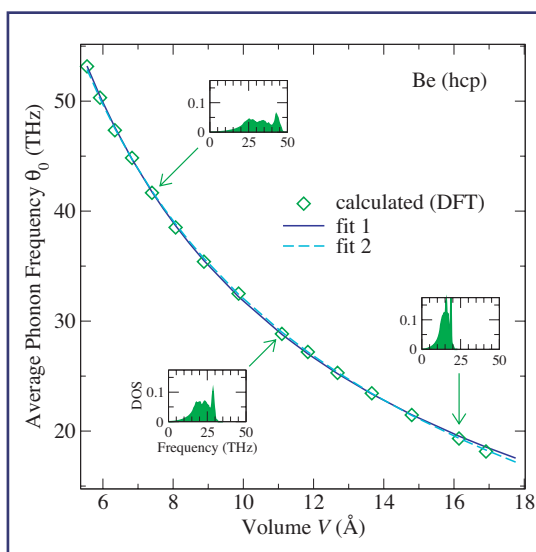


Figure 2—
Calculated average phonon frequency θ_0 for Be in the hcp crystal structure as a function of volume. The functional form of the two fits gives either a linear (fit 1) or a quadratic (fit 2) relation between the Grüneisen parameter Γ and the volume V .

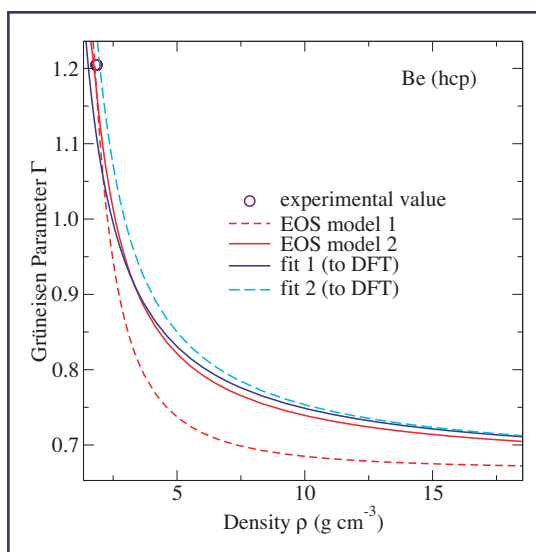


Figure 3—
Grüneisen parameter Γ for Be. The two fits to the DFT calculations lie very close to each other but differ somewhat from the old EOS model (model 1). A slight change in the model (now model 2) gives better agreement. All curves are forced to tend towards $2/3$ with increasing density ρ .

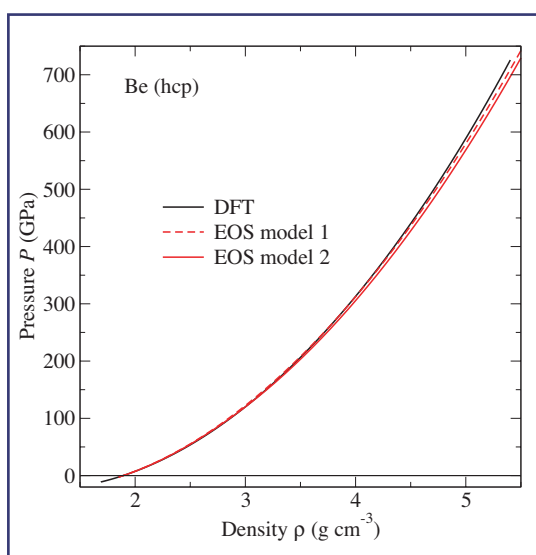
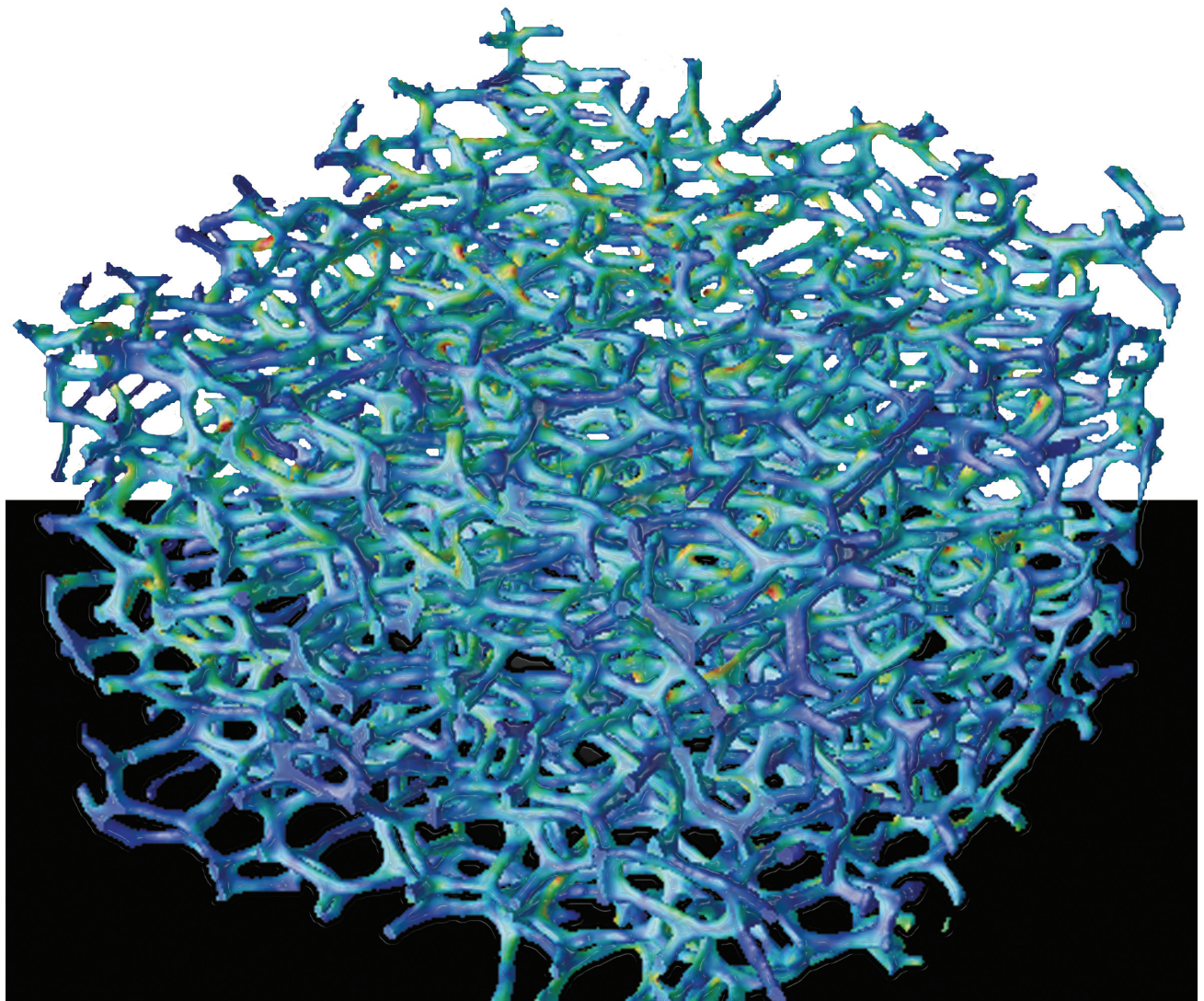


Figure 4—
Cold curves for Be. The curve calculated with DFT is in good agreement with both the original EOS model (model 1) as well as the model that was refit (model 2) to agree better with the calculated Grüneisen parameter.

CONDENSED MATTER, MATERIALS SCIENCE, AND CHEMISTRY



Nonspherical Void Growth Theories

Brad E. Clements and Eric M. Mas (T-1),
and Paul J. Maudlin (T-3)

This work is a continuation of our efforts to develop a nonspherical void growth model to be used in important U.S. Department of Defense (DoD) and Department of Energy (DOE) applications. An example of a problem of interest is HY-100 steels. Metallographic fractography shows that low concentrations of manganese sulfide (MnS) impurities have a significant role in the fracture of HY-100 steels [1]. Examination of spalled HY-100 samples reveal that the MnS impurities act as microvoid initiation sites necessary for ductile fracture to occur. The MnS impurities form, during the rolling process, into high-aspect ratio-aligned inclusions. The alignment is the origin of the orientation dependence observed in fracture. Consequently, to model the fracture occurring in these steels it is important to include the nonspherical shape and orientation of the MnS impurities. There are several candidate theories in the scientific literature that might provide a good beginning point to modeling the damage processes occurring in these steels and in this work we focus on Continuum Damage Mechanics (CDM) and Gologanu-Leblond-Devaux (GLD) theory [2]. Background literature on CDM can be found in Lemaitre and Chaboche [3]. On the other hand, GLD theory provides a useful description of a flow surface for a material containing axial-symmetric ellipsoidal voids subjected to axial-symmetric loading and provides an important extension of Gurson's work [4] on flow stress surfaces for materials containing spherical voids. In FY04 we merged CDM, Gurson, and GLD theories to introduce a flow surface for nonsymmetric ellipsoidal voids with nonaxial-symmetric loading. In the present analysis we compare the predictions of these theories.

Continuum Damage Mechanics is based on the conjecture that there exists an effective stress $\tilde{\sigma}$ defined such that the complete

continuum mechanics of a damaged material can be described by invoking a corresponding set of constitutive equations, given for an undamaged material, but with the simple replacement, $\sigma \rightarrow \tilde{\sigma}$. This replacement includes, for example, the stresses appearing in inelastic constitutive equations. The second conjecture of CDM is that $\tilde{\sigma}$ is then simply the stress carried by the undamaged cross-sectional area and a damage variable D can be introduced that is the fraction of damaged to the total cross-sectional areas.

For prolate ellipsoidal voids (aligned with the z axis) the GLD flow surface has the form:

$$F_{GLD} = \frac{C}{Y^2} (\sigma_{zz} - \sigma_{xx} + \eta \sigma_h)^2 - 1 - qf^2 + 2qf \cosh \left[\frac{\kappa \sigma_h}{Y} \right] = 0$$

In the limit of aspect ratio, β , equaling one, the GLD flow surface becomes the Gurson flow surface. In these expressions $(\sigma_{xx}, \sigma_{yy}, \sigma_{zz})$ are the three normal components of the stress tensor, C, k, η and σ_h are complex functions of the void and unit cell ellipsoid eccentricities, and β . Y is the flow stress of the matrix material, q_0 is an adjustable material parameter (taken equal to unity here), and f is the void volume concentration. In this expression the flow stress of the voided material Σ is

$$\Sigma_{GLD}^2 = Y^2 \left(1 + qf^2 - 2qf \cosh \left[\frac{\kappa \sigma_h}{Y} \right] \right).$$

From CDM theory we can derive (omitting the details)

$$F_{CDM} = \left(\frac{\sigma_{xx}}{1-D_1} - \frac{\sigma_{yy}}{1-D_2} \right)^2 + \left(\frac{\sigma_{xx}}{1-D_1} - \frac{\sigma_{zz}}{1-D_3} \right)^2 + \left(\frac{\sigma_{zz}}{1-D_3} - \frac{\sigma_{yy}}{1-D_2} \right)^2 - 2(\Sigma/\alpha)^2 = 0$$

where

$$\Sigma_{CDM}^2 = (Y/\alpha)^2 \left(1 + qf^2 - 2qf \cosh \left[\frac{3\tilde{p}}{2(Y/\alpha)} \right] \right),$$

and \tilde{p} and α are functions of the damage fields.

Figure 1 shows the flow stress surface, expressed in stress space. The flow stress surface is the locus of points $(\sigma_{xx}, \sigma_{zz})$,

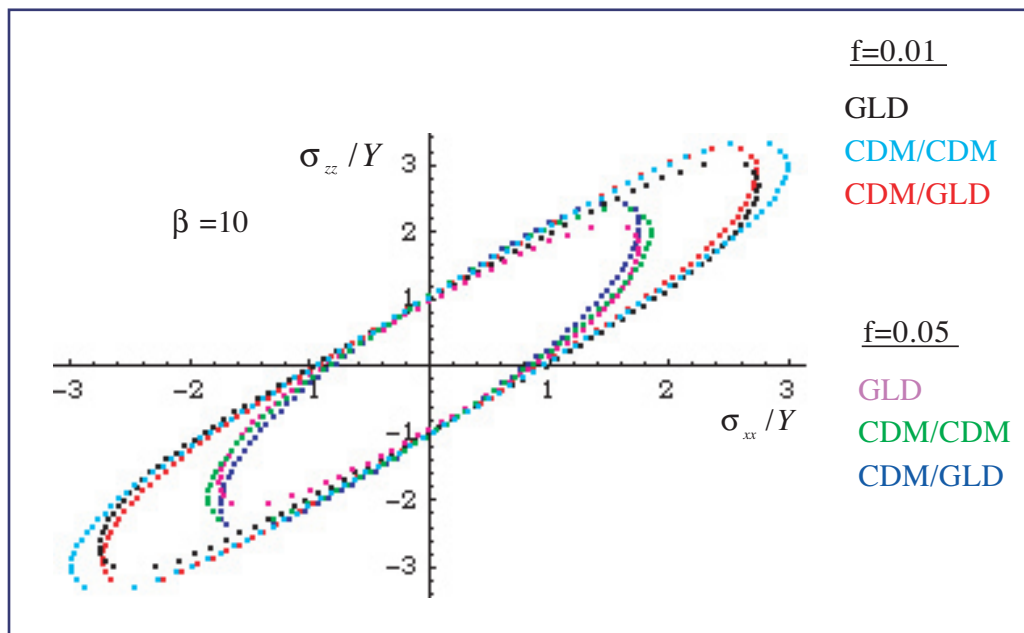


Figure 1—
Flow stress surfaces
predicted by GLD,
CDM, and CDM-GLD
merged theories.

normalized by dividing by the matrix flow stress Y , that satisfy the condition $F = 0$. In F_{CDM} we can use two choices for Σ , namely the GLD and CDM forms, giving three flow surfaces to compare. Qualitatively and even quantitatively we see little difference between the three flow surfaces. Consequently, we assert that F_{CDM} compares well to F_{GLD} in this special case and moreover is general enough to handle nonaxial-symmetric prolate ellipsoids and arbitrary loads.

Acknowledgements

We would like to acknowledge NNSA's Advanced Simulation and Computing (ASC), Materials and Physics Program, and the Joint DoD/DOE Munitions Technology Development Program for financial support.

- [1] R.K. Everett and A.B. Geltmacher, *Scripta Materialia*, **40**, 567–571 (1999).
- [2] M. Gologanu, J.-B. Lablond, and J. Devaux, *J. Mech. Phys. Solids*, **41**, 1723–1754 (1993).
- [3] J. Lemaitre and J.L. Chaboche, *Mechanics of Solid Materials* (Cambridge University Press, Cambridge, UK, 1990).
- [4] A.L. Gurson, *ASME J. Enging Mat. and Tech.*, **99**, 2–15 (1997).

For more information, contact
Brad E. Clements (bclements@lanl.gov).

Large-Scale Dislocation Dynamics Simulation of Bulk Deformation

Richard LeSar (T-12), and Nasr Ghoniem and Zhiqiang Wang (University of California at Los Angeles)

In most engineering-level calculations of materials response, the deformation properties are described by empirical constitutive relations, usually in terms of the stress, strain, strain rate, etc. The quality of the predictions of materials behavior in such calculations depends largely on the fidelity of the constitutive relations. These relations consist of sets of models designed to describe different aspects of materials deformation, with the overall parameters found by comparing the net behavior to experiment. Thus, while it is possible to infer some information about the accuracy of the models that make up the constitutive relation, it is not possible, in general, to directly test the underlying physics of the individual models. The overall goal of this project is to develop better understanding and phenomenology of the fundamental processes of deformation and to use that to create better descriptive models for use in engineering-level simulations.

Plastic deformation in crystalline metals is a consequence of the collective motion of large numbers of dislocations, which are curvilinear defects that interact via complex, long-ranged interactions. In a typical deformable material, such as a metal, dislocation densities range from about 10^{10} to $10^{15}/\text{m}^2$, i.e., 10^{10} to 10^{15} meters of dislocations in a cubic meter of material, values that typically increase rapidly under applied stress (or strain). The mobility of dislocations gives rise to plastic flow at relatively low stress levels compared to the theoretical strength. Dislocations form organized structures such as walls, cells and pile-ups. Differences owing to the topological constraints placed by

crystallography greatly add to the complexity of describing dislocation microstructural evolution and dynamics.

To develop a better understanding of the complexity of dislocation structures and dynamics, we have been developing a robust computer simulation method employing the technique of Dislocation Dynamics (DD). In DD simulations, the underlying atomic structure is ignored, the dislocations are the simulated entities and their movement is tracked during the simulation. In the past few years, there has been an increasing use of direct three-dimensional simulation of the evolving dislocation microstructures employing the DD technique. There are a number of groups working to develop these methods, including the Advanced Simulation and Computing (ASC) program at Lawrence Livermore National Laboratory and others. Dislocation Dynamics simulations are very expensive computationally, limiting the maximum stress, and the consequent dislocation density, that can be applied to the sample. They can, however, provide “data” about specific processes not available experimentally, which can then be used in the development of models of deformation.

Recently Ghoniem and his group at University of California at Los Angeles have developed a new approach to DD simulations, in which the dislocations are described as a set of nodes and a spline interpolation between the nodes is employed to determine the location of the dislocation line. The forces and energies are obtained by numerical integrations along the loops. While this approach is very promising, a great deal of computational development is needed before it could handle sufficiently large numbers of dislocations to be applied to problems of interest. Rather than develop a Los Alamos National Laboratory version of his code, we have begun a collaboration to develop a parallel 3D DD code that employs a multipolar expansion for the stress, which reduces the computational burden tremendously.

The first step in our collaboration was to ensure that the basic methodology was sound. In a collaboration with an experimental effort in the Materials Science and Technology Division (funded through

Office of Science), we performed the first detailed comparisons between discrete dislocation simulations and experiments [1]. In the experiments, the 3D position of a set of dislocations in a thin foil of copper was determined. The system was strained and then the new positions were found. We started the simulations at the experimental initial conditions, applied the same strain, and calculated the final positions. In Fig. 1 we show a comparison between the experimental and calculated final positions. The good agreement between experiment and simulations results shows that the basic methodology is sound.

Once we had assured ourselves as to the accuracy of the method, we began a project to improve the computations. We started by creating a parallel version of the dislocation dynamics code, based on the hierarchical tree structure developed in the MONDO project (M. Challacombe, T-12, also supported by the ASC program) [2]. We find very good scaling, with a loss of efficiency of less than 15% up to about 60 processors. In Fig. 2, we show simulated dislocation microstructures in copper at 0.1% strain. Note the beginnings of the development of structure. Parallelization is not sufficient, however, as dislocations interact with long-range forces, with a computer time that scales as the square of the length of dislocations. To achieve much higher dislocation densities, we are implementing a multipole method to reduce computational time to be approximately linear with the length of dislocations [3].

We are now well poised to begin detailed simulations of the fundamental processes of deformation at a dislocation level. The next steps are to finish implementation of the multipole methods and to port the parallel code to Los Alamos machines with much larger number of processors. We will then be able to simulate dislocation structures and

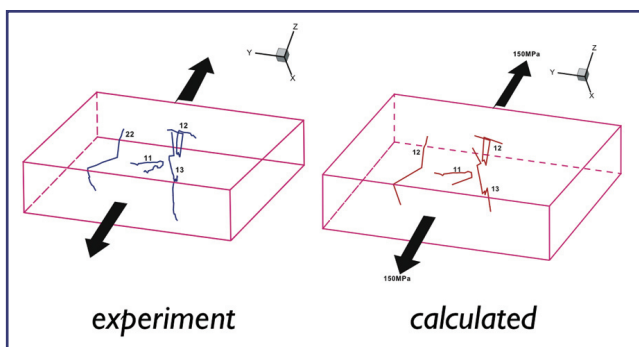


Figure 1— Experimental and calculated dislocation positions. This was the first study to directly compare calculated dislocation motion and experimental results in three dimensions.

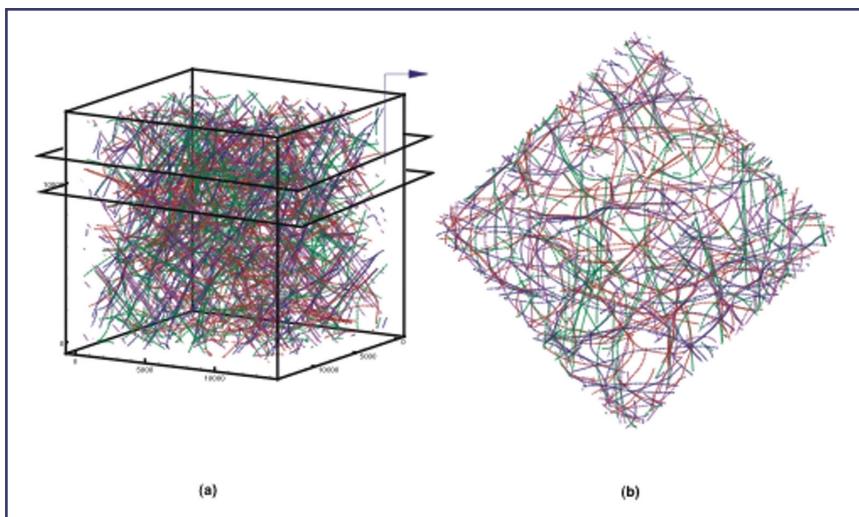


Figure 2— (a) Calculated dislocation microstructure in copper strained to 0.1%. The colors indicate the slip plane. The system size is $5\ \mu\text{m} \times 5\ \mu\text{m} \times 5\ \mu\text{m}$. (b) A view through the slice shown in the full cube. The final dislocation density is about $1.45 \times 10^{13}/\text{m}^2$.

dynamics in real systems under conditions of interest to Los Alamos.

- [1] Z. Wang, et al., "Dislocation Motion in Thin Cu Foils: A Comparison between Computer Simulations and Experiment," *Acta Mater.* **52**, 1535-42 (2004).
- [2] Z. Wang, et al., "Parallel Algorithm for 3D Dislocation Dynamics," submitted to *J. Comput. Phys.*
- [3] Z. Wang, N.M. Ghoniem, and R. LeSar, "Multipole Representation of the Elastic Field of Dislocation Ensembles," *Phys. Rev. B* **69**, 174102 (2004).

For more information, contact
Richard LeSar (ral@lanl.gov).

Acknowledgements

We would like to acknowledge NNSA's Advanced Simulation and Computing (ASC), Materials and Physics Program for financial support.

N-Scaling Materials Response by Density Matrix Perturbation Theory

Anders M.N. Niklasson (T-1),
Matt Challacombe (T-12), and
Valéry Weber (T-12 and University of
Fribourg, Switzerland)

During the last decade a new computational approach has evolved in electronic structure theory, where no critical part of a calculation is allowed to increase in complexity more than linearly, $O(N)$, with system size, N [1]. This linear scaling electronic structure theory extends conventional tight-binding, Hartree-Fock, or Kohn-Sham methods to the study of very large complex systems previously out of reach. This is critical for applications to new important areas of research, such as biology, medicine, and nanoscience, which requires the ability to handle much larger systems than previously possible.

Until recently most attention was focused on linear scaling $O(N)$ methods for calculating the ground state electronic energy. However, an important problem that so far has received little attention is the $O(N)$ computation

of materials response properties, such as interatomic potentials, vibrational frequencies, the polarizability, nuclear magnetic resonance, and Raman intensities.

We have introduced a new and surprisingly simple reduced complexity quantum perturbation theory [2, 3]. The approach is based on $O(N)$ spectral purification projection schemes for the zero-temperature density matrix [4, 5]. The new perturbation theory makes it possible to calculate the adiabatic response properties for nonmetallic materials to any order within linear scaling effort.

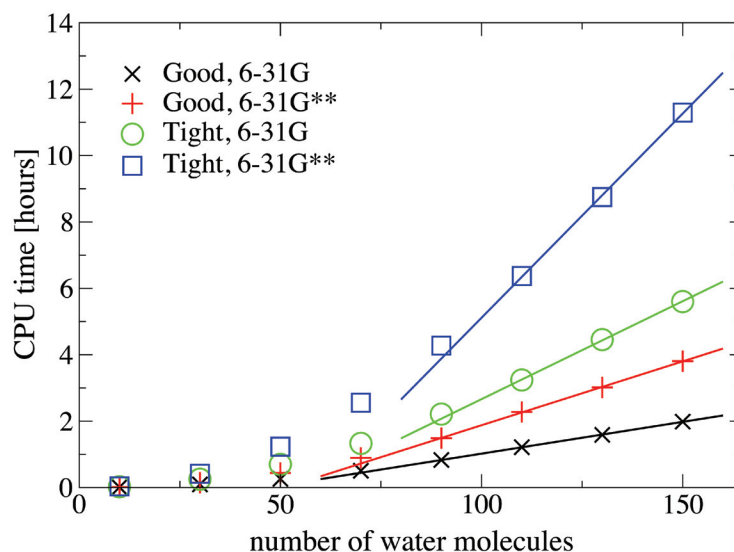
The numerical efficiency of density matrix purification projection methods is based on the quantum locality (or nearsightedness) of nonmetallic systems, manifested in the approximate exponential decay of the density matrix with interatomic separation. Using efficient sparse matrix algebra, neglecting matrix elements below a chosen numerical threshold, the density matrix can be constructed with a computational cost that scales linearly with system size.

The general idea behind purification is that the density matrix D can be described recursively as

$$D = \theta(\mu I - H) = \lim_{n \rightarrow \infty} F_n(F_{n-1}(\dots F_0(H)\dots)), \quad (1)$$

where $F_n(F_{n-1}(\dots F_0(H)\dots))$ is an iterative expansion of the Heaviside step function $\theta(\mu I - H)$. The functions F_n are low order polynomials, projecting eigenvalues to fix points at 0 for unoccupied states and to 1 for

Figure 1—
The computational cost for the first hyperpolarizability of water clusters as a function of basis set and cluster size [6].



occupied states, thereby “purifying” the approximate density matrix. By choosing the purification projectors F_n to be polynomials, only matrix-matrix operations have to be performed. This is achieved with linear scaling $\mathcal{O}(N)$ complexity for sufficiently sparse systems.

The main problem with density matrix perturbation theory is the discontinuous relation between the zero temperature density matrix and the Hamiltonian given by the step function in Eq. 1. This makes an expansion of D around a perturbation in H difficult. At finite temperatures the discontinuity disappears, but instead the analytic Fermi-Dirac distribution involves problems with matrix exponentials and the chemical potentials. However, within the recursive purification scheme an initial perturbation in H can be carried through at each projection level, either exactly or to any order. The resulting perturbed projection scheme provides an efficient technique for the calculation of materials response properties within a reduced complexity formalism [2, 3].

Our new perturbation theory has been implemented in MondoSCF, a suite of parallel linear scaling program for the *ab initio* calculation of electronic structure properties. Linear scaling complexity was demonstrated for the computation of higher order response properties of 3D structures. Figure 1 shows the computational cost for calculating the first electric hyperpolarizability of large water clusters by solving the coupled perturbed self-consistent field equations [3, 6]. After about 50–100 water molecules the computational cost scales approximately linearly with system size.

The locality of the density matrix is described by the approximate exponential decay of its matrix elements as a function of interatomic separation. This behavior is found also for the density matrix derivatives corresponding to the polarizability and hyperpolarizabilities, as illustrated in Fig. 2.

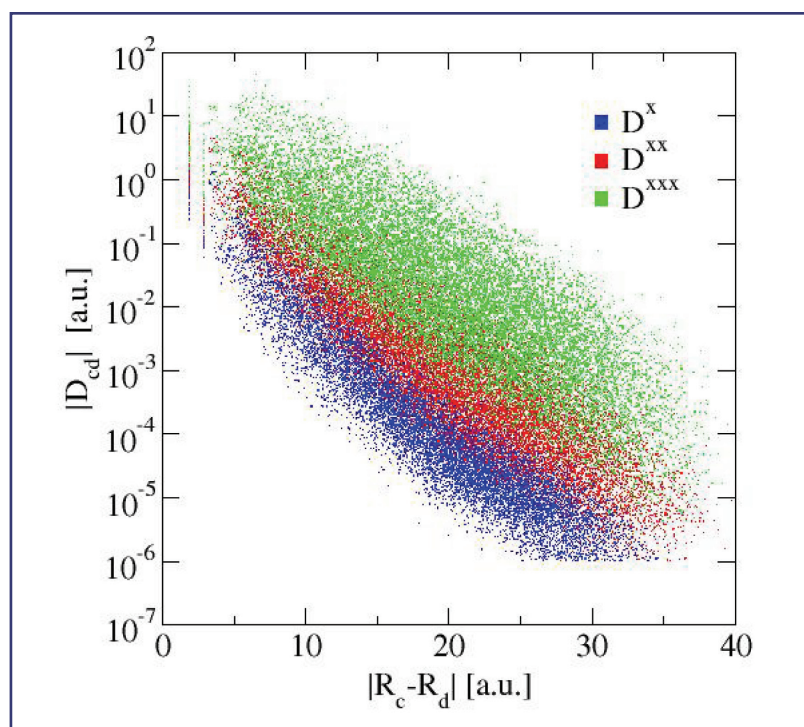


Figure 2—
The approximate exponential decay of the density matrix and its derivatives as a function of interatomic separation.

The density matrix perturbation theory can be applied in many contexts and we are currently extending the theory to new problems, including structural response within nonorthogonal representations for the calculation of vibrational frequencies.

- [1] S. Goedecker, *Rev. Mod. Phys.* **71**, 1085 (1999).
- [2] A.M.N. Niklasson and M. Challacombe, *Phys. Rev. Lett.* **92**, 193001 (2004).
- [3] V. Weber, A.M.N. Niklasson, and M. Challacombe, *Phys. Rev. Lett.* **92**, 193002 (2004).
- [4] A.M.N. Niklasson, *Phys. Rev. B* **66**, 155115 (2002).
- [5] A.M.N. Niklasson, C.J. Tymczak, and M. Challacombe, *J. Chem. Phys.* **118**, 8611 (2003).
- [6] V. Weber, A.M.N. Niklasson, and M. Challacombe, submitted to *J. Chem. Phys.* (2004).

For more information, contact
Anders M.N. Niklasson (amn@lanl.gov).

Acknowledgements

We would like to acknowledge NNSA's Advanced Simulation and Computing (ASC), Materials and Physics Program for financial support.

A Model for Heterogeneous Materials Including Phase Transformations

*Frank L. Addessio and
Todd O. Williams (T-3), and
Brad E. Clements and Eric M. Mas (T-1)*

An extension to the Method of Cells (MOC), which includes phase transformations of the constituents, has been developed. The MOC [1] is a homogenization technique that has demonstrated versatility. It has been applied to numerous composite materials and is applicable to general loading conditions. A diverse set of constitutive models has been used in the framework of the MOC both for the constituents and the interfaces. This approach is applicable to any ordered composite structure that can be idealized with a microstructural unit cell (UC), which generates the entire composite through a periodic repetition. The macroscopic stress state, which is calculated for the UC, is taken to be the stress state at the corresponding location in the equivalent homogeneous continuum. The homogenized stress state is obtained as a solution for the mechanical response of the repeating UC to an applied macroscopic strain state, knowing the response of the constituents and the interfaces of the composite. The MOC has been implemented into engineering design analyses and used to model composite structures.

Many heterogeneous or composite materials contain constituents that undergo phase transformations during a deformation process. Examples include metal matrix composites that use titanium, which may be found in either the hexagonal close packed (hcp) alpha, the body-centered (bcc) beta, or the hexagonal (hex) omega phase, depending on the pressure and temperature of the composite. Similarly, polymer-bonded, high-explosive (PBX) materials contain a large

percentage (approximately 95% by weight) of high-melting point explosive (HMX) and a polymer binder. HMX may be found in four solid phases. An important reaction step in the initiation of HMX is the phase transformation from the beta (monoclinic) phase to the more reactive delta (hexagonal) phase.

In the conventional weapons community, depleted uranium (DU) alloys such as U-0.75 Ti have demonstrated effectiveness as kinetic energy, long-rod penetrators (LRPs). Unfortunately, uranium alloys present environmental problems ranging from fabrication to battle-field cleanup. Consequently, replacement materials have been pursued. Based on economic consideration and thermomechanical properties, tungsten heavy alloys (WHAs) have been considered as candidates for LRP applications. A typical WHA is composed of approximately 93 wt.% W, 5 wt.% Ni, and 2 wt.% Fe. The microstructure includes high strength, high melting point ($T_{\text{melt}} \sim 3410$ K), and rate-sensitive spherical grains of body-centered cubic (bcc) tungsten (W). The W particle size is roughly uniform (30 to 60 μm) and the microstructure is regular. There are no other phase transformations in the W grains between room temperature and the melting point. The W grains are dispersed in a softer, lower melting point ($T_{\text{melt}} \sim 1750$ K) face-centered cubic (fcc) W-Ni-Fe “matrix.” The matrix material for a typical WHA has a composition of approximately 36 wt.% W, 45 wt.% Ni, and 19 wt.% Fe. Because of the low melting point of the matrix material, local melting is anticipated during a penetration event. For the above reasons, the ability to model phase transformations in composite materials remains an important problem.

A model for heterogeneous materials, which includes phase transformations, has been developed. The homogenization approach is a generalization of the MOC. An idealized UC is identified as a 3D rectilinear brick (Fig. 1). The UC contains eight subcells ($\alpha, \beta, \lambda=1,2$), which may correspond to different materials with different constitutive responses. The dimensions of the subcells are $d_\alpha, l_\beta, h_\lambda$. It is assumed that the relative volume fractions of the constituents (i.e., subcell dimensions) remain constant during the deformation process. For this description,

the density and temperature fields are assumed to be piecewise constant, and the velocity field is assumed trilinear within each subcell. These approximations result in a consistent set of fields. Within subcells undergoing phase transformations, it is assumed that the temperature and stress fields are equal for each of the phases. Separate mass, momentum, and energy equations are solved for the subcells using the constraints of periodic boundary conditions and continuity of displacements and tractions across the subcells. This approach is computationally efficient and may be coupled to a design analysis to provide the constitutive response for a composite material that may be used as part of an engineering structure.

A simulation of a particulate composite composed of SiC particles embedded in a Ti matrix is provided in Fig. 2. Free energies for the Ti are obtained from electronic structure calculations [2]. A nonlinear elastic/plastic material model was used for the Ti. Nonlinear elasticity was modeled by obtaining the equation of state (EOS) directly from the free energies for Ti. Bodner-Partom plasticity was used for the inelastic response. The SiC was modeled as a simple nonlinear elastic material, using a Mie-Gruneisen EOS. Biaxial strain conditions were used in the simulations provided in Fig. 2. Simulations for four different compositions of SiC (0%, 30%, 60%, and 100%) are provided. A volume average temperature versus a volume average strain (ϵ_{11}) is plotted in Fig. 2. In the figure, the phase transformation for the pure Ti (0% SiC) simulation begins and ends at strains of about -0.0046 and -0.025, respectively. The phase transformation in Ti becomes less evident as larger amounts of SiC are added. In the pure SiC simulation, of course, there is no phase transformation present during the deformation. Included in Fig. 2 is the response for a 30% SiC composition using the original MOC formulation, which excludes phase transformations. An isothermal response is obtained for the MOC simulation because the model does not include an energy equation.

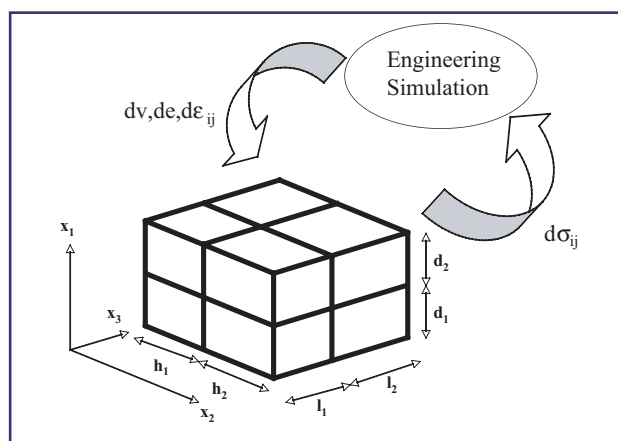


Figure 1—
Representative Unit
Cell used in the
homogenization
approach.

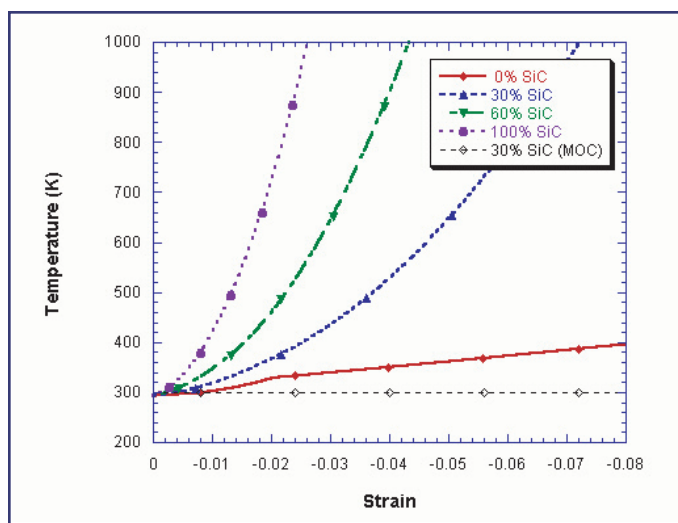


Figure 2—
Biaxial compression
simulation of a SiC-Ti
particulate composite
for two different
compositions of SiC,
temperature
versus strain.

Additional simulations have demonstrated the versatility and robustness of the model. Future applications, which address high-rate deformations of WHA and materials of interest to the nuclear weapons community, will be pursued.

- [1] J. Aboudi, *Mechanics of Composite Materials: A Unified Micromechanical Approach* (Elsevier, New York, NY 1991).
- [2] C.W. Greeff, D.R. Trinkle, and R.C. Albers, "Shock-Induced α , ω Transition in Titanium," *J. Appl. Phys.* **90** (5) 2221 (2001).

For more information, contact
Frank L. Addessio (addessio@lanl.gov).

Acknowledgements

We would like to acknowledge the Joint DoD/DOE Munitions Technology Development Program for financial support.

An Implicit Thermomechanical Composite Model of PBX 9501

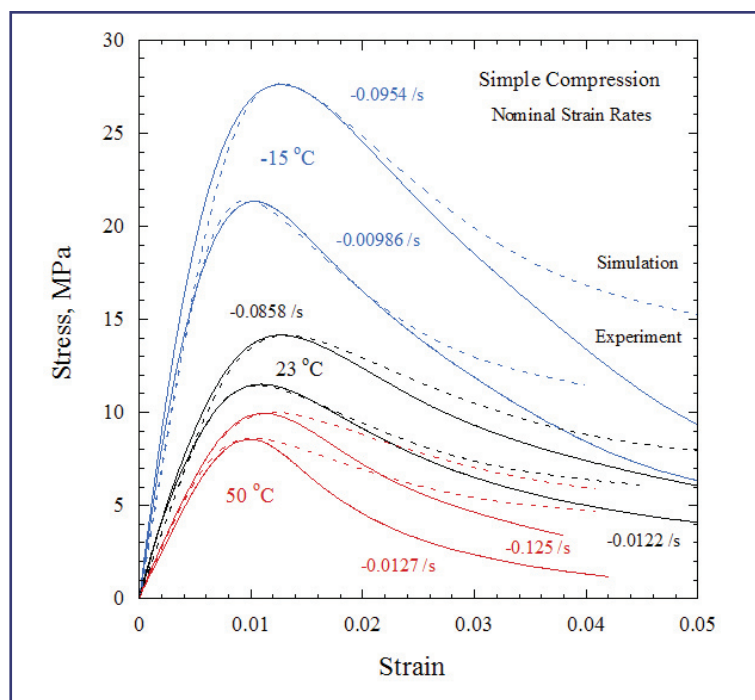
Curt A. Bronkhorst and Todd O. Williams (T-3), Darla G. Thompson (DX-2), and Cheng Liu (MST-8)

The high explosive PBX 9501 is an aggregate composite composed of approximately 93 volume % HMX crystals and 7 volume % plasticized Estane®. The HMX phase is a mixed combination of one part fine size fraction and three parts coarse size fraction. The particle size distribution peak for the fine fraction is at approximately 5 microns whereas the coarse fraction peak is at approximately 200 microns. At room temperature the HMX crystals are in the monoclinic phase and are believed to behave largely as a brittle solid. In contrast the plasticized Estane® is a highly compliant rubbery polymer. Some small amount of dispersed void space (~ 1%) is also believed to exist in PBX 9501. Our efforts are meant to represent this material in a physically realistic but computationally practical way.

We are using a coupled thermomechanical generalized method of cells [1] composite model to represent PBX 9501. This model allows for the discrete representation of binder and HMX phases through the use of a representative volume element consisting of 8 cells. Each of the cells is assigned a material, and in the case of PBX 9501, a viscoelastic filled binder constitutive model [2] and an elastic-brittle HMX constitutive model [3, 4]. Through the use of an appropriate energy equation, thermal energy production, storage, and conduction are also accounted for. The fit of this model to the simple compression data of Thompson is given in Fig. 1. The simulation results are qualitatively consistent with the experiments; however, work is underway to more adequately represent the deformation behavior of this very complex material.

This composite model together with the two constitutive models has been implemented semi-implicitly into the commercially available finite element code ABAQUS. The implementation uses an analytic mechanical Jacobian for each constitutive model along with a rate of convergence algorithm to allow for variable time stepping. The stress and Jacobian tensors at each material point for the composite are taken to be the volume average of the each quantity in each composite cell.

Figure 1— Comparison of simulation results to those of experiments used to evaluate material parameters. The red curves represent results for an initial temperature of 50°C, the black curves for 23°C, and the blue curves for -15°C. The nominal strain rate for each pair of curves is also listed.



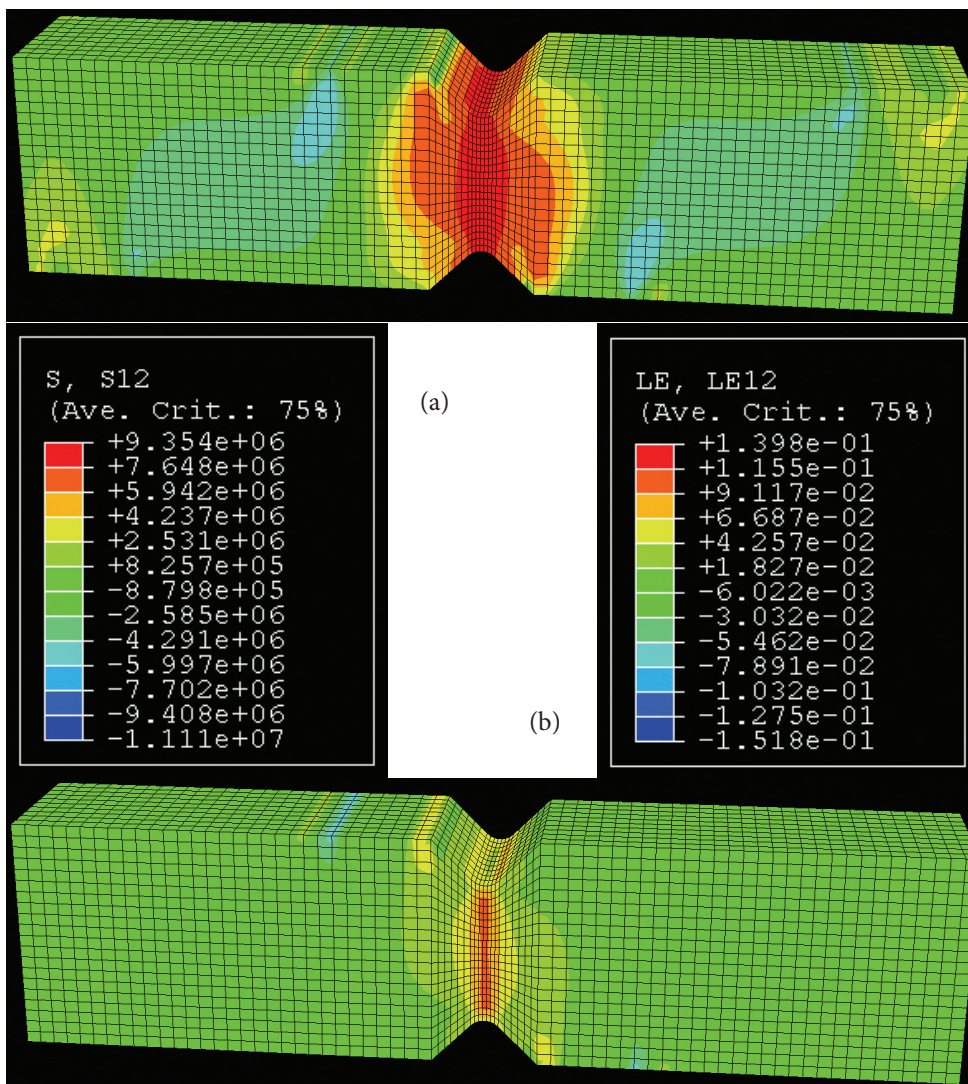


Figure 2—
Three-dimensional
simulation results
showing (a) shear stress
and (b) shear strain in
a deformed Iosipescu
sample of PBX 9501.

Results of a three-dimensional simulation of an Iosipescu shear sample used for PBX 9501 can be found in Fig. 2. Quantitative comparison between these simulation results and the experimental shear results of Liu [5] are currently underway.

[1] T.O. Williams, J. Aboudi, *J. Thermal Stresses* **22**, 841 (1999).

[2] E.M. Mas, et al., "Viscoelastic Model for PBX Binders," Los Alamos National Laboratory report LA-UR-01-3492 (June 2001).

[3] F.L. Addessio, J.N. Johnson, *J. Appl. Phys.* **67**, 3275 (1990).

[4] R.M. Hackett, J.G. Bennett, *Int. J. Numer. Meth. Engng.* **49**, 1191 (2000).

[5] C. Liu, personal communication.

For more information, contact
Curt A. Bronkhorst (cabronk@lanl.gov).

Acknowledgements

We would like to acknowledge NNSA's Advanced Simulation and Computing (ASC), Materials and Physics Program; and Campaign 2, Dynamic Materials Properties, for financial support.

Modeling Phase Transformations with Strength in Zirconium

Eric N. Harstad, Francis L. Addessio,
Q. Ken Zuo, and Todd O. Williams (T-3);
and Carl W. Greeff (T-1)

The previously developed free energy approach to modeling materials with phase transformations has been updated to include a linear hardening plasticity algorithm and improved kinetics more representative of the observed behavior of zirconium. The material model has been implemented into a 3D Lagrangian finite-element code.

The plasticity is based on the assumption that in a multiphase material, the phase that has the lowest yield strength will receive all of the deformation. An implicit formulation for the deviatoric stress invariant when the yield condition is satisfied is given by

$$\tau = \frac{\sigma_y^{\min} + \sigma_y^{\min} / 3\bar{\mu}\xi^{\min}\tau^*}{1 + \sigma_y^{\min} / 3\bar{\mu}\xi^{\min}}, \quad (1)$$

where the minimum yield surface value is

$$\sigma_y^{\min} = \min(\sigma_y^{\alpha}, \sigma_y^{\beta}, \sigma_y^{\gamma}),$$

the mass fraction of the minimum nonzero

$$\text{phase is } \xi^{\min} = \min(\xi^{\alpha}, \xi^{\beta}, \xi^{\omega}),$$

the composite shear modulus is

$$\bar{\mu} = \sum_{k=\alpha,\beta,\omega} \frac{1}{\xi_k / \mu_k},$$

and τ^* is the trial stress. The trial stress is the stress invariant that would be realized if all the deformation was accommodated elastically,

$$\tau^* = \sqrt{\frac{3}{2} \underline{\underline{S}}^* : \underline{\underline{S}}^*}, \quad \underline{\underline{S}}^* = 2\bar{\mu} \underline{\underline{D}}', \quad (2)$$

where $\underline{\underline{S}}^*$ is the trial deviatoric Cauchy stress tensor, and $\underline{\underline{D}}'$ is the deviatoric rate of deformation tensor. The deviatoric stress is

$$\underline{\underline{S}} = \underline{\underline{S}}^* \frac{\tau}{\tau^*}. \quad (3)$$

The yield surfaces for each phase evolve using a linear hardening rule in equivalent plastic strain.

The transformation rate (for the α - ω phase transition) is given by phenomenological model

$$\xi = (1 - \xi_{\omega}) \nu \frac{G_{\alpha} - G_{\omega}}{B} \exp\left(\frac{G_{\alpha} - G_{\omega}}{B}\right)^2 \quad (4)$$

where G_{phase} is the Gibbs free energy for each phase and (ν, B) are material constants.

The material model was coded in FORTRAN 90 in a modular form for simplified implementation into Advanced Simulation and Computing codes. The modular form was inserted into a 3D Lagrangian finite-element test-bed code for verification.

A plate on plate impact problem was used to verify the implementation. Both 1D and 3D calculations were performed for a sapphire plate impacting an alpha phase zirconium plate at 658 m/s. Figure 1 shows the evolution of the mass fractions of each phase, the yield stresses of each phase, and the von Mises stress as a function of time for the one dimensional plate on plate impact. For the 3D simulation, Fig. 2 compares the velocity and phase distribution for three times.

[1] C.W. Greeff, P.A. Rigg, M.D. Knudson, R.S. Hixson, and G.T. Gray III, "Modeling Dynamic Phase Transitions in Ti and Zr," AIP, **CP706**, 209-212 (2003)

[2] F.L. Addessio, Q.H. Zuo, and T.A. Mason, and L.C. Brinson, "A Model for High-Strain-Rate Deformation of Uranium-Niobium Alloys," *J. Appl. Phys.*, **93**, 12, 9644 (2003).

For more information, contact
Eric N. Harstad (enh@lanl.gov).

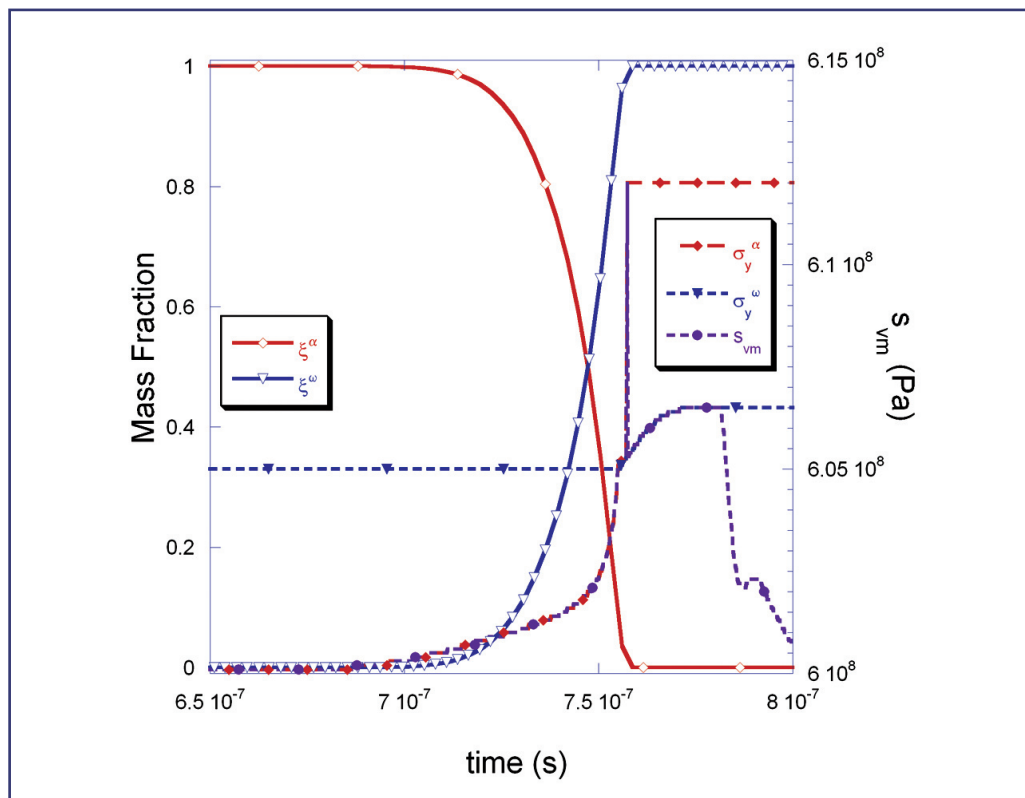


Figure 1—
One-dimensional plate
on plate impact: mass
fraction of each phase
and deviatoric stress
evolution in time.

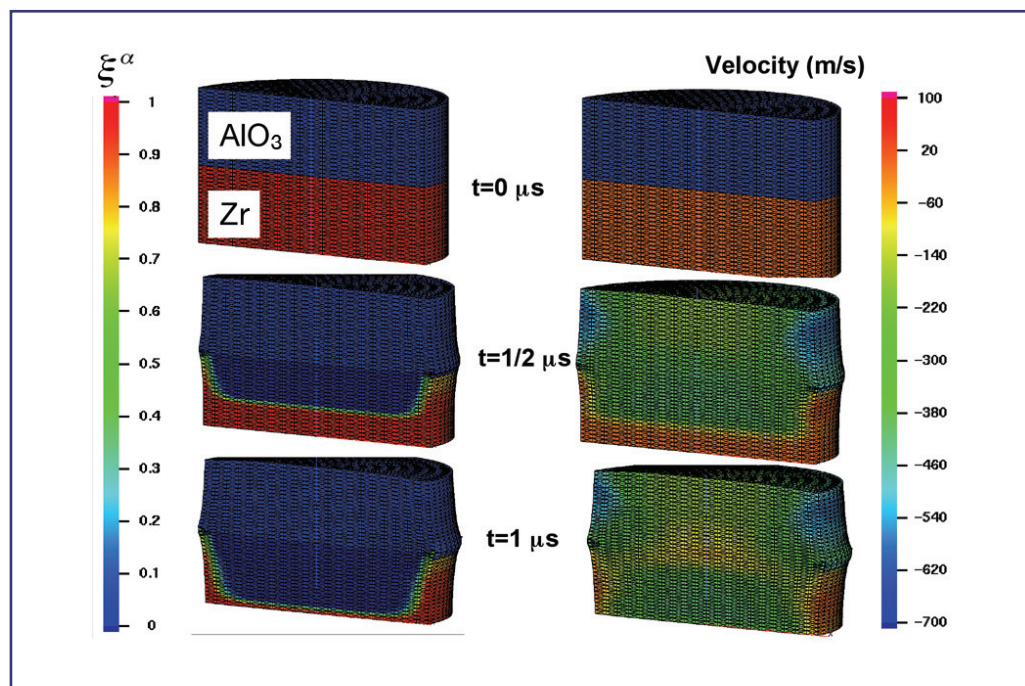


Figure 2—
Three-dimensional plate
on plate impact: velocity
and phase transition
waves.

Acknowledgements

We would like to acknowledge NNSA's Advanced Simulation and Computing (ASC), Materials and Physics Program, and the Joint DoD/DOE Munitions Technology Development Program for financial support.

Direct Numerical Simulation of Polycrystal

Manjit S. Sahota, Rick M. Rauenzahn,
Frank L. Addessio, and
Francis H. Harlow (T-3)

We performed several direct numerical simulations to investigate the polycrystal behavior in certain metals when subjected to strong shocks. Figure 1 shows the initial configuration and a shock generated by PBX 9501 at Chapman-Jouguet (C-J) pressure on the left side of the structure passing through a $50 \times 50 \mu\text{m}$ metal plate composed of two distinct phases of different densities and compressibilities. Each element of $100 \times 100 \times 1$ hexahedral grid was subdivided into four prisms to generate a triangular grid of 40000 prismatic elements to resolve interfaces between the two phases. It is not possible to complete this calculation in a Lagrangian mode because of the amount of turbulence generated at later times. Thus the calculation was carried out by moving the entire mesh "window" with the average fluid velocity of the domain. The CHAD code [1, 2] with the interface tracking/reconstruction capability turned off was employed for this calculation. The left boundary was modeled by a constant-velocity piston until the shock cleared the plate, and then it was changed into an inflow-outflow pressure-specified boundary. The right boundary was treated as

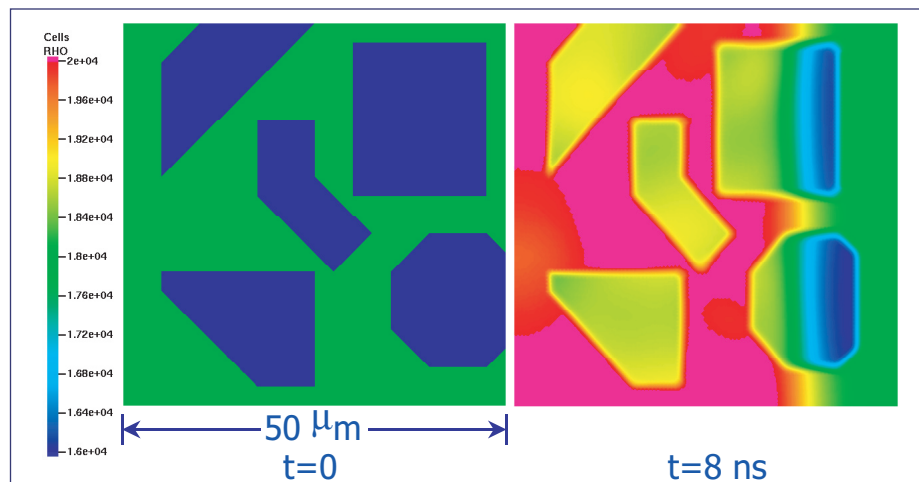
inflow/outflow pressure-specified boundary throughout the transient. The bottom and top boundaries were reflective.

Figure 2 shows the comparison of initial density and density at 1000 ns, about 990 ns after the shock has passed the plate. A considerable distortion and mixing are observed at this time. A clear evidence of mixing and turbulence is shown by the vorticity contours of Fig. 3.

Figure 4 shows the fluctuating component of x-direction velocity $\overline{u'u'}$ and its normalized value as a function of time. The exact expressions of how the fluctuation component is defined also are given in Fig. 4. These values are averages over the entire domain and not over any cross section. The cross-sectional values are not meaningful because a meaningful estimate would require numerous calculations with different polycrystal sizes and orientations. By the same argument the data in Fig. 4 are also not meaningful before ~ 20 ns because it took ~ 10 ns for the shock to pass through the calculational domain. A significant finding of this calculation is the surprising amount of $\sim 15\%$ kinetic energy in the turbulence field near 100 ns. Such strong turbulence could have significant implications for integral system calculations.

We plan to perform a macrocalculation using a statistically similar sample of several mm size under similar hydrodynamics conditions using the BHR turbulence model [3]. It will be interesting to find out if such a model could predict a similar amount of turbulence kinetic energy.

Figure 1—
Initial shock propagation of a strong shock through the two phases of a polycrystal structure. The continuous phase has higher density but lower sound speed.



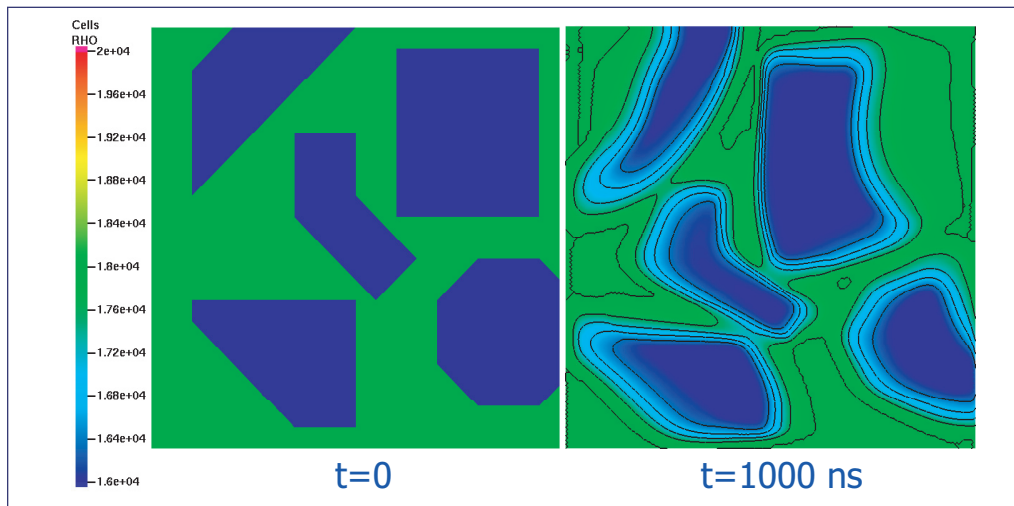


Figure 2—
Comparison of the
initial density contours
with those at 1000 ns.

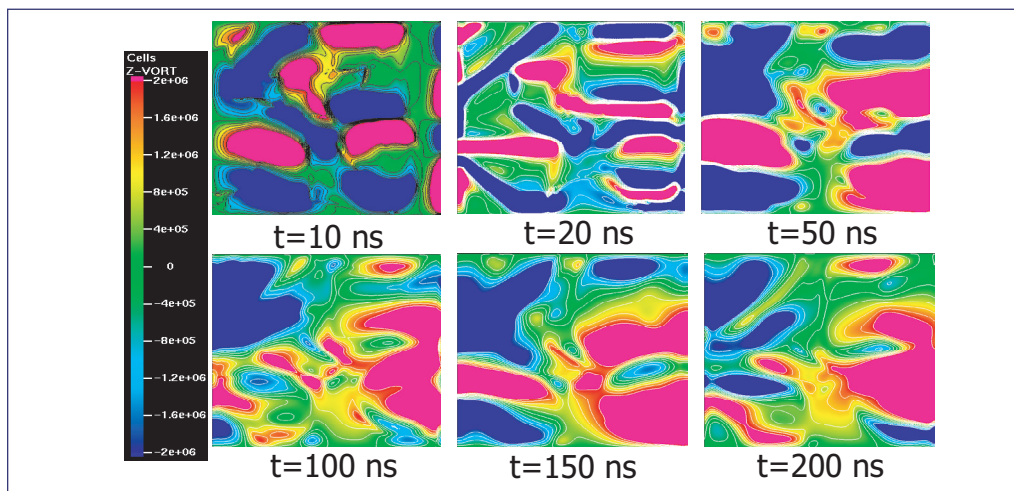


Figure 3—
Snapshots of vorticity
contours.

[1] P.J. O'Rourke and M.S. Sahota, "CHAD: A Parallel, 3-D, Implicit, Unstructured-Grid, Multimaterial, Hydrodynamics Code for all Flow Speeds, Los Alamos National Laboratory report, LA-UR-98-5663 (October 1998).

[2] P.J. O'Rourke and M.S. Sahota, *J. Comp. Phys.* **143** (1998), pp. 312-345.

[3] Didier Besnard, et al., "Turbulence Transport Equations for Variable-Density Turbulence and Their Relationship to Two-Field Models," Los Alamos National Laboratory report LA-12303-MS (June 1992).

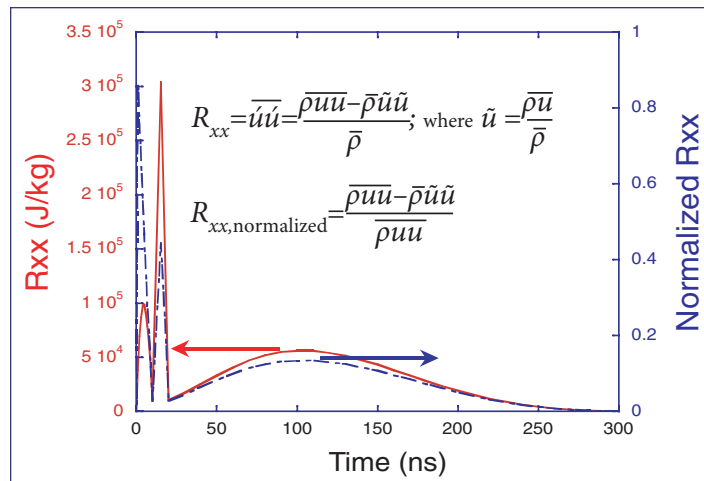


Figure 4—
Turbulence kinetic
energy history.

For more information, contact
Manjit S. Sahota (sahota@lanl.gov).

Acknowledgements

We would like to acknowledge NNSA's Advanced Simulation and Computing (ASC), Materials and Physics Program for financial support.

Damage Surface Based on the Critical Crack Orientation

Q. Ken Zuo and Frank L. Addessio (T-3),
John K. Dienes (T-14)

Addessio and Johnson [1] proposed a constitutive model (ISOSCM) for the dynamic response of brittle materials (e.g., ceramics, high explosives, berylliums) based on the work of Dienes. They assumed that during the damage process the distribution of cracks remains random and isotropic, and that the crack probability density function is exponential in the crack size. The macroscopic crack strains and an isotropic damage surface are found by averaging the crack strains as well as the instability condition for a single crack over all crack orientations. The resulting isotropic damage surface involves only the mean crack size, the von Mises stress and pressure, and takes two different forms depending on the sign of the pressure. The damage evolution is given through the growth of mean crack size when the stress state is on or above the damage surface. The model is compatible with the incremental continuum formulation inherent to existing design computer codes and can be easily implemented into the codes. The model was applied to simulate damage in ceramics under impact conditions, and the predictions compared favorably with shock compression and release experiments.

Due to its numerical efficiency and mathematical simplicity and its origin in micromechanics, the model has been adopted by many researchers as the starting point for their models. Bennett et al. [2] extended ISOSCM to include the viscous effects of the binder materials to study the non-shock ignition of a plastic bonded explosive. Lee et al. [3] adopted the damage surface and the crack growth law developed in ISOSCM for modeling damage of fiber composites. There are still two issues in ISOSCM that warrant further improvement, namely, (1) a discontinuity in the damage surface as the pressure in the material changes sign, and (2) when the principal stresses have mixed

signs, only the open cracks should contribute to the open crack strain. In ISOSCM, however, whether a crack would contribute to the open crack strain or not depends solely on the sign of the pressure in the material, not on its orientation (hence the sign of the traction). As discussed by Lewis and Schreyer [4], both issues could lead to thermodynamic inconsistency, which manifests into energy creation under certain cyclic load paths. The objectives of the current work are to develop an improved version of ISOSCM and to apply it to problems of damage and spall in beryllium under dynamic loading. Here, we present our new formulation for the damage surface which removes the discontinuity in the damage surface in ISOSCM.

When the applied stress is large enough, some cracks in the material can become unstable and grow in size. We assume here that the material accumulates additional damage if the crack with average size \bar{c} along some orientation is unstable. The generalized Griffith instability criterion for a single crack is $F(\boldsymbol{\sigma}, \mathbf{n}, \bar{c}) \equiv f(\boldsymbol{\sigma}, \mathbf{n}) - \pi(2 - \nu)G\gamma / (2\bar{c}(1 - \nu)) = 0$, $\boldsymbol{\sigma}$ where is the remote stress tensor, \mathbf{n} the unit normal of the crack, γ the surface energy of the material, and the elastic constants G and ν are the shear modulus and Poisson's ratio, respectively. The expression for the function $f(\boldsymbol{\sigma}, \mathbf{n})$, which is proportional to the energy release rate, depends on whether the crack is open (the normal component of traction is tensile) or closed (the normal component is compressive and controls the interfacial friction, see [5] for details). The crack instability surface $F(\boldsymbol{\sigma}, \mathbf{n}, \bar{c}) = 0$ in the $\sigma_n - S_n$ plane, along with the Mohr circles, which conveniently relate the normal and shear components of traction on a surface to the principal stresses, is given in Fig. 1. It is interesting to note that the instability surface for closed cracks coincides with the Mohr-Coulomb failure envelope. The instability condition for a penny-shaped crack may provide a justification for the Mohr-Coulomb criterion for brittle materials and the means to relate the cohesion constant to the defects (crack radius) in the materials.

The damage surface for the material, $\bar{F}(\sigma, \bar{c}) = 0$, is found by applying the instability condition to the critical (most unstable) crack orientation. For a given crack size and stress state, the critical

crack orientation, \mathbf{n}^c maximizes the function $f(\boldsymbol{\sigma}, \mathbf{n})$, and under the assumption of a random, isotropic distribution of cracks, the crack along that direction will first become unstable when the applied stress is high enough.

We have recently found [5] the critical crack orientation and determined the load that is needed for the crack along that orientation to become unstable. Figure 2 is a comparison of the new damage surface based on the instability condition of the critical crack orientation and that based on averaging the crack instability condition over all crack orientations [1] for the same set of material constants. The state of stress is taken to be triaxial with uniform lateral confinement. The Poisson's ratio and friction coefficient are $\nu = 0.25$ and $\mu = 0.2$, and the pressure and von Mises stress are normalized with respect to $P_t = \sqrt{\pi G \gamma / (\bar{c}(1-\nu))}$, the hydrostatic tensile stress the material can sustain before it accumulates additional damage. It may be observed that the surface based on the critical crack orientation is continuous, whereas the surface based on averaging has a jump in the von Mises stress as the pressure changes sign. It is also seen that both surfaces predict the same value when material is under hydrostatic tension, as expected, since in this case all orientations are equally critical and the two approaches are identical. Both approaches also predict no damage evolution (crack growth) under hydrostatic compression, consistent with crack mechanics.

For a non-isotropic stress state ($\tau > 0$), the current approach predicts less shear a material can sustain before additional damage accrues than the previous approach. This is consistent with the assumptions in the current approach that damage grows when the critical orientation becomes unstable while the previous approach assumes that damage can grow only when the "averaged" orientation becomes unstable.

[1] F.L. Addessio and J.N Johnson, "A Constitutive Model for the Dynamic Response of Brittle Materials," *J. Appl. Phys.* **67**, 3275 (1990).

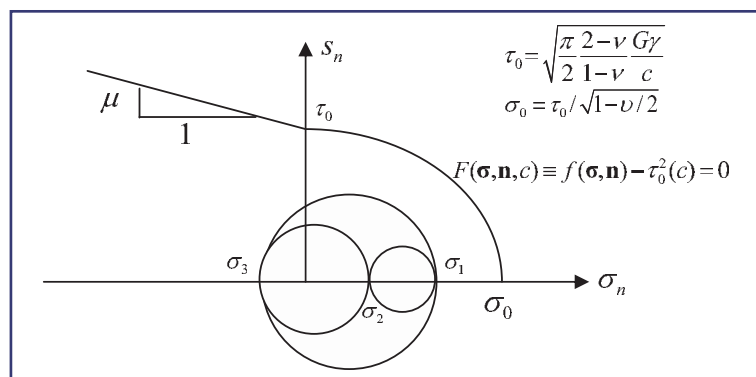


Figure 1—
The instability surface of a penny-shaped crack under combined shear (s_n) and normal (σ_n) stresses with interfacial friction.

- [2] J.G. Bennett, et al., "A Constitutive Model for the Non-shock Ignition and Mechanical Response of High Explosives," *J. Mech. Phys. Solids*, **46**, 2303 (1998).
 [3] H.K. Lee, S. Simunovic, and D.K. Shin, *Comput. Mat. Sci.* **29**, 459 (2004).
 [4] M.W. Lewis and H.L. Schreyer, "A Thermodynamically Consistent Description of Dynamic Continuum Damage," in *High Pressure Shock Compression of Solids*, L. Davison, D.E. Grady, and M. Shahinpoor, Eds. (New York: Springer-Verlag 1996) Vol. II, p. 452.
 [5] Q.H. Zuo and J.K. Dienes, "On the Stability of Penny-Shaped Cracks with Friction: The Five Types of Brittle Behavior," *Int. J. Solids Struct.* **42**, 5–6 1309–1326 (March 2005).

For more information, contact Q. Ken Zuo (zuo@lanl.gov).

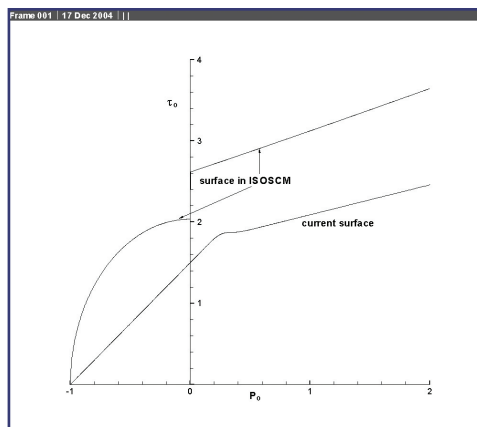


Figure 2—
Comparison of the new damage surface and that developed previously [1].

Acknowledgements

We would like to acknowledge NNSA's Advanced Simulation and Computing (ASC), Materials and Physics Program, and the Joint DoD/DOE Munitions Technology Development Program for financial support.

Numerical Simulation of Realistic Foam Microstructures

*Andrew Brydon and
Scott Bardenhagen (T-14)*

Foams are a class of material with unique properties and applications. They are lightweight and designed to undergo very large deformations. They are typically used in packaging and to absorb energy. Their properties are the result of the foam microstructure, a complex three-dimensional (3D) network of struts and, possibly, membranes, which undergo large deformations and contact during deformation. Foam deformation has been studied extensively and significant understanding has been obtained using idealized models. Experimental work has also served to demonstrate the complexity of foam deformation. However, as with other complex materials, developing a correspondence between characteristics of the microstructure and the bulk response is a grand challenge.

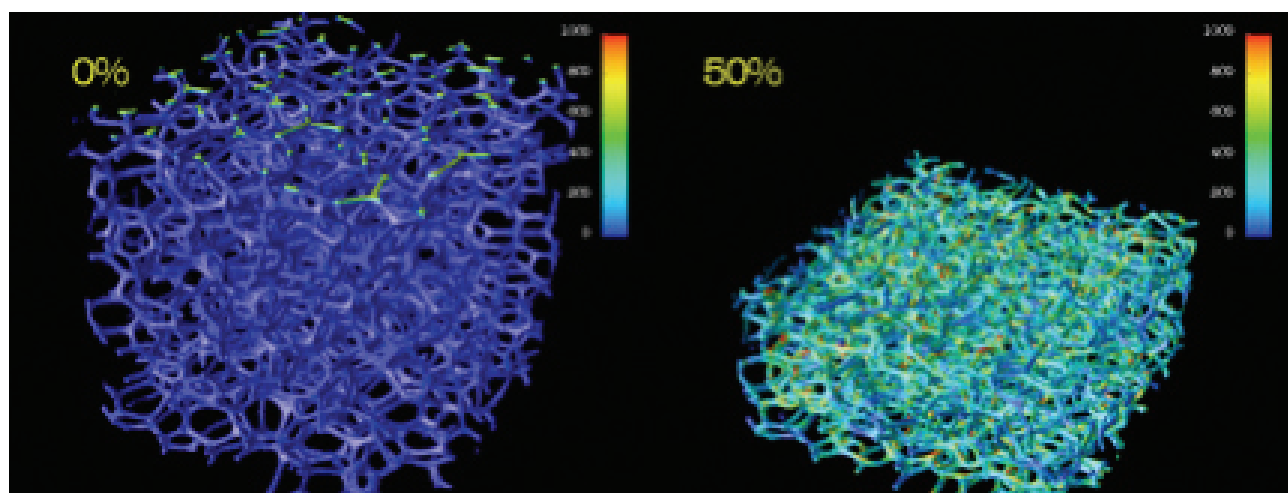
This scenario is fertile ground for numerical simulation but also a well-established computational challenge for several reasons. The reasons are: (1) the deformations of interest are large, both on average (macroscale) and on the microscale, (2) extensive “self-contact” must be simulated as the microstructure collapses, and (3) realistic foam microstructures, effectively a subject in rheology, are very complex and must be discretized. Recent developments in particle-in-cell (PIC) methods indicate that these numerical techniques are suitable for precisely this class of problem. Simulations have been performed that are extremely encouraging from several perspectives. Verification calculations have been performed to assess numerical accuracy in the simulation of quasistatic compression of homogeneous elastic material to 10% of its initial volume with good results. Macroscopic foam stress/strain curves agree qualitatively with experimental results and

accepted model estimates of key deformation parameters. Simplified foam microstructures have been compressed to “full densification” and residual porosity studied, indicating incompressibility may not be a good assumption near full densification [1, 2].

Most recently, the compatibility of particle discretization and x-ray microtomography has been demonstrated. Figure 1 depicts an open cell foam microstructure obtained experimentally and discretized using a PIC method. The foam microstructure was obtained from Professor Gerald Seidler at the University of Washington (UW). The data are a 3D array of grey-scale values detailing relative x-ray cross-section. This data set was filtered to remove experimental artifacts and we used thresh-holding to improve contrast. The result is a regular array (voxels) with nonzero elements indicating the spatial position of material. The foam initial configuration was discretized by mapping from the voxels to a regular computational grid and placing polymer particles in computational cells for which the voxels indicate presence of material. The use of particles to generate the initial configuration provides a clear advantage over competing methods, where the generation of appropriate body fit meshes presents a formidable challenge.

Quasistatic compression of the foam microstructure was simulated using a PIC method. This run, to 90% compression, was done on the Linux cluster Grendels using 48 processors for about 300 hours. Of interest is the morphology of the deformed configurations as pore space is removed and the material is densified. Characterization of the deformed morphologies is a very challenging image-analysis task, which our collaboration with UW is also intended to address.

A connection between microstructural simulation and macroscopic (continuum) theory has also been sought. The development of macroscopic models of foam response is challenging. Existing models either determine the response of a specific microstructure and loading direction, or account for microstructure by scaling material parameters in more traditional, uniform continuum formulations. A new approach is under



development in which macroscopic response is determined from unit cell mechanics models and microstructural geometry statistics. These statistics are evolved throughout deformation. These simulations can provide precisely these data.

- [1] S.G. Bardenhagen, A.D. Brydon, and J.E. Guilkey, "Insight into the Physics of Foam Densification via Numerical Simulation," *J. Mech. Phys. Solids* **53**, 3, 597 (2005).
- [2] A.D. Brydon, et al., "Simulation of the Densification of Real Open-Celled Foam Microstructures," submitted to *J. Mech. Phys. Solids*.

**For more information, contact
Andrew Brydon (abrydon@lanl.gov).**

Acknowledgements

We would like to acknowledge NNSA's Advanced Simulation and Computing (ASC), Materials and Physics Program; and Campaign 2, Dynamic Materials Properties, for financial support.

**Figure 1—
Realistic foam microstructure initial configuration (left) and simulated compressed state (right). Material is colored by a norm of the stress tensor.**

Strain-Induced Phase Transformations in Shape Memory Alloys

Rajeev Ahluwalia, Turab Lookman, and Avadh Saxena (T-11)

Shape memory materials are characterized by the ability to generate large strains by applying moderate stresses with almost no plastic deformation. Above a structural transition temperature the deformation is completely recovered on removing the load. This behavior is also termed “pseudoelasticity.” Some materials, such as NiTi alloys can recover strains up to 10%, making these materials suitable for a large number of technological applications. This property arises due to a strain-induced, diffusionless, shear-driven structural transformation. The transformation makes the stress-strain curves highly nonlinear and a plateau, analogous to plasticity, is observed. However, upon removing the load, the material transforms back to the parent crystal structure and all the deformation is recovered.

We have developed a framework to model the pseudoelasticity of these materials, in particular FePd which undergoes a cubic to tetragonal transformation. The modeling is based on continuum elasticity with a nonlinear elastic free energy. The free energy is written as an expansion in the components of the strain tensor. The main criterion in constructing this free energy expansion is that the underlying point group symmetry of the crystal is satisfied. The dynamics and microstructural evolution are simulated by using force balance equations for the displacement fields. Dissipation is accounted for by a viscous damping force in terms of the strain rates. The displacement field method ensures that elastic compatibility relations are automatically satisfied.

All parameters in the free energy are fitted to FePd experimental data for elastic constants, lattice parameters, phonon dispersion, and mobilities. The equations of motion are numerically solved on a $64 \times 32 \times 32$ grid using finite differences and periodic boundary conditions are assumed. Preliminary results for small systems that simulate a block of material $.08 \times .04 \times .04 \mu\text{m}^3$ for roughly several nanoseconds, with a uniaxial strain loading at a rate of $10^6/\text{s}$, are shown in Fig. 1. The microstructure in terms of strains is shown at a point on the stress-strain curve. Note how the system nucleates domain walls on overcoming a barrier to the formation of tetragonal variants. This barrier decreases as the strain rate decreases. These simulations allow us to understand the influence of strain rate on nucleation processes at the mesoscale. Our work is currently being applied to materials that transform from cubic to orthorhombic (CuAlNi, U6Nb) and cubic to monoclinic (NiTi, Pu), as some of these materials are of strategic interest to Nuclear Weapons programs.

For more information, contact
Turab Lookman (txl@lanl.gov).

Acknowledgements

We would like to acknowledge NNSA's Advanced Simulation and Computing (ASC), Materials and Physics Program for financial support.

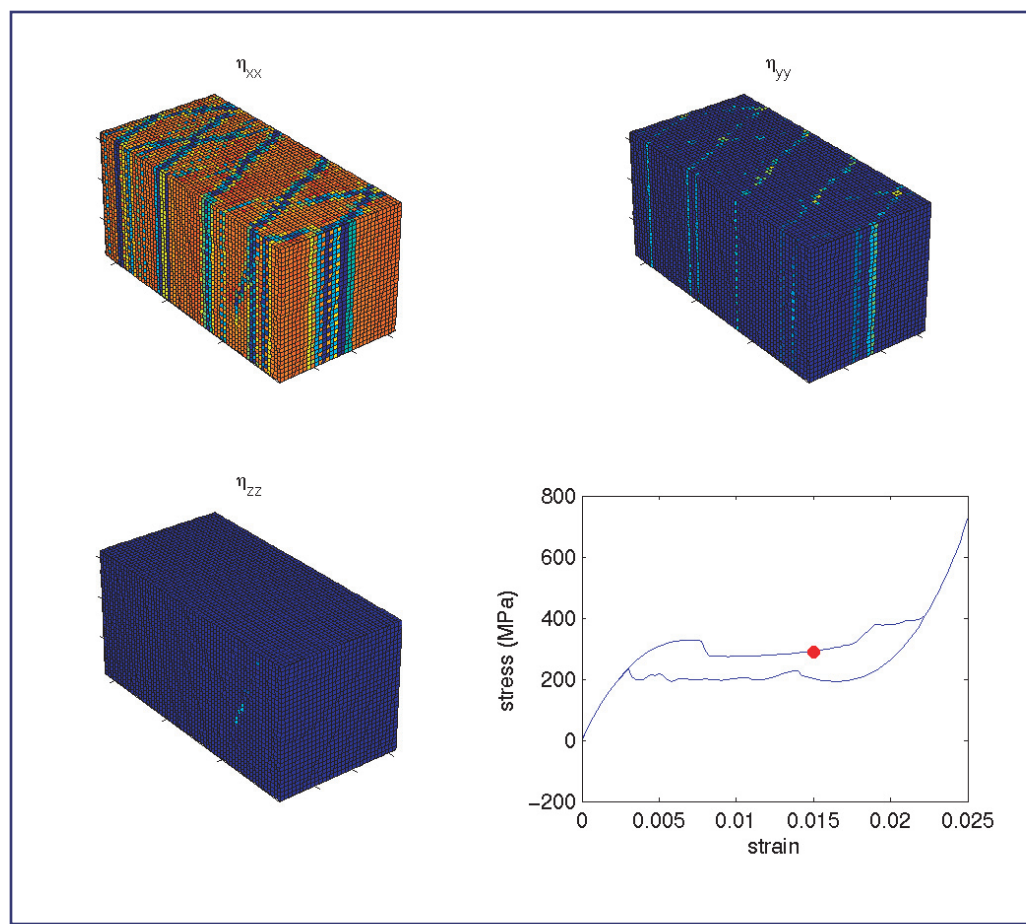


Figure 1—
Strain tensor
components η_{xx} , η_{yy} ,
 η_{zz} at a given point on
the stress-strain curve.
Red corresponds to
large positive values
and blue to zero.
The strain loading is
in the direction of the
tetragonal variant
along the x direction.

Mesoscale Simulations of Crack Propagation

*V. Dwivedi [University of California at Santa Barbara (UCSB)/T-11];
Rajeev Ahluwalia, Turab Lookman,
and Avadh Saxena (T-11); and
S. Bannerjee (UCSB)*

Fracture patterns show signs of coherent dynamical behavior. For example, after a short transient, the speed of a propagating crack often reaches some limiting average speed. When the crack speed is still low, the crack surface is usually rather smooth. However, when the speed is above a threshold value of the order of the asymptotic speed, the crack surface suddenly becomes much rougher and the crack speed often exhibits strong fluctuations. Above the critical speed, inspection of the crack surface shows that the crack branches. Fast crack growth in brittle solids typically reveals complex patterns of crack branching; for example, the shattering from a rock impact of a plastic that leads to a pattern of repeated branching of a crack into multiple side-branches. Supporting numerical analysis at the continuum level, using finite-element methods based on prescribed cohesive laws to govern the separation of surfaces under the tensile mode, reveals the effect of the crack propagation speed on the branching and surface roughness characteristics of such fast moving cracks.

What makes a theoretical or numerical analysis of crack propagation difficult is that one cannot use continuum elastic theory alone. A continuum elastic theory in which the crack is taken as a mathematically sharp cut is prone to singular behavior—one really has to put in the breaking of bonds or the dissipation of energy near the crack tip into the model to obtain a proper description. Numerically it has indeed become possible, in recent years, to do large-scale molecular dynamics simulations (sometimes matched to continuum elastic models on large scales), which do reproduce many of the

experimental features, including the splitting of cracks. However, from such simulations it is still difficult to separate the essentially long-range dynamical behavior from what is intrinsic to a particular short-range molecular potential.

Recently, we have studied mesoscale models based on local Landau potentials to describe crack dynamics. The model introduces a continuum order parameter or “phase field” to describe a stiff solid or a broken material which does not support stresses, and which interpolates between these two extremes in a thin zone. In the present context, this transition zone is the “process zone” where the breaking occurs. Within such a model, the atomistic breaking of bonds is not incorporated realistically, but it is mimicked by having energy dissipate there. The numerical advantage of such models is that their simulations are relatively simple, and they allow one to study coherent behavior, which is independent of the precise atomistic details. Also, they allow for computations to realistic length and time scales.

The problem we consider is a very thin plate with an initial central crack under a Mode I fracture. Plain strain conditions are assumed to exist. A tensile loading is applied through an imposed strain field. The material is assumed to be elastic; we consider both the isotropic case as would apply to a brittle plastic such as PMMA (poly-methyl-methacrylate) and anisotropic case for a system with two-dimensional square symmetry that is uniform in the third direction. Our model contains dynamics derived using force balance with inertial and dissipative effects included. Phase field models have not previously been applied to study branching or crack propagation. Our objective is to show the efficacy of the method in modeling not only the natural initiation and growth of the crack, but also the branching characteristics and the effect of branching on the mechanical strength of the material.

Figure 1 shows how a crack evolves as a function of a time varying strain, using an applied strain rate of 0.005 in the normal direction. The initial crack shape is elliptical with length less than a tenth of the width seeded at the center. The dark regions

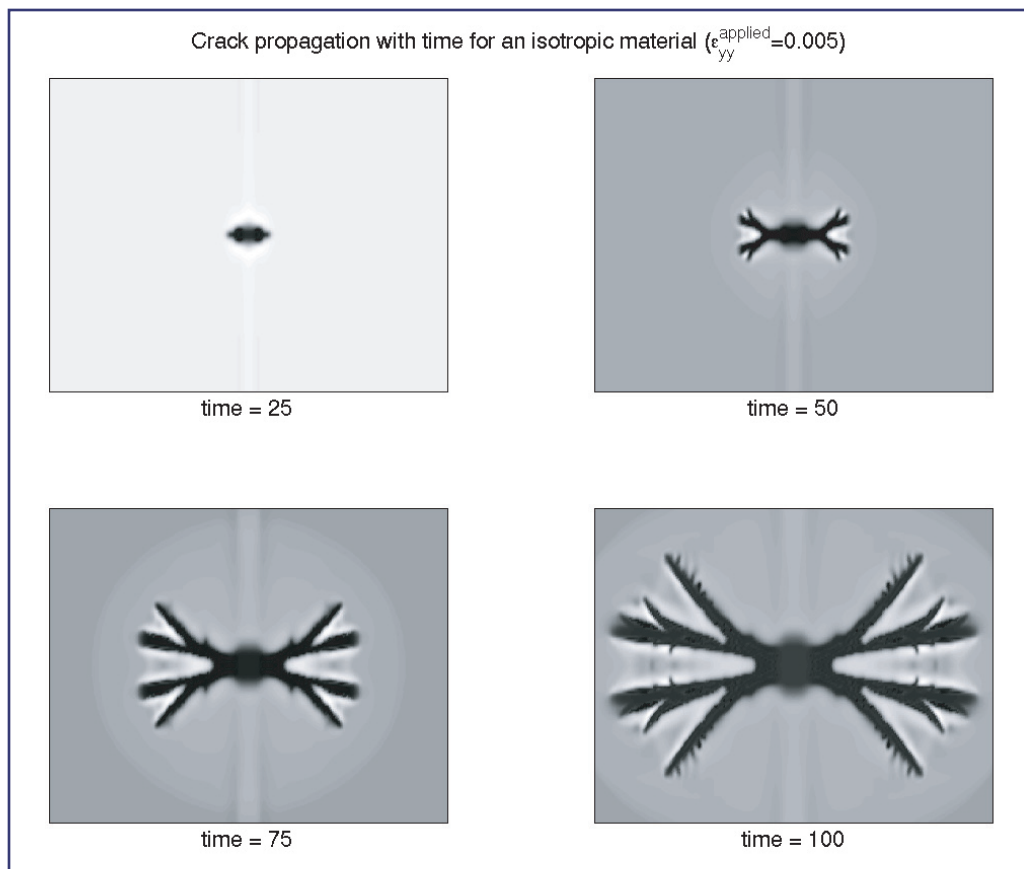


Figure 1—
The figure shows how a crack evolves as a function of a time varying strain, using an applied strain rate of 0.005 in the normal direction. The dark regions represent the crack.

represent the crack. Stresses develop near the crack tips, which start to grow once the imposed strain reaches a critical value. The crack rapidly side-branches and even these subbranches break up readily.

*For more information, contact
 Turab Lookman (txl@lanl.gov).*

Acknowledgements

We would like to acknowledge NNSA's Advanced Simulation and Computing (ASC), Materials and Physics Program for financial support.

Viscoelastic Behavior of Polymers

*David Hall and Turab Lookman (T-11),
and Edward Kober (T-14)*

The behavior of complex fluids, such as polymer blends and multiblock copolymers (e.g., Estane®) is intermediate between that of solids and fluids. For short times, the response is elastic and the stress is proportional to the applied strain. On the other hand, for late times a fluid-like response with stress proportional to the strain rate is typically observed. The effect of viscoelasticity on polymer morphology becomes even more important as the “dynamical asymmetry” between the polymer components increases. The behavior of the “slow” and “fast” components leads to deformation and phase separation properties that are quite unlike those observed for symmetric systems.

The “two-fluid” model, in which separate velocities are needed for the monomeric components to describe viscous drag effects and the viscoelastic nature of the polymeric chains, has been reasonably successful in understanding blends and homopolymers. However, a phenomenological Ginzburg-Landau free energy is used to describe the composition or density of the chains. In contrast, we have developed a scheme that couples the chemical potentials from a Self-Consistent Mean Field Method (SCFT) within the framework of a two-fluid model so that the polymeric nature of the fluids is taken into account, albeit within a mean field approximation that is good for dense systems or melts. This Hydrodynamic Self-Consistent Field Theory (HSCFT) extends the SCFT technique to nonequilibrium regimes, retaining its thermodynamic detail while accessing experimentally relevant timescales. An advantage of this approach is that it is easily extensible to systems of arbitrary complexity for which it is difficult to construct a Ginzburg-Landau free energy.

Many of the mesoscale properties of the system relax on timescales shorter than thermodynamic timescales and are effectively in local equilibrium on hydrodynamic timescales, which allows us to employ SCFT techniques to calculate their properties. The hydrodynamic model thus simulates the large-scale convective and diffusive flows, as well as the polymer’s viscoelastic behavior. By employing parallelized pseudo-spectral techniques, we are able to model relatively large systems in three dimensions with high accuracy and long time-scales.

The HSCFT approach provides a new tool that can be employed to perform numerical experiments on a wide range of complex polymer systems under various processing conditions. Although our code is currently limited to modeling the properties of diblocks in the low shear linear viscoelastic regime, with a reasonable effort it can easily be extended to more complex systems such as linear multiblocks copolymers and star and branched copolymers. Additionally, the system can be extended to include particles of arbitrary shape and size using compatible phase-field techniques. One example of interest might be a system of polymers mixed with carbon nano-tubes. Some progress has also been made toward modeling systems with complex wall geometries to capture the behavior of polymers in thin films or in the presence of microfluidic channels.

Figure 1 shows a diblock copolymer system that has been rapidly quenched from its homogenous well-mixed phase into a microphase-separated region. The blue and yellow in the cross-section are the two monomer components and the interior shows the yellow matrix of one component that is embedded in the other component. In Fig. 2, we can see that the early stages of phase separation are dominated by purely diffusive effects. However, at later times cooperative convective flows contribute in a nontrivial way. The free energy as a function of time shows a significant drop coincident with the phase-ordering process that takes place over the diffusive time scale. Further decrease in the free energy is accompanied by rearrangement of larger scale motions due to convection, which occurs on a second, much longer timescale.

For more information, contact David Hall
(halldm@lanl.gov).

Acknowledgements

We would like to acknowledge NNSA's Advanced Simulation and Computing (ASC), Materials and Physics Program; and Campaign 2, Dynamic Materials Properties, for financial support.

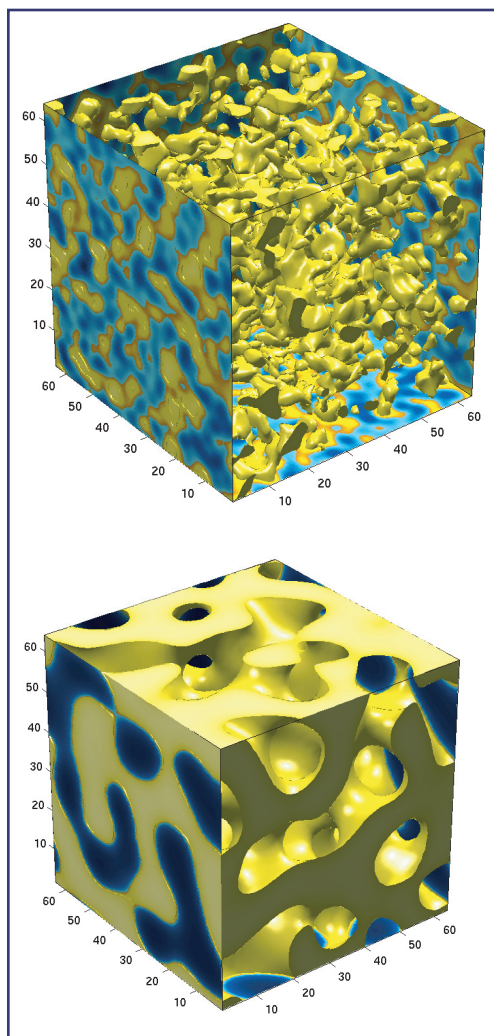


Figure 1—
Early and intermediate stages of microphase separation in a diblock copolymer melt. The yellow and blue zones represent areas of high concentration of the two dissimilar monomers. In the interior, one monomer species is removed to reveal the complex defect-filled morphologies that are typical of these materials.

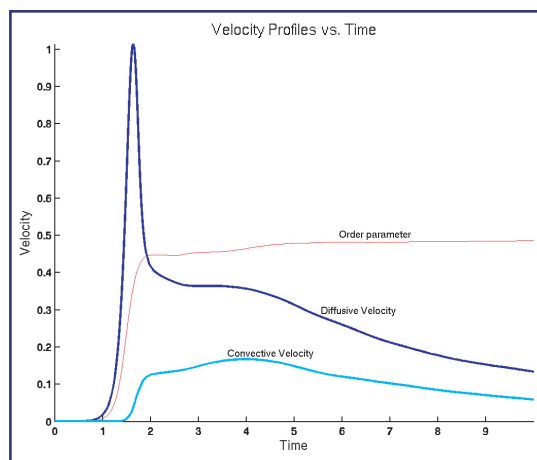


Figure 2—
Diffusive velocity (w) and convective velocity (v) vs time.

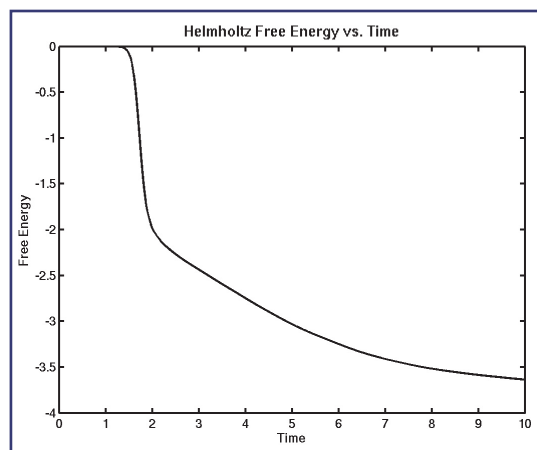


Figure 3—
Helmholtz free energy vs time.

Impurities Block the α to ω Martensitic Transformation in Titanium

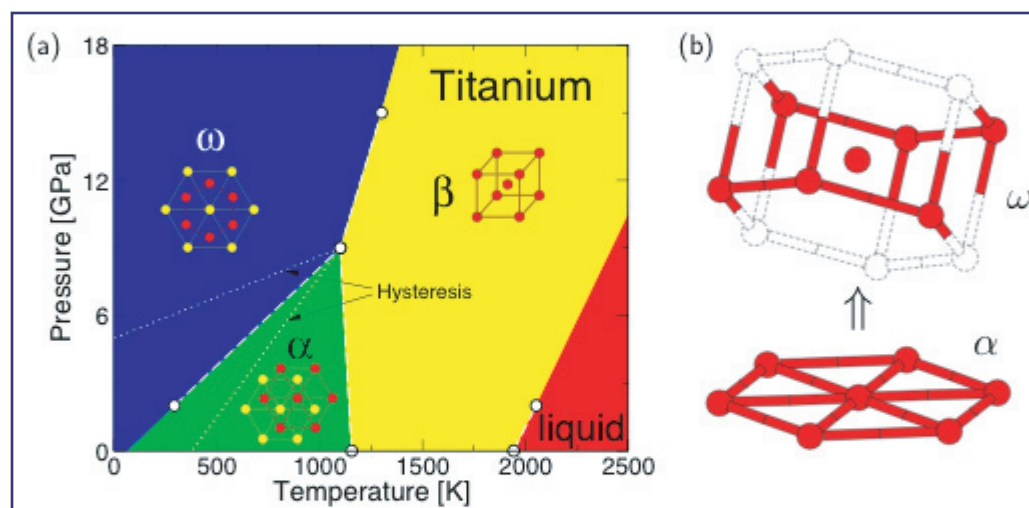
Richard G. Hennig, Dallas R. Trinkle, and John W. Wilkins (Ohio State University); Johann Bouchet and Robert C. Albers (T-11); and Srivilliputhur G. Srinivasan (MST-8)

Impurities control phase stability and phase transformations in nature. Experiments and empirical databases are still central to tuning the impurity effects, since a broad theoretical underpinning is missing. Consider, for example, the titanium martensitic transformations, diffusionless structural transformations proceeding near the speed of sound. Pure Ti transforms from ductile α to brittle ω at 9 GPa creating serious technological problems for β -stabilized Ti alloys. Impurities in the Ti alloys A-70 and Ti-6Al-4V (wt. %) suppress the transformation up to at least 35 GPa enhancing their technological utility as lightweight materials. These and other empirical breakthroughs in technological materials call for broad theoretical understanding. Impurities pose two theoretical challenges: the effect on the relative phase stability and the energy

barrier of the transformation. *Ab initio* methods calculate both changes due to impurities. In general, these effects are central to understanding structural phase transformations.

We have determined the energy and location of impurities in α and ω Ti and shown how they suppress the martensitic $\alpha \rightarrow \omega$ transformation (the phase diagram is shown in Fig. 1). Our approach exploits the basic observation that for any martensitic transformation the impurities are trapped in their local environment. We study a range of impurities, including those in the commercial Ti alloys A-70 and Ti-6Al-4V: interstitial O, N, C and substitutional Al and V. The interstitial impurities occupy the octahedral site in α and transform into the octahedral and hexahedral sites in ω . (See Fig. 2.) The impurities affect the transformation by shifting the relative stability of and energy barrier between the α and ω phases. Interstitial impurity effects are governed primarily by their size; they retard the transformation by increasing the energy barrier and shifting the relative stability. Substitutional impurities affect the transformation by changing the d-electron concentration; Al retards and V assists the transformation. (See Fig. 3.) The most important impurities, O in A-70 Ti and Al in Ti-6Al-4V, more than double the transition barrier and decrease the stability of ω , explaining the observed suppression of the transformation. The effect of impurities on relative energies and energy barriers is central to understanding structural phase transformations.

Figure 1— Structural phase transitions in Ti. (a) The phase diagram of Ti as a function of temperature and pressure shows martensitic transformations between the α , β , and ω phases. (b) The transformation from α to ω proceeds via the TAO-1 mechanism [1]; shown is the transformation of one hexagonal basal plane of α to make the honeycomb and hexagonal planes in ω .



[1] D.R. Trinkle, R.G. Hennig, S.G. Srinivasan, D.M. Hatch, M.D. Jones, H.T. Stokes, R.C. Albers, and J.W. Wilkins, "A New Mechanism for the Alpha to Omega Martensitic Transformation in Pure Titanium," *Phys. Rev. Lett.* **91**, 025701 (2003).

For more information, contact Robert C. Albers (rca@lanl.gov).

Acknowledgements

We would like to acknowledge NNSA's Advanced Simulation and Computing (ASC), Materials and Physics Program for financial support.

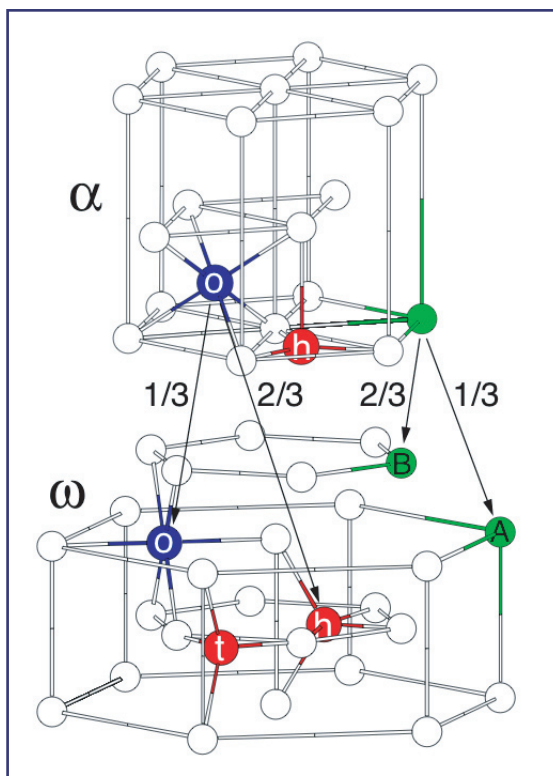


Figure 2— Impurity sites in α and ω . Octahedral (o), tetrahedral (t), and hexahedral (h) sites for interstitial impurities as well as A and B sites for substitutional impurities in the α and ω phases. The α and ω phases each contain one unique o, t, and h site. The α_{tet} site relaxes to the nearby α_{hex} site for all three impurities (O, N, C). The hexahedral site is a distorted double-tetrahedral site with five neighbors. The arrows indicate the transformation of the impurity and lattice sites in the TAO-1 mechanism [1] and the relative ratios. For clarity, the relative orientation of α and ω in TAO-1 is not shown.

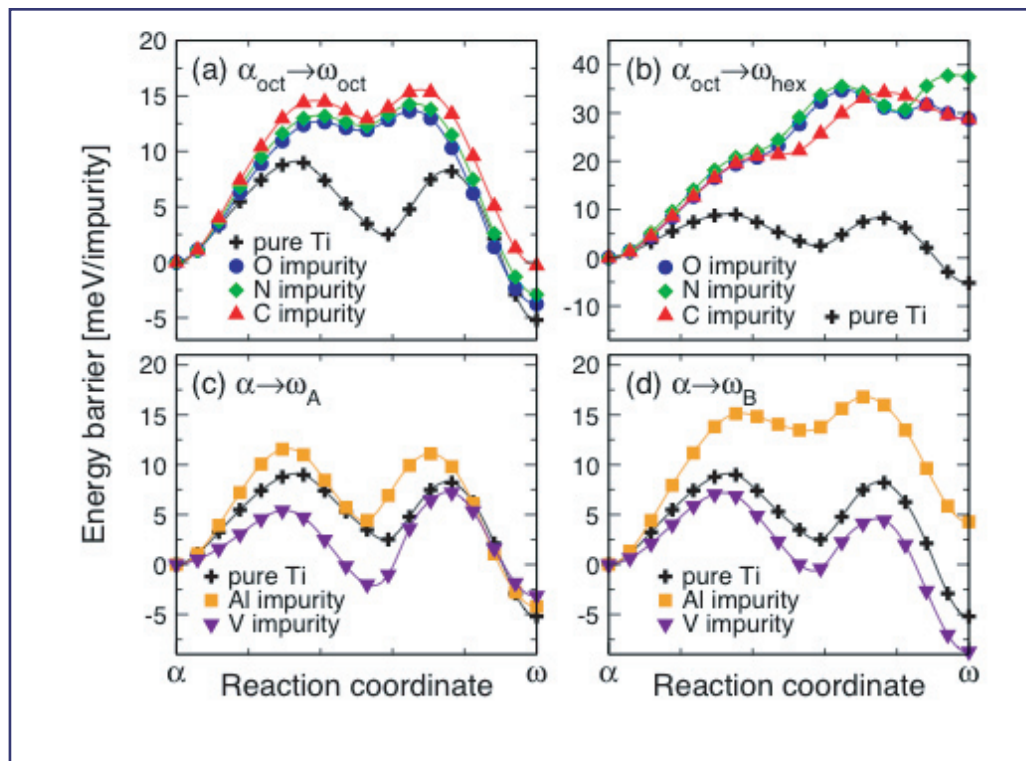


Figure 3— Impurities change the energy barrier of the $\alpha \rightarrow \omega$ transformation. The energy barriers for the TAO-1 transformation [1] of interstitial and substitutional impurities in Ti are shown relative to the α phase in units of MeV per impurity atom. The defect concentration is 2 at. %. The endpoint energies match the formation energies for a defect concentration of 1 at. % within 1 meV/atom, providing an accuracy estimate for the barrier. The interstitial O, N, and C impurities occupy the α_{oct} and transform into either (a) ω_{oct} or (b) ω_{hex} , with a 1:2 ratio. The substitutional Al and V impurities transform in ω to either (c) the A site or (d) the B site, with a 1:2 ratio.

Towards Modeling Elastic Properties of Estane®

Kim Ø. Rasmussen and Turab Lookman (T-11), Panagiotis Maniadis (CNLS/T-11), and Edward M. Kober (T-14)

We have, as reported earlier, developed a methodology based on self-consistent field theory by which we can determine the morphological properties of multiblock copolymer self-assemblies. We have done this in an effort to achieve modeling capabilities of morphological and elastic properties of the commercially available segmented polymer Estane®. Our interest in Estane® arises from the fact that this material acts as the polymeric binder component in the high explosive PBX 9501 and it has been strongly suggested that aging effects in this composite arise from chemical and physical changes in the binder. Estane® 5703 is a segmented block copolymer whose strength arises from the self-organization it undergoes. The chemical structure is shown in Fig. 1. The “hard” segments are comprised of methylenediphenylisocyanate (MDI) units (with 1–3 repeats), and the “soft” segments are butyleneadipate (BA) oligomers of 5 segments. These components are repeated about 28 times as shown in Fig. 1. Our self-consistent field models can effectively and precisely determine the morphological structures emerging from the self-assembly of these segmented chains.

In order to further enable this methodology to also characterize the elastic properties resulting from these self-assemblies we have constructed a self-consistent field theory that in addition to the polymer density also incorporates the local stress and strain fields in the material. The development is based on previous work by Fredrickson [1] who recently developed a self-consistent field theory for homopolymer melts which incorporates polymer density, stress, and strain fields simultaneously. The strain is included at the microscopic level via a single chain expression due to Doi and Edwards [2]. The stress field arises as the conjugate to the strain field. We have extended this theory to self-assembling polymer systems, and we have initially computer-implemented this theory for the simplest such system, namely diblock copolymers.

Within this theory we cannot only determine the morphological properties of the polymer density but also the corresponding internal stress distributions in the self-assembled structures. An example of this is shown in Fig. 2 for the hexagonal phase of a diblock copolymer. In this particular case a block copolymer composed of just two chemical species (say A and B) in the volume ratio 30:70 self-assembles into cylinders rich in the minority species (A), which are packed hexagonally in a matrix formed by the majority species (B). Together with a 2D projection of polymer density we show a similar projection of the σ_{xx} component of the stress tensor. Similarly, we can determine the remaining components of the stress tensor. Further, this model allows us to follow the local stress development in all components of the stress tensor as the self-assembly is strain

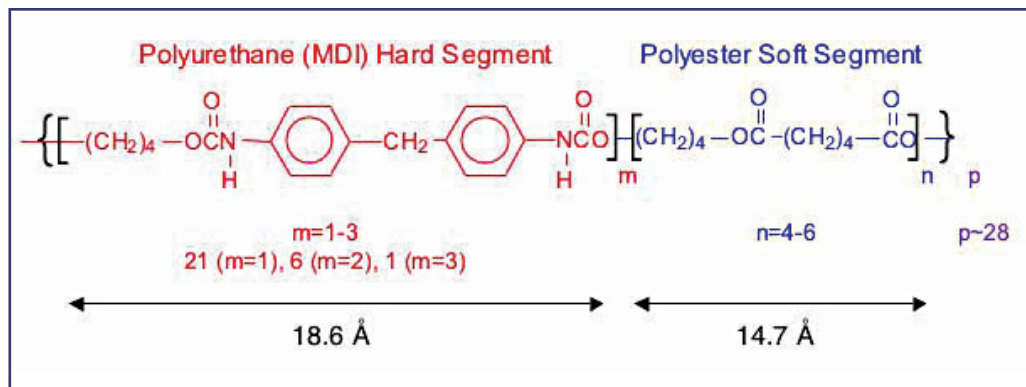
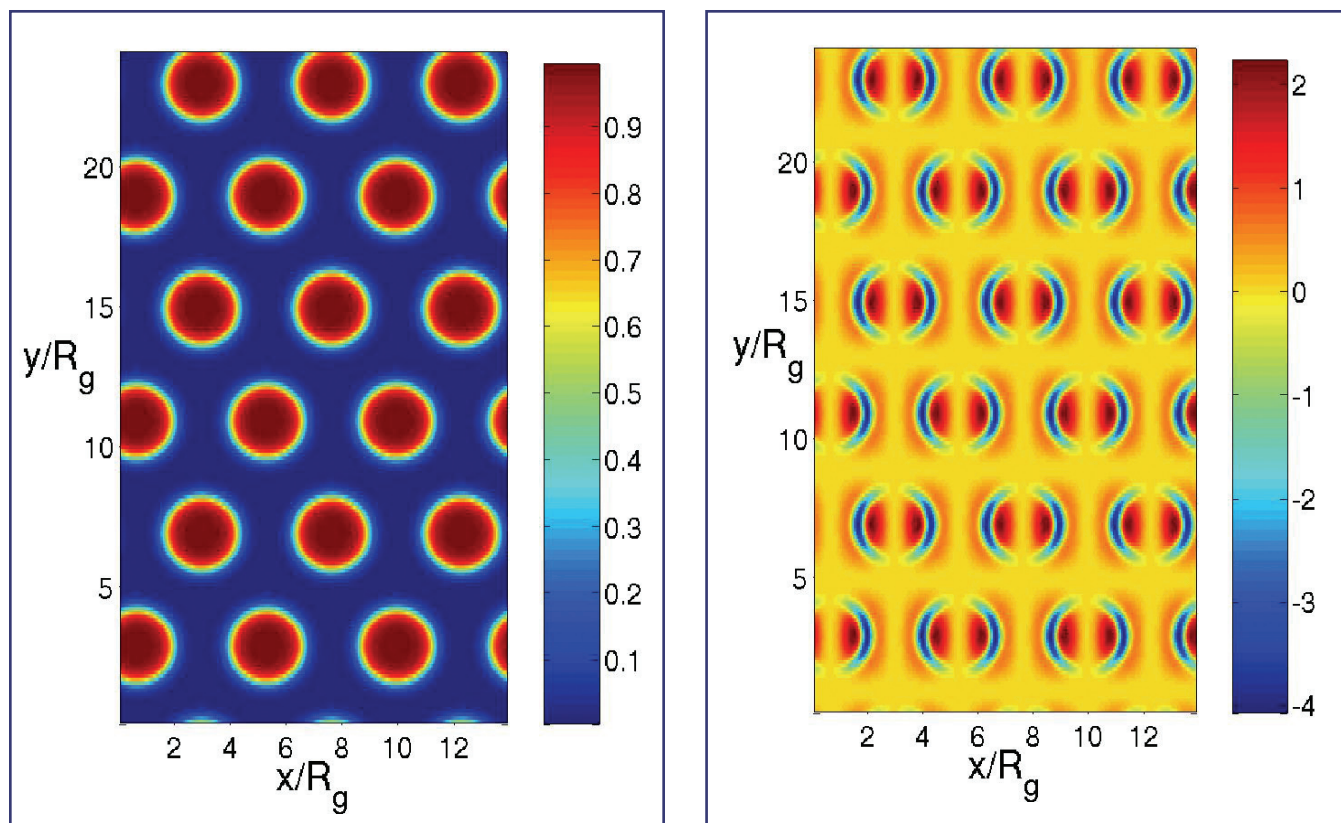


Figure 1—
The chemical structure
of Estane®.



loaded, and consequently the complete set of elastic moduli can be calculated.

We plan to apply this new technique to the more involved segmented polymer model that applies directly to Estane® and thereby help formulate a response model for this material.

[1] G.H. Fredrickson, *J. Chem. Phys.* **117**, 6810 (2002).

[2] M. Doi and S.F. Edwards, *The Theory of Polymer Dynamics* (Clarendon Press, Oxford, 1986).

*For more information, contact
Kim Ø. Rasmussen (kor@lanl.gov).*

Acknowledgements

We would like to acknowledge NNSA's Advanced Simulation and Computing (ASC), Materials and Physics Program; Campaign 2, Dynamic Materials Properties; and Campaign 8, Enhanced Surveillance, for financial support.

Figure 2—

Left: Two-dimensional projection of hexagonal cylindrical phase in 30:70 diblock copolymer self-assembly. Density of minority component is shown such that red indicates high density and blue low density.
Right: The σ_{xx} component of the stress tensor corresponding to the density.

World Record: Large-Scale Molecular- Dynamics Simulation of 19 Billion Particles

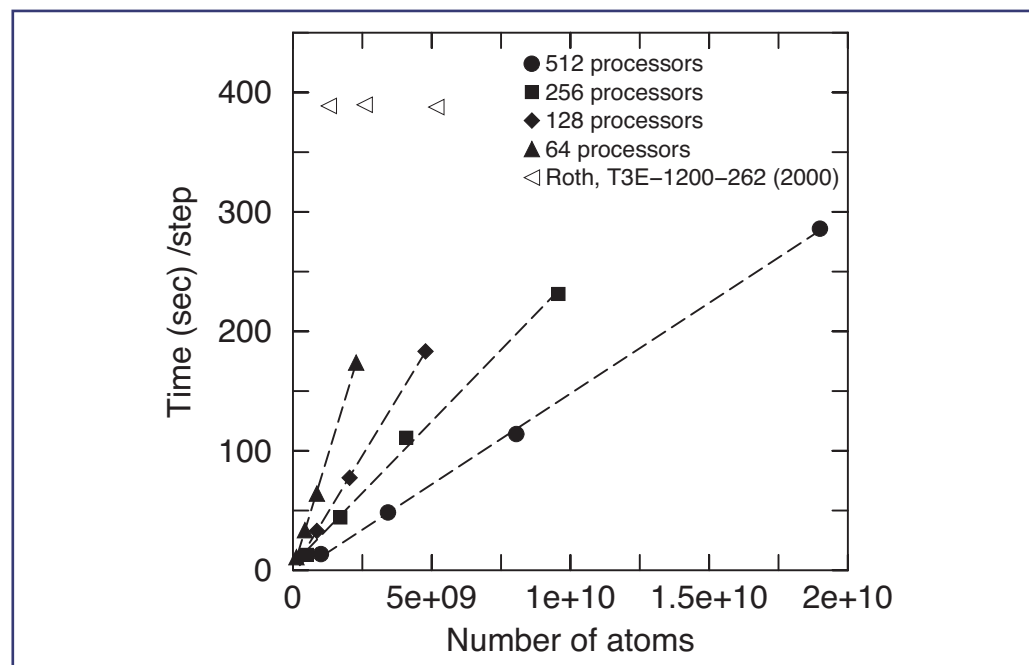
Kai Kadau (T-14),
Timothy C. Germann (X-7), and
Peter S. Lomdahl (T-11)

In the early 1990s, Lomdahl, Beazley, and coworkers did pioneering work on large-scale molecular-dynamics (MD) simulations [1, 2] with up to 131 million particles on a variety of parallel platforms, including the Connection Machine 5. Ever since, large-scale MD simulations have been used intensively to get insight into atomic processes on the pico-second time scale for various solid-state material science issues. It has been demonstrated that on today's largest parallel supercomputers MD simulations with one billion atoms are feasible.

However, such ultra-large-scale simulations present an analysis problem due to the enormous datasets that are produced. For example, the memory needed to save one configuration of one billion atoms in single precision is more than 15 Gbyte, which makes it problematic and inconvenient to save all the raw data and analyze the data in a postprocessing fashion, even on modern platforms with Tbytes of hard-disc capacity. For example, in the configuration of the (X-, Y-, Z-) particle position each of these four numbers takes usually four bytes in single precision. However, for a restart of the system usually the position and velocity vectors are needed in double precision, which makes the memory consumption about 45 Gbyte for one billion particles. Rather, an on-the-fly analysis during the simulation run is desired.

The MD code SPaSM [1, 2] (Scalable Parallel Short-range Molecular dynamics) has multiple tools to analyze the simulation results during the course of the simulation. The methods implemented include generation of pictures of configurations (particle as well as cell based), local and global quantities like stress tensor elements, temperature, energy, displacement, centrosymmetry parameter, etc. It also allows for calculating histograms and correlation functions for the whole system as well as for subsets of the system (see [3] for examples).

Figure 1—
Timings for runs on
a different number of
PN for varying number
of atoms. Time used
per integration step
on a fixed number of
processors increases well
linearly with the number
of atoms for system sizes
up to some 20 billion.
A slight increase of
the time used can be
seen, if the number of
atoms per PN is fixed
and the number of PN
is increased. The data
is compared to earlier
demonstration runs by
Roth et al. using 128,
256, 512 PN on a T3E
(left to right).



Here, we demonstrate the capability of the SPaSM library to run and analyze systems containing up to approximately 20 billion atoms on the QSC-machine at Los Alamos National Laboratory [4]. Furthermore, we introduce a new parallel sphere rendering capability that we developed in order to generate high-resolution pictures of configurations containing millions to billions of particles. To the best of our knowledge this is the largest MD simulation reported to date. According to the good linear scaling of the simulation time with the number of particles, it would be possible to run 100 billion atoms on a large partition of the current Q-machine. This potential enables future simulation of a physical problem on the micrometer-scale, which so far only has been theoretically investigated by continuum methods.

The flexibility of the SPaSM library can be exploited in other ways, for instance by opening up the possibility of large-scale agent-based simulations. Smaller-scale agent-based models for the spread of epidemics can now scale up to encompass the entire world population of 6.3 billion people.

[1] P.S. Lomdahl, P. Tamayo, N. Gronbech-Jensen, and D.M. Beazley, *Proceedings of Supercomputing 93*, G.S. Ansell, Ed. (IEEE Computer Society Press, Los Alamitos, CA, 1993), p. 520.

[2] D.M. Beazley and P.S. Lomdahl, *Comput. Phys.* **11**, 230 (1997).

[3] K. Kadau, T.C. Germann, P.S. Lomdahl, B.L. Holian, *Science* **296**, 1681 (2002).

[4] K. Kadau, T.C. Germann, P.S. Lomdahl, *Int. J. Mod. Phys. C* **15**, 193 (2004).

For more information, contact Kai Kadau (kkadau@lanl.gov).

Acknowledgements

We would like to acknowledge NNSA's Advanced Simulation and Computing (ASC), Materials and Physics Program for financial support. Some specific portions of the research reported here were supported by Laboratory Directed Research and Development.

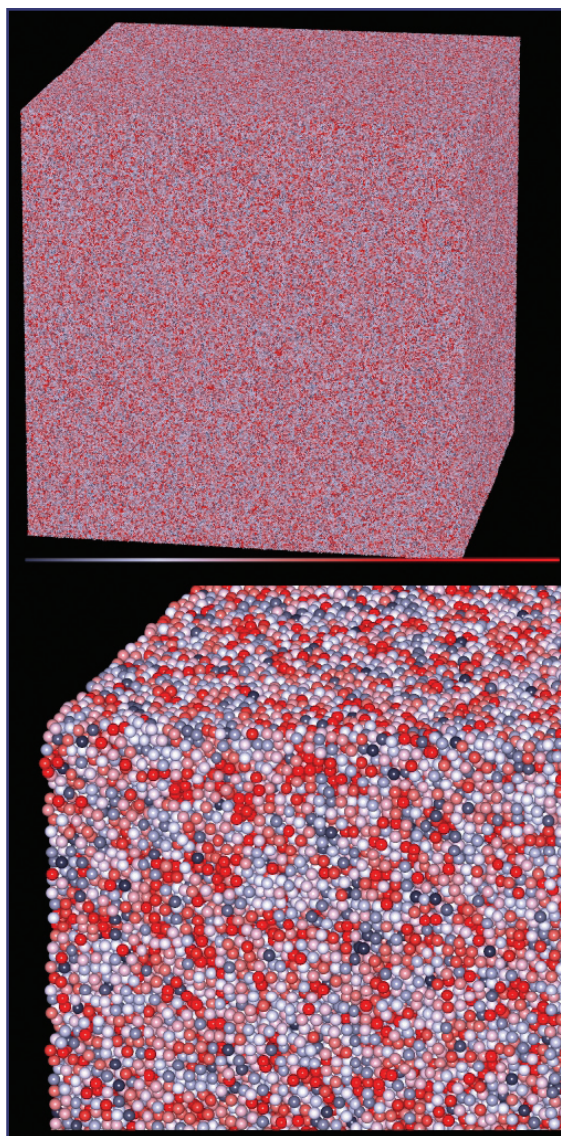


Figure 2—
Approximately 37 million particles rendered on four PN with a resolution of 5000 pixel by 5000 pixel (top). The bottom shows a close-up of the same picture file. The color represents the potential energies of the atoms: dark gray = -6 and red = -2.

Thermal Decomposition of Nitromethane using Reactive Molecular Dynamics

Si-ping Han (T-14 and California Institute of Technology) and Alejandro Strachan (T-14)

The development in recent years of reactive interatomic potentials has enabled, for the first time, the accurate simulation of the thermal- or shock-induced decomposition of energetic materials under realistic loading conditions. Reactive molecular dynamics (MD) simulations provide a molecular-level, full-chemistry, and full-physics description of the chemistry and mechanical processes in energetic materials making no assumptions or simplifications other than those intrinsic to the force field description of the interactions, the fact that we use classical mechanics to describe atomic dynamics and the size of the simulation cell. Such molecular level characterization is essential for the development of predictive, physics-based, materials models.

We study the decomposition of liquid and solid samples on nitromethane (CH_3NO_2) at high temperatures (2000–3000 K) and high density (1.97 g/cm^3) using molecular dynamics with the first-principles-based reactive force field ReaxFF. The first chemical reactions observed in the decomposition of nitromethane are either an intermolecular proton transfer leading to the ions CH_3NOOH and CH_2NO_2^- (favored at higher temperatures) and an isomerization reaction involving the scission of the C-N bond the

formation of a C-O bond to form methyl nitrate (CH_3ONO) (favored for the lower temperature cases studied). Also early in the decomposition process we observe intramolecular proton transfer events leading to the aci-acid form: $\text{CH}_2\text{NO}_2\text{H}$.

We show in Fig. 1 five snapshots of the isomerization reaction obtained from our MD simulation starting from a liquid structure at $T = 2500 \text{ K}$; the time elapsed between the second and fourth snapshots is 20 fs. The central structure depicts roughly the transition state, the corresponding C-N and C-O bond distances at this point in the reaction are 1.89 and 1.60 Å, respectively. There has been some controversy in the literature regarding the structure of the transition state between nitromethane and methyl nitrate; see for example [1]. Some authors have predicted a loose transition state (with C-N and C-O bond distances longer than 3 Å) while others predict a tight transition state with bond distances around 2 Å. Our MD simulations predict a tight transition state in agreement with the most recent and accurate *ab initio* results [1].

In Fig. 2 we show the time evolution of the population of nitromethane as well as several important products (H_2O , CO , N_2 , and NH_3) and the intermediate (H_3CNOOH) for both liquid and crystalline structures and two temperatures. As already mentioned the formation of CH_3NOOH via a proton transfer is the first reaction that appears in the populations plot. The formation of H_2O (the main product) occurs after most of the original nitromethane molecules have undergone the initiation reactions. The final population of H_2O is not very sensitive to temperature; we find about 0.8 H_2O molecules per nitromethane. Other important products are N_2 , CO_2 , and NH_3 . As expected the population of these small molecules is larger at $T = 3000 \text{ K}$ than at $T = 2000 \text{ K}$, in particular we find almost no N_2 molecules at $T = 2000 \text{ K}$.

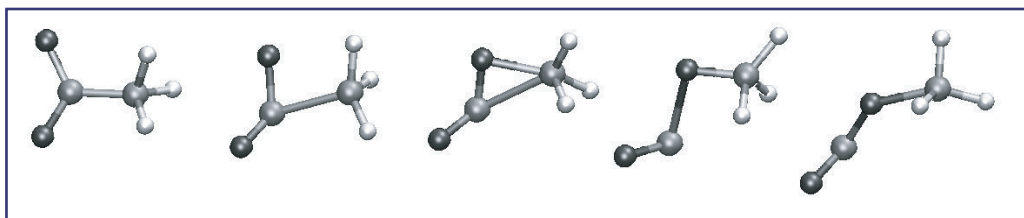
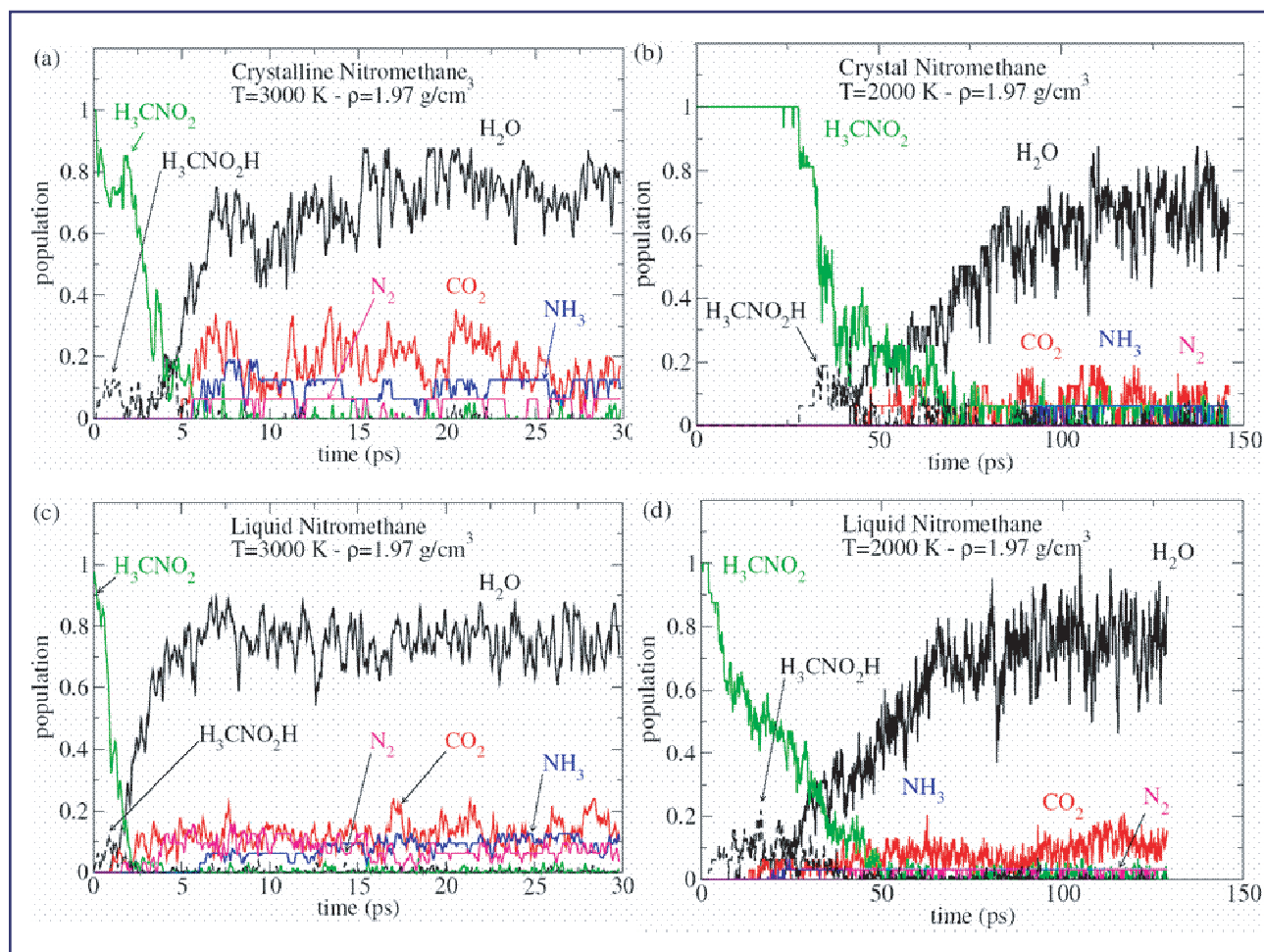


Figure 1—Molecular dynamics snapshots of the process of isomerization of nitromethane leading to methyl nitrate.



Our results for the crystalline sample at $T = 3000$ K are in excellent agreement with recent quantum mechanically (QM)-based MD simulations [2] regarding the detailed chemistry of decomposition and the time-scales associated with the reactions. Furthermore the pressures obtained from our simulations at $T = 1000$ and 4000 K and high pressure $\rho = 2.2$ g/cm³ are in excellent agreement with the QM results. Note that while *ab initio* data on nitromethane has been used to develop ReaxFF (chemical reactions and vibrational properties) none of the QM MD results in Ref. [2] were included in any way into the ReaxFF parameterization. This provides an important direct validation of the ReaxFF description of interatomic forces in energetic materials.

[1] M.T. Nguyen, et al., *J. Phys. Chem.* **107**, 4286 (2003).

[2] M.R. Manaa, et al., *J. Chem. Phys.* **120**, 10146 (2004).

For more information, contact
Alejandro Strachan (strachan@lanl.gov).

Acknowledgements

We would like to acknowledge NNSA's Advanced Simulation and Computing (ASC), Materials and Physics Program for financial support. Si-ping Han would like to thank the Seaborg Institute for a summer fellowship.

Figure 2—
Time evolution of nitromethane (green lines), several important products [H_2O (black), CO_2 (red), N_2 (magenta), and NH_3 (blue)] and the intermediate H_3CNOOH (dashed lines) for the liquid and crystalline structures at $T = 3000$ K and $T = 2000$ K. Populations are given per nitromethane molecule.

Micromechanical Modeling of the Binder Material of PBX 9501

David Hanson (T-12)

Theoretical Division participates in the important but extremely difficult materials science task of predicting the lifetime of nuclear weapons. As part of Los Alamos National Laboratory's (LANL's) Enhanced Surveillance Campaign, we study PBX 9501—a plastic-bonded high explosive (HE) composed of a 1:1 (by weight) mixture of a nitroplasticizer (NP) and a polyurethane (Estane® 5703). Estane® is copolymer composed of multiple methyl di-isocyanate (MDI) units connected by random lengths of polyester. The weight-averaged molecular weight is approximately 80 K Daltons. Over a time period of weeks, some of the hard segments (MDI units) phase separate, forming a three-dimensional (3D) random network of nodes (MDI units) and chains (polyester soft segments). The binder derives its mechanical strength by virtue of this highly interconnected network.

Chemical and physical changes that occur as the binder material ages will affect its mechanical properties, and this can impose an ultimate lifetime on the HE charge. How the NP affects the mechanical properties of the binder has been an important issue. A straightforward analysis of tensile stress/strain experiments that covered a range of Estane®:NP mixtures suggests that the NP acts mostly as a diluent in the binder. Figure 1 shows the tensile stress at various strains as a function of the NP fraction ($f_{NP} = 1 - f$), where f is the weight fraction of Estane®.

We fit the experimental data to various power laws and find that the relation $S = S_0 f^3$ provides reasonable agreement for strains between 100% and 900%. Although the experiments did not explicitly include the case of 100% NP ($f = 0$), it is obvious that since NP is a liquid, the stress must go to zero (if the Estane® fraction is zero, then no network can exist). Clearly, one factor of f suffices to impose this condition. Our conjecture is that the other factor of f^2 represents a network formation probability, i.e., the probability that two MDI units will bind together to form a hard domain is proportional to the square of the local MDI density. This would be analogous to a reaction rate for classical gas phase dimerization being proportional to the square of the monomer concentration. In this case, however, it is

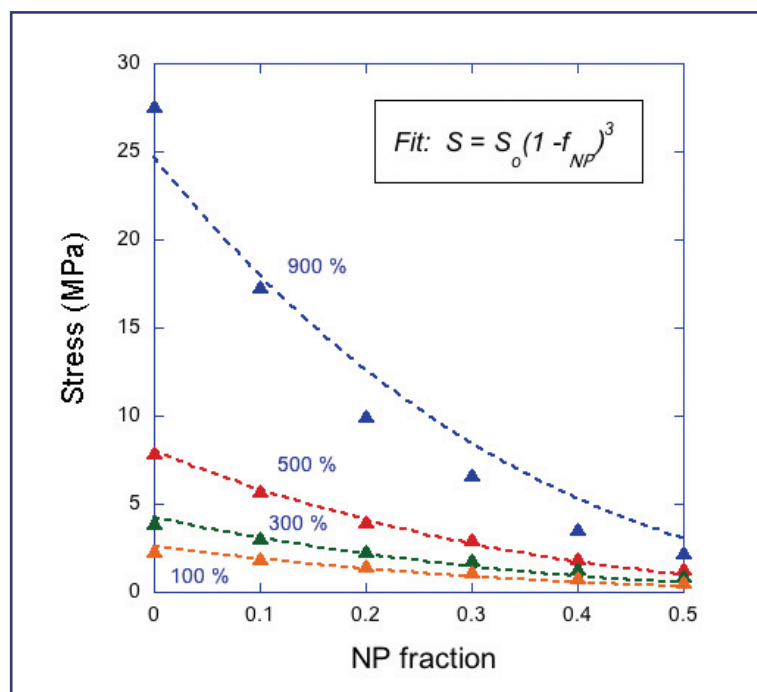


Figure 1—Least square fits of the experimental tensile stress (Bruce Orlor, from Group MST-7 at LANL) to the cube of the Estane® weight fraction ($S = S_0 f^3$), parametric on strain.

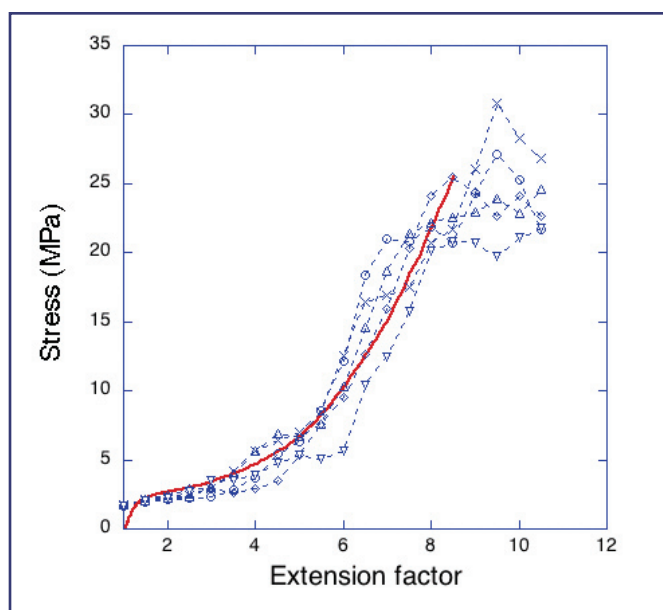


Figure 2—
Model network simulations of tensile stress/strain in neat Estane®, dashed lines, compared to experimental data (Bruce Orler, from Group MST-7 at LANL) solid line.

the time-integrated rate that matters, so the analogy is not perfect. Establishing that the NP acts as a diluent provides confidence that theoretical and experimental studies of neat Estane® are relevant to understanding the behavior of the binder. Although the influence of NP on mechanical properties appears to be simple, that is not the case for the chemical degradation of the Estane®; here the role of NP appears to be quite complex [1].

Previously, under Laboratory-Directed Research and Development funding, we developed an explicit, 3D numerical network model (EPnet) [2] to simulate the micromechanical behavior of cross-linked and/or filled polymers (e.g., silica-filled polydimethylsiloxane) for various static strains. The molecular forces required to stretch a chain or disrupt its binding to a filler particle were estimated from atomistic simulations. Because the network produced by the polymer phase separation in Estane® yields a node-and-chain morphology similar to that of a filled polymer, we believe that we can apply this model to the study of Estane®. Figure 2 shows a comparison of five statistically independent random network simulations (dashed lines) compared to a tensile stress/strain experiment by Bruce Orler, from the Polymers and Coatings Group (MST-7) at LANL (solid line).

The volume element simulated (a 90-nm cube) included 1500 nodes interconnected by about 8000 chains. Parameter values used in the model, which were adjusted to obtain agreement with experiment, are consistent with estimates obtained from atomistic simulations or experimental data. Not only does the model provide a quantitative prediction for the yield stress, but it is also able to capture the phenomenon of tensile failure. The agreement between simulation and experiment is an important result because it gives us confidence that we understand the mechanisms that produce strength in the HE binder. We will use this picture to understand how chemical changes can affect the mechanical properties.

[1] Denise K. Pauler and Joel D. Kress, “Decomposition of Nitroplasticizer in Plastic-Bonded Explosive PBX 9501,” in this volume on p. 58.

[2] D.E. Hanson, *Polymer* **45**, 1055 (2004).

For more information, contact
David Hanson (deh@lanl.gov).

Acknowledgements

We would like to acknowledge Campaign 8, Enhanced Surveillance, for financial support.

Quantum Molecular Dynamics Simulations of Liquid Plutonium and Hydrogen/Metal Mixtures

Joel D. Kress (T-12) and
Lee A. Collins (T-4)

Warm, dense matter appears in a wide variety of celestial and terrestrial environments—from the interiors of gaseous planets and atmospheres to the plasmas generated by high-energy-density machines and lasers. Other examples include shock-compressed solids and cryogenically cooled liquids, ultracold plasmas, and various stages in primary and secondary nuclear weapons. In general these systems span temperatures from 10^2 K to 10^6 K and beyond, and densities from about 1/100 to 100 the density of a solid. Recently, quantum molecular dynamics (QMD) has been used to accurately predict properties of hydrogen, aluminum, and oxygen-nitrogen mixtures in the warm, dense state. In this report we describe recent work on transport in liquid plutonium and mixtures of metal in hydrogen and metals.

To model such systems, we have applied QMD simulation methods that treat the rapidly moving electrons quantum mechanically and the sluggish nuclei classically. In order to provide a systematic representation of the quantum mechanical effects, we have treated the electrons with a state-of-the-art finite-temperature density functional theory (DFT) approach. Specifically, the calculations used the Vienna *ab initio* Simulation Package with the following common characteristics: a plane-wave basis to represent the wave functions, the generalized gradient approximation density functional, relativistic PAW (projector augmented wave) pseudopotentials without spin-orbit coupling to represent the core electrons. An additional advantage of the

QMD methods comes from their integrated nature. Having established the elemental particle interactions, then all the static, dynamical, and optical properties rest on an internally consistent set of principles, whereas in many models of dense media, the representations of these processes arise from different approaches at different levels of approximation.

Plutonium may well be the most complex of elements. At atmospheric pressure, the phase diagram shows six equilibrium solid phases as well as a liquid phase. A study of plutonium introduces another level of complexity because electron spin (magnetic behavior) must also be considered. Although the spin-DFT calculations for the face centered cubic (fcc) lattice structure (δ -Pu) predict an antiferromagnetic (AF) state (in disagreement with the observations of a nonmagnetic state), the predicted structure is quite good, with an atomic volume (V) about 9% less than experiment. We proceeded to study liquid Pu with QMD to explore whether the quantum-derived forces provide a better description than the classical Modified Embedded Atom Method (MEAM) interatomic potential. We worked under the hypothesis that the predicted spin-DFT structural behavior will dominate over the predicted magnetic behavior, especially because the latter should be diminished by the disorder introduced in the liquid structure. An AF-like solution was found for the spin-DFT calculation (net zero magnetic moment with spins allowed to fluctuate on each atom during the MD trajectory). Radial distribution functions were calculated and self-diffusion coefficients (D) were derived from the mean-squared-displacement of the atoms determined from the MD trajectory. In Fig. 1, we compare QMD and classical MD (employing the MEAM potential) calculations of the viscosity of liquid Pu with experimental data. In the classical MD calculations [1], a 1024-atom simulation cell and nonequilibrium (NE) driven-slab boundary conditions were employed to compute the viscosity directly. In the QMD simulations, we calculated the D from the mean-squared-displacement of the atoms determined from an equilibrium MD trajectory with a 54-atom cell; the viscosity (η) was then calculated from a Stokes-Einstein relationship. The MEAM potential was developed to describe the solid

phases of Pu, therefore the results from the liquid simulations are a prediction. In this light, the MEAM values in Fig. 1 are in fair agreement with experiment (within a factor of 5). The preliminary QMD results agree reasonably well with experiment, although we note that a 54-atom simulation is probably too small to provide a definitive answer. Preliminary simulations for 108 atoms (requiring at least 32 Pentium processors in parallel) are yielding results consistent with the result in Fig. 1.

The effect of low to moderate concentrations of titanium metal on the properties of warm, dense hydrogen was studied. The simulations were carried out with a fixed number of particles (either 128 or 512) with a fixed particle density equivalent to a pure hydrogen density of $\rho = 5 \text{ g/cm}^3$. The titanium concentration Ti was varied from 0 to 16 mol % by replacing more and more hydrogen atoms with titanium atoms. A snapshot from a QMD calculation for 3.9 mol % (Ti) for 512 total particles is shown in Fig. 2. The equation of state (pressure, P) for $\rho = 5 \text{ g/cm}^3$ as a function of Ti at $T = 5$ and 10 eV increased quadratically, from $P = 11$ and 14 TPa, respectively, for $\text{Ti} = 0$ mol %, as Ti was increased up to 16 mol %. As the larger Ti atoms replace the smaller H atoms in the fixed volume, the pressure naturally increases. The self-diffusion coefficient D for hydrogen was also calculated for these conditions. The inverse of D for hydrogen is shown in Fig. 3 for titanium/hydrogen mixtures as a function of Ti. As discussed above, the viscosity η of a liquid is inversely proportional to D; therefore, η increases nearly linearly as Ti is increased. As the smaller H atoms are replaced with larger Ti atoms, there is more crowding in the fixed volume, and therefore the resistance to the flow of hydrogen goes up.

- [1] F.J. Cherne, M.I. Baskes, and B.L. Holian, *Phys. Rev. B* **67**, 092104 (2003).
- [2] E.D. Chisholm and D.C. Wallace, Los Alamos National Laboratory report LA-UR-03-6847 (2003).
- [3] L.V. Jones et al., *Trans. Am. Soc. Metals* **55**, 819 (1962).

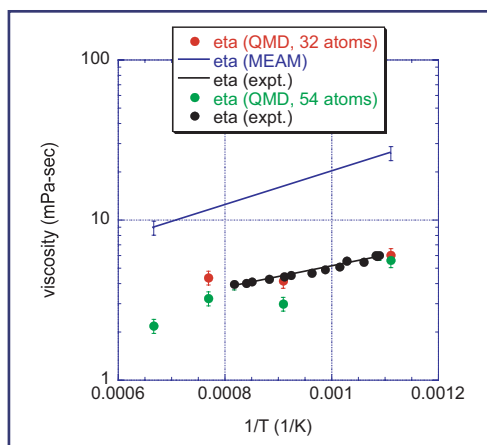


Figure 1—
Temperature dependence of plutonium viscosity η . QMD results are for samples of 32 atoms (red circles) and 54 atoms (green circles). Experimental data [3] (black circles).

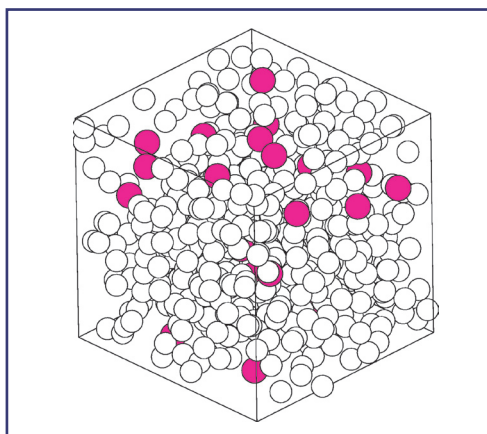


Figure 2—
Snapshot from a QMD simulation (512 total atoms) for a 3.9 mol % Ti mixture of hydrogen/titanium.

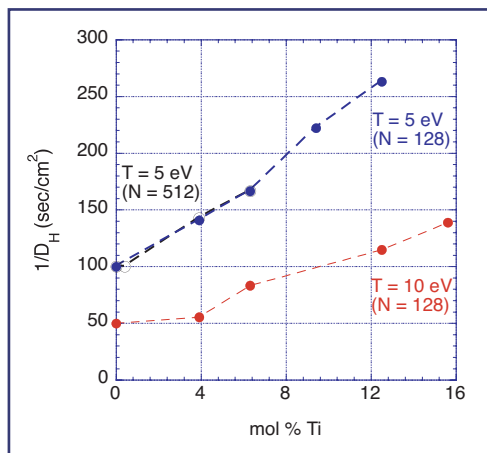


Figure 3—
Inverse hydrogen self-diffusion coefficient for hydrogen/titanium mixtures as a function of titanium concentration. Two different temperatures and particle samples (N) are shown for fixed particle density equivalent to 5 g/cm^3 of pure hydrogen.

For more information, contact Joel D. Kress
(jdk@lanl.gov).

Acknowledgements

We would like to acknowledge NNSA's Advanced Simulation and Computing (ASC), Materials and Physics Program for financial support.

Energy Exchange between Mesoparticles and Their Internal Degrees of Freedom

Brad Lee Holian (T-12) and
Alejandro Strachan (T-14)

Large-scale atomistic simulations enable a detailed understanding of complex, many-body problems in physics, chemistry, materials science, and biology. Unfortunately, despite the advances in methodologies and computer power, a wide range of phenomena is beyond present capabilities. In many of these cases, all-atom molecular-dynamics (MD) simulations are neither necessary nor desirable: coarse-grained descriptions of matter, where groups of atoms are described by a single mesoparticle, provide the required detail in a computationally efficient manner. The first task of mesodynamics is to describe the effective interactions between mesoparticles via a realistic mesopotential [1]. These mesoparticles can represent molecular groups in polymers, molecules in molecular crystals or grains in polycrystalline metals. While these approaches can be formulated to give accurate treatment of mechanical properties, there has been, up to now, no realistic thermomechanical treatment of the energy exchange between the mesoparticle and its internal degrees of freedom (DoFs).

The propagation of shockwaves in molecular crystals is particularly challenging to a mesodynamics description, since high energies and fast processes are involved. The shockwave initially excites long-wavelength, low-energy intermolecular DoFs (the ones described explicitly at the mesoscale), resulting in short-lived overheating of these (few) modes. Part of this energy then “cascades” to higher-energy, higher-frequency intramolecular

DoFs, which are only implicitly treated in mesoscopic descriptions, on a time scale that depends on the details of the molecular vibrational spectrum. This equilibration process continues until the internal and molecular temperatures reach the same value. One hopes to formulate mesodynamics that accurately predicts the final shocked state of materials.

The local velocity $\langle \mathbf{u} \rangle_i$ in the neighborhood of a given particle i is defined in terms of its own velocity and the velocities of its neighbors \mathbf{u}_j , averaging over the neighborhood with a short-range weighting function $w(r_{ij})$ that decays monotonically with interparticle distance r_{ij} :

$$\langle \mathbf{u} \rangle_i = \frac{\sum_j w(r_{ij}) m_j \mathbf{u}_j}{\sum_j w(r_{ij}) m_j}, \quad (1)$$

where the sum is over all particles. By analogy, the local neighborhood temperature T_i in d spatial dimensions is given by:

$$dkT_i = \frac{\sum_j w(r_{ij}) m_j |\mathbf{u}_j - \langle \mathbf{u} \rangle_i|^2}{\sum_j w(r_{ij})}. \quad (2)$$

In the thermomechanical mesodynamics equations of motion, the local energy of the mesoparticle must be transferred from external to internal DoFs in a Galilean invariant manner. As consequence, the common practice of adding a viscous-damping deceleration term to the velocity update equation cannot be justified. We couple the local mesoparticle temperature T_i in the vicinity of particle i to the internal temperature T_i^0 by means of an additional contribution to the mesoparticle velocity in the coordinate update equation (rather than adding a viscous deceleration in the velocity update, as is customary in all other thermostating techniques). The dissipative term contains a factor proportional to the temperature difference between internal and mesoscopic DoFs. The thermal energy of the internal DoFs is described via their specific heat C_i^0 , which is in general a function of T_i^0 . The mesodynamics equations of motion are then given by:

$$\begin{aligned}\dot{\mathbf{r}}_i &= \mathbf{u}_i + v \left(\frac{T_i - T_i^0}{\theta} \right) \frac{\mathbf{F}_i}{m_i \langle \omega^2 \rangle}, \\ \dot{\mathbf{u}}_i &= \frac{\mathbf{F}_i}{m_i}, \\ \dot{T}_i^0 &= v \left(\frac{T_i - T_i^0}{\theta} \right) \frac{\mathbf{F}_i}{C_i^0 m_i \langle \omega^2 \rangle},\end{aligned}\quad (3)$$

where v is a coupling rate that determines the time-scale of equilibration between internal and external DoFs (it can be obtained by requiring the mesoscale description to match the equilibration rate of all-atom simulations).

As an example of this new mesodynamics with internal thermostats, we report here on shockwave propagation in the crystalline polymer poly (vinylidene fluoride) (PVDF), with monomer $\text{CH}_2\text{-CF}_2$ in its β phase (a polar crystal with all-trans bonds). The crystal is formed by infinite, parallel chains. In the plane perpendicular to the chains, it forms a quasihexagonal phase.

The all-atom MD simulations in this article were performed using an accurate force field denoted MSXX [2]. For the mesodynamics simulations, we represent each polymer chain by one mesoparticle in two dimensions (retaining the directions perpendicular to the polymer chains). The interaction between mesoparticles is a pairwise-additive Rydberg potential that reproduces the stress in uniaxial compression of PVDF as described by the MSXX potential.

Figure 1 shows the rise of the local temperature of a thin slab of material (one unit cell wide) as a shockwave with $u_p = 3$ km/s passes through it. In the all-atom MD simulations, we obtain two types of local temperatures: (1) the *molecular* temperature, defined as the fluctuations of the c.m. velocities of each polymer chain around the c.m. translational velocity of the whole slab; and (2) the *internal* temperature, defined as atomic velocity fluctuations around the c.m. velocity of each molecule. The two all-atom temperatures have well-defined counterparts in the mesoscopic description;

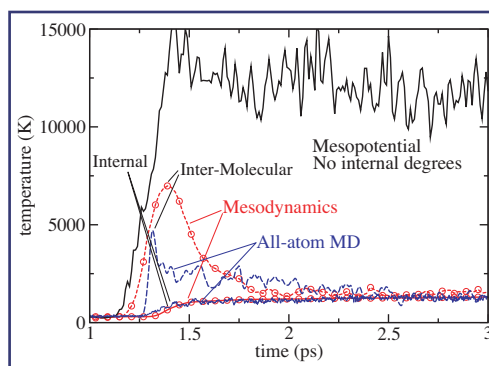


Figure 1—
Time dependence of the local temperature of a thin slab of PVDF as a shock passes through. We show molecular and internal temperatures for all-atom MD, as well as mesodynamics, both with and without coupling to internal modes.

the internal temperature is just T_i^0 , and the intermolecular temperature T_i is calculated from the velocity of the mesoparticles. The all-atom MD simulation (blue lines) shows that the shockwave initially excites the long-wavelength molecular modes; thus, the intermolecular temperature (dashed line) rises faster than the internal temperature (solid line) and initially overshoots its final value. As the higher-frequency internal DoFs get excited, intermolecular and intramolecular DoFs equilibrate, and both temperatures converge to the same value. The bare mesopotential without coupling greatly overestimates the final temperature, due to the reduced number of DoFs available to accommodate the energy increase. The new mesodynamics (red lines) correctly predicts the final temperature and rise times of the shocked material.

The new thermo-mechanical formulation of mesodynamics is generally applicable, extending the spatial and temporal range of more expensive all-atom simulations to thermodynamically realistic mesoscopic simulations, with the possibility of solving a wide variety of problems in physics, chemistry, materials science, and biology.

[1] B.L. Holian, *Europhys. Lett.* **64**, 330 (2003).

[2] N. Karasawa and W.A. Goddard III, *Macromolecules* **25**, 7168 (1992).

For more information, contact
Alejandro Strachan (strachan@lanl.gov).

Acknowledgements

We would like to acknowledge NNSA's Advanced Simulation and Computing (ASC), Materials and Physics Program for financial support.

Decomposition of Nitroplasticizer in Plastic-Bonded Explosive PBX 9501

Denise K. Pauler (T-12 and Cornell University) and Joel D. Kress (T-12)

The goals of the Constituent Aging Study (CAS) are to investigate the accelerated aging of various constituents of plastic-bonded explosive PBX 9501, detect chemical reactions that occur, and identify decomposition products and possible mechanisms for chain scissioning and crosslinking of the polyester (urethane) Estane® 5703 [1]. The constituents of PBX 9501 are HMX explosive crystals, Estane®/nitroplasticizer (NP) binder, and diphenylamine or Irganox stabilizer. The NP, a liquid consisting of a 50/50 mixture (by wt.) of bis-2,2-dinitropropyl acetal (BDNPA) and formal (BDNPF), softens the Estane®, and together this binder markedly decreases the mechanical sensitivity of PBX 9501. Experimental evidence from NMR and ESR spectroscopy strongly suggests that NP degradation products may attack the Estane® and oxidize the polyurethane segment. Very little is known of the mechanisms for the oxidation of polymers by oxidants other than molecular oxygen. As the first step in the aging of PBX 9501 in a low moisture and low oxygen environment, we propose that NP decomposes into oxidizing gasses (NO_2 and NO). In this report, we present a plausible reaction mechanism for the decomposition of NP based on: (1) the results of the CAS, (2) an existing mechanism for liquid nitroethane, and (3) density functional electronic structure calculations.

During the 3-year duration of the CAS, the accelerated aging was performed in a dry oxygen-free environment at various temperatures (48°, 56°, and 64°C). Over one thousand samples were analyzed for small molecule reaction products such as CO_2 , N_2O , Ar, O_2 , NO , N_2 , CO , H_2 , and small organics. For example, the amount of N_2O ,

NO , CO , and CO_2 gas evolved as a function of time for a sample of pure NP aged at 64°C is shown in Fig. 1. The amount of N_2O and NO gas evolves at a nearly constant rate from time zero to approximately 120 weeks, whereas the CO and CO_2 gas evolution appears to have a delayed threshold starting at 26 weeks. One goal is to explain this result from our theoretical investigation of NP.

To minimize the computational effort for the electronic structure calculations, 2,2-dinitro-1-methoxypropane (first molecule in Scheme 1) was chosen as a model compound since it resembles half of the NP molecule. A library of key reactions was prepared and the electronic structure studied using the *Gaussian 03* suite of programs. The relative energies ΔE (products relative to reactants) were calculated using the hybrid density functional B3LYP and a 6-31G(d,p) basis set. Melius and Piqueras proposed a mechanism for the decomposition of nitroethane, a compound similar but less complex than NP. There are two potential pathways to begin the mechanism. The first is NO_2 scission, where the activation energy is equivalent to the bond dissociation energy. The second is a five-centered HONO elimination, which has a lower activation energy than NO_2 scission. While NO_2 scission dominates at high temperatures, as evidenced by the kinetics studies on nitromethane and nitropropane by Zhang and Bauer, the HONO elimination dominates at low temperatures of relevance to the CAS and naturally aged PBX 9501.

A series of five reactions (Scheme 1) for the decomposition mechanism of NP were selected from the library of reactions as follows. There are three possible products resulting from HONO elimination, but only two result in substituted alkenes and are therefore lower in energy. The *trans* HONO elimination product (first step in Scheme 1, $\Delta E = -3$ kcal/mol) is chosen since it is more stable due to steric hindrance in the *cis* alkene. After the elimination step, HONO remains trapped in the liquid and then adds to the alkene backbone of the NP fragment. HONO readdition can lead to various structural isomers depending on whether the H-ONO or HO-NO bond is broken. Addition of HO-NO leads to a nitroso-alcohol compound (second step in

Scheme 1, $\Delta E = -4$ kcal/mol) which decomposes (third step in Scheme 1, $\Delta E = -31$ kcal/mol) to produce methyl formate and a nitro-oxime. Esters can react further to produce CO and CO₂ (final step in Scheme 1, $\Delta E = 22$ and -23 kcal/mol, respectively), which were observed in the CAS study (Fig. 1). The nitro-oxime can decompose into acetaldehyde and NO, the latter which may account for the N₂O and NO gases observed in the CAS study (Fig. 1).

In conclusion, the key reactions involved in the decomposition of NP, including NO₂ scission and HONO elimination, have been identified. A proposed mechanism for low temperatures illustrated that HONO elimination can lead to esters that react further to produce CO and CO₂ gasses, and to nitro-oximes that can decompose into oxidizing gasses (NO). The next goal is to investigate NP decomposition kinetics with detailed Estane® polymer chain scission and crosslinking kinetics.

[1] J.D. Kress, et al., 34th Annual PolyMAC Symposium, Albuquerque, NM, June 8–10, 2004, book of abstracts, p. 18.

For more information, contact
Denise K. Pauler (dkpauler@lanl.gov).

Acknowledgements

We would like to acknowledge the NNSA Advanced Simulation and Computing Program (ASC), Nuclear Survivability Program, and Campaign 8, Enhanced Surveillance, for financial support.

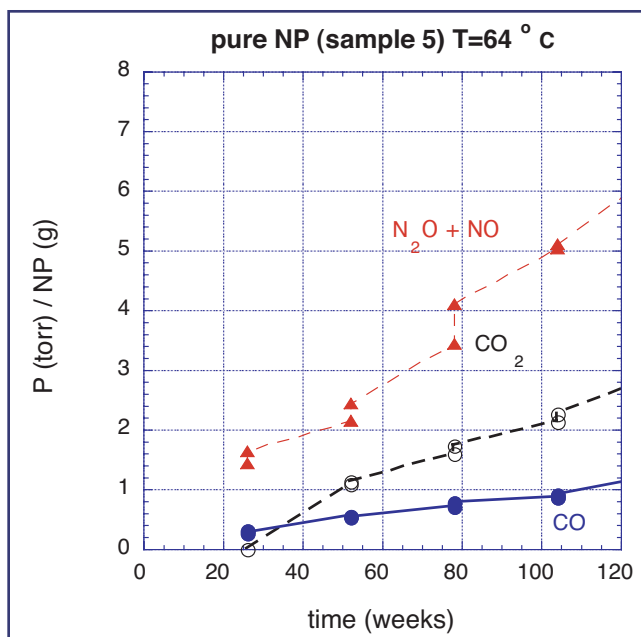
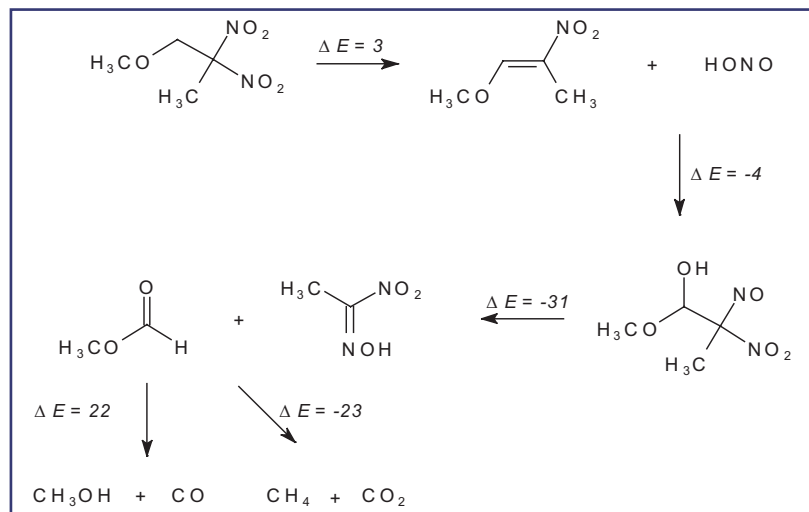


Figure 1—
Gas (partial pressure) evolved per gram of nitroplasticizer (NP) aged at 64 °C.



Scheme 1—
Proposed mechanism for nitroplasticizer (NP) model compound. Energies in kcal/mol.

SHOCK AND DETONATION PHYSICS



Design of a Fragment Generator

Eric M. Mas (T-1), Paul Maudlin (T-3), and Jon Mace (DX-2)

There is much continuing interest in the defense community about fragments hitting conventional munitions. This includes conventional munitions in the field and those in storage that may be bombarded with fragments generated from another munition detonating either intentionally or unintentionally. This can also include the possibility of defeating a munition that has already been deployed. The conventional munitions can encounter a single fragment or several fragments. This paper represents the first stages of an experimental and theoretical study recently undertaken to investigate these scenarios.

We first need to design the mechanism that will “throw” the fragments. Later, these fragments will be directed at targets, or acceptors, and the resulting impacts will be studied for various scenarios including prompt initiation, delayed initiation, and preconditioning of the acceptor relative to a

subsequent impact. The fragment generator needs to be compact enough to facilitate directing it at the acceptor from various directions and it needs to be able to throw the fragment over a wide range of speeds. The fragments generated should be of reproducible shape and preferably experience limited plastic deformation during the generation process. The design also needs to be simple and use widely available materials in order to be manufactured quickly, in large numbers, and in a standard, uniform way at a variety of sites.

We investigated a variety of potential designs by conducting finite element analysis simulations using the code EPIC. Figures 1–4 depict four designs we investigated. All of the designs are axially symmetric. The first is the “back tampered sandwich.” Tamper refers to the back metal plate, which provides inertial confinement of the expanding gases, directing them down and providing extra push to the fragment. In Figs. 1–3 green and red depicts metal and pink the high explosive and all of the designs generate fragments moving down. Using an analysis pioneered by Gurney [1] we were able to conclude that the back-tampered sandwich could not attain fragment speed necessary for this study.

The next design, the back and side tampered sandwich is shown in Fig. 2. While Gurney’s analysis predicts that this configuration could produce adequate velocities for this study, simulations with EPIC showed that no available steel could produce adequate confinement to generate the necessary speeds, so this configuration was abandoned.

In Fig. 3 we illustrate the Forest Flyer configuration, first created at Los Alamos National Laboratory by C. Forest [2]. In this case the EPIC simulations indicated that the design could reach the desired speeds, but that the damage to the fragment was quite extensive. We tried a variety of modifications to the design, but whenever we attained the desired speed the damage was too extensive. At lower speeds, however, the damage was much less severe.

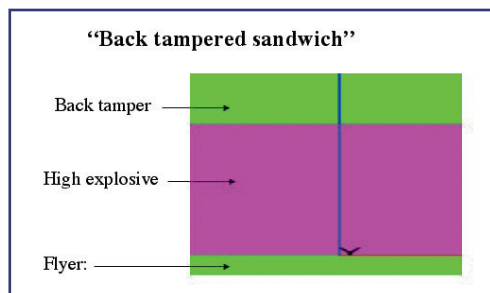


Figure 1—
The back-tampered sandwich design.

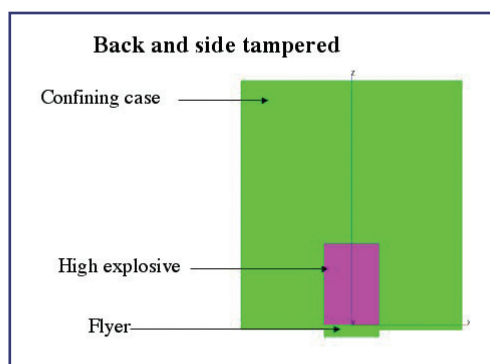


Figure 2—
The back- and side-tampered design.

Finally, we modified the design of M. Held [3] to accommodate our desired fragment configurations. In this design as seen in Fig. 4 there is no back or side tamper, but there is an axial confinement to the fragment which also serves to direct the expanding gases to further push the fragment. The axial confining ring also serves to suppress damage in the fragment and the 10-degree angle ensures that the remnants from the ring are not directed towards the acceptor. We found that we could attain the desired speeds with this configuration and that there was damage to the fragment but not to the extent observed with the Forest Flyer. Figure 5 shows the simulated flyer after it has been fully accelerated by the high explosive. The colors represent the amount of plastic flow experienced by the flyer, and the lines are contours. As can be seen there is little deformation except at the edges of the flyer, which was considered to be acceptable.

We passed on our designs of the fragment generator to experimentalists in Dynamic Experimentation Division where they will build and test the generator. Unfortunately the recent laboratory stand down has delayed that aspect of the study. In the meantime we will continue to study fragments impacting acceptors.

- [1] R.W. Gurney, "The Initial Velocities of Fragments from Bombs, Shells, and Grenades," Army Ballistic Research Laboratory Report BRL 405.
- [2] C.A. Forest, et al., *11th International Det. Symposium*, Snowmass Village, CO, 332 (1998).
- [3] M. Held, *Propellants, Explosives, Pyrotechnics* 25, 8 (2000).

For more information, contact Eric Mas (mas@lanl.gov).

Acknowledgements

We would like to acknowledge the Joint DoD/DOE Munitions Technology Development Program for financial support.

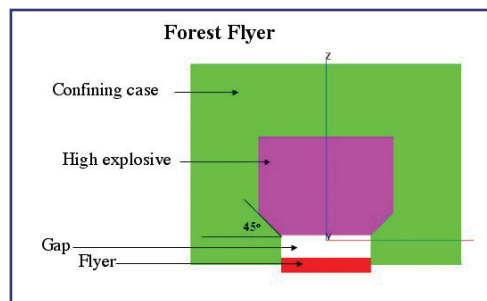


Figure 3—
The "Forest Flyer"
design.

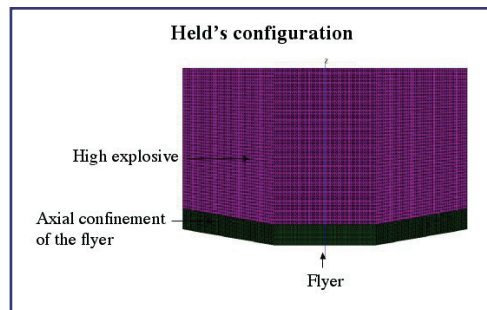


Figure 4—
The M. Held design.

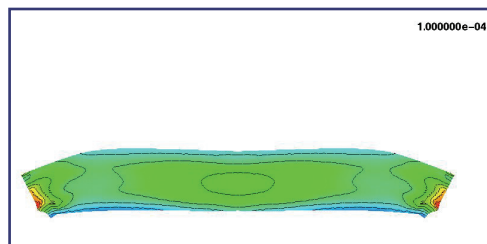


Figure 5—
An image of the flyer af-
ter being accelerated by
the thrower. The colors
represent the amount of
plastic deformation.

Shock Passage Over an Interface

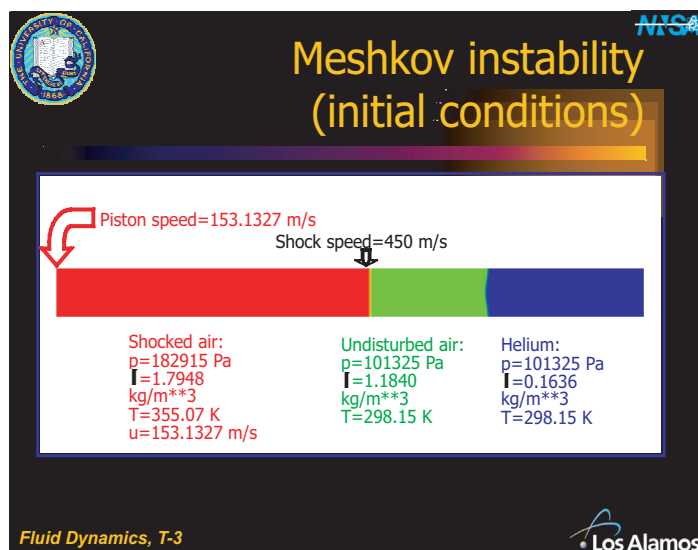
*Rick Rauenzahn, Manjit Sahota,
and Francis Harlow (T-3);
Robert Gore (X-2); Michael Steinkamp
(X-3); and Jon Weisheit (T-15)*

When a shock passes over an interface between two materials, the result is an instability that produces growth of fine-scale perturbations. A consequence is the interpenetration of each material into the other to form a growing mix layer. To describe theoretically how this dynamical process occurs, investigators perform numerical experiments by solving finite-difference approximations to the equations of fluid dynamics. One type of calculation follows with fine resolution the detailed behavior of a specific initial configuration, including the three-dimensional structure of the perturbations. Some results from a resolved calculation of a shock passing over an initially perturbed interface are shown in Figs. 1 and 2. Another technique uses turbulence transport equations to describe the ensemble-averaged behavior of mix-layer growth, while a third procedure is based on a two-field approach that describes the motion of fluid globules through and past each other.

For many applications the detailed resolution of perturbation response is too costly for practical problem solving. On the other hand, turbulence transport equations and two-field representations are of questionable validity for an accurate description of what is going on. To attain sufficient accuracy we use a combined theoretical and experimental program. Los Alamos National Laboratory's (LANL's) Theoretical (T) Division contributions to this program consist of complementary calculations with the turbulence transport equations and the two-field equations, close collaborations for the design and analysis of experiments performed with the gas curtain apparatus in LANL's Dynamic Experimentation Division, and interactions with investigators in other divisions of the Laboratory who are also examining the applicability of calculation techniques to representative problems.

In both types of the T-Division calculations the mean flow dynamics within the interface are examined with very fine resolution. The initially perturbed structure is described by a postulated uniform variation of ensemble-averaged fluctuations in density. For the single point mean scale of the fluctuations, S , we chose a distance corresponding to the dominant size in the directions parallel to the nominal surface. A necessary property of the calculation results is mesh convergence, i.e., asymptotic approach to a result that is independent of the finite-difference cell size as that size becomes small. But does the converged value

Figure 1—
Schematic of initial
conditions for shock-
perturbed interface
calculation. The
shocked air on the left
will interact with the
air-He interface
to amplify the initial
interface perturbation.



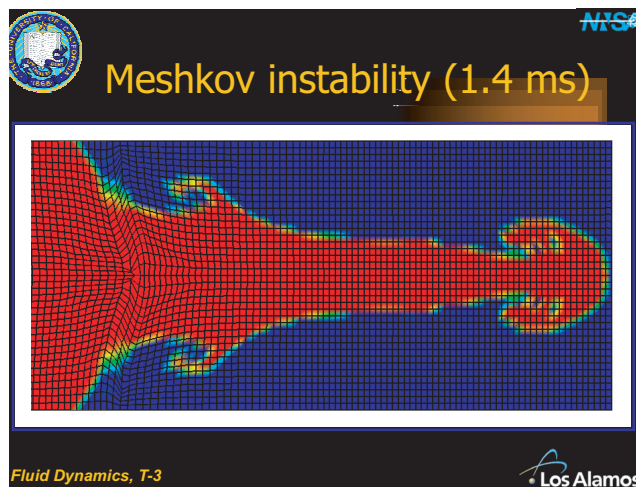


Figure 2—
At 1.4 ms, the shocked air has penetrated the helium and the mix width has grown dramatically. The background computational mesh is shown in black, and colors indicate the material type (red = air).

for mixing rate agree with what actually happens in the laboratory? As we wait for accurate experimental data, we compare results from the transport approach with those of the two-field approach. If the converged results of these very different techniques are essentially the same, we develop confidence that the calculations may indeed be correct.

As an example of what we are learning, we have found that mesh convergence for the transport approach requires that the scale, S , does not change appreciably during and after the transit of the shock through the layer. This result is consistent with our expectations that the dominant scale transverse to the mean flow is nearly constant as the shock interacts with the perturbed interface. For many other circumstances in which turbulence is developed, the value of S changes rapidly, decreasing as the turbulence is driven by mean-flow gradients and growing after the driver recedes in strength. Because our turbulence transport equations were developed for this latter class of circumstances we conclude that a significant modification to the transport equation for S is required for shock-interface investigations.

The two-field formulations are well understood but require several additional parameters to model mass, momentum, and energy exchange between phases.

Such exchange rates depend very strongly on the flow regime and are almost always determined through indirect experimental measurements. However, a two-field approach is computationally tractable even for full-system calculations and has been successfully applied to track fluid globules in the past. We are applying this approach to study the mixing of materials in the presence of shocks.

Theoretical Division is also developing a program to apply and test our turbulence transport equations for astrophysical investigations. In particular, we are calculating the interaction of a supernova shock with nearby, primordial gas clouds confined within dark matter potential wells [1]. The goal is to examine the mixing of supernova ejects (metals) with pure hydrogen/helium gas, in order to explain both the very uniform metallicity among the $\sim 10^6$ stars of an individual globular cluster and the considerable variation in metallicity from cluster to cluster in a galaxy.

[1] E. Scannapieco, J. Weisheit, and F. Harlow, "Triggering the Formation of Halo Globular Clusters with Galaxy Outflows," Los Alamos National Laboratory report LA-UR-04-2665 (to be published in *Astrophys. J.*).

For more information, contact Manjit Sahota (sahota@lanl.gov).

Acknowledgements

We would like to acknowledge NNSA's Advanced Simulation and Computing (ASC), Materials and Physics Program for financial support.

Numerical Simulation of Plastic-Bonded Explosives

Scott Bardenhagen and
Andrew Brydon (T-14)

Homogeneous continuum models have been developed to describe the response of material to dynamic loading, including equation of state, strength, and reactive burn models. However many strategic materials—in particular plastic-bonded explosives (PBXs)—are heterogeneous at the microscale. PBXs are composites containing energetic grains, ranging in size from less than one to a few hundred micrometers, embedded in a matrix of high-polymer binder. Low levels of applied stress can cause substantial material damage and even lead to violent reactions due to the heterogeneity of the material state at the microscale.

To develop accurate, quantitative, and predictive models, it is imperative to develop a sound physical understanding of the grain-scale material response. The orientationally dependent properties of the individual crystals and the presence of material interfaces result in strongly heterogeneous stress and energy distribution under loading.

Because events of interest such as damage and chemical decomposition depend strongly on the extremes (tails) of these distributions, it is important to understand what factors affect them. The goal of this work is to characterize the heterogeneity of stress and energy distribution as a function of material microstructure.

The Material Point Method (MPM) has been used to perform numerical simulations indicating the importance of accurately modeling microscale composite material response. The computational technique is a particle method that provides a convenient framework for tracking and modeling material interfaces. Stress wave propagation simulations on idealized composite microstructures, granular packings consisting of photoelastic polymeric cylinders, illustrate differences in stress distributions due to granular contact conditions (see Fig. 1).

More recently, advantages of the MPM for discretizing geometrically complex material microstructures have been exploited. In particular, the compatibility of particle discretization and x-ray microtomography has been demonstrated [1]. X-ray microtomography generates three-dimensional (3-D) spatial variation of a composite's x-ray cross section (see Fig. 2). For PBXs, a sophisticated image-processing step is required to extract individual entities (individual grains, binder). Once constituents have been identified, discretization via particles is straightforward.

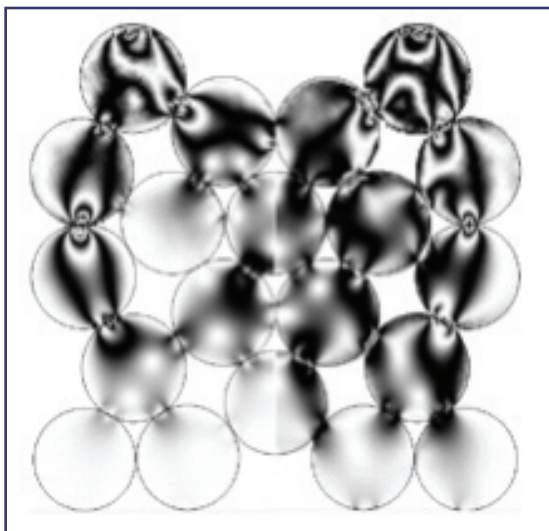


*Figure 1—
Wave propagation
through a collection of
disks. Frictionless con-
tact (left) is contrasted
with no slip contact
(right).*

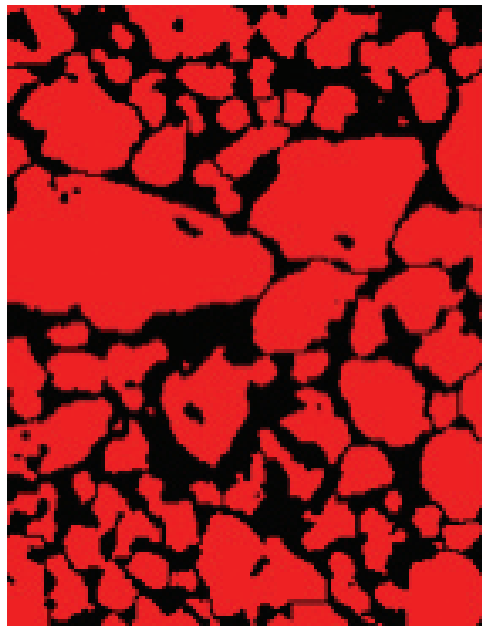
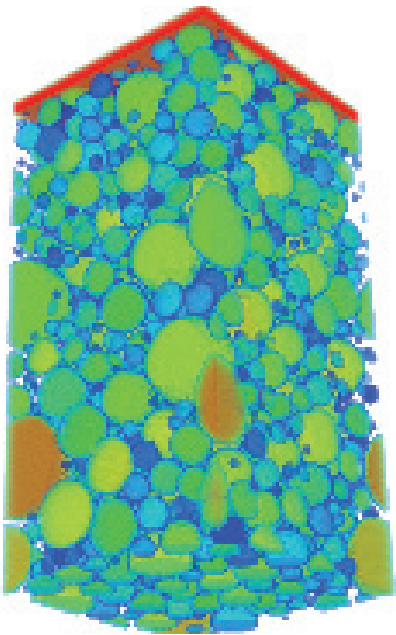


*Figure 2—
Idealized (left) 3D
granular packing and
experimentally obtained
(right) 2D slice through
a PBX.*

Researchers S. Lecume and C. Boutry, SNPE, Centre de Recherches du Bouchet, France, have obtained 3D x-ray microtomography data for a particular formulation (PBX N109), analyzed this data, and successfully extracted individual grains and binder. We are collaborating with SNPE to replace existing idealized models (packed spheres) with experimentally obtained granular packings. We have received one data set and are in the process of discretizing it in order to assess the impact of grain shape on material state distribution under various loadings.

[1] Andrew Brydon and Scott Bardenhagen, “Numerical Simulation of Realistic Foam Microstructures,” in this volume on p. 36.

*For more information, contact
Scott Bardenhagen (bard@lanl.gov).*

Acknowledgements

We would like to acknowledge NNSA’s Advanced Simulation and Computing (ASC), Materials and Physics Program; and Campaign 2, Dynamic Materials Properties, for financial support.

The Nexus between Reactive MD Simulations of RDX and the Reactive Euler Equations

Shirish M. Chitanvis (T-14)

In the past we have focused on pre-ignition phenomena that cause a local temperature rise when a single void in high-melting explosive (HMX) collapses under the action of a shock wave. Working in the melting regime, a timeline can be associated with the collapse of a single void through a consideration of the time scales on which these mechanisms are activated.

Among the phenomena we studied, the hydrodynamic mechanism is generally considered to be an important pre-ignition step. In this mechanism, the shock-driven incident side of the void impinges on the shadow side of the void and is brought to rest, causing a considerable temperature rise in the HMX. This mechanism comes into consideration as the void closes up under the action of the shock wave. The resulting increase in pressure and temperature causes a shock wave to emanate from the collapse. This shock wave very quickly attains cylindrical symmetry in our two-dimensional (2D) calculation. (See Fig. 1.) If the energy contained in this outgoing shock wave is sufficiently high, and the size of the hotspot is sufficiently large, it could produce a local microdetonation.

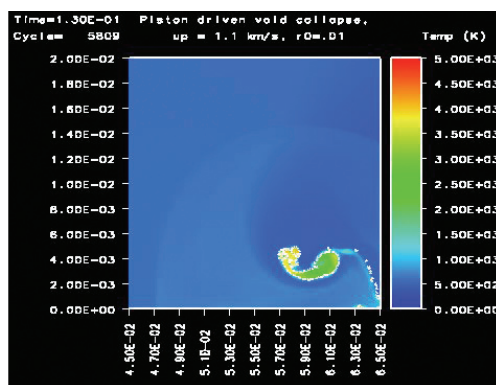


Figure 1—
Numerical simulation
of a collapsing spherical
void approximately
0.145 microseconds
after the launch of a
shock wave.

In order to study the energy release provided by the hydrodynamic collapse of the void, one needs to understand the chemical reaction pathway through which this homogeneous explosive decomposes. Very recently A. Strachan (T-14) found that the complicated reaction pathway in Royal Demolition Explosive (RDX) can be simply represented as a single-step energy release step governed by Arrhenius kinetics. The activation energy is about 1 eV and is weakly pressure-dependent. This result was obtained by using the ReaxFF potential developed at California Institute of Technology in cook-off-like simulations of RDX at high temperature and pressure. These simulations were performed at various temperatures and pressures, and it is of interest to investigate the applicability of the resulting parameterization of the kinetics at a macroscopic scale.

The incorporation of the single-step Arrhenius rate into continuum dynamics can be accomplished by solving the reactive Euler equations. The width of the reaction zone which develops as the rarefaction Taylor wave behind the von Neumann pressure spike may be estimated in an order of magnitude sense by the product of the sound speed (typically a kilometer per second or less) and the characteristic chemical time scale, viz., picoseconds. This yields a scale of the order of 1/100th of a micron. Since voids in explosives are expected to be of the order of microns, it follows that a numerical solution of the reactive Euler equations would be at best a difficult job in two dimensions.

An alternative solution is to develop a subgrid model, such as Bdzil's Detonation Shock Dynamics (DSD). This technique consists of performing an asymptotic (perturbative) expansion of the reactive Euler equations in a shock-based frame of reference and coordinate system. The formalism eventually reduces to the solution of a transcendental equation for the relation between the detonation velocity normal to the shock front (D_n) and the local curvature (κ). It is possible to obtain from this analysis an estimate of the minimum size and energy of the hotspot that would be required to sustain a microdetonation during void collapse in a melted homogeneous RDX sample.

The reaction rate obtained by Strachan can be written down as:

$$\begin{aligned}
 R(T, \rho) &= \kappa(\rho) \exp(-(E_a + f\rho_a/\rho)\kappa T)(pico - s) \\
 \kappa(\rho) &= \exp(a - b\rho_a/\rho) \\
 a &= 1.82561 \\
 b &= 0.290392 \\
 f &= 0.356 \\
 E_a &= 21.472 \text{ (kcal/mol)} \quad (1)
 \end{aligned}$$

where ρ_a is the initial density of the material.

If T_{CJ} is the Chapman-Jouguet temperature, the rate R may be written as:

$$\begin{aligned}
 R(T, \rho) &= \kappa \exp(-1/\epsilon) \exp\left(\frac{T - T_{CJ}}{\epsilon}\right) \\
 &\quad \exp(-f\rho_a/\rho/\kappa T + E_a/\kappa T_{CJ}) \\
 \epsilon &= \frac{\kappa T_{CJ}}{E_a} \sim 0.13 \\
 T - T_{CJ} &\sim \epsilon \quad (2)
 \end{aligned}$$

Thus ϵ provides one with a small dimensionless parameter with which to perform an asymptotic analysis of the reactive Euler equations. One can now use the methods developed in [1], where the reactive Euler equations are written in the shock-based frame of reference to obtain a formal solution to $\mathcal{O}(\epsilon)$ as:

- Note that an extra assumption has been made in this model, viz., that the factor of $(1 - \lambda_r)$ which appears in the conventional form for the single-step Arrhenius rate has been replaced by $(1 - \lambda_r)^{1/2}$. Physically this allows the reaction to be complete within a reaction zone of finite width. This is a reasonable assumption as long as the major fraction of the energy is released within a short distance. We have experimented with retaining the linear factor of $(1 - \lambda_r)$ in our analysis, unsuccessfully.

- Furthermore, for the moment we utilized a polytropic equation of state to describe the explosive. We expect to replace it shortly with a realistic equation of state obtained directly from the MD simulations.

A nonlinear $D_n - \kappa$ relation was obtained from this formalism and used to compute the shape of a steady-state detonation front for the case of an unconfined cylinder of macroscopic dimension (Fig. 2), thereby completing the initial phase of the transportation of the reactive MD simulations to the continuum level.

[1] M. Short and J.B. Bdzil, "Propagation Laws for Steady Curved Detonations with Chain-Branching Mechanisms," *J. Fluid Mech.* **479**, 39-64 (2003).

For more information, contact
Shirish M. Chitanvis (shirish@lanl.gov).

Acknowledgements

We would like to acknowledge NNSA's Advanced Simulation and Computing (ASC), Materials and Physics Program for financial support.

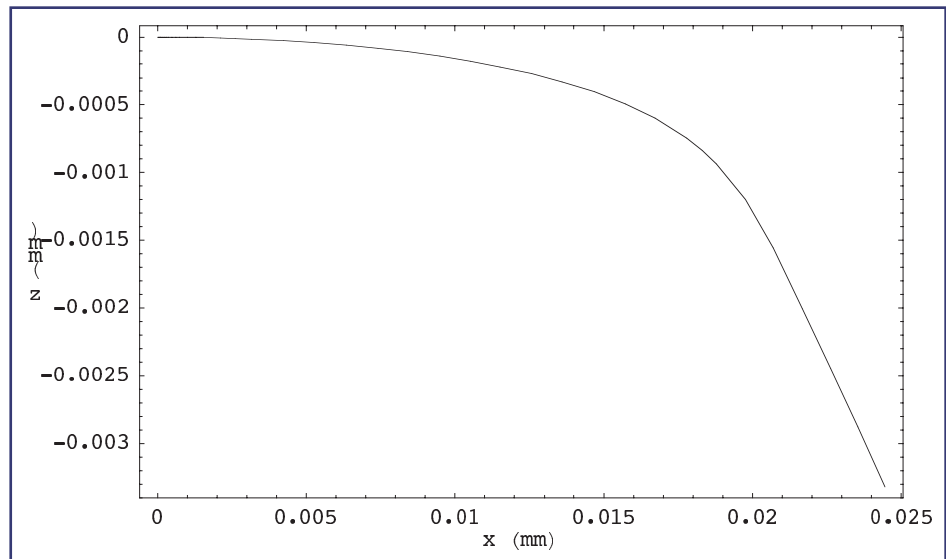


Figure 2—
Shape of the detonation front for an unconfined cylinder.

Atomistic Studies of PBX 9501 Constituents and Interactions Among Them

Eugenio Jaramillo and Thomas D. Sewell (T-14); Chee Kwan Gan and Matt Challacombe (T-12); and Hemali Davande, Dmitry Bedrov, Oleg Borodin, and Grant D. Smith (University of Utah)

We are performing a variety of simulations designed to provide specific information or qualitative insights regarding the physical behaviors of the constituents of PBX 9501. The common thread among them is that they are based on calculations at the atomistic scale. The work is part of a larger effort to provide physically based continuum constitutive models for PBX 9501 on the basis of processes that occur at subcontinuum length scales. Our present work is a continuation of a research program that has been underway for several years and that involves close interactions between theorists working at atomistic and mesoscopic scales, as well as collaborations between theorists and experimentalists.

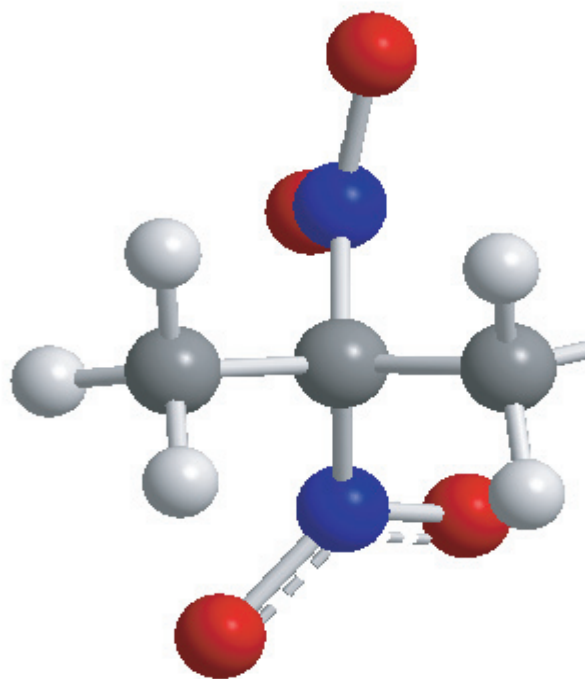
The zero Kelvin isotherm has been computed for β -HMX crystal in the pressure interval 0–10 GPa using the MondoSCF quantum chemistry code, at the PBE/6-31G** level of theory (Fig. 1). The zero Kelvin isotherm can serve as a reference curve for the construction of a P-V-T equation of state for a material at elevated temperatures. Whereas similar calculations for PETN yielded excellent agreement with experiment, the results for β -HMX reveal systematic discrepancies from data. Understanding this is an area of ongoing investigation.

In previous work, quantum-chemistry-based force fields were developed for HMX and Estane®. We are presently in the final stages of developing an analogous force field for bis(2,2-dinitropropyl) formal/acetal (BDNPF/A), which is the plasticizer in the binder for PBX 9501 (Fig. 2). Upon completion of this force field, we will have a consistent, quantum-chemistry-based potential function for all of the major constituents of PBX 9501. This will enable us to study detailed physical interactions in that material; for example, the nature of the high-explosive/binder interface and the influence of plasticization on the properties of the binder.

For more information, contact
Thomas D. Sewell (sewell@lanl.gov).

Acknowledgements

We would like to acknowledge NNSA's Advanced Simulation and Computing (ASC), Materials and Physics Program, and the ASC and university alliance Center for Simulation of Accidental Fires and Explosions (C-SAFE) for financial support.



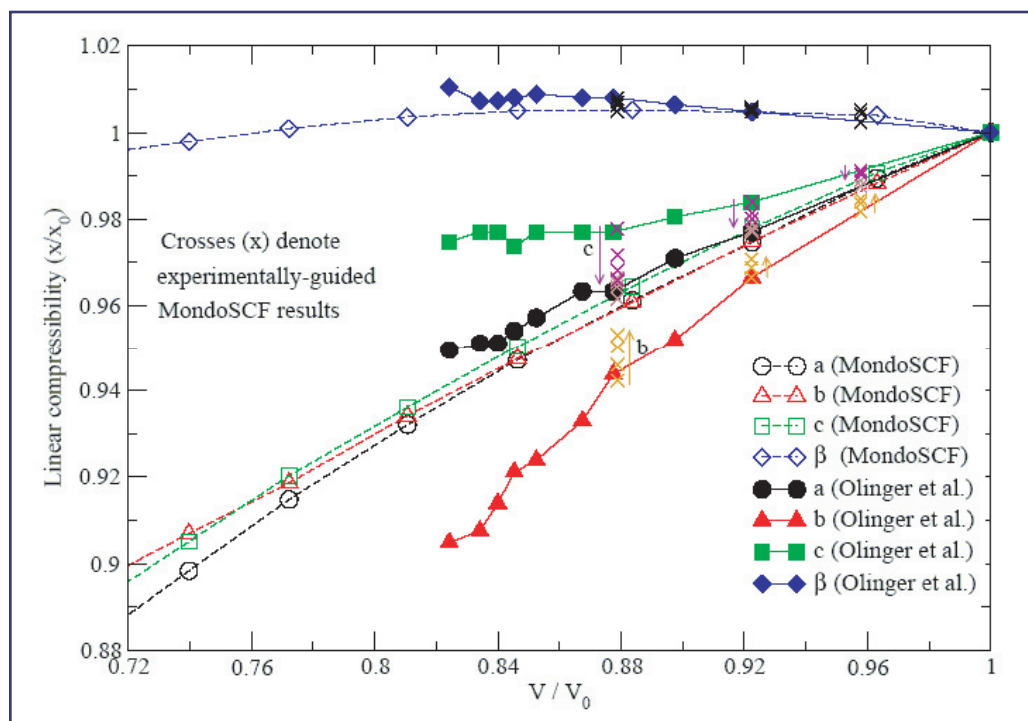


Figure 1—
Linear compressibilities
for β -HMX.

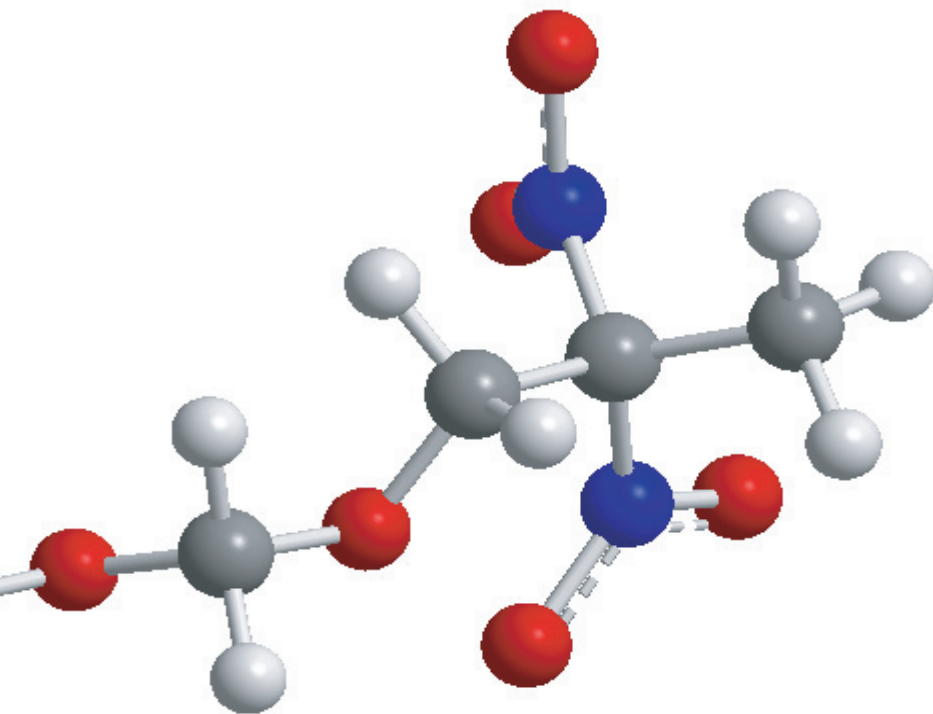


Figure 2—
Chemical structure of
BDNPF plasticizer.

Large-Scale Simulations of Shock-Induced Transformations in Gallium, on the Way to Plutonium

Kai Kadau (T-14), Timothy C. Germann (X-7), Peter S. Lomdahl (T-11), Brad L. Holian (T-12), Ramon J. Ravelo (University of Texas/X-7), Frank J. Cherne (DX-2), and Michael I. Baskes (MST-8)

The Modified Embedded Atom-Method (MEAM) [1] applies to metals with greater covalent bonding than the conventional Embedded Atom Method (EAM) [2], which is restricted to nearly-free-electron (simple fcc) metals. MEAM can also describe different crystallographic structures of one element or compound correctly. As a result of the angular bonding terms, semiconductors like Ga [3] and complex elements like Pu can be described reliably.

Shock-induced phase transformations are of principal and programmatic interest and have been investigated in some detail for Fe [4]. Here, we utilize a MEAM potential for Ga [3] to investigate the shock-induced transformation in Ga. The large-scale simulations were performed with the MD code SPaSM (Scalable Parallel Short-range Molecular dynamics) [5, 6, 7] and made use of 256 CPUs of the QSC machine at Los Alamos National Laboratory for 8 hours for each run shown in Fig. 1. Ga has an interesting phase diagram with an orthorhombic ground state structure with a significant amount of dimerization (A11, GaI). It also has at least two more solid phases and a melting temperature of about 300 K at zero pressure.

The ongoing work of atomistic large-scale simulations to understand the dynamics of shock-induced plasticity in Ga will pave the way to tackle the even more challenging dynamics of Pu and its alloys.

- [1] M.I. Baskes, *Phys. Rev. B* **46**, 2727 (1992).
- [2] M.S. Daw and M.I. Baskes, *Phys. Rev. Lett.* **50**, 1285 (1983); M.S. Daw and M.I. Baskes, *Phys. Rev. B* **29**, 6443 (1984); M.S. Daw, S.M. Foiles, and M.I. Baskes, *Mater. Sci. Rep.* **9**, 251 (1993).
- [3] M.I. Baskes, S.P. Chen, and F.J. Cherne, *Phys. Rev. B* **66**, 1041007 (2002).
- [4] K. Kadau, T.C. Germann, P.S. Lomdahl, and B.L. Holian, *Science* **296**, 1681 (2002).
- [5] P.S. Lomdahl, P. Tamayo, N. Gronbech-Jensen, and D.M. Beazley, *Proceedings of Supercomputing* **93**, G.S. Ansell, Ed. (IEEE Computer Society Press, Los Alamitos, CA, 1993), p. 520.
- [6] D.M. Beazley and P.S. Lomdahl, *Comput. Phys.* **11**, 230 (1997).
- [7] K. Kadau, T.C. Germann, and P.S. Lomdahl, *Int. J. Mod. Phys. C* **15**, 193 (2004).

For more information, contact Kai Kadau (kkadau@lanl.gov).

Acknowledgements

We would like to acknowledge NNSA's Advanced Simulation and Computing (ASC), Materials and Physics Program for financial support.

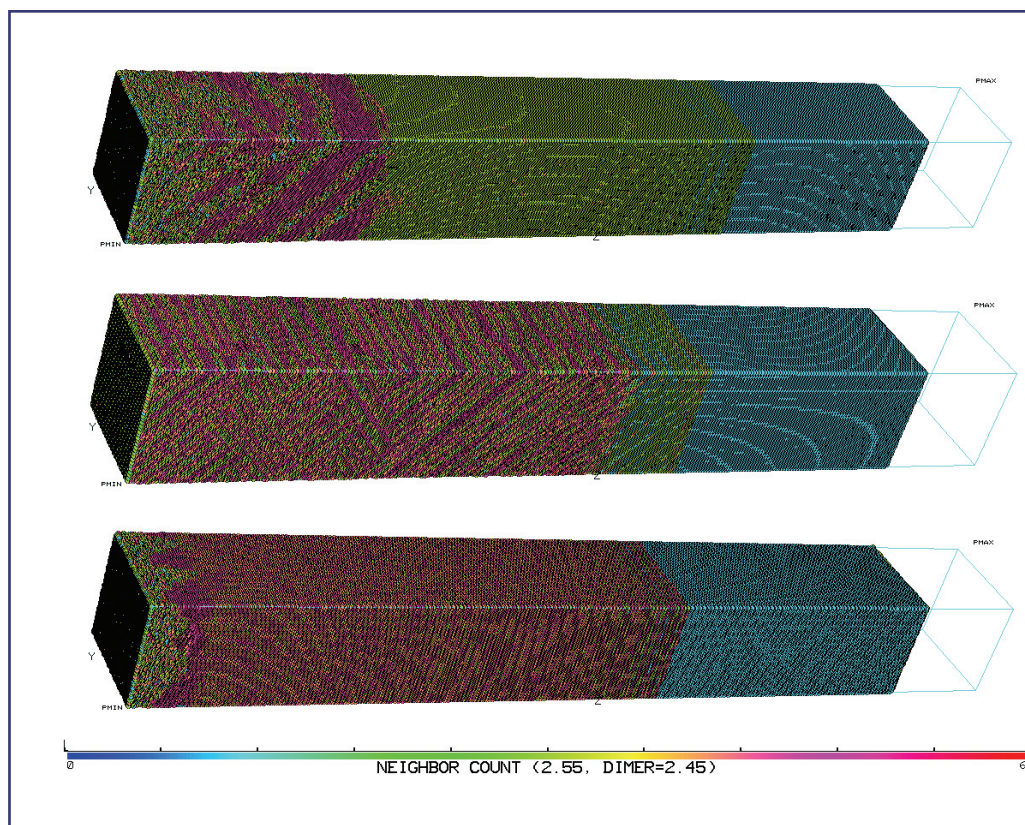


Figure 1—

Samples containing about 2 million Ga atoms (about 17 nm x 17 nm x 140 nm) as modeled by a MEAM potential after 25.5 ps. Piston velocity is 600 m/s and the shock wave traveled from the left to right. Different crystallographic shock directions ([100], [010], [001] top to bottom) result in differences in the resulting structures behind the shock front. The atoms are colored according to the number of neighbors within a radius (2.55 Angstrom) that is slightly larger than the dimer distances of the A11 ground structure (2.45 Angstrom). In all three cases the unshocked A11 structure is blue (neighbor count = 1). In the [100] and [010] cases the following elastic wave is green and the slower plastic wave is marked by the red color. In the case where the shock travels along the dimer direction, i.e., [001] the uniaxially compressed region has more neighbors as in the two other cases and is thus marked by the red color as well; here the plastic front has just started to develop at the very left side.

Atomistic Investigations into the Dependence of Detonation Properties on Material Parameters using Molecular Dynamics

Edward Kober and Andrew J. Heim (T-14)

In order to experimentally test the dependence of detonation characteristics, e.g., shock velocity (u_s , on a high explosive's (HE's) material properties, e.g., its exothermicity (Q), one is forced to simultaneously vary multiple parameters upon which the detonation may depend. Computational simulations can be used to reduce this complexity and allow the more direct assessment of significant changes in materials properties and how they affect the detonation response.

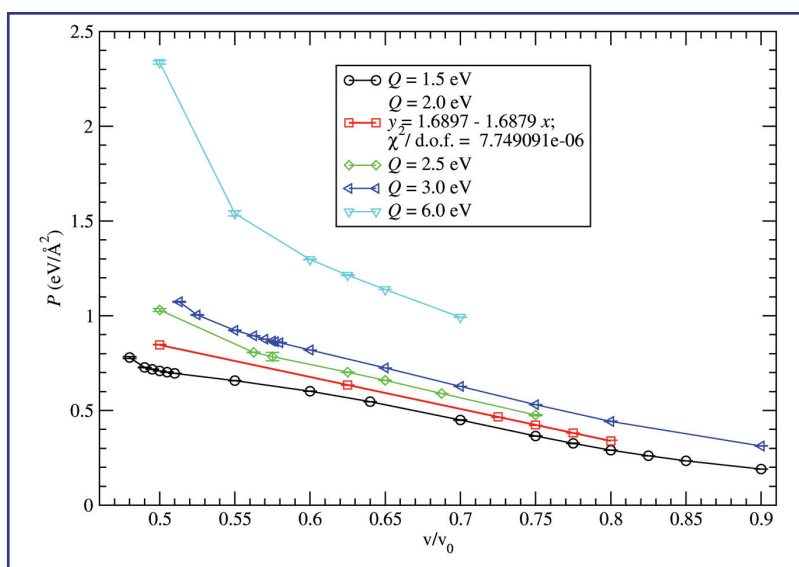
Molecular dynamics (MD) have been used to simulate detonations. With it one can either attempt to reproduce a known material, or to generate a model material whose parameters can be set arbitrarily. To simulate the detonation process one needs only a representative interaction potential. Here, we use the model potential of Brenner et al. [1] (REBO) that has been the basis of several studies. It is a many-body potential that simulates covalent bonds in an empirical way, thus enabling rapid computation. It describes a simple exothermic reaction: $2AB \rightarrow A_2 + B_2 + 2Q$. The actual code used to model detonation is SPaSM, short for Scalable Parallel Short-range MD, and developed at Los Alamos National Laboratory.

In the systematic process of probing the characteristics of detonation on an HE's material parameters, we follow the work of Haskins and Cook [2], in which they varied Q for their model (based on the simple

dissociative reaction $A_2 \rightarrow 2A$) from 1 eV to 10 eV. Similar to their results, we found a linear and increasing relationship between Q and u_s^2 . Intuitively, this makes sense. The kinetic energy of the detonation shock front, which is related to the square of u_s , should increase with the energy used to drive it, Q . This simple argument suggests that the slope of the linear correlation should be 1, while a value of 0.6 is actually observed. So other factors must be playing a significant role here.

A more complete model for detonation shows that the velocity of an unsupported detonation front can be determined by the initial state of the HE in front of the detonation front and the Chapman-Jouget (CJ) state behind it [3]. The CJ state can be determined by drawing a straight line through the initial state and tangent to the Hugoniot curve (H) on a pressure-volume (PV) state diagram. This line is called a Rayleigh line (R). It is an expression of the conservation of mass and momentum across the detonation front. Its slope is $-(\rho_0 u_s)^2$, where ρ_0 is the initial density of the HE. H is an expression of the conservation of energy across the detonation front. The point where H and R are tangent is the CJ state [3].

In order to quantify the relationship between u_s and Q , we mapped out H for several values of Q . To do this we run a set of microcanonical ensembles (NVE) at a given specific volume (v) until we find the value of the specific internal energy (E) that satisfies H. Then we repeat for different values of v until we can determine the CJ state from the tangency condition. The rather surprising results for the Hugoniots are shown in Fig. 1. We had expected to observe simple non-ideal gas behavior, which would result in smooth hyperbolic-type curves on this plot. Instead, the Hugoniot curves have extensive regions that are near linear, which is rather unusual behavior. The curve for $Q = 1.5$ eV is more complex yet with a downward concave region, which suggests the presence of a phase transition. Despite this unusual behavior, the CJ states determined by the tangency condition show a smooth linear increase with Q . The numbers for u_s from the dynamic simulations of detonation are within 4% of those found by the NVE simulations with the less accurate simulations being of lower



Q and closer to failure. This further verifies that these systems are behaving as ideal CJ detonations, and that the u_s dependence on Q is explained by changes in the product equation of state.

The origin of these unexpected changes was determined by a more careful study of the atomistic geometry at the CJ conditions. A snapshot of an NVE at CJ for $Q = 3.0$ eV is shown in Fig. 2. In it, trimer formation is evident. Such formation has been confirmed by radial distribution calculations in an NVE simulation and potential surface contours of the interaction potential as a function of the distances between three inline particles, A-B-A. The potential surfaces indicate a minimum for trimer formation. Higher oligomers are apparent for the systems with lower values of Q . This dimer-oligomer transition then explains the “phase transition” behavior observed in the Hugoniot curves.

It had not been originally intended that such complex chemistry would result from a seemingly simple potential. Given its presence, the rather simple Q vs u_s dependence is a rather surprising result and raises a cautionary flag in interpreting “obvious” results too quickly. Modifications to this potential have now been developed that eliminate this trimer/oligomer formation [4] and comparative studies are underway.

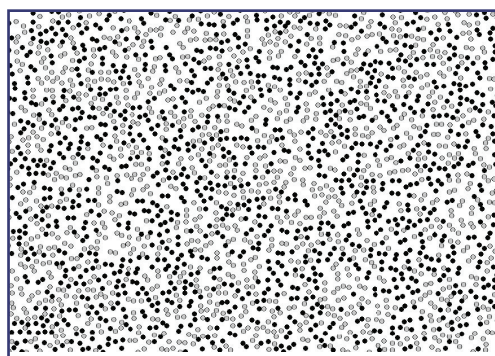


Figure 1—
In order to quantify the relationship between u_s and Q , we mapped out H for several values of Q . To do this we run a set of microcanonical ensembles (NVE) at a given specific volume (v) until we find the value of the specific internal energy (E) that satisfies H . Then we repeat for different values of v until we can determine the CJ state from the tangency condition. The rather surprising results for the Hugoniot are shown in the figure.

Figure 2—
Snapshot of NVE at CJ. A atoms are black and B gray.

- [1] D.W. Brenner, et al., “Detonations at Nanometer Resolution using Molecular Dynamics,” *Phys. Rev. Lett.*, **70**, 2174 (April 1993); 76, 2202 (1996).
- [2] P. J. Haskins, et al., “Molecular Dynamics Studies of Fast Decomposition in Energetic Molecules,” in *Eleventh Symposium (International) on Detonation* (1998), p. 897.
- [3] W. Fickett and W.C. Davis, *Detonation* (University of California Press, Berkeley, 1979).
- [4] B.M. Rice, et al., “Molecular-Dynamics Study of Detonation, ii. The Reaction Mechanism,” *Phys. Rev. E*, **53**, 1 (January 1996) p. 623.

For more information, contact Edward Kober
(emk@lanl.gov).

Acknowledgements

We would like to acknowledge NNSA's Advanced Simulation and Computing (ASC), Materials and Physics Program for financial support.

Detonation Products Equation of State

M. Sam Shaw and C. J. Tymczak (T-14)

Most high explosives in common use have a chemical formula of the form $C_a H_b N_c O_d$, where a , b , c , and d are integers.

Upon detonation, the products are composed of a molecular fluid mixture of N_2 , CO_2 , H_2O , some CO , and other minor molecular species. In addition, solid carbon clusters are produced in predominately graphite or diamond phases with surface restructuring and/or surface groups capping dangling bonds. Typical conditions are pressure around 30 GPa, temperature 3000 K, and density 2.4 g/cm^3 .

We are using a wide variety of methods to characterize detonation products equation of state (EOS). The EOS schemes range from empirical forms fit to a large data set, to thermodynamic perturbation theory, to a Composite Monte Carlo method [1, 2, 3] giving chemical equilibrium composition including the dense fluid mixture and solid carbon clusters. This presentation will focus on an *ab initio* method that looks like it could predict an accurate detonation products EOS.

High density fluid nitrogen has been chosen as the first test case for this method. Subsequent studies will involve other major detonation product species and their mixtures, with the final goal being an accurate predictive EOS for typical high explosives. The *ab initio* studies will either be used directly or as a benchmark to calibrate other methods.

There are two major aspects of a high density fluid EOS, an accurate evaluation of the energy of important configurations and a thermodynamic sampling of the chosen configurations.

Configurational energies are determined using the MondoSCF [4] code which gives very efficient (linear scaling) many-particle *ab initio* electronic structure calculations. With configurations of around 100 molecules

and periodic boundary conditions, the focus is on the accurate evaluation of the many-body energy in those configurations. An extensive study of basis set dependence for individual molecules, pairs of molecules, and full many-body configurations was conducted along with an evaluation of the accuracy of various density functional methods.

At high density, a significant many-body contribution was found. The PBE0 density functional was found to give a good representation of the nitrogen energy and bond length. A 6-31G** basis set was found to give convergent results for the difference in energy between fluid configurations and isolated N_2 molecules (using ghost basis functions). Even with the high efficiency of MondoSCF, a single configuration requires a substantial amount of computer time (~2 days on a single processor).

The standard Monte Carlo and molecular dynamics methods require a very large number of configurations for evaluation of the thermodynamics. In order to control the number of configurations required, we have developed a method that gives qualitative results with 10 configurations and accurate statistics with 100. First, a reference simulation is made in the NPT ensemble with a reference pair potential that is very close to the many-body interaction. In this case, a fit to the calculated two-body anisotropic interaction was used. Then the full many-body electronic structure energy was evaluated using MondoSCF for uncorrelated sample configurations from the reference sample. Instead of relying on a perturbation expansion, each sample configuration was reweighted for the full energy thermodynamic distribution. In principle, this is exact, but in practice the reference distribution is peaked in the wrong location for the full sample. By choosing the P and T of the full simulation to be different from that of the reference simulation, the peaks of the two distributions can be adjusted to have maximum overlap and good statistics after all.

For the nitrogen fluid, a large set of EOS points has been calculated over the range of around 5–40 GPa. Temperatures are chosen to be near those of the Hugoniot. Using the shock jump conditions, a theoretical

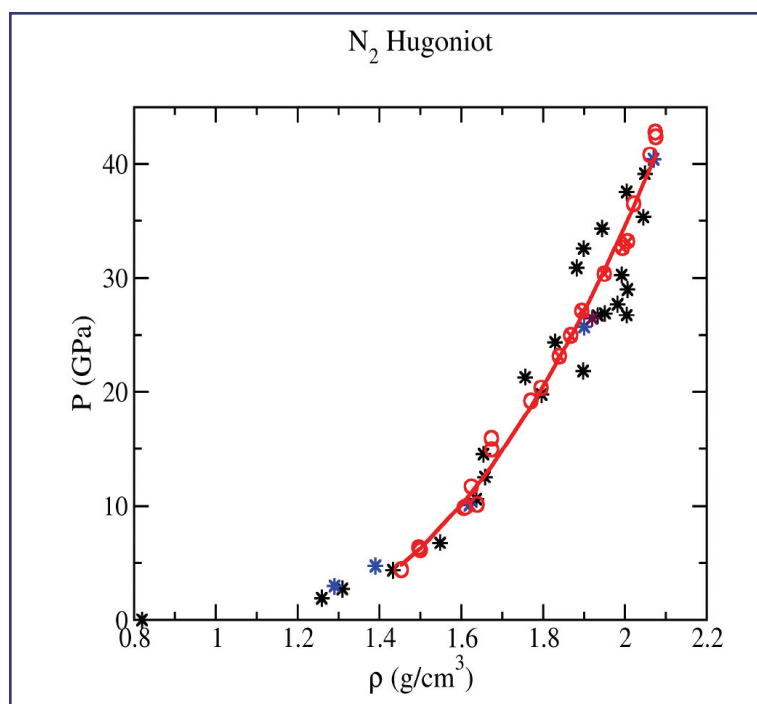


Figure 1—
 N_2 Hugoniot. Data (*, *), *ab initio* MondoSCF configurational energy in a reweighted Monte Carlo sample (O,X), quadratic fit to theory (line).

Hugoniot has been calculated. The results are in excellent agreement with experiment and look to be predictive. In Fig. 1, the Hugoniot data are given with the * symbols. Calculated results are given in red. The open circles are from samples with 10–20 configurations per EOS point. The X is included in the circle to denote samples with 30–50 configurations and correspondingly smaller statistical uncertainty. Additional configurations are being calculated to improve the statistics. The red line is a fit to the set of calculations.

The many-body results are in excellent agreement with experiment. (Previous calculations with an *ab initio* pair potential are roughly 20% higher in pressure.) The next step will be to calculate CO_2 , H_2O , and CO fluids. Then combinations of these will be evaluated in mixtures. The results for high explosives products are very sensitive to the details of the interactions of unlike molecules because of resulting shifts in chemical equilibrium. These calculations along with limited experimental data can be used to make significant improvements in the precision and predictability of EOS models.

[1] M. Sam Shaw, “Direct Simulation of Detonation Products Equation of State by a Composite Monte Carlo Method,” (to be published in *Proceedings of the 12th Detonation Symposium*).

[2] M. Sam Shaw, “A Hybrid Monte Carlo Method for Equilibrium Equation of State of Detonation Products,” in *Shock Compression of Condensed Matter - 2001*, edited by M.D. Furnish, N.N. Thandhani, and Y. Horie (AIP, 2002), p. 157.

[3] M. Sam Shaw, “Direct Simulation of Detonation Products Equation of State,” (to be published in *Proceedings of the 2003 APS Topical Conference on Shock Compression of Condensed Matter*).

[4] Matt Challacombe, et al., “MondoSCF, A Program Suite for Massively Parallel, Linear Scaling SCF Theory and *ab initio* Molecular Dynamics,” Los Alamos National Laboratory computer code LA-CC 01-2.

For more information, contact Sam Shaw
(mss@lanl.gov).

Acknowledgements

We would like to acknowledge NNSA's Advanced Simulation and Computing (ASC), Materials and Physics Program for financial support.

Anisotropic Plasticity of NiAl under Dynamical Loading

Alejandro Strachan (T-14) and
Sheng-Nian Luo (P-24)

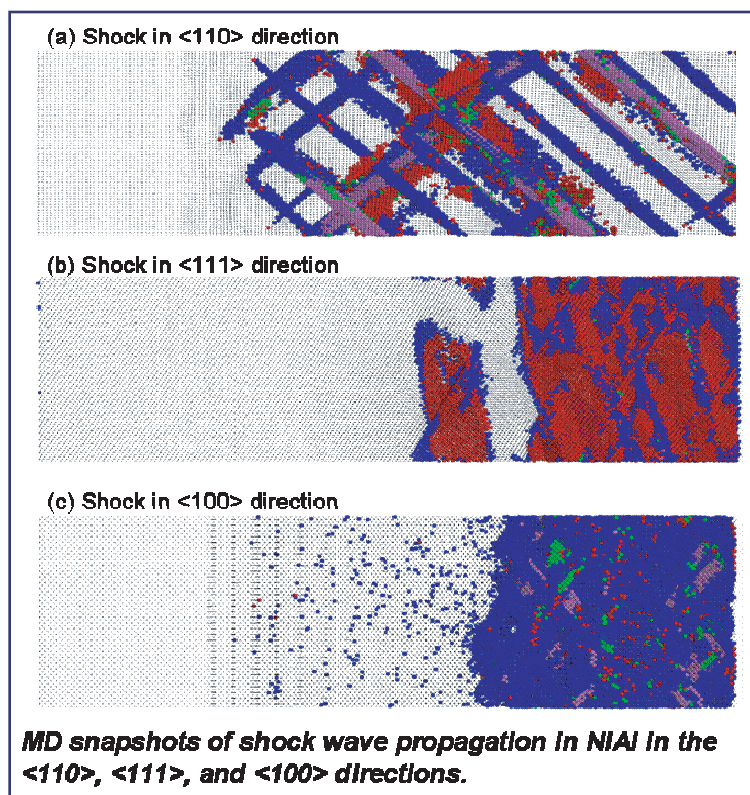
Ordered intermetallic alloys have attracted significant attention due to their potential application as structural materials in high temperature environments. NiAl, a metallic alloy with the B2 crystal structure, is among the most promising materials for such applications due to its low density, high melting temperature (1912 K) and excellent corrosion resistance. However, NiAl suffers from poor ductility at room temperature and its mechanisms of plastic deformation are poorly characterized. An atomic-level understanding of plasticity in B2 metallic alloys is a critical step towards the development of new alloys with optimized properties.

We use molecular dynamics (MD) with an accurate interatomic potential to study the mechanical response of NiAl when shocked along $\langle 110 \rangle$, $\langle 111 \rangle$, and $\langle 100 \rangle$ directions. For strong enough shockwaves, plastic deformation relaxes the uniaxial compression of the shock; we focus on this relaxation phenomenon.

Figure 1 shows snapshots from our simulations. We color atoms according to the plastic slip they have undergone: blue atoms have slipped by $1/2a\langle 111 \rangle$, purple ones have done so by $a\langle 111 \rangle$, red by $a\langle 100 \rangle$, and green by $a\langle 110 \rangle$ (where a is the lattice parameter); elastically deformed and unshocked atoms are shown as small black dots.

Our results show that for shocks in the $\langle 110 \rangle$ direction, the first event regarding plastic deformation is the nucleation of $1/2\langle 111 \rangle$ loops (blue atoms); the edge components of these loops move toward and away from the shock front. The B2 lattice is not invariant against translations by $1/2a\langle 111 \rangle$; thus, the area swept by these loops is left defective [with an antiphase defect (AFD)] and their growth is energetically unfavorable. Thus, a second $1/2\langle 111 \rangle$ loop is nucleated inside the original ones leading to $\langle 111 \rangle$ slip

Figure 1—
The figure shows snapshots from our simulations. We color atoms according to the plastic slip they have undergone: blue atoms have slipped by $1/2a\langle 111 \rangle$, purple ones have done so by $a\langle 111 \rangle$, red by $a\langle 100 \rangle$ and green by $a\langle 110 \rangle$ (where a is the lattice parameter); elastically deformed and unshocked atoms are shown as small black dots.



(purple atoms). At later times we observe the nucleation of $\langle 100 \rangle$ slip, predominantly at the intersection of $1/2\langle 111 \rangle$ loops. We find that the plastic wave moves at the same speed of the shock front. For shocks in the $\langle 111 \rangle$ direction plastic deformation also begins with the nucleation of $1/2\langle 111 \rangle$ loops, but in this case the nucleation of the second $1/2\langle 111 \rangle$ loops inside the original ones lead to $\langle 100 \rangle$ slip (red atoms). In this case, the plastic wave does not catch up with the shock front: the plastic wave propagates slower than the shockwave and an elastic precursor develops. Finally, for loading in the $\langle 100 \rangle$ direction we observe multiple, almost simultaneous, nucleation of $1/2\langle 111 \rangle$ loops and the frequent intersection thereof; this entanglement severely limits their mobility and even leads to local amorphization.

In summary, we used MD simulations to characterize the details of the plastic response of NiAl single crystals under compressive uniaxial loading. While in all cases plastic deformation starts with the nucleation of $1/2\langle 111 \rangle$ loops, the subsequent phenomena exhibits marked anisotropy. Shocks in $\langle 110 \rangle$ have a single wave structure with the plastic wave traveling at the shock speed; on the other hand for $\langle 111 \rangle$ and $\langle 100 \rangle$ loading we find a two-wave structure with the plastic wave following an elastic precursor.

***For more information, contact
Alejandro Strachan (strachan@lanl.gov).***

Acknowledgements

We would like to acknowledge NNSA's Advanced Simulation and Computing (ASC), Materials and Physics Program and Campaign 11, Advanced Simulation and Modeling, for financial support.

Mesodynamical Simulations with Quantum Mechanical Description of the Thermal

Alejandro Strachan (T-14) and
Brad Lee Holian (T-12)

We have recently developed new equations of motion for particle-based mesodynamics simulations that lead to a thermodynamically accurate description of the energy exchange between explicit (mesoscopic) and implicit degrees of freedom (DoF). In a mesodynamical description one describes groups of atoms (molecules or crystalline grains) with a single mesoparticle. The new mesodynamics equations of motion:

$$\begin{aligned}\dot{r}_i &= u_i + \chi_i F_i \\ \dot{u}_i &= \frac{F_i}{m_i} \\ \dot{E}_i^{\text{int}} &= \frac{\dot{T}_i^{\text{int}}}{C_i^{\text{int}}} = \chi_i F_i \cdot F\end{aligned}\quad (1)$$

where $\chi \propto \gamma (T_i^{\text{ext}} - T_i^{\text{int}})/T_0$, T_i^{ext} and T_i^{int} are the external and internal temperatures, respectively, C_i^{int} is the specific heat of the internal DoFs, and γ determines the characteristic time of the coupling between internal and explicit modes.

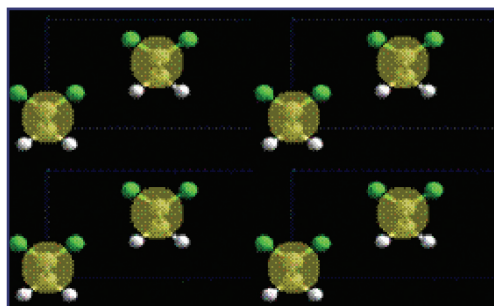


Figure 1—
All-atom and mesoscopic representation of the PVDF crystal. Each mesoparticle represents a polymer chain.

The new mesodynamics description satisfies the following desirable properties:

- total energy (mesoparticles plus internal DoFs) and center-of-mass velocity of the system are conserved,
- exchange of energy is done on a spatially local basis,
- implicit DoFs are described by their specific heat that can be calculated from first principles enabling a quantum mechanical description of the thermal role of the implicit DoFs,
- equations of motion are Galilean invariant and the ballistic limit is described correctly, and
- as the coupling between internal and external modes is reduced to zero, Newton's equations of motion are recovered.

In order to validate the new mesodynamics we compare its description of a shockwave propagating in a crystalline phase (denoted β) of the ferroelectric polymer poly(vinylidene difluoride) [PVDF, $(\text{CH}_2\text{CF}_2)_n$] with all-atom molecular dynamics (MD) simulations. We replace each polymer chain with a single mesoparticle (see Fig. 1). We use the classical harmonic approximation to obtain the specific heat of the internal degrees of freedom ($C_i^{\text{int}} = N_i^{\text{int}} k_B$). Our method yields results that are essentially identical to those of all-atom simulations, both in final temperature achieved and in the profile of temperature with distance throughout the shock front.

All-atom MD is classical in nature (in equilibrium and under the harmonic approximation every DoF); thus, the internal specific heat of the polymer molecules is largely overestimated at low temperatures (see upper panel of Fig. 2). The new mesodynamics Eq. 1 naturally enables for a quantum mechanical description of the thermal role of the implicit DoFs. The lower panel in Fig. 2 shows the temperature rise of a thin PVDF slab as shockwaves with particle velocity of 1 and 2 km/s pass through it. As expected, the lower QM specific heat leads to higher temperatures than those obtained under the classical approximation (which are in excellent agreement with all-atom MD). Thus, the new mesodynamics not only provides a computationally more efficient

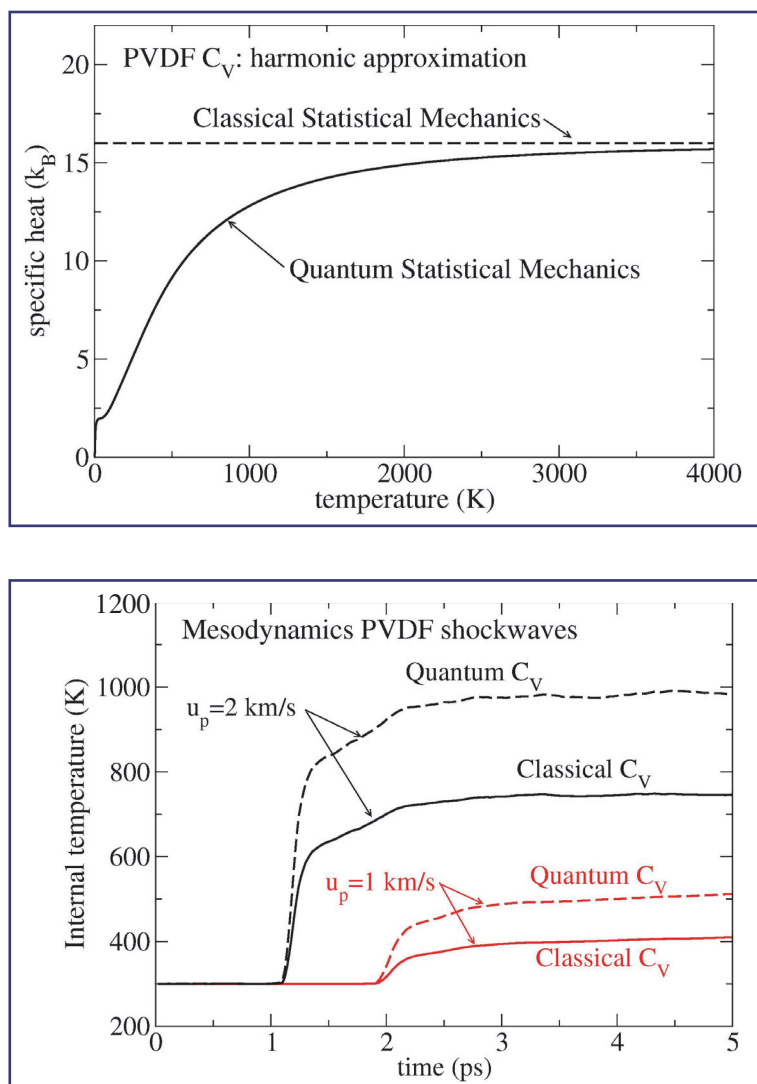


Figure 2—
 (Top) Specific heat of the internal degrees of freedom as a function of temperature under the classical harmonic approximation (dashed line) and calculate using QM (solid line).
 (Bottom) Temperature rise as a shockwave passes through a thin slab of PVDF.

method but also more accurate than all-atom MD.

This new thermomechanical formulation of mesodynamics that describes the exchange of energy between explicit and implicit DoFs is generally applicable to a wide variety of problems in chemistry, biology, materials science, and physics enabling more accurate and computationally efficient particle-based mesoscopic simulations.

For more information, contact
Alejandro Strachan (strachan@lanl.gov).

Acknowledgements

We would like to acknowledge NNSA's Advanced Simulation and Computing (ASC), Materials and Physics Program for financial support.

Influence of Elastic Shear Stiffness on Richtmyer-Meshkov Instability

*JeeYeon N. Plohr (T-1) and
Bradley J. Plohr (T-13)*

In 1953, R. D. Richtmyer wrote a Los Alamos Scientific Laboratory report, published as Ref. [1], about what happens when a shock wave strikes an interface between two fluids head on. By analogy with the classical Rayleigh-Taylor instability [2, 3] of an interface subjected to constant acceleration, he expected that the impulsive acceleration of the shock wave would cause deviations of the interface from perfect flatness to grow in time. The combined mathematical and computational analysis in Ref. [1] confirmed this expectation. This fluid instability was seen experimentally by E. Meshkov [4] and is now called the Richtmyer-Meshkov instability.

What happens if the two materials are solids rather than fluids? One difference between a solid and a fluid is elastic shear stiffness, which should resist the growth of perturbations. This tendency is seen in the influence of elastic shear stiffness on the Rayleigh-Taylor instability in the small-amplitude regime [5]: the growth rate of perturbations is reduced, and short wavelength perturbations are stabilized altogether. We have investigated the elastic Richtmyer-Meshkov instability in the small amplitude regime. Our finding is that shear stiffness, however small, causes perturbations of any wavelength to remain small: Richtmyer-Meshkov flow for elastic solids is stable.

Richtmyer-Meshkov flow is described by the Euler equations, a set of partial differential equations (PDEs), involving several flow variables (mass density, particle velocity components, and specific energy), that embodies conservation of mass, momentum,

and energy. To determine whether a particular flow (the “background flow”) is unstable, one rewrites the Euler equations in terms of the deviations of the flow variables from their background values (the “perturbation”). So long as the perturbation remains small, the rewritten equations are close to the “linearized equations” that neglect terms of quadratic and higher order in the perturbation. The linearized equations are then studied to see whether an initially small, but nonzero, perturbation grows in time.

For classical instability problems, such as the Rayleigh-Taylor problem, the linearized equations are amenable to exact mathematical analysis, primarily because the coefficients appearing in the linearized equations are independent of space and time. For the Richtmyer-Meshkov problem, however, this is not true; analysis reduces the problem to a PDE for one space and one time dimension, but this PDE has no (known) analytical solutions. Richtmyer’s essential innovation was to use an early digital computer to simulate the reduced PDE. He found that Richtmyer-Meshkov flow for fluids is unstable, with the perturbation amplitude growing roughly linearly with time.

Our work on elastic solids [6, 7] follows Richtmyer’s approach and later refinements [8] but is more complicated because representation of solid deformation requires a nine-component tensor, whereas a single scalar, the volume, suffices for a fluid. A nonstandard formulation of elasticity [9, 10] casts the governing equations as a system of conservation laws. Equations of state for the solids are needed to complete the governing equations; the ones we developed are thermodynamically consistent and allow for arbitrarily large volumetric deformation combined with a small shear deformation. The background flow is constructed by solving the one-dimensional problem of shock transmission/reflection at a material interface, and the initial values for the perturbation are constructed by solving a two-dimensional version of this problem when the angle of incidence is small. The conservation laws are linearized around the background flow, as are the jump conditions, which are

implied by the conservation laws, for the discontinuous waves (the longitudinal and shear shock waves and the material interface). For each sinusoidal mode, we obtain linear conservation laws, with source terms and spatially varying coefficients, in one space and one time dimension. The initial-value problem is solved numerically using a finite difference method supplemented by a front tracking scheme.

The plot of amplitude vs time from our simulations is shown in Fig. 1. Our simulations support the following conclusions concerning the growth rate and amplitude of perturbations of a frictionless material interface between elastic solids when it is struck normally by a shock wave:

- Even a small shear modulus changes the late-time asymptotic behavior of the growth rate. Rather than approaching a constant so that the amplitude grows linearly, it oscillates in such a way that the amplitude remains bounded. In particular, the linear theory remains valid at late time.
- The amplitude oscillates around an asymptotic value with a frequency that grows with the shear moduli (see Fig. 2) and is independent of the strength of the incident shock wave.
- If the shock strength is increased, the amplitude oscillates about a smaller asymptotic value and the oscillations increase in variation.
- Varying the bulk modulus has little effect on the behavior of the material interface.

We explain the striking difference between fluid and elastic solid behavior in Richtmyer-Meshkov flow in the following way. The role of the shock wave in Richtmyer-Meshkov is to deposit vorticity on the perturbed interface. This sheet of vorticity is subject to Kelvin-Helmholtz instability. In (inviscid, incompressible) fluid dynamics, the vorticity remains on the interface, so that Kelvin-Helmholtz instability leads to growth of perturbations. In contrast, for elastic solids, the vorticity propagates at the shear wave speeds and thus escapes the interface, so that perturbations of the interface do not grow.

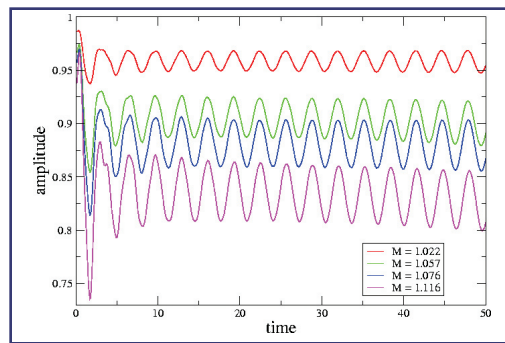


Figure 1—
Amplitude vs time for tantalum/aluminum and various Mach numbers of the incident shock wave.

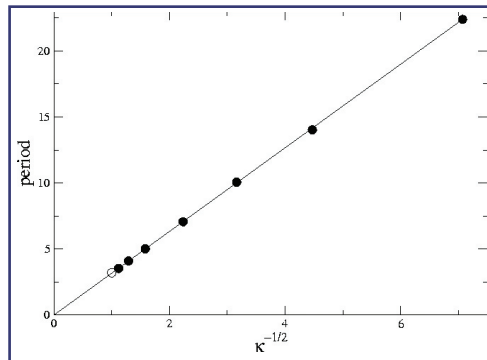


Figure 2—
Period of oscillations vs $1/\sqrt{\kappa}$ for various values of the interpolation parameter κ , which determines the shear moduli κG_{Ta} and κG_{Al} of the model solids.

- [1] R. Richtmyer, *Commun. Pure Appl. Math.* **13** (1960), 297–319.
- [2] Lord Rayleigh, *Scientific Papers, Vol. II* (Cambridge Univ. Press, Cambridge, England, 1900), p. 200.
- [3] G.I. Taylor, *Proc. R Soc. London A* **201** (1950), 192–196.
- [4] E. Meshkov, NASA Tech. Trans. **F-13** (1970), 074.
- [5] B. Plohr and D. Sharp, *Zeit. angew. Math. Phys.* **49** (1998), 786–804.
- [6] J. Nam, Ph.D. thesis, State University of New York at Stony Brook, 2001.
- [7] J. Plohr and B. Plohr, to be published in *J. Fluid Mech.*, 2005.
- [8] Y. Yang, Q. Zhang, and D. Sharp, *Phys. Fluids* **6** (1994), p. 1856–1873.
- [9] B. Plohr and D. Sharp, *Adv. Appl. Math.* **9** (1988), 481–499.
- [10] B. Plohr and D. Sharp, *Adv. Appl. Math.* **13** (1992), 462–493.

For more information, contact JeeYeon Plohr (jplohr@lanl.gov).

Acknowledgements

We would like to acknowledge NNSA's Advanced Simulation and Computing (ASC), Materials and Physics Program for financial support.

Modeling Plastic Instability and Strain Localization in Explosively Driven U6 Hemi

*Q. Ken Zuo and Paul J. Maudlin (T-3),
and Lawrence M. Hull (DX-3)*

Straining localization refers to the formation of a highly localized deformation in the form of thin planar bands (of the order of $10\ \mu\text{m}$) as the result of material softening, which occurs when the material becomes plastically unstable. Tensile tests of uranium alloyed with 6% niobium (U6) show stable behavior in the as-received condition but unstable behavior at very modest strain level in the post-shocked condition. The post-shock condition refers to the material properties after being processed by a large amplitude shock wave, as is the situation when a shell is accelerated by in-contact explosives. Hemispheres filled with explosives are used here to test our ability to predict the onset of plastic instability in expanding U6 shells. The ultimate goal is to develop the ability to predict the onset of instability, the dynamics of the unstable motion, the fracture of the shell into individual fragments, and the size and spatial distribution of the fragments and fragmentation debris.

The filled hemi consists of a hemispherical U6 shell filled with explosive (PBX 9501) and initiated at the center (Fig. 1, see [1] for a detailed description of the test setup). A series of experiments has been conducted using filled hemispherical shells (with the thickness of 1-2 mm) and applying various diagnostics. Radiographs and fragment recovery provide experimental information on the onset of material instability. Proton radiographs (pRad) are taken normal to the pole of the hemi at a sequence of times, and the images are shown in Fig. 2. It is observed that localized thinning occurs at early time ($8.2\ \mu\text{s}$), and at later time these localizations coalesce into the ultimate fragmentation

pattern. Fragment recovery experiments using a water medium have also yielded significant information on the behavior of the filled-hemisphere geometry. In the recovery experiments, the shell is immersed in the water initially so that there is no metal/water impact process that could induce additional material damage. The recovered fragments represent an approximation to the conditions at the time fragmentation is complete (the fragments are fully separated, as in the $16.8\ \mu\text{s}$ radiograph).

Pre-shot computations were conducted to model one such experiment using EPIC, a 3D, explicit, finite-element code for large strain, high strain rate dynamic applications. The computational study focused on the effect of a large amplitude shock on U6 material in the dynamic response of the hemi, in particular, the prediction of the onset of material instability. Figures 3 and 4 are the snapshots of plastic strain distribution in the shell at $5\ \mu\text{s}$ after the detonation wave hits the shell (which corresponds to about $8\ \mu\text{s}$ in the pRad images), for U6 with two different processing conditions, i.e., as-received and shock-hardened, respectively. Figure 3 shows a relatively uniform deformation (the equivalent plastic strain ranges from 0.5 to 0.75), a typical result of a stable material, while Fig. 4 shows pronounced strain localization (the plastic strain reaches 1.00 in several cells while most of the hemi has a strain of about 0.6), resulting from the unstable material behavior of the shock-processed U6. Since the deformation remains stable and symmetrical (about the horizontal axis) for the as-received material, only a 2D cut (in the R-Z plane) is shown. For the shocked-processed material (Fig. 4), the expansion is initially axisymmetric, while the material is still stable but quickly loses the axisymmetry and becomes 3D as the instability develops.

The numerical results are consistent with our understanding of material instability and strain localization, namely, the critical strain at which material loses stability increases with the hardening modulus (the slope on the stress-strain curve) and decreases with the yield stress. The main effects of pre-shock on U6 are to raise the initial yield point and to significantly reduce the hardening modulus.

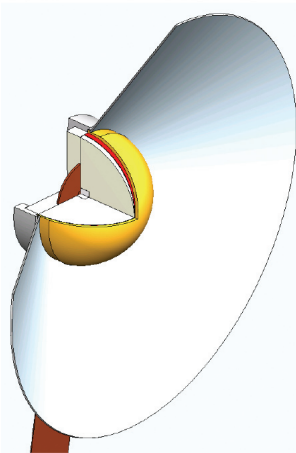


Figure 1—
Schematic of the filled
hemisphere experiment.

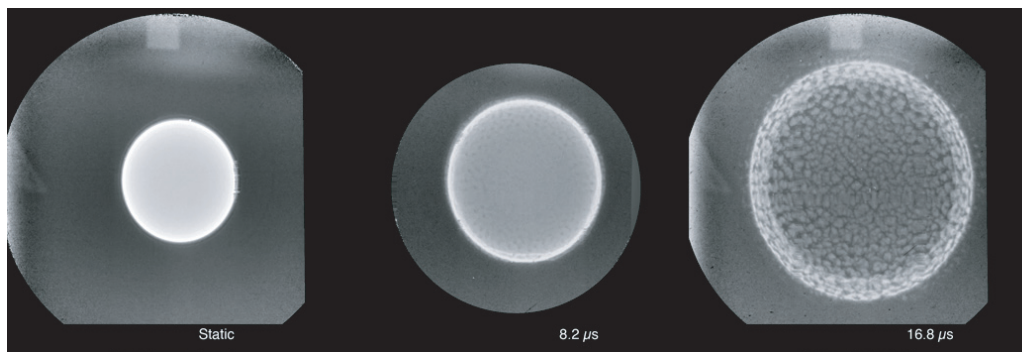


Figure 2—
Proton radiographs
of the expansion of
a filled hemi.

Consequently, the shock-hardened U6 becomes unstable shortly after the detonation wave hits the shell and the shell expands nonuniformly while the calculation of the as-received U6 remains stable during the expansion. The experimental data supports the computations qualitatively and to some degree quantitatively. At 8 μ s, localization is evident in the experiment as thinning in small spots. The recovered fragments show background strain of about 60%, and this compares well to the calculated background strain at 8 μ s. The comparison of the background strain in the recovered fragments to the calculated strain at 8 μ s requires the assumption that once localization begins, all the subsequent strain is concentrated in the localizations. In other words, the background strain ceases to increase when localization commences. The validity of this assumption remains to be checked. There is also at present no method of seeding the localization on a physical basis, so detailed comparisons of the experimentally determined spatial distribution of the thinned regions will not be expected to accurately match the calculated distribution.

This summary is a part of a more comprehensive article on modeling deformation and damage of metals under high-rate loadings [1].

[1] G.T. Gray, P.J. Maudlin, L.M. Hull, Q.K. Zuo, and S.R. Chen, "Predicting Material Strength, Damage, and Failure-The Synergy Between Experiments and Modeling," *Los Alamos Science* 29, 80–93 (2005).

For more information, contact Q. Ken Zuo (zuo@lanl.gov).

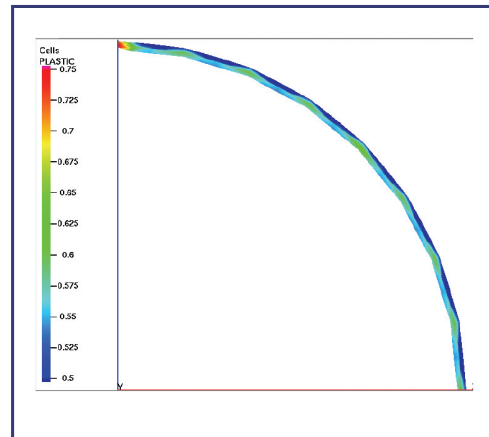


Figure 3—
Calculation of
as-received U6.

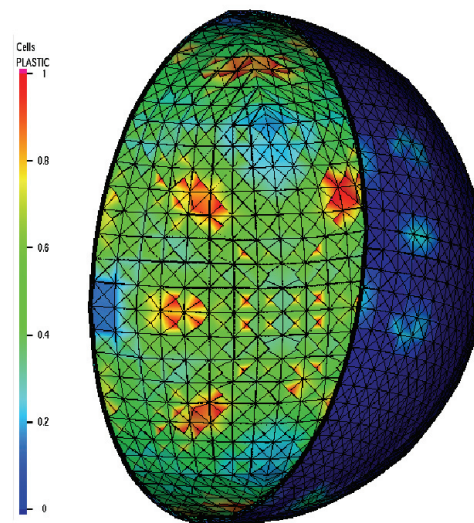
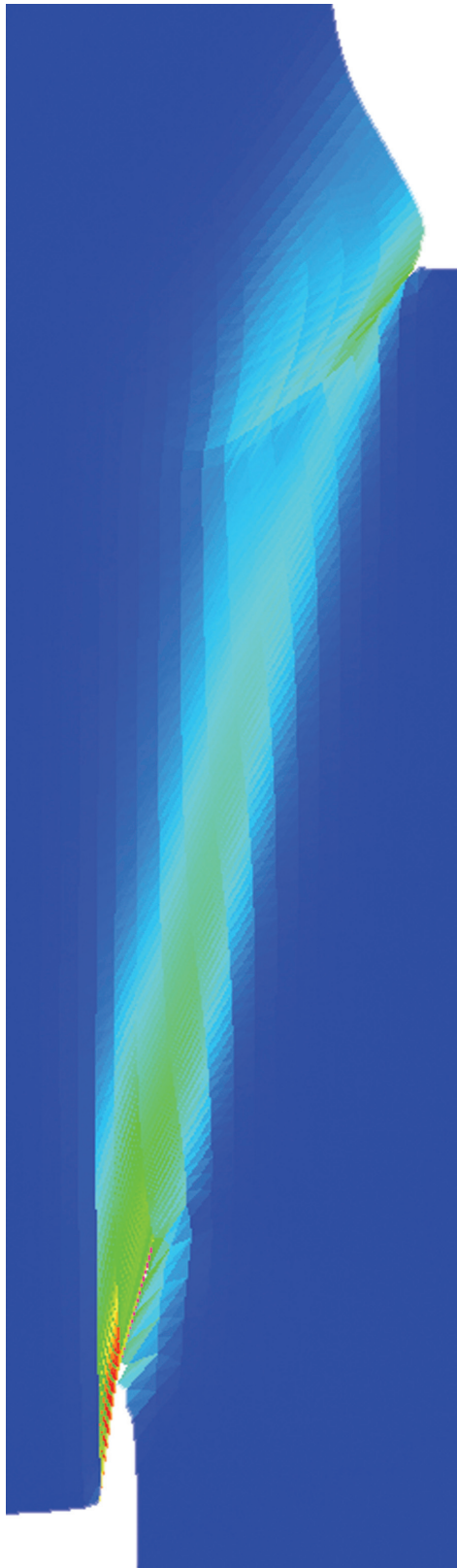


Figure 4—
Calculation of
shock-hardened U6.

Acknowledgements

We would like to acknowledge NNSA's Advanced Simulation and Computing (ASC), Materials and Physics Program; and the Joint DoD/DOE Munitions Technology Development Program, for financial support.



FLUID DYNAMICS

Flux Calculations in the Heat Transfer Component of TELLURIDE

*Travis Austin, Markus Berndt,
J. David Moulton, and
Mikhail Shashkov (T-7)*

The TELLURIDE project at Los Alamos is a strategic computing effort aimed at producing high fidelity simulations of metal solidification processes. Its code provides numerical simulations of solidification, fluid flow, heat transfer, phase transformations, mechanical deformation, and welding processes on the kinds of meshes seen in Fig. 1. The simulation of each component is driven by a discretization of the continuum equations describing the physical processes. The components are then coupled in a way that describes their true physical interaction.

The ability of projects like TELLURIDE to model physical reality depends on several factors: accurate numerical models, stable computer implementations, realistic test data, and fast parallel algorithms. So when the simulations are unable to approximate reality, it can be quite difficult to find where things went awry. However, prior to executing any simulation, one can perform

component testing, whereby ensuring that each component accurately models the physics it is supposed to describe. Here, we investigate inaccuracies in the heat transfer component that are due to a poor approximation of the heat flux using existing methodologies. Furthermore, we describe a robust approximation scheme for calculating the heat flux that is based on the support-operators (SO) methodology [1].

The flux calculations within the heat transfer component arise within the nonlinear equation that describes the temporal change of specific enthalpy. The equation is discretized using finite volumes on a hexahedral mesh, and then flux values are computed on cell faces given cell-centered temperature values. There are two approaches to computing the flux. Both obtain the flux by combining a gradient calculation with knowledge of the conductivity and the normal vector. Where they differ is how the gradient is computed. Approach **A** computes the gradient on each face via the definition of the directional derivative. This yields a gradient that depends on the difference of the temperature values at the two adjacent cells and the vector directed from one cell center to the other. Approach **B** is a much more sophisticated algorithm that depends on surrounding cells. See [2] for a detailed description. The limitations of the two approaches are that approach **A** is inaccurate for nonorthogonal meshes, while approach **B** is inaccurate when there are jumps in the conductivity.

We observe the two approaches' limitations for a simple problem on the unit cube. Specifically, for a smooth meshing of the unit cube (Fig. 2), a conductivity and a temperature distribution are defined. Then the normal component of the flux is calculated for each face and its deviation from the true value is measured. We use a conductivity of $\kappa = 1$ for $x \leq 1/2$ and $\kappa = 100$ for $x > 1/2$, and a temperature distribution given by

$$T(x, y, z) = \begin{cases} x, & \text{for } x \leq 1/2 \\ \frac{1}{200}(2x + 99), & \text{for } x > 1/2 \end{cases}$$

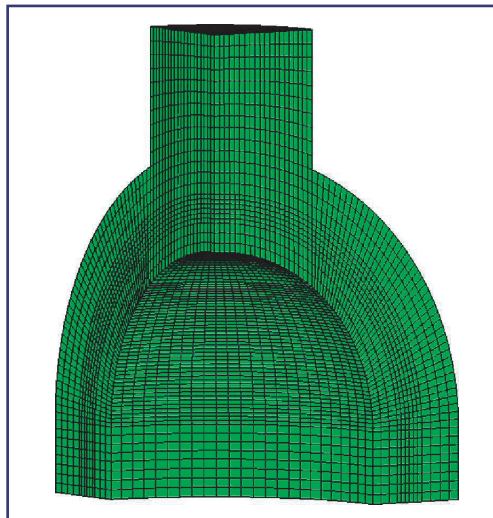


*Figure 1—
Typical TELLURIDE
mesh.*

For a sequence of smooth grids like in Fig. 2, we illustrate with the blue lines in Fig. 3 the lack of convergence of the interior and boundary root mean-squared error for approach **A**. We see the same type of divergence for approach **B**.

The SO approach relies on the SO discretization for diffusion-type equations. Similar to the approach **B** method, the computed flux depends on more than just the two adjacent cell-centered temperature values. However, in contrast to approach **B**, the SO approach correctly incorporates conductivity information so that inaccuracies do not arise from discontinuous conductivities. Again, see [1] for further details.

In the heat transfer we use SO in the following way. To begin, we explicitly compute a flux rather than taking an intermediate step of computing a gradient. However, like approach **A**, we do compute a vector for each face of each cell that depends on the difference of the temperature between the two adjacent cells. We then employ this vector as the right-hand side of the appropriate matrix problem, i.e., a system of the form $Au = f$. Finally, we must solve this large system of algebraic equations using an iterative solution method. That is, we find the solution, say u , by making an initial guess and then iteratively improving it until we have the accuracy that we desire. For the same problem for which approach **A** showed no convergence, we get convergence for the SO approach. This is seen in red in Fig. 3.

The SO approach to heat flux calculations offers a drastic improvement to the current approaches when the mesh is severely distorted or the conductivity jumps across material interfaces. The approach however is more costly. Yet, because all other approaches suffer from their inaccuracies for more difficult problems, the cost of the SO approach is an adequate price to pay. Moreover, in the future, we will be investigating the accuracy of more efficient local solution methods.

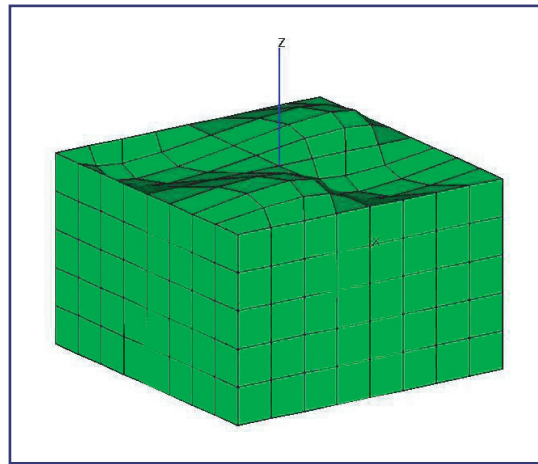


Figure 2—
Slice of smooth 3D mesh.

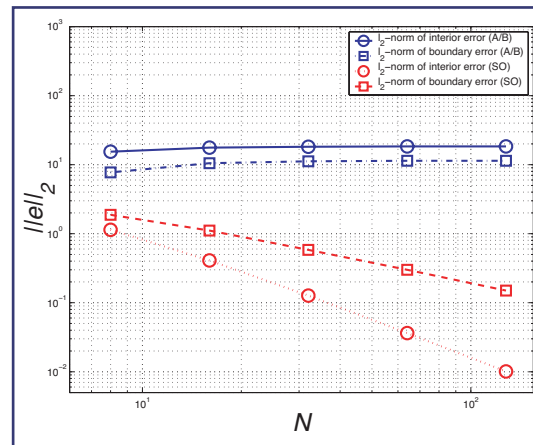


Figure 3—
Illustration of lack of convergence for existing approach (A/B), and illustration of convergence for support-operators (SO) on a sequence of finer grids.

- [1] J. Hyman, et al., "Mimetic Finite Differences for Diffusion Equations," *Comput. Geosc.* **6**, pp. 333–352, 2002.
- [2] T.J. Barth, "Aspects of Unstructured Grids and Finite-Volume Solvers for Euler and Navier-Stokes Equations," *KI/NASA/AGARD Special Course on Unstructured Grid Methods for Advection Dominated Flows* (AGARD Publication R-787), 1995.

For more information, contact
Markus Berndt (berndt@lanl.gov).

Acknowledgements

We would like to acknowledge NNSA's Advanced Simulation and Computing (ASC), Materials and Physics Program for financial support.

Shear Localization in Tantalum Top Hat Samples

Curt A. Bronkhorst and Paul J. Maudlin (T-3), and Ellen K. Cerreta, Thomas A. Mason, and George T. Gray III (MST-8)

The ductile failure process for polycrystalline metals is a sophisticated sequence of physical events occurring at different length scales. One element of that process is believed to be shear localization and subsequent shear band formation. In general, the shear localization process involves initiation and growth where initiation is expected to be a stochastic process in material space where anisotropy in the elastic-plastic behavior of single crystals and intercrystalline interactions serve to form natural perturbations to the material's local stability. A common sample geometry used by the Structure/Property Relations group in the Materials Science and Technology Division (MST-8) to study shear localization growth is the "top hat." As the name implies, it is an axisymmetric sample with an upper "hat" portion and a lower "brim" portion with the gage section between the hat and brim. Figure 1(a) shows one-half of the cross-sectional geometry (line of symmetry along Z-axis) for a typical sample. The gage section length is generally on the order of 0.9 mm. The samples were deformed in a Split-Hopkinson Pressure Bar system at maximum top-to-bottom velocity in the range of 10–25 m/sec. We have attempted to model these experiments through both continuum and polycrystal plasticity finite element models.

Experimental and continuum model results for an initial sample temperature of -100°C can be found in Figs. 1 and 2. Figure 1 shows contour plots of equivalent plastic strain at 50 μsec after the wave hits the hat. Figure 2 shows the mean top surface traction applied to the sample during loading.

For the continuum model, the finite element code EPIC was used with a Mie-Grüneisen equation of state and the rate and temperature sensitive MTS flow stress model. Adiabatic conditions were assumed. The numerical results suggest a maximum strain rate on the order of 10^5 s^{-1} in the gage section. The model also suggests that a temperature in the neighborhood of 800°C is reached within the gage section due to the substantial plastic deformation (up to 500%), which takes place over a small period of time.

Using a polycrystal plasticity approach we are attempting to link the localization behavior of these samples to the crystallographic characteristics of tantalum. Figure 3 shows shear stress results of simulations where groups of elements were used to represent a single crystal, each group with a different initial crystallographic orientation. A total of 127 crystals spanned the gage section region. The finite element code ABAQUS along with a rate and temperature-dependent crystal plasticity model was used. The crystal plasticity model allowed for slip to occur on the twelve $\{110\}\langle 111 \rangle$ and twelve $\{112\}\langle 111 \rangle$ slip systems. The model determined active slip systems based upon loading conditions and crystallographic orientation. Figure 3 shows the high level of heterogeneity that one might expect in the sample gage section for a polycrystalline material. The shear stress contour results suggest a factor of three difference between high and low values.

For more information, contact
Curt Bronkhorst (cabronk@lanl.gov).

Acknowledgements

We would like to acknowledge NNSA's Advanced Simulation and Computing (ASC), Materials and Physics Program, the Joint DoD/DOE Munitions Technology Development Program; and Campaign 2, Dynamic Materials Properties, for financial support.

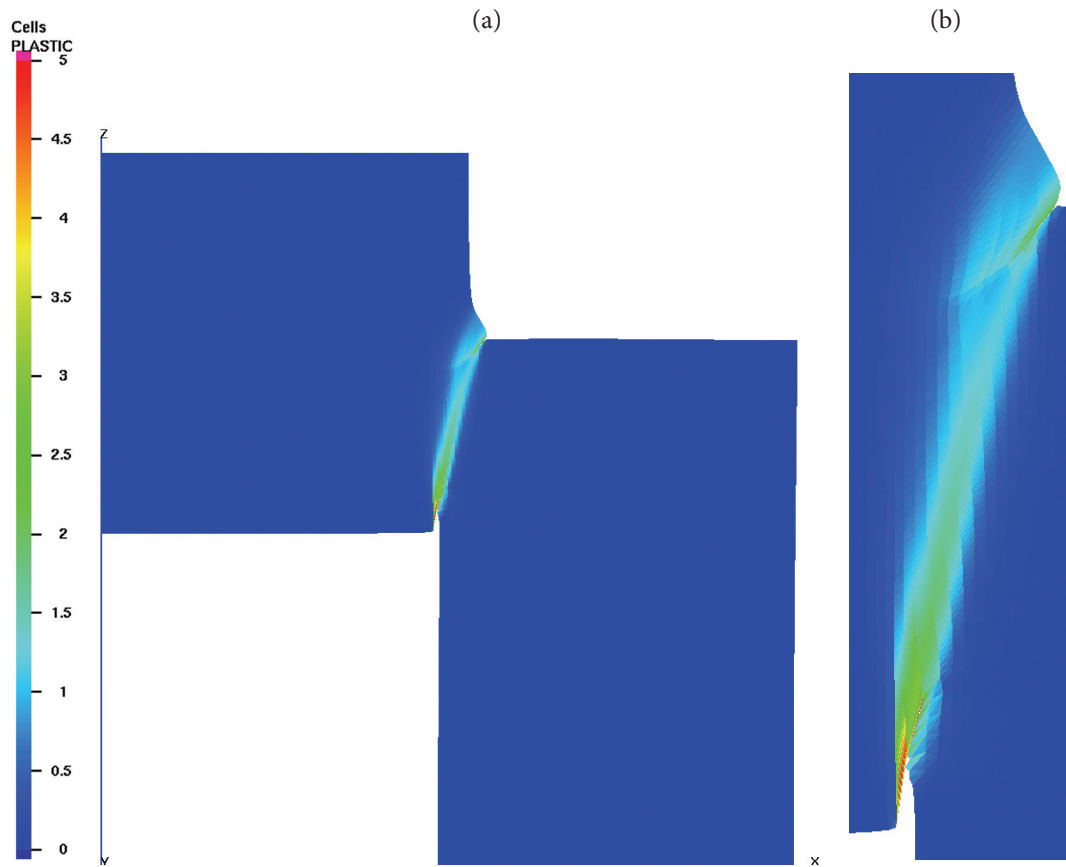


Figure 1—
Total equivalent plastic strain at a time of 50 μsec for an initial temperature of -100°C; (a) axi-symmetric continuum model; (b) gage section only.

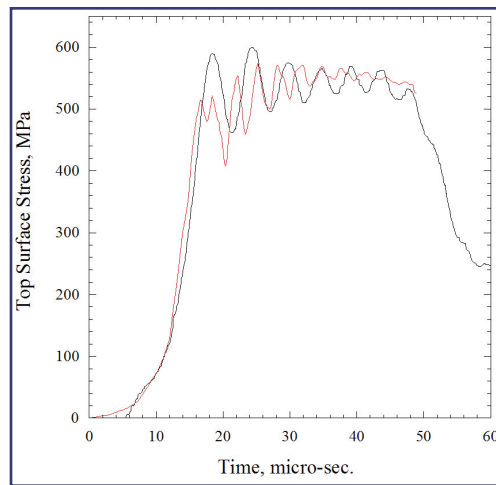


Figure 2—
Experimental (black) versus continuum simulation (red) top-surface stress response for an initial sample temperature of -100°C.

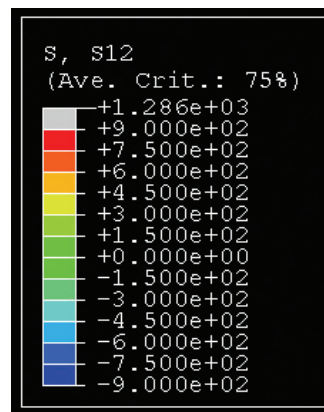


Figure 3—
Shear stress within the gage section of a polycrystal plasticity simulation.

Compressible Particle Model for Turbulent Mix Calculations

Michael C. Cline, Manjit S. Sahota, Peter J. O'Rourke, and David J. Torres (T-3), and Margaret S. Hubbard (X-3)

A compressible particle model supported by the Advanced Simulation and Computing (ASC) Turbulence/Mix Project is currently under development using the T-3 CHAD code as a test bed.

In order to test the particle model compressible terms, a test case driven by pressure gradient and including high-speed flow was needed. Such a case is the axisymmetric, supersonic nozzle discussed in Ref. [1]. The nozzle geometry and computational mesh is shown in Fig. 1. The top is the nozzle wall and the bottom is

the centerline. Subsonic flow enters from the left and supersonic flow exits from the right. The CHAD code is first used to calculate the steady flow without particles. Figure 2 shows the steady-state Mach number contours. Then the particles are introduced at the left. Figure 3 shows the particles approaching the throat region (top) and passing through the throat region (bottom). From this figure, the large amount of shear in the throat region is evident.

Figure 4 shows the effect on particle velocity of varying the particle drag coefficient (CD). The oscillations are due to the fact that the particles communicate with the gas flow through the nearest element vertex. An improved procedure that interpolates inside an element is being developed. Other studies varying the particle density, initial velocity, and injection location are in progress.

[1] L.E. Thode, et al., "Comparison among Five Hydrodynamic Codes with a Diverging-Converging Nozzle Experiment," Los Alamos National Laboratory report LA-13653 (Sept. 1999).

For more information, contact Michael Cline (mcc@lanl.gov).

Figure 1—
Nozzle geometry and computational mesh.

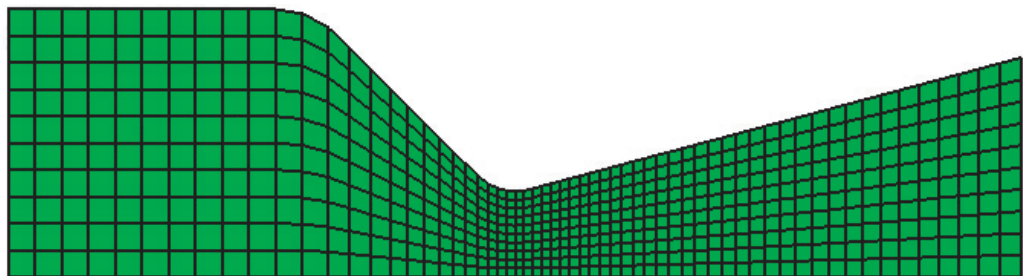
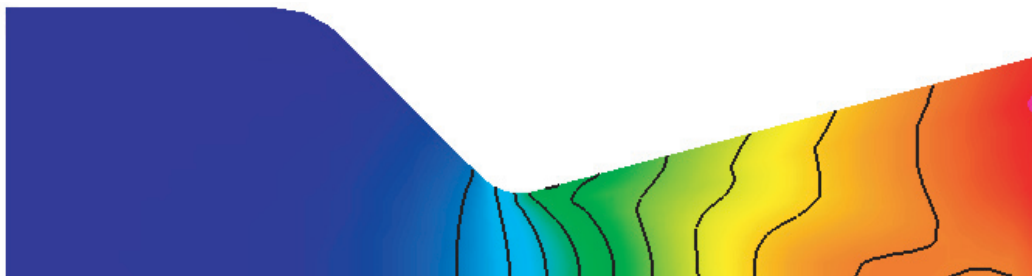


Figure 2—
Steady-state Mach number contours (blue = 0.034, red = 3.4).



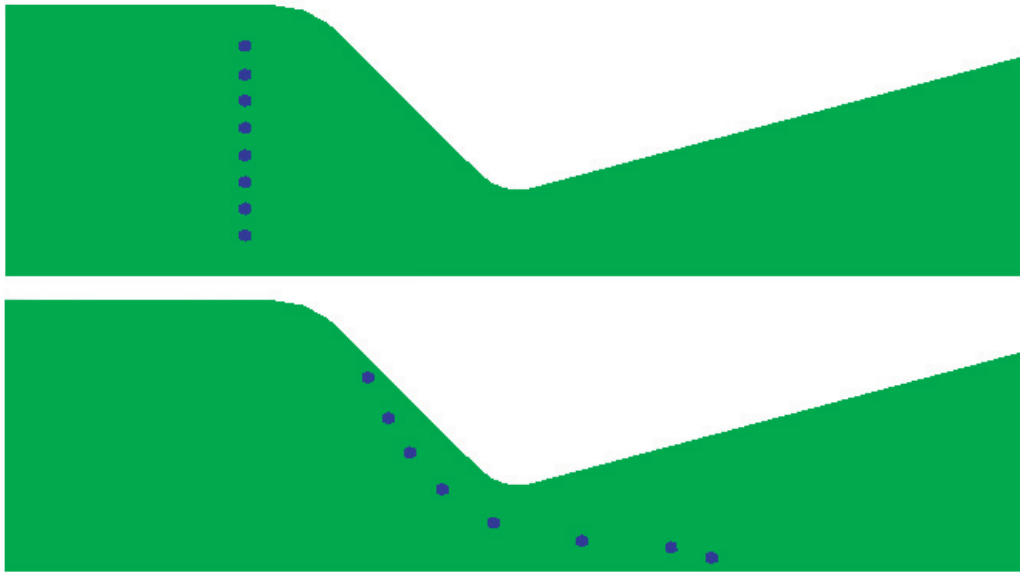


Figure 3—
Particles approaching the throat region (top) and passing through the throat region (bottom).

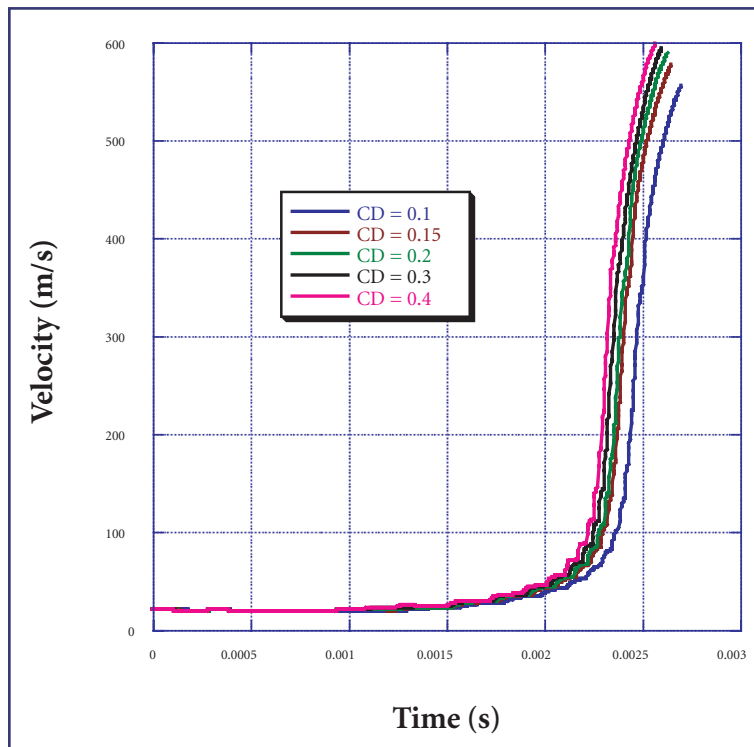


Figure 4—
Effect on particle velocity of varying the particle drag coefficient (CD).

Acknowledgements

We would like to acknowledge NNSA's Advanced Simulation and Computing (ASC), Materials and Physics Program for financial support.

Phase Separation Simulations using Annular Centrifugal Contactors

*Nely T. Padial-Collins,
W. Brian VanderHeyden, Qisu Zou,
and Duan Z. Zhang (T-3), and
Scott Sportsman (NMT-2)*

Annular centrifugal contactors are apparatus consisting of two concentric cylindrical zones. The spinning rotor and the stationary housing wall form the external annular zone. Typically, an aqueous and an organic phase are rapidly dispersed in this mixing zone. Upon mixing, solutes can be transferred from one phase to the other facilitating recovery. After mixing, the two-phase flow enters the inner rotating cylinder through an annular opening in the bottom. In this zone, the phases are separated by high centrifugal forces and each liquid leaves the device through tangential exit ports on top. Figure 1 shows a cutaway view of the centrifugal contactors used at Los Alamos National Laboratory for actinide recovery.

Our goal is to use the advanced multiphase flow simulation tools of T-3 to evaluate and optimize advanced designs for contactors of the Actinide Process Chemistry group (NMT-2). CartaBlanca is the multiphase flow solver used in this simulation.

As a first step, we simulate the hydraulics of the separation zone. Figure 2 shows a mesh of a quarter of the separation zone and a simplified outlet zone. In this simulation, the lighter fluid (fluid 2, organic) leaves through one small opening at the center of the outside wall of the central cylindrical region at the top. The heavier fluid (fluid 1, aqueous) leaves through another small opening, also at the center of the outside wall of the external cylindrical region at the top.

We studied the behavior of a mixture, with a ratio of organic to aqueous material equal to one, entering the device at a rate of 500 mL/minute. The density of the aqueous fluid is 1.025 g/cm³ and the density of the organic fluid is 0.8175 g/cm³. The drag time constant used in the calculation was 1.95e-3 seconds. This value was determined by empirically matching experimental data.

Figure 3 shows the aqueous phase density distribution on a plane through the center of the quarter mesh for the rotor speeds of 500 rpm, 1000 rpm, 1500 rpm, and 3000 rpm.

Figure 1—
Cutaway view of the centrifugal contactors used at Los Alamos National Laboratory for actinide recovery.

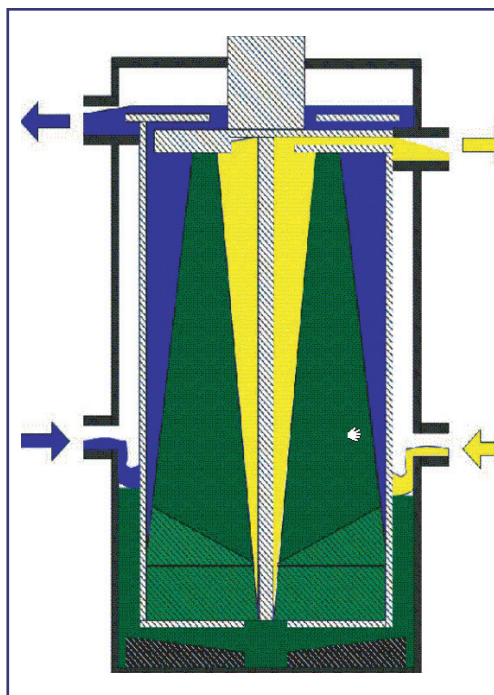
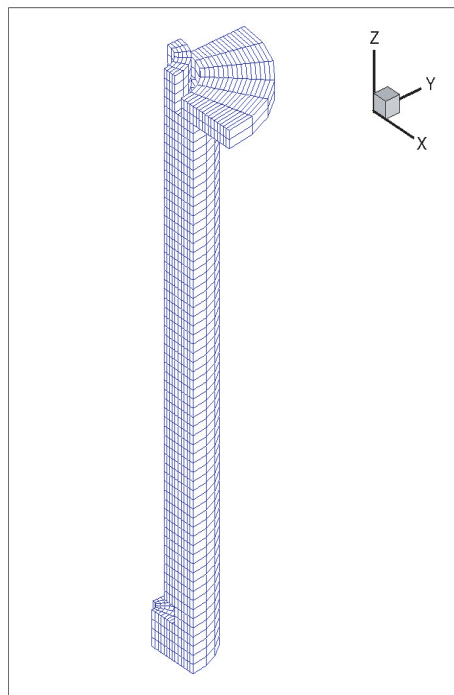


Figure 2—
Mesh of the separation zone.



As the rotation rate is reduced, the effective separation diminishes as expected. At 500 rpm, it is possible to see a cone-like density distribution seen also in the idealized drawing in Fig. 1.

In Table 1, we show the contamination of both phases when they leave the device.

| Rotor Speed (rpm) | Organic Phase in Aqueous Stream | Aqueous Phase in Organic Stream |
|-------------------|---------------------------------|---------------------------------|
| 500 | Less than 0.01% | Up to 40% |
| 1000 | Non-discernible | Up to 15% |
| 1500 | Non-discernible | Up to 4% |
| 3000 | Non-discernible | Less than 0.4% |

Table 1—
Phase contamination at the outlets.

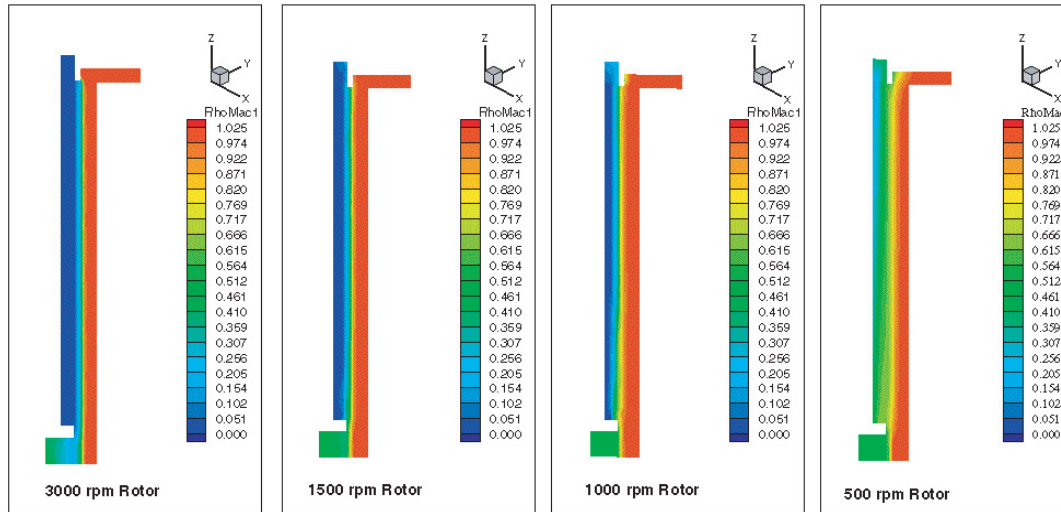


Figure 3—
Aqueous phase density for different rotor velocities.

This table compares qualitatively with the experimental data collected in the Nuclear Materials Technology (NMT) laboratories. These results are encouraging to us, as they seem to show that we have captured the essence of the hydraulic phenomena of the separators in a three-dimensional simulation. As noted in previous reports, we have built into our simulation the capability to simulate the mass transfer of solute between phases and the ability to represent internals such as vanes using a particle technique. We believe that we can continue our progress toward a journal publication detailing our results and further refinements of our simulation capabilities ultimately to provide a tool for process and unit optimization.

For more information, contact
Nely T. Padial-Collins (nelylanl@lanl.gov).

Acknowledgements

We would like to acknowledge the LANL Materials Stabilization Project for financial support.

The Effect of Initial Conditions on the Turbulent Rayleigh-Taylor Flow

Praveen Ramaprabhu (CNLS),
Guy Dimonte (X-4), and
M.J. Andrews (Texas A&M University)

The interface between two fluids of different densities is Rayleigh-Taylor (RT) unstable, if the light fluid accelerates the heavy. This means that small disturbances with a periodicity λ , present at the interface, grow exponentially in time. When these disturbances grow to be large, their growth rate can no longer be sustained, and their velocities saturate to a constant value, proportional to λ . Physically,

the flow is comprised of *bubbles* of light fluid penetrating the heavy, while the finger-like structures of the displaced heavy fluid are referred to as *spikes*. If a glass filled with water is suddenly overturned, the air *bubble* rises along the center, while the displaced water escapes along the sides of the glass in the form of *spikes*. Such instabilities can be observed in the remnants of supernovae, effluent discharge into rivers and estuaries, and during the implosion phase of the inertial confinement fusion process, where the RT-driven mixing reduces the thermonuclear yield. Central to the control of RT-driven flows in such applications is an appreciation of the role of initial conditions on the late-time dynamics. We have studied this problem using carefully formulated high-resolution numerical simulations of the turbulent RT flow.

If a spectrum of modes is present at the interface, we may expect nonlinear interactions between modes, resulting in a proliferation of scales and turbulence (Fig. 1). Furthermore, this flow is self-similar because the dominant lengthscale of the flow at any instant is not externally imposed, but generated from either (a) the coupling of short-wavelength modes (also called “bubble merger”), or (b) from the growth and saturation of individual modes in the initial spectrum (“bubble competition”). A recent bubble model [1] proposes that in the first scenario, the growth rate of the flow is independent of the initial conditions, because the dominant lengthscales are formed out of the merging of two or more bubbles, which were in turn generated in the same way. Thus, the flow is primarily dominated by intrinsic scales, which can develop from a narrow-band spectrum of modes. Conversely, in the second scenario, successively longer wavelengths are “sampled” from the modes present in a broadband initial spectrum, causing the flow to remain sensitive to the initial amplitudes of modes. Our high-resolution simulations [2, 3] initialized to evolve through both these routes, validate these ideas (Fig. 2).

Furthermore, as seen in Fig. 2, the bubble merger process represents a lower-bound limit in the value of the turbulent growth rate α . We believe this explains the long-standing discrepancy in the values of α

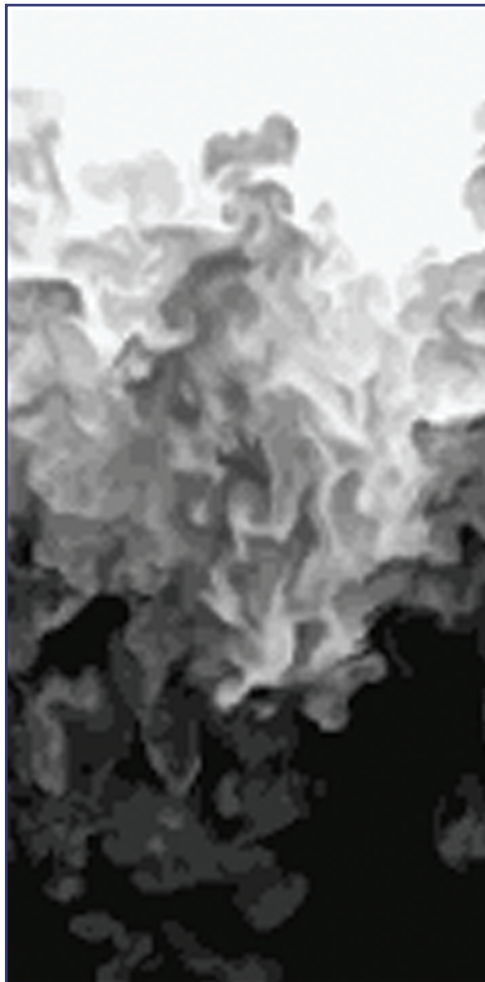


Figure 1—
Vertical slice from
3D simulations of
turbulent RT, showing
leading bubbles
(center of image)
penetrating the heavy
fluid.

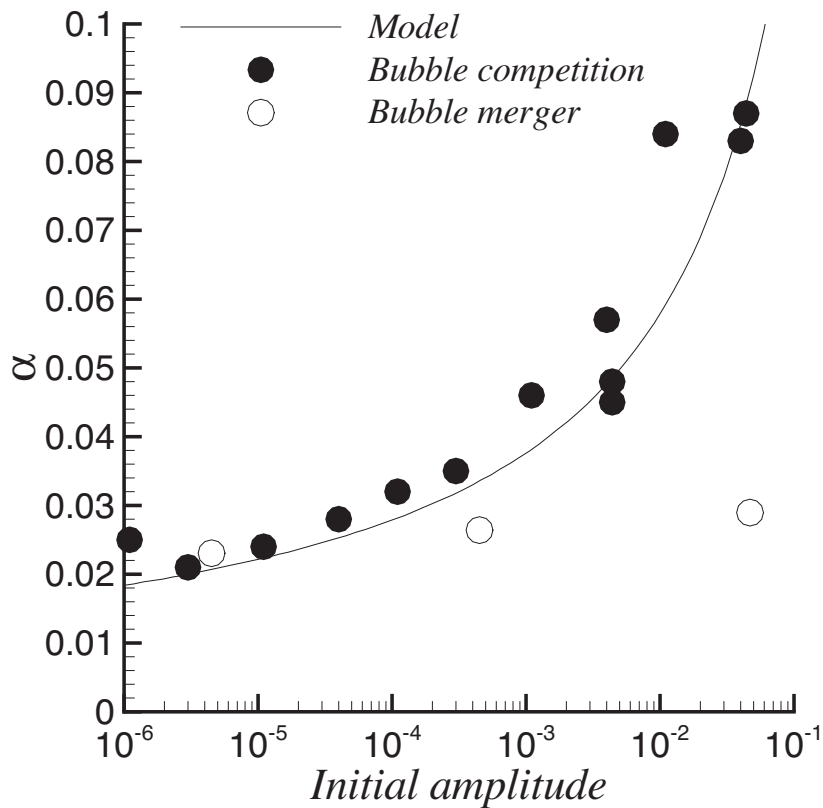


Figure 2—
Comparison of growth rates α from simulations and the bubble model of [1]. Open circles represent the bubble merger cases that are insensitive to initial amplitudes.

from experiments and numerical simulations; experiments have reported α values that are higher by 100% than the values obtained from numerical simulations. This is because numerical simulations are initialized with a narrow-band annular spectrum, and consequently evolve according to (a), while experiments have a broadband distribution of modes, imposed due to laboratory conditions, and evolve through (b). These ideas may be used in devising effective control strategies for the turbulent RT flow.

[1] Guy Dimonte, *Phys. Rev. E* **69**, 056305 (2004).

[2] Guy Dimonte et al., *Phys. Fluids* **16**, 1668 (2004).

[3] P. Ramaprabhu, Guy Dimonte, and M.J. Andrews (submitted to *J. Fluid Mech.*).

For more information, contact
Praveen Ramaprabhu (praveen@lanl.gov).

Nuclear Weapons Effects: Agent Defeat Simulations

Manjit S. Sahota, Rick M. Rauenzahn, and W. Brian VanderHeyden (T-3), and Merri M. Wood-Schultz (X-2)

We performed several nuclear weapons effects simulations for neutralizing chemical agents through nuclear detonations. These calculations involved performing coupled radiation-hydrodynamics calculations in an implicit manner in the presence of multiple materials requiring complex equations of state. Figure 1 shows a 1.5-kT earth penetrator at detonation inside an underground bunker (modeled as a sphere) and the blast wave at 8 μ s after detonation. This part of the blast wave calculation was done in Lagrangian mode as a separate component by resolving a three-dimensional (3D) sphere. The results of the calculation were then mapped onto the full system grid. Merri Wood-Schultz had earlier observed that the radiation from such a small detonation never escapes the blast wave because of very high opacity of iron. This calculation confirms her finding.

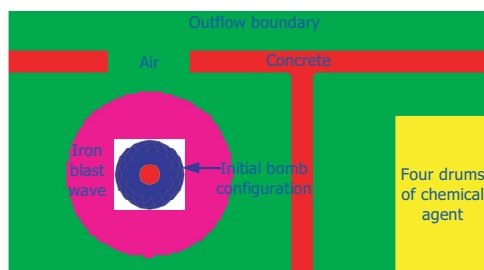


Figure 1—
A ground-penetrated 1.5-kT nuclear detonation inside an underground storage room. The pink (large) sphere shows the location of the blast wave at 8 microseconds. All radiation energy for such a small yield remains confined within the blast wave and does not directly contribute towards the agent's destruction.

Figure 2 shows the bunker geometry just at the time of the impact of concrete with the chemical agent (at 51 μ s after the detonation). Shortly after the impact, a strong shock propagates through the agent and results in sustained temperature (for several hundred μ s) exceeding 10,000 K that is sufficient to completely destroy the agent.

We are currently performing similar agent-defeat calculations on a much larger scale involving hundreds of agent drums stored inside storage sheds above ground. Figure 3 shows the vorticity plots at three different times for an above-ground explosion of the same 1.5 kT device in an area the size of a football field containing two storage sheds, one containing 100 55-gal. drums containing solid radioactive waste, and the other one containing 100 55-gal. drums containing a chemical agent. Only the right bottom part of the mushroom cloud is visible in the figure because the rest of the cloud already has escaped the problem domain. The calculation indicates a significant amount of turbulence is being generated even before the cloud starts interacting with the structures. Because of the size of the problem, it is not possible to calculate this turbulence through direct numerical simulation even on our massively parallel supercomputers. We plan to invoke turbulence transport models available in our code to capture the effects of this turbulence. Only an implicit multimaterial shock hydrodynamics code that solves the full Navier-Stokes equations could realistically be expected to perform such calculations. We have this unique capability.



Figure 2—
Bunker wall and agent geometry just before the concrete wall impacts the agent (at 51 μ s after the nuclear detonation).

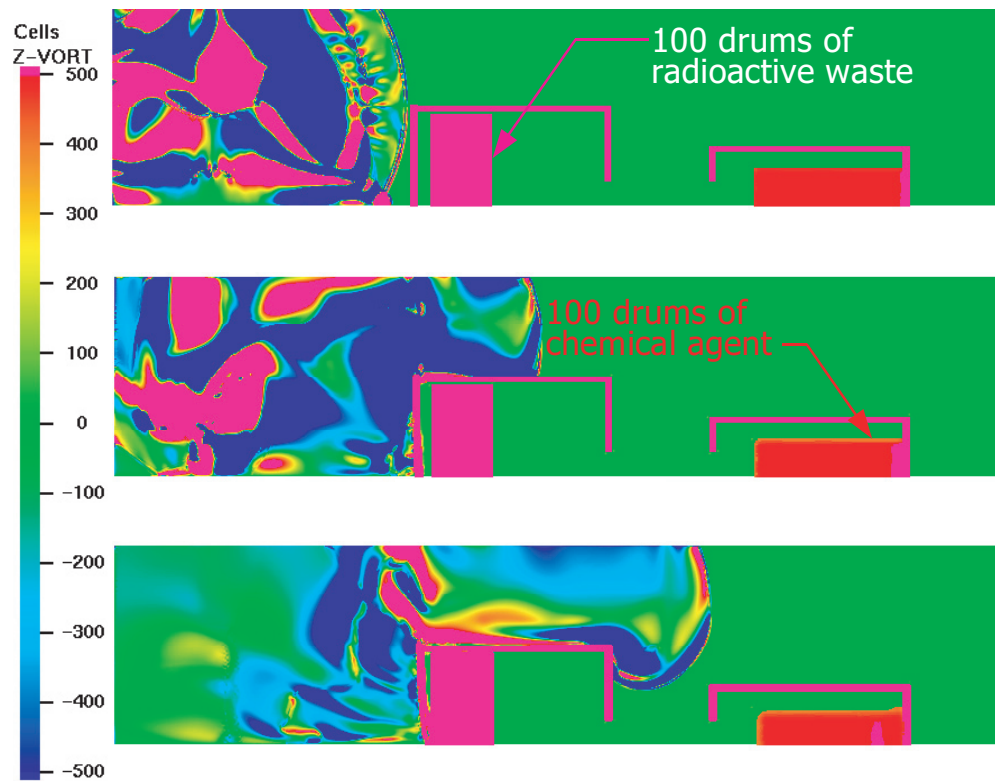


Figure 3—
Color-coded vorticity contours in the right bottom part of the mushroom cloud following an above ground 1.5-kT nuclear explosion.

We also performed detailed 3D coupled radiation-hydro calculations simulating a 10 kT nuclear detonation inside the U16B tunnel at the Nevada Test Site (Fig. 4). The mountain above the tunnel was modeled also to include the effects of fluid-structure interaction. A detonation of about this magnitude was found necessary for radiation to penetrate through the entire length of the tunnel indicating that such yields might be necessary to guarantee agent destruction stored inside large tunnel complexes.

For more information, contact
Manjit S. Sahota (sahota@lanl.gov).

Acknowledgements

Funding for this work was provided by the Principal Associate Director for Nuclear Weapons under the Advanced Concepts Program.

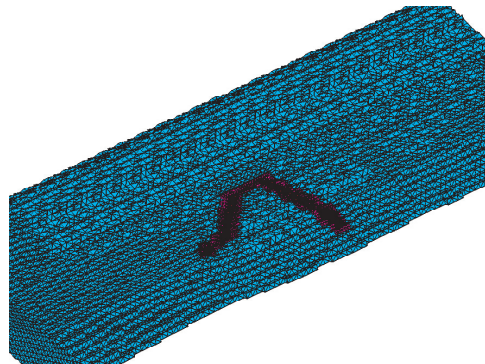


Figure 4—
U16B tunnel including the mountain above the tunnel. Part of the mountain is stripped off in this figure to make the tunnel visible.

Parallel Epic Porting, Simulations, and Performance

Manjit S. Sahota, Eric N. Harstad, and Paul J. Maudlin (T-3); Thomas A. Mason (MST-8); and Eric M. Mas (T-1)

We ported and investigated the parallel performance of a parallel version of the Epic code to Los Alamos National Laboratory (LANL) computers. This required extensive debugging of the existing code and numerous code modifications and model improvements especially related to the TEPLA model.

Figure 1 shows Epic simulations of a miniature-detonator experiment conducted at LANL (a tantalum cylinder driven by a cylinder of PETN high-explosive detonated at the center of the outside surface) using a single processor and 21 processors on SGI Origin 2000. The 21-processor calculation has much higher mesh resolution, but the two calculations show about the same results indicating that the lower-resolution single-processor calculation is fully converged.

The agreement between these calculations and the experimental data also was observed to be excellent. Because of the complex eroding slide line logic in Epic, the net Epic speedup (after accounting for higher mesh resolution and increased number of cycles) on 21 processors was observed to be only about a factor of 10. However, without the use of parallel computing, such a study would have been much more inconvenient because it would have taken about 12 days to complete the fine-mesh calculation on a single processor of SGI Origin 2000 (as compared to little over a day in parallel mode).

Epic parallel performance is much better than the foregoing example when there are no eroding slide lines in the problem. Figure 2 shows normalized Epic speedup with increasing number of processors for a shear-localization experiment. The speedup is almost linear with the increasing number of processing elements (PEs) before it saturates at an element/PE ratio of about 1000 when the computational load on each PE starts to become much smaller than the communication cost.

We are currently in the process of porting and assessing Epic's performance on the Linux clusters.

For more information, contact
Manjit Sahota (sahota@lanl.gov).

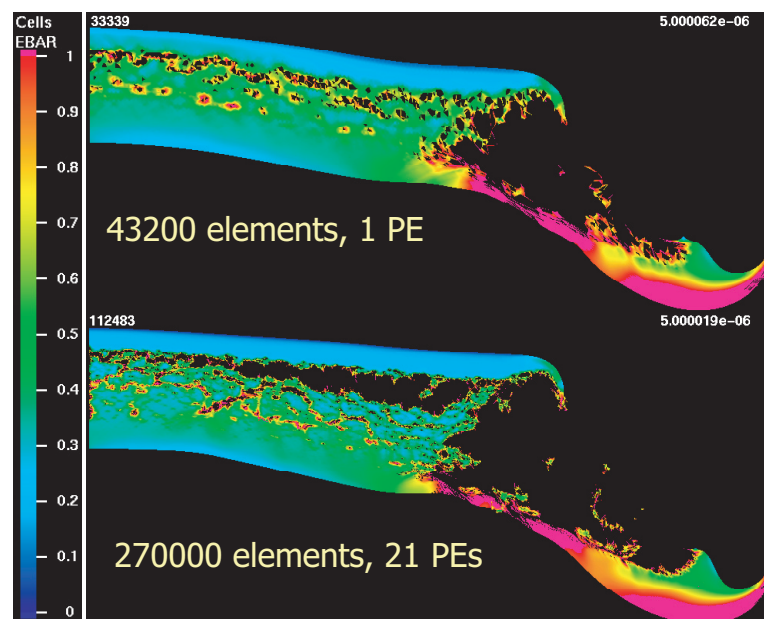


Figure 1—
Comparison of serial and parallel Epic calculations showing the color-coded contours of equivalent plastic strain for a miniature-detonator experiment.

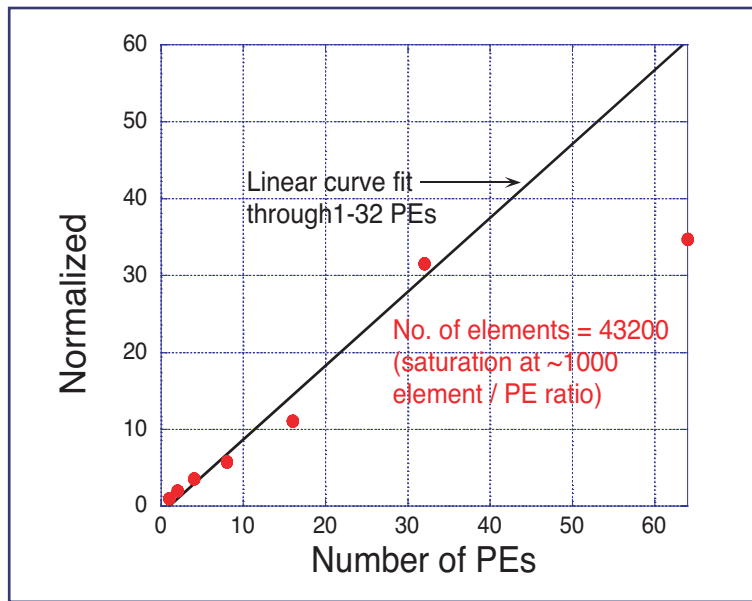


Figure 2—
Epic parallel performance on SGI Origin 2000 for shear-localization experiment. The calculation used 43,200 elements and required no eroding slide lines.

Acknowledgements

We would like to acknowledge NNSA's Advanced Simulation and Computing (ASC), Materials and Physics Program, and the Joint DoD/DOE Munitions Technology Development Program for financial support.

High-Explosive Safety Study Update

Qisu Zou, Duan Z. Zhang,
W. Brian VanderHeyden, and
Nely Padial-Collins (T-3)

We investigate nonshock initiation of high explosive (HE) material. Currently we focus on the effects of sand grits on the surface in contact with HE. Theoretical models about frictional heating, subgrid ignition have been developed and implemented into a general multipurpose Computation Fluid Dynamics code called CartaBlanca. A particle-in-cell method is used to model the solid HE with mechanical strength. Chemical reactions, gas generation, and mechanical and thermal interactions between the solid HE and gas are considered by solving appropriated equations numerically. Simulations are performed for the Dyer and Taylor experiment and the drop-skip experiment (Figs. 1 and 2).

It is believed that in both of the experiments, the ignition is caused by the heating from grit sliding on a surface. A grit-sliding friction temperature model is developed to describe this process. The model is based on the following picture: a particle of grit is embedded in a HE and is sliding on a plate surface. Heat is generated from the friction and also carried away by the plate. When the melt temperature of the HE is reached on

the grit, the surrounding HE of the grit melts and some liquid HE is getting into the contact surface gradually. Thus, some time (delay time) after the melting temperature is reached, the friction coefficient between the grit and the plate is reduced significantly due to the lubricating effect, and temperature drops. The time-delay effect on the melt-lubrication is a key element in the model. The modeled grit temperature is a function of time and is dependent on the material properties, the sliding velocity, the contact pressure, and the grit size. Besides, a model coefficient is used so there are two adjustable parameters in the model: the grit size and the model coefficient. A typical temperature profile is shown in Fig. 3. The red line is the temperature with consideration of delay time in the melting. A temperature peak is seen in the figure. The deep drop in temperature is the result of melting. We believe that the temperature peak is the reason for ignition. The black line in Fig. 3 is the grit temperature without considering the time-delay effect on the melt-lubrication and it does not have a temperature peak. The time-dependent grit temperature can serve as a sub-grid model in a macroscopic finite-element or finite volume simulation for the prediction of explosion. Our simulations gave reasonable results on the ignition result and the ignition time for both the experiments with a minimum of parameters.

Our simulation also indicates that gas motion is important in certain aspects like hot-spot interactions. When the plate is sliding under the HE, the bottom layer of the HE heats up and may melt, hot spots with higher

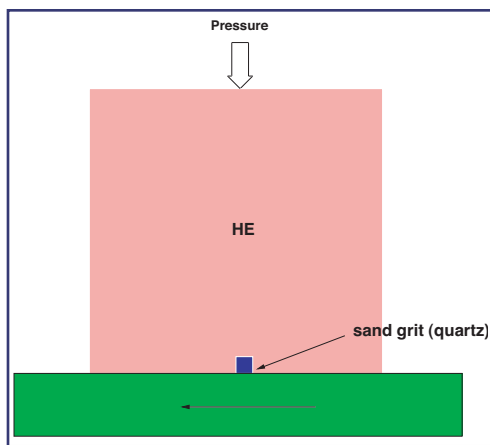


Figure 1—
The Dyer and Taylor experiment.

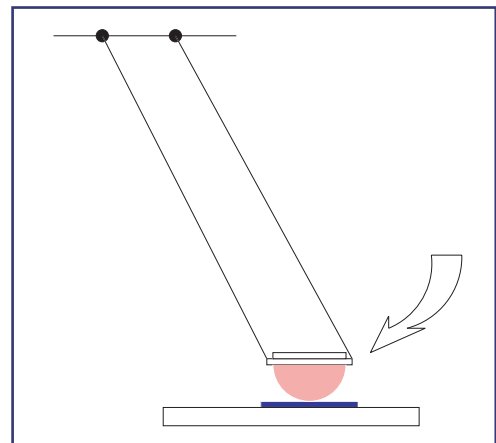


Figure 2—
The drop-skid experiment.

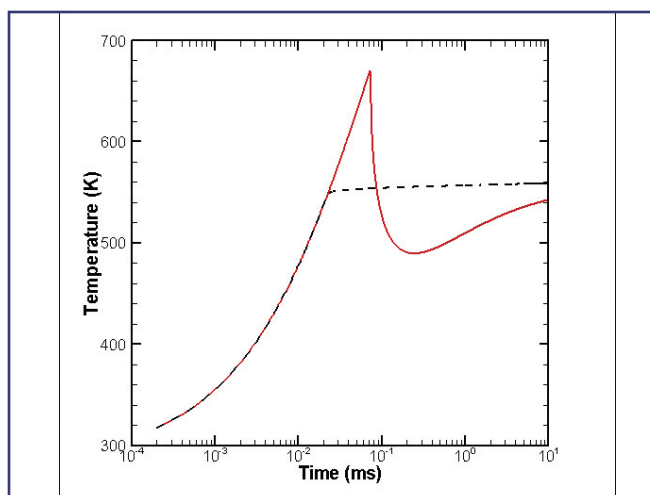


Figure 3—
Grit temperature development based on the friction ignition model.

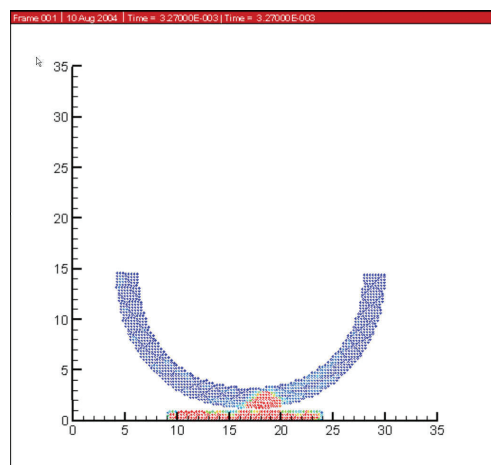


Figure 5—
A snapshot of the drop-skid simulation.

temperature are also generated around sand grits, and chemical reaction can generate some product gas near the hot spots. The liquid HE, together with the gas, is carried downstream by the sliding plate and heating up the HE downstream. Thus, the hot spot downstream will have a higher temperature, enhances the tendency of explosion. Figure 4 is a comparison of results with one hot spot and two hot spots in the Dyer and Taylor experiment. A solid phase (HE) and a gas phase (product gas from HE reaction) are used in the simulation. The plots are the

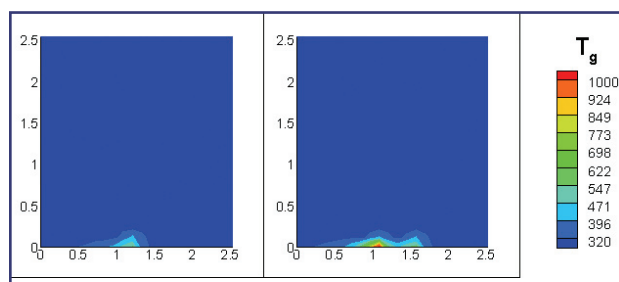


Figure 4—
Comparison of one and two hot-spots.

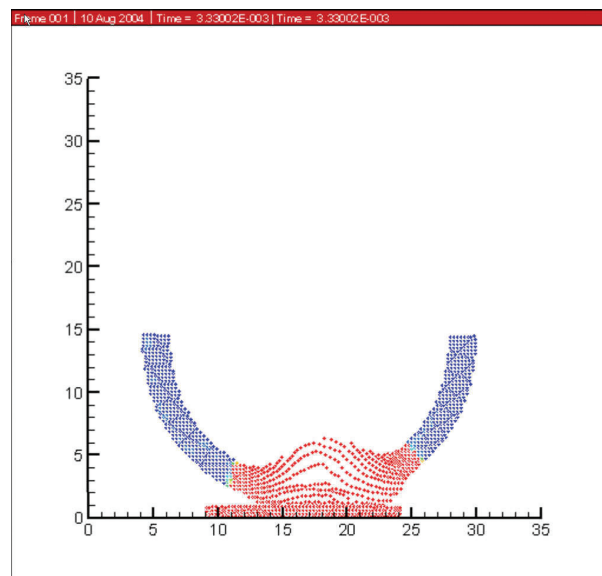


Figure 6—
A snapshot of the drop-skid simulation.

gas temperature at the same time for one initial hot spot (left) and for two initial hot spots (right), which eventually leads to an explosion.

Currently we are studying the pressure-dependent reaction, which may explain the quenching effect due to gas leakage. Two snapshots of the 2D drop-skid simulation are in Figs. 5 and 6, which show a partial break of the HE.

For more information, contact Qisu Zou
(qisu@lanl.gov).

Acknowledgements

We would like to acknowledge NNSA's Advanced Simulation and Computing (ASC), Materials and Physics Program, and the Joint DoD/DOE Munitions Technology Development Program for financial support.

Nano-hydrodynamics Simulations: An Atomistic View of the Raleigh-Taylor Instability

Kai Kadau (T-14), Timothy C. Germann (X-7), Peter S. Lomdahl (T-11), Brad L. Holian (T-12), Guy Dimonte (X-4), Nicolas G. Hadjiconstantinou (Massachusetts Institute of Technology), and Berni Alder (Lawrence Livermore National Laboratory)

The Rayleigh-Taylor (RT) instability occurs when a heavy fluid lies on top of a light fluid in the attendance of a gravitational field g ; the fluids will subsequently mix in a more or less turbulent process. Its relevance ranges from astrophysical supernova explosions, to

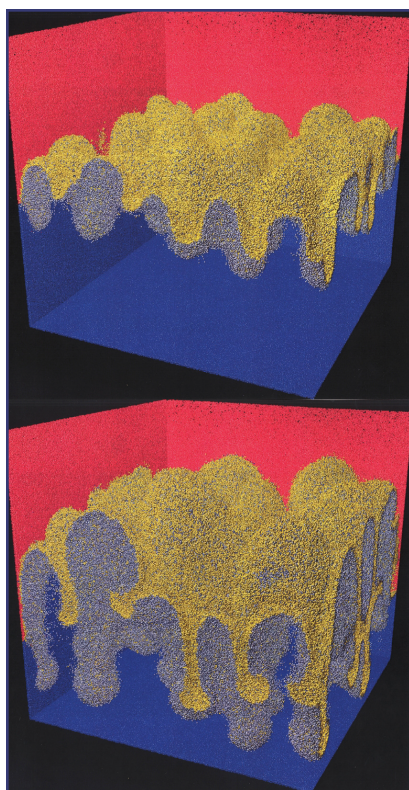
geophysical formations like salt domes and volcanic islands, all the way down to inertial confinement fusion, as well as to the general turbulent mixing of fluids.

Molecular dynamics simulations have been performed on RT instability as an example and validation of nanohydrodynamics [1]. The R-T simulations require a large number of particles in an MD calculation to resolve fluid structures at late times, as well as the imposition of an enormous gravitational field, in order to reduce the most unstable wavelength to the nanoscale, as well as to mix the fluids on the nanosecond time scale. This most unstable mode of wavelength λ must be several times smaller than the width of the simulation cell in order to develop several bubbles and spikes. From linear stability analysis, the most unstable wavelength decreases with increasing g , and thus a value of g approximately 10 billion times larger than the gravity on Earth is required. Whether such a large g distorts the instability process depends on whether g is a scalable variable up to that magnitude, which can be validated by comparison to experiment and to continuum descriptions of the hydrodynamical problem as described by the Navier-Stokes (NS) equations, which assume scalability.

Using 1600 CPUs of the Advanced Simulation and Computing (ASC) Q computer system, we simulated 100,589,840 atoms (Fig. 1) for 250,000 integration time steps (400,000 CPU hours) with the Scalable Parallel Short-range MD (SPaSM [2]) code. Smaller simulations were performed on the ASC QSC computer system (1024 CPUs), and a 256-CPU Linux cluster (Grendels). The simulations presented here needed an estimated total of 600,000 CPU hours. Accounting for different processor speed on the used systems this is more than a week on all 4096 CPUs of the ASC Q computer system.

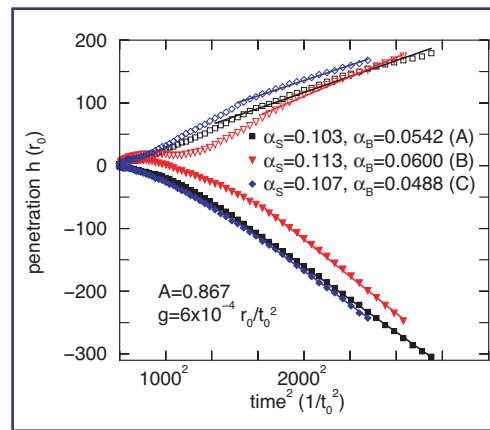
The growth from an interface perturbed only by fluctuations was found to be dominated quickly by the wave number corresponding to linear stability analysis, which then determines the initial number of bubbles and spikes (Fig. 1). For example, the fully 3D system should, according to linear stability analysis, have 3.5 spikes along the edge of the simulation cell, while actually 4 were observed at early times. In some cases

Figure 1— Rayleigh-Taylor mixing of 100,589,840 atoms by molecular dynamics of a heavy fluid (red/yellow spheres) on top and a light fluid (blue/gray spheres) below, under the influence of a gravitational field. The predicted most unstable mode emerges quickly for an interface initially perturbed only by thermal fluctuations (upper panel, time = 18t0). Spikes and bubbles grow mushroom caps and start to interact with each other (lower panel, time = 24t0). Only atoms at the interface of the two fluids are shown (yellow/gray), red and blue atoms mark the boundaries of the simulation box.



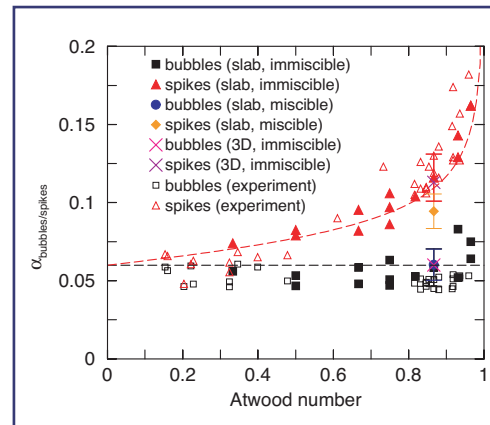
the deviations from the theoretically most unstable mode predictions were larger due to the presence of multiple modes and the finite edge length. At later times the spikes and bubbles develop mushrooms at their tips, which eventually interact and merge in a process that can be described as turbulent (see movie on the Web [1]). The penetration distance h of the spikes and bubbles is characterized at long times by the coefficient α (Fig. 2). Somewhat surprisingly, there was no statistically significant difference between the average value of α , as determined from the large number of simulations done with a slab geometry at Atwood Number $A = 0.867$ and a single fully 3D system. The growth of the bubbles and spikes as given by the value of α determined by the simulations were found to agree with experiment as well as Youngs' theoretical model (Fig. 3). This remarkable quantitative agreement with experiment at late times (in the turbulent regime) is a significant validation of nanohydrodynamics. At the longest time of penetration of the spikes in the simulations, the depth reached 30% of the experimental value, measured in terms of the most unstable wavelength. Different continuum hydrodynamic calculations show a range of α values for bubbles between 0.03 and 0.08, compared to an experimental range of 0.05 to 0.08.

With MD simulation it is possible to quantitatively determine how α depends on initial conditions, such as the surface tension and imposed disturbances. It was found that the α values of the spikes in the miscible case are reduced compared to the immiscible case at high Atwood number. In the miscible case, the interface gets blurred by diffusion. This can be interpreted as a reduction of the effective Atwood number, leading to a reduction in the α of the spikes but not bubbles, since their α value is nearly independent of A . It was also found that an initial single-mode perturbation of the interface enhances the mixing process at short times—an effect also observed experimentally. However, at distances large compared to the initial perturbing mode, the effect is washed out, and α is similar to the value from a fluctuation-perturbed



interface. This suggests a memory loss about the initial perturbations in time in the atomistic simulations due to the chaotic nature of the underlying equations of motions.

- [1] K. Kadau, T.C. Germann, P.S. Lomdahl, B.L. Holian, Guy Dimonte, Nicolas G. Hadjiconstantinou, and Berni Alder, *PNAS* **101**, 5851 (2004).
- [2] P.S. Lomdahl, P. Tamayo, N. Gronbech-Jensen, and D.M. Beazley, *Proceedings of Supercomputing* **93**, G.S. Ansell, Ed. (IEEE Computer Society Press, Los Alamitos, CA, 1993), p. 520.
- [3] G. Dimonte and M. Schneider, *Phys. Fluids* **12**, 304 (2000).



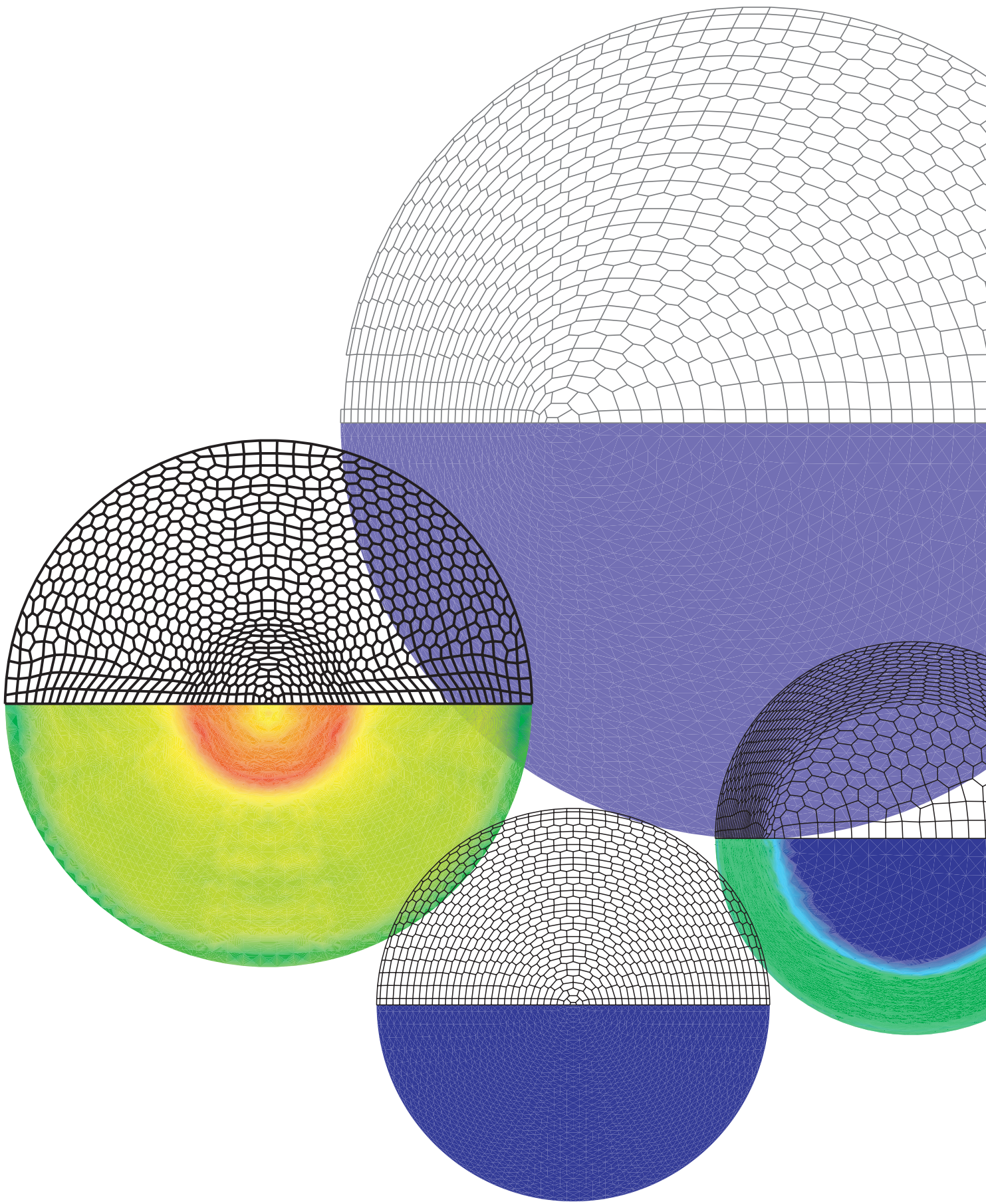
For more information, contact Kai Kadau (kkadau@lanl.gov).

Acknowledgements

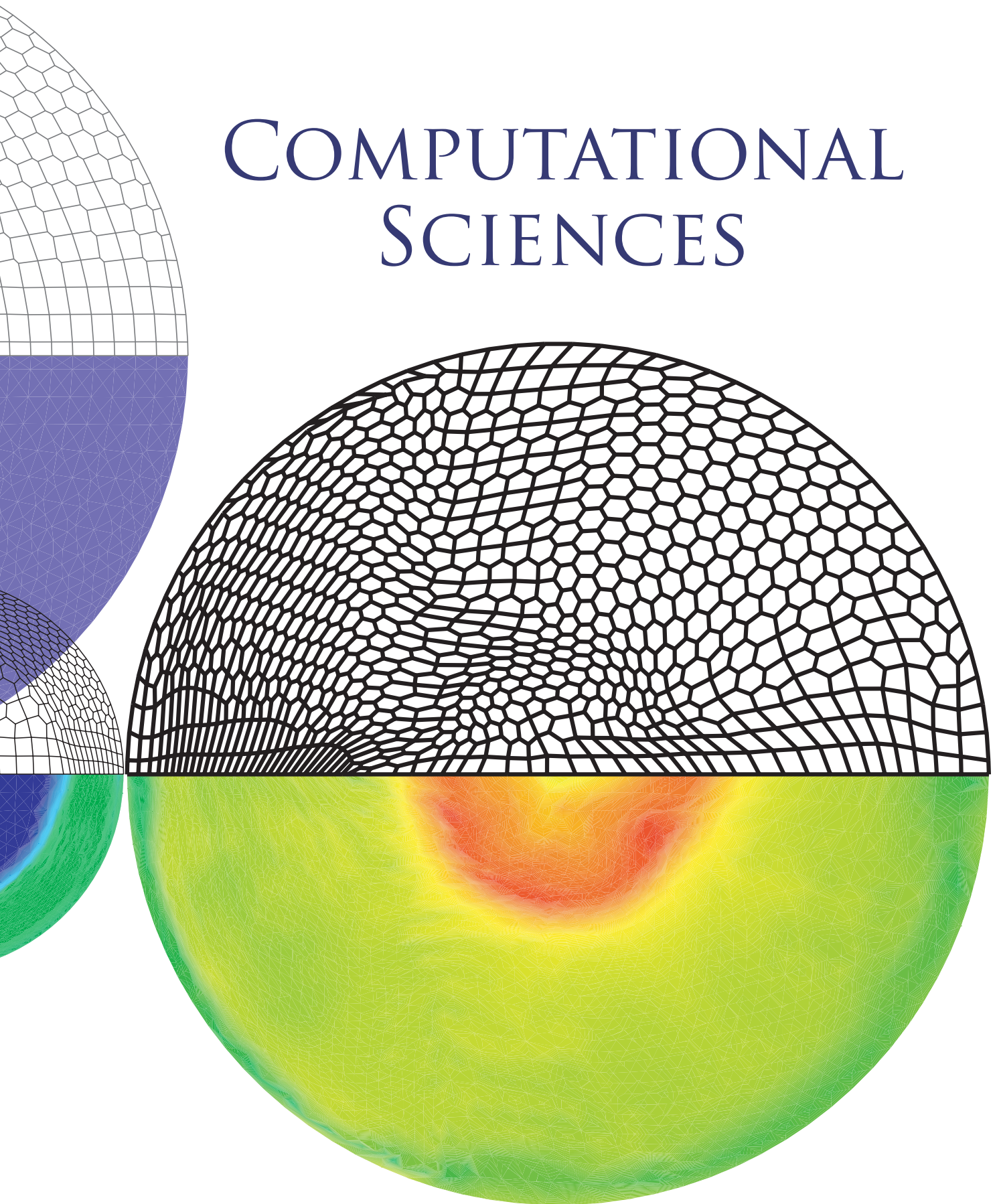
We would like to acknowledge NNSA's Advanced Simulation and Computing (ASC), Materials and Physics Program for financial support. Some specific portions of the research reported here were supported by LDRD.

Figure 2— Penetration h of bubbles (open symbols) into the heavy fluid and spikes (closed symbols) into the light fluid as a function of the square of the time at Atwood number. The long-time slope of the growth rate α (solid lines) of the thin slab (A: black squares) and the fully 3D MD simulation (B: red triangles) are, to within statistical error, the same. An initial single mode perturbation with wavelength $l = 70r_0$ and amplitude $d = 0.02l$ (C: blue diamonds) does not change the long-term slope. However, when l is not small compared to the system height $H = 612.5r_0$ (and thus the fall height of spikes and bubbles) the mixing can be enhanced (not shown).

Figure 3— The α values for various Atwood numbers A from MD simulations compared to experimental data [3], and Youngs' model with $C = 3.67$ (dashed lines). For large A , α approaches the free fall value of 0.5 at $A = 1$. At $A = 0.867$, 3 miscible and 19 immiscible simulations were made and the error bars indicate the standard deviation, rather than the smaller confidence interval.



COMPUTATIONAL SCIENCES



Accelerated Inexact Newton Method for Casting Simulations

Andrew P. Kuprat (T-1)

This year T-1 implemented a fast nonlinear solver in the 3D Truchas casting simulation code. Truchas is the main product of the ASC-funded TELLURIDE project (a collaboration involving MST, CCS, T, and other divisions). Truchas simulates the entire casting process: flow of molten alloy, heat transfer, solidification of alloy, induced stresses, etc.

Truchas has to solve for the heat transfer and elastic displacement fields at each time step, and for both of these fields this amounts to solving a large nonlinear system of equations

$$\mathbf{f}(\mathbf{x}) = \mathbf{0},$$

where $\mathbf{f}(\mathbf{x})$ and \mathbf{x} are vectors with dimension of order the number of cells in the simulation—typically hundreds of thousands.

The classic Newton iteration to solve this problem could be written as

$$\begin{aligned} \text{Do until done} \\ \mathbf{u}_i \leftarrow \text{IJ}[\mathbf{f}(\mathbf{x}_i)] \end{aligned}$$

$$\mathbf{x}_{i+1} \leftarrow \mathbf{x}_i - \mathbf{u}_i$$

Here, $\text{IJ}[\mathbf{f}(\mathbf{x}_i)]$ means take the residual vector $\mathbf{f}(\mathbf{x}_i)$ and multiply it on the left by the Inverse of the Jacobian of \mathbf{f} evaluated at \mathbf{x}_i .

Although Newton's method has the advantage of being rapidly convergent in a neighborhood of the root, it is typically very expensive to evaluate the Jacobian matrix. Indeed, evaluation of the residual function $\mathbf{f}(\mathbf{x})$ and its Jacobian $\mathbf{f}'(\mathbf{x})$ may involve evaluating expensive "subscale" models. For example, if $\mathbf{f}(\mathbf{x})$ is the residual for heat transfer, it may require evaluation of a microscale phase change model if a casting is undergoing solidification. Evaluation of the Jacobian $\mathbf{f}'(\mathbf{x})$ will be in general even more expensive than evaluation of $\mathbf{f}(\mathbf{x})$ itself, and

so the classic Newton's method is seen to be relatively expensive.

In the 1990's, Carlson and Miller [1] designed a method, now called the Accelerated Inexact Newton (AIN) Method, that reduced or eliminated the need for evaluation of the exact Jacobian. This method can be described as

$$\begin{aligned} \text{Do until done} \\ \mathbf{u}_i \leftarrow \text{AIJ}[\mathbf{f}(\mathbf{x}_i)] \\ \mathbf{x}_{i+1} \leftarrow \mathbf{x}_i - \text{FPA}(\mathbf{u}_i) \end{aligned}$$

Here, $\text{AIJ}[\mathbf{f}(\mathbf{x}_i)]$ signifies application of an Approximate Inverse Jacobian matrix to the residual $\mathbf{f}(\mathbf{x}_i)$. This approximate Inverse Jacobian could be an "old" exact Inverse Jacobian evaluated at a point $\tilde{\mathbf{x}}$ close to but not necessarily equal to \mathbf{x}_i . In fact, the Approximate Inverse Jacobian may be the application of a "preconditioner" subroutine that doesn't correspond to any exact Inverse Jacobian evaluated at any point whatsoever. The reason this iteration converges is the presence of "FPA" which means "Fixed Point Accelerator."

FPA monitors changes in the inputs \mathbf{u}_i fed to it, and deduces ways to correct the \mathbf{u}_i 's in order for the composition $\text{FPA} \circ \text{AIJ}$ to produce corrections closer what would have been produced by the true Inverse Jacobian IJ if it had been available.

We have implemented the AIN method for heat transfer and thermomechanics solves, with the AIJ operations being "preconditioners" for the two respective systems. (The preconditioners amount to approximate evaluation of the Jacobian, and then a small number of sweeps of Symmetric Successive Over-Relaxation (SSOR), in order to approximately invert this approximate Jacobian.) The result of implementing the AIN method in Truchas has been a speed-up of the nonlinear heat transfer and thermomechanical displacement solves in both serial and parallel. Speed-ups of up to 4x have been observed when compared to the existing Newton-Krylov method used by the Truchas code. In Figs. 1 and 2, we see elastic displacement field components computed by the Truchas code.

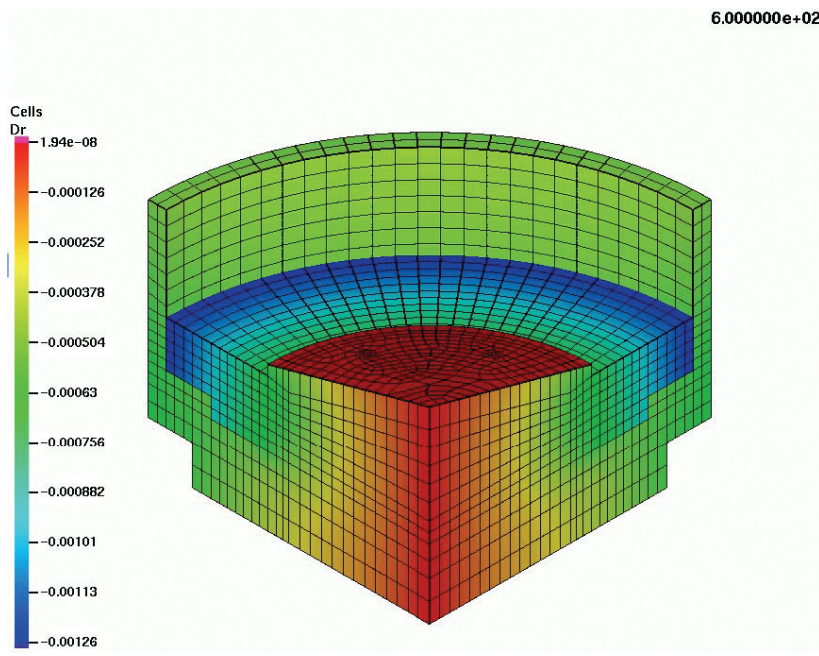


Figure 1—
Radial displacement
field computed by the
Truchas code on a
typical metal casting.
Courtesy Kin Lam,
ESA-WR.

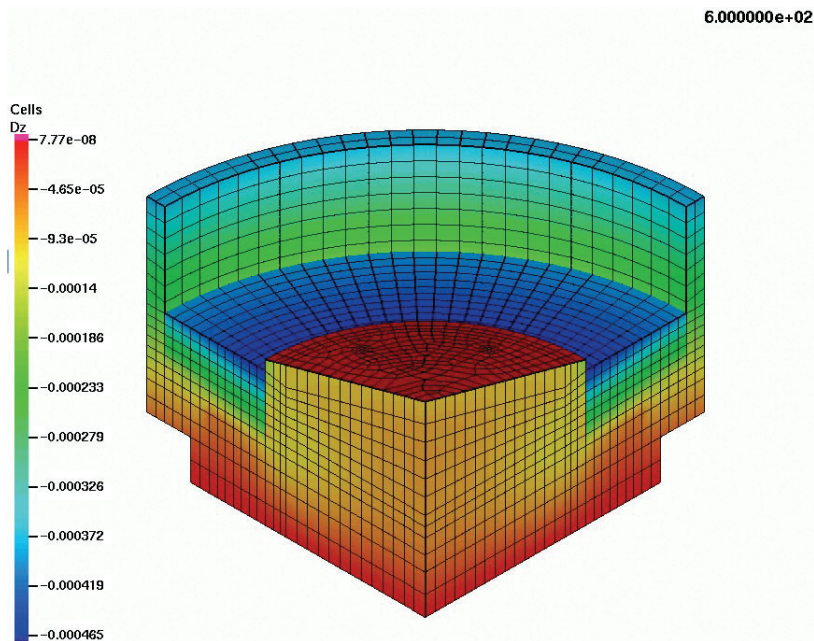


Figure 2—
Axial displacement
field, same casting.

[1] Neil N. Carlson and Keith Miller, “Design and Application of a Gradient-Weighted Moving Finite Element Code I: In One Dimension,” *SIAM J. Sci. Comput.* **19**, 3, pp. 728–765, 1998. (See Section 9.)

For more information, contact
Andrew P. Kuprat (kuprat@lanl.gov).

Acknowledgements

I would like to acknowledge NNSA’s Advanced Simulation and Computing (ASC), Advanced Applications Program for financial support.

A Memory Efficient Parallel Tridiagonal Solver

Travis M. Austin, Markus Berndt, and J. David Moulton (T-7)

Large tridiagonal systems of linear equations appear in many numerical analysis applications. In our work, they arise in line relaxations needed by robust multigrid methods, such as the parallel BoxMG code [1], for structured grid problems. We present a new memory-efficient partitioning algorithm for the solution of diagonally dominant tridiagonal linear systems of equations that scales well on distributed-memory parallel computers. Its multilevel recursive design makes it well suited for distributed-memory parallel computers with very large numbers of processors.

On a serial computer, Gaussian elimination without pivoting can be used to solve a diagonally dominant tridiagonal system of linear equations in $O(N)$ steps. This serial algorithm is commonly referred to as the Thomas algorithm [2]. Unfortunately, this algorithm is not well suited for parallel computers. The first parallel algorithm for the solution of tridiagonal systems was developed by Hockney and Golub. It is now usually referred to as cyclic reduction. Stone introduced his recursive doubling algorithm in 1973. Both cyclic reduction and recursive doubling are designed for fine-grained parallelism, where each processor owns exactly one row of the tridiagonal matrix. In 1981, Wang proposed a partitioning algorithm aimed at more coarse-grained parallel computation typical for shared memory clusters, where $N_p \ll N$. There has also been attention directed toward a parallel partitioning of the standard LU algorithm. In 1986, Sun et al. introduced the parallel partitioning LU algorithm that is very similar to Bondeli's divide and conquer algorithm. These algorithms, while well suited for problems distributed across a moderately large number of processors, do not scale well to very large numbers of processors.

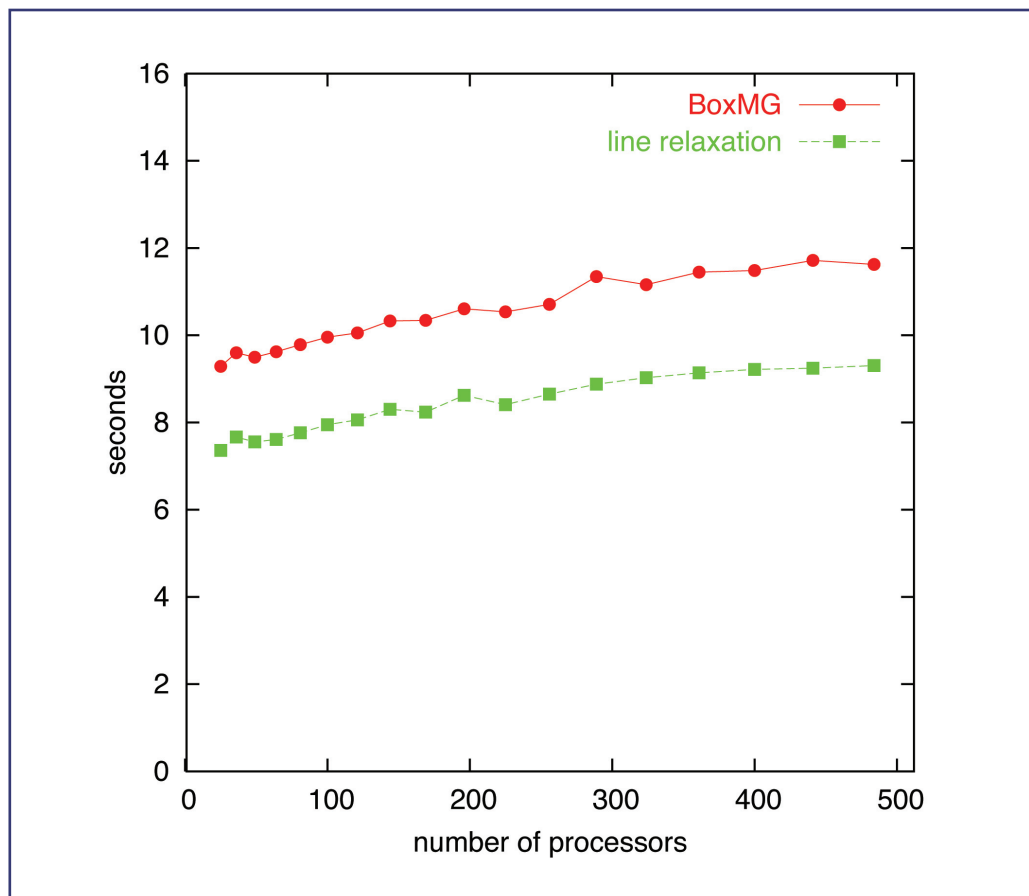
Our algorithm can be described as a recursion with a partitioning algorithm as its basis. We begin by describing this partitioning algorithm. The tridiagonal linear system is assumed to be distributed across a large number of processors, such that each processor owns a contiguous number of rows. Each processor transforms its piece of the tridiagonal matrix into a matrix with a sparsity pattern such as

$$A_{\text{local}} = \begin{pmatrix} \times & \times & & & & & \times \\ & \times & \times & \times & \times & & \\ & & \times & \times & \times & \times & \\ & & & \times & \times & \times & \times \\ & & & & \times & \times & \times \\ & & & & & \times & \times \\ & \times & & & & & \times \end{pmatrix}.$$

Gathering the first and last rows (red) from every processor yields an interface system that is again tridiagonal and diagonally dominant. This interface system can be solved by gathering all equations to one processor, using the Thomas algorithm there, and then scattering the solution back to all N_p processors. Then the interface unknowns can be eliminated from the local systems, yielding N_p local tridiagonal systems (blue \times 's). These local systems can be solved efficiently by the Thomas algorithm and do not require any further communication.

Although this nonrecursive single-level approach scales reasonably well for moderate numbers of processors, it does not scale well for very large number of processors: gather and scatter operations typically scale linearly with the number of processors. Our remedy is to gather only pieces of the complete interface system to a subset of all processors, such that each of these subset-processors owns a contiguous piece of the interface system. Then we apply the partitioning outlined above to each piece of the interface system. This yields a lower-level interface system on the subset of processors. We proceed with further recursion if the subset of processors is sufficiently large or solve the new interface system directly on one of the processors in the subset.

We describe our algorithm as memory-efficient because the partitioning step is organized such that the interface system is generated without overwriting the original tridiagonal system.



Efficient Smoothing of Unstructured Grids

Markus Berndt and
J. David Moulton (T-7)

The smoothing of unstructured grids in large-scale 2D and 3D simulations is a critical component of many projects related to the Advanced Simulation and Computing (ASC) Program. Many techniques have been developed to perform this smoothing, but few are capable of handling large unstructured meshes in complex geometries. For example, most smoothers generate unacceptable or even invalid grids in the neighborhood of extremely convex or concave boundaries. In contrast, a smoothing technique was developed [1, 2] that is robust with respect to these geometric complexities. This grid smoothing methodology is based on the concept of harmonic coordinates, and hence, has a natural variational formulation. Specifically, this formulation defines a system of quasilinear elliptic partial differential equations (PDEs) with one equation for each of the grid coordinates. The only coupling in this system arises through the components of the metric tensor, which plays the role of a diffusion tensor. Thus, the system may be described as a set of quasilinear diffusion equations with a solution-dependent diffusion tensor. The grid smoothing is driven by defining a target metric, which in 2D is based on a dual grid. Since the quasilinear system of PDEs arises naturally from a variational formulation, a standard vertex-based Finite Element Method (FEM) is used to discretize this nonlinear system.

The Newton-Krylov approach is used to solve the discrete nonlinear system of equations. Specifically, the exact Jacobian is formed at each iteration and this linear system is then solved iteratively with a preconditioned Krylov method for each Newton iteration. In this preliminary work we focus on improving the efficiency and scaling of this

approach. We comment on Jacobian-Free Newton-Krylov methods as well as other preconditioners in our conclusions below.

The exact Jacobian offers a significant challenge for iterative solvers. In particular it may be written in the form,

$$J = \mathcal{D} + \mathcal{N}$$

where \mathcal{D} is a symmetric block diagonal operator (the Picard linearization) and \mathcal{N} is nonsymmetric with no derivatives. The difficulty posed by this system is threefold. First the coefficients of entries in \mathcal{N} involve gradients of the current target metric tensor, and hence, can be either positive or negative. In addition, their magnitude may be large, implying strong coupling of the components. Finally, the exact Jacobian is nonsymmetric.

Thus far, our work has focused on evaluation of solver performance in the 2D research code that was developed for [1]. This code used BPKIT to provide a preconditioner comprised of Block ILU (1) in conjunction with two global passes of SSOR for FGMRES. While performance of this solver is adequate for small test problems, it is clear that it will not scale well enough to handle the large 2D and 3D problems of interest to the ASC program. In particular, the linear scaling in solution cost required by large-scale simulations can only be provided by robust multilevel solver and preconditioning algorithms. Thus, the primary objective of our preliminary investigation was to demonstrate that the nonsymmetric linear system involving the full Jacobian could be preconditioned effectively with the well-known Ruge-Stüben serial Algebraic Multigrid Solver (AMG). To this end we have provided the option to use AMG both as a linear solver and as a preconditioner for GMRES in this research code. It is important to note that this is the basis for the parallel Los Alamos Algebraic Multigrid (LAMG) solver by Wayne Joubert (LA-CC 03/107).

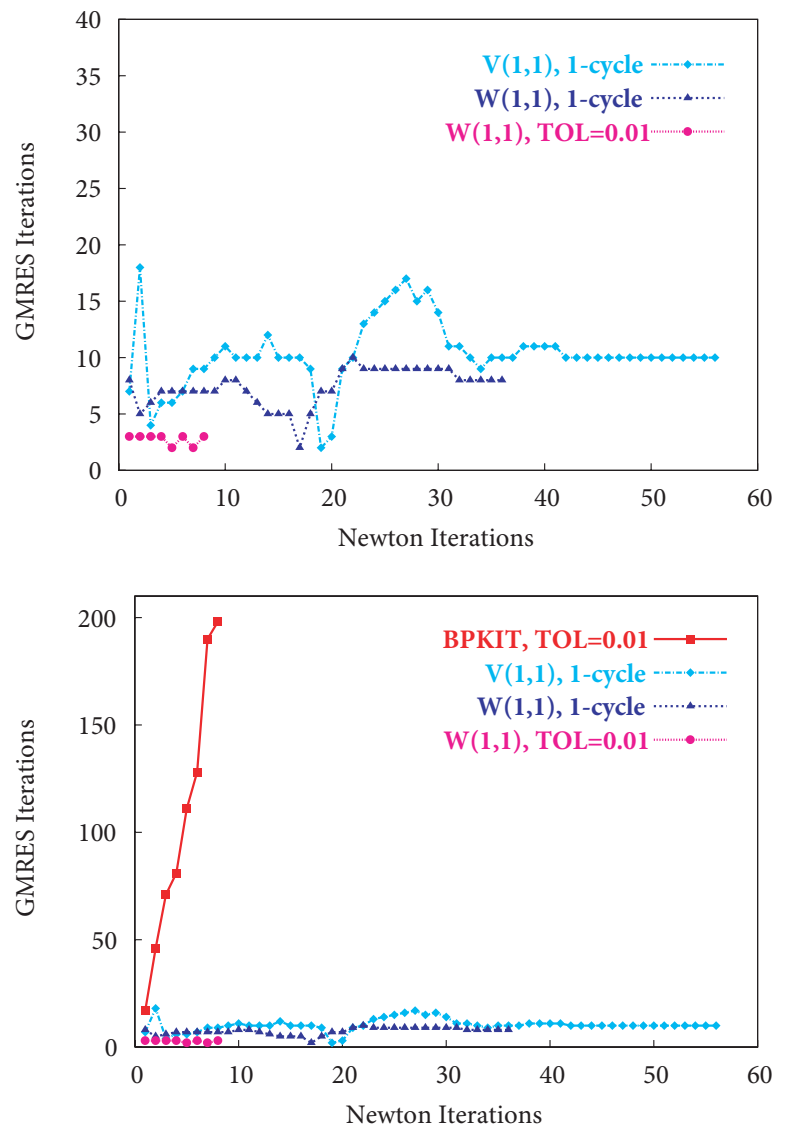
The preliminary performance study was conducted on a rectangular horseshoe domain with an initial grid defined by transfinite interpolation. This provided a logically rectangular grid of 64×64 points.

A relative convergence criterion for the Newton iteration of 10^{-6} in the two norm is used for all solvers. The performance of AMG as a preconditioner is quite impressive, with a bounded number of iterations per Newton step for both single V(1,1) and W(1,1) cycles, as well as for the more practical W(1,1) cycles, that used a relative convergence criteria of 10^{-2} . This is clearly shown in the top figure, while the comparison with the BPKIT preconditioner is shown in the bottom figure. Most notably, for the BPKIT preconditioner the number of GMRES iterations/Newton iteration increases linearly as the Newton iteration converges. In addition to this poor scaling it is important to note that BPKIT preconditioned GMRES iterations will grow with increasing grid size, while the number of AMG preconditioned GMRES iterations should remain constant with increasing grid size.

This preliminary study has demonstrated the significant gains in efficiency that are possible by using advanced solvers such as AMG preconditioned GMRES. In particular, we have developed a solution algorithm that should scale linearly with the number of grid points. In the near future we hope to conduct more detailed scaling and robustness studies. In addition, future work will consider using the Jacobian-Free approach in conjunction with the use of the Picard linearization, \mathcal{D} , as a preconditioner. This combination has been shown to work very well for scalar quasilinear diffusion equations. Furthermore, this preconditioner is symmetric and block diagonal, and hence, it fully decouples into n scalar systems. Thus, solving the preconditioning system with AMG will be very efficient.

[1] G. Hansen, A. Zardecki, D. Greening, and R. Bos, "A Finite Element Method for Unstructured Grid Smoothing," *J. Comp. Phys.* **194** (2), 611–631 (2004).

[2] G. Hansen, A. Zardecki, D. Greening, and R. Bos, "A Finite Element Method for Three-Dimensional Unstructured Grid Smoothing," Los Alamos National Laboratory report LA-UR-03-8671 (2004).



For more information, contact
J. David Moulton (moulton@lanl.gov).

Acknowledgements

We would like to acknowledge NNSA's Advanced Simulation and Computing (ASC), Advanced Applications Program, for financial support.

Figure 1—
Smoothing is performed on a rectangular horseshoe domain with an initial grid defined by transfinite interpolation. In the top plot, three different cycling options are shown for AMG preconditioned GMRES, demonstrating that the number of GMRES iterations/Newton iteration is bounded. This is in contrast to the linear growth in the number of BPKIT preconditioned GMRES iterations, which are shown in the lower plot.

Interface Reconstruction on General Polygonal Meshes

Rao V. Garimella, Mikhail J. Shashkov, and Blair K. Swartz (T-7)

Numerical simulation of multimaterial, multiphase flows in an Eulerian framework often requires special procedures to explicitly track interfaces between multiple materials and phases [1, 2].

We are developing new and efficient means for reconstructing piecewise linear interface representations in complex flow simulations when the volume fractions of the different materials are specified in the elements of the mesh. Our methods are designed to work on general polygonal meshes in 2D

and polyhedral meshes in 3D. Moreover, the reconstruction algorithms we are developing are applicable to flow simulations where more than two materials may come together to form a material junction. While previous efforts with multimaterial interface reconstruction require processing of the materials in a user-specified order to get the correct interface topology, we are developing methods which will eventually allow automatic determination of material ordering. Our algorithms are also designed to produce interfaces that are continuous, as far as possible, across element boundaries.

Initial results from the developed procedures indicate that the procedure is fast and reproduces interfaces accurately.

[1] S.J. Mosso, B.K. Swartz, D.B. Kothe, and R.C. Ferrell, "A Parallel, Volume-Tracking Algorithm for Unstructured Meshes," in P. Schiano, A. Ecer, J. Periaux, and N. Satofuka, Eds., *Parallel Computational Fluid Dynamics: Algorithms and Results Using Advanced Computers* (Elsevier Science B.V., 1997) pp. 368–375.

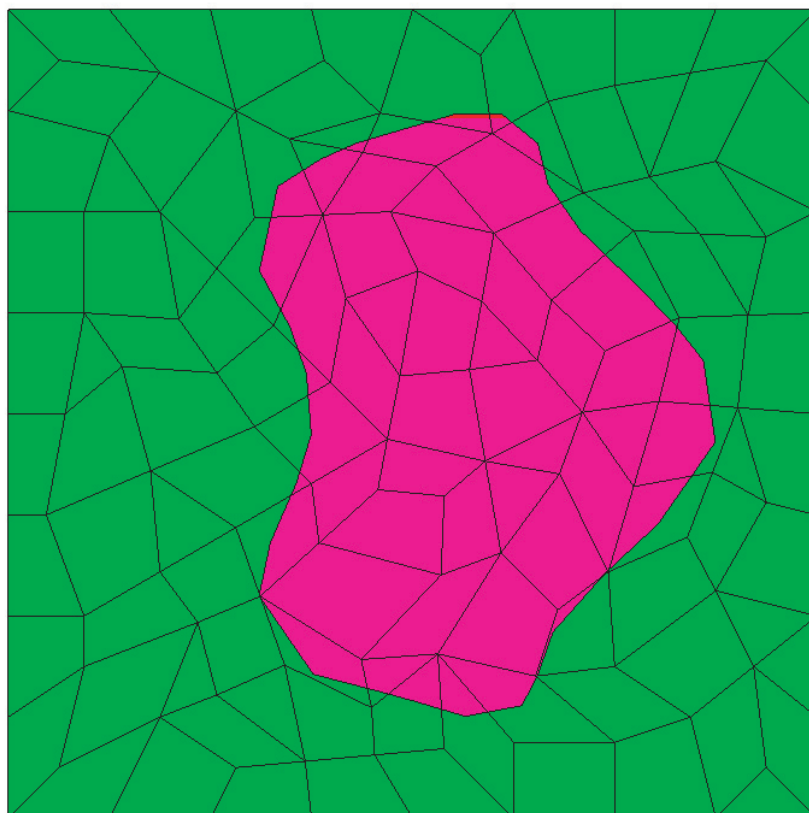


Figure 1—
Interface reconstruction
of a general shape on an
unstructured mesh.

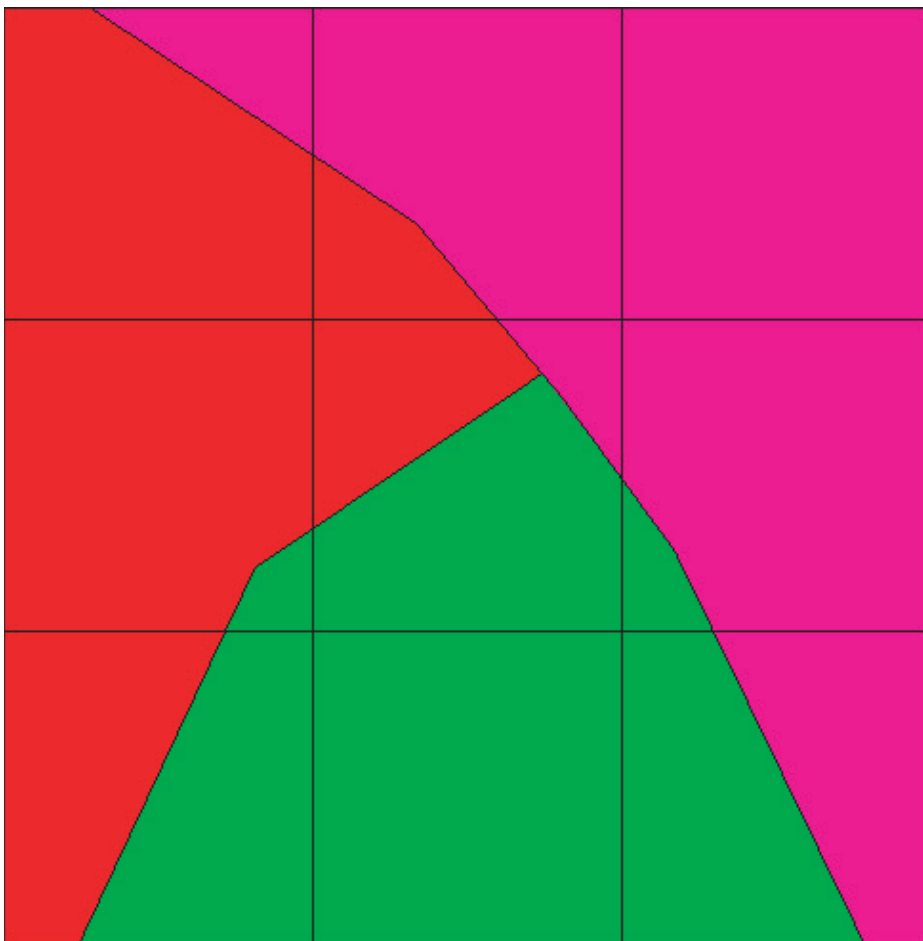


Figure 2—
*Multisegmented
reconstruction
of a three-material
interface.*

[2] R.D. Giddings, “HELMIT—A New Interface Reconstruction Algorithm,” in E.F. Toro, Ed., *Godunov Methods: Theory and Applications* (Kluwer Academic/Plenum Publishers, 2001) pp. 367–376.

For more information, contact
Rao V. Garimella (rao@lanl.gov).

Acknowledgements

We would like to acknowledge NNSA’s Advanced Simulation and Computing (ASC), Advanced Applications Program, for financial support.

Mimetic Discretizations of Diffusion Equation on Polygonal Meshes

Konstantin Lipnikov and
Mikhail Shashkov (T-7), and
Yuri Kuznetsov (University of Houston)

As the mathematical modeling of a fluid flow becomes more sophisticated, the need for discretization methods handling meshes with mixed types of elements has appeared. Practice and experience show that the most effective discretization methods mimic the underlying properties of original continuum differential operators. For the linear diffusion problem such methods mimic the Gauss divergence theorem needed for local mass conservation, the symmetry between the continuous gradient and divergence operators needed for proving symmetry and positivity of the resulting discrete operator, and the null spaces of the involved operators needed for stability of the discretization.

We have developed a new family of mimetic discretizations [1] for diffusion-type equations on general polygonal meshes:

$$\operatorname{div} \mathbf{u} = Q,$$

$$\mathbf{u} = -K \operatorname{grad} p.$$

Here p and \mathbf{u} denote the fluid pressure and velocity, respectively, K denotes a full tensor, and Q denotes a source function.

The novel discretization is locally conservative and exact for piecewise linear solutions (see Fig. 1). This is one of the major advances over the capabilities of the existing discretizations [2]. For sufficiently smooth solutions, our method exhibits a second-order convergence rate for the fluid pressure and a first-order convergence rate for the fluid velocity. It confirms the convergence rates observed in other types of lower order discretizations (finite elements and finite volumes) on nonsmooth triangular and quadrilateral meshes.

Another important feature of our method is the ability to treat meshes with degenerate and nonconvex polygons (see Fig. 2). Such meshes frequently occur in applications. For example, nonmatching meshes and locally refined meshes with hanging nodes are examples of conformal polygonal meshes. Recall that a hanging node occurs when two (or more) elements share an edge with one element. If we consider the hanging node as an additional vertex of this element, we get a conformal polygonal mesh with degenerate elements. As shown in Fig. 3, our method allows a very strong mesh refinement and elements with very small edges.

Nowadays, the use of polygonal meshes is limited by a small number of accurate discretization schemes. We mention here the finite volume scheme proposed by T. Palmer [3]. The scheme is exact for uniform flows but results in a nonsymmetric

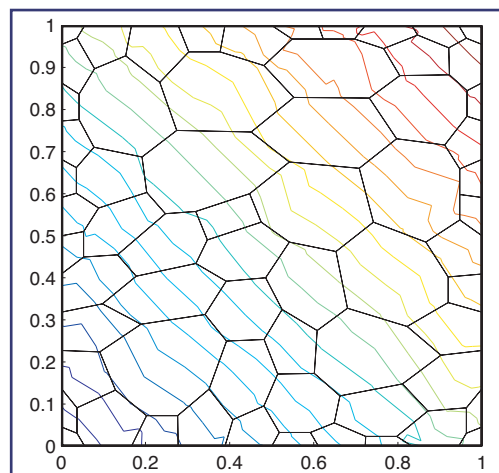
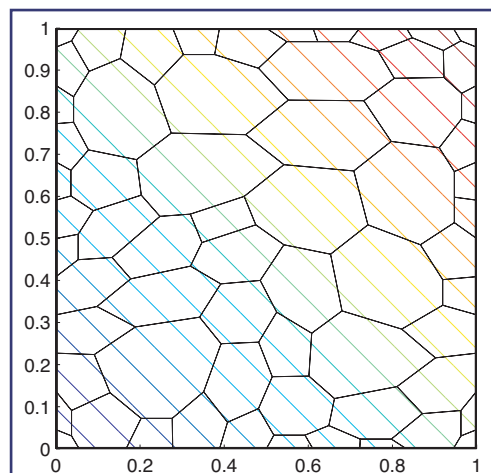


Figure 1—
Isolines of a linear solution in the old (right) and new (left) methods.

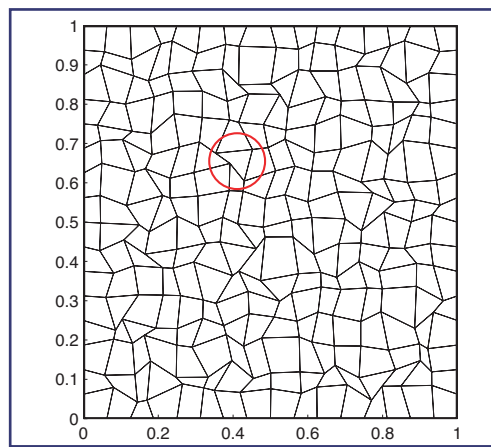
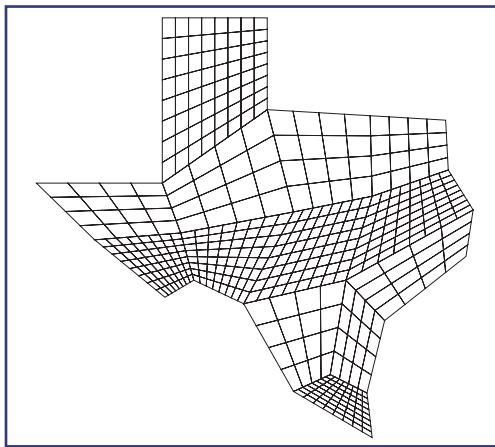


Figure 2—
Polygonal meshes with degenerate and nonconvex polygons. One of the nonconvex elements is marked by a circle.

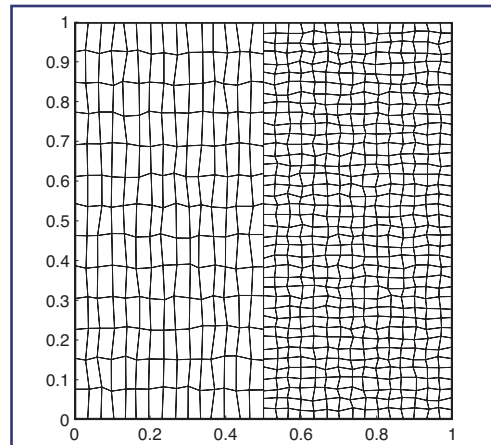
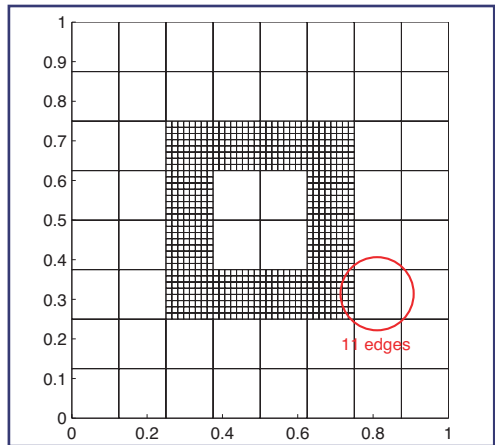


Figure 3—
Left picture shows a mesh with a strong local refinement. The element with 11 edges is marked by a circle. The right picture shows a non-matching mesh. Some of the polygons have very small edges.

coefficient matrix. Therefore, it requires the use of nontraditional iterative solvers. In contrast, our new discretization method results in an algebraic problem with a symmetric positive definite matrix. Therefore, the problem may be solved with the conjugate gradient method.

Our newly developed discretization methodology is based on the divide and conquer principle. First, we consider each mesh polygon as an independent domain and generate an independent discretization for this polygon. Second, the system of element-based discretizations is closed by imposing boundary conditions and continuity conditions for the fluid pressure and normal velocity component on polygon edges.

The new discretization methodology can be extended to unstructured polyhedral meshes and to other partial differential equations

such as Maxwell's equations, Navier-Stokes equations, and equations of linear elasticity.

- [1] Y. Kuznetsov, K. Lipnikov, M. Shashkov, "The Mimetic Finite Difference Method on Polygonal Meshes for Diffusion-Type Problems," Los Alamos National Laboratory report LA-UR-03-7608 (October 2003), accepted to *Comp. Geosciences*.
- [2] J. Hyman et al., "Mimetic Finite Difference Methods for Diffusion Equations," *Comp. Geosciences* **6** (3–4) (2002), 333–352.
- [3] T. Palmer, "Discretizing the Diffusion Equation on Unstructured Polygonal Meshes in Two Dimensions," *Ann. Nucl. Energy*, **28** (2001), 1851–1880.

For more information, contact
Konstantin Lipnikov (lipnikov@lanl.gov).

Acknowledgements

We would like to acknowledge NNSA's Advanced Simulation and Computing (ASC), Advanced Applications Program, for financial support.

An Arbitrary-Lagrangian-Eulerian Code for Polygonal Mesh: ALE INC(ubator)

Raphaël Loubère and
Mikhail Shashkov (T-7)

In this work we have developed a 2D unstructured Arbitrary-Lagrangian-Eulerian (ALE) code. This code is devoted to solve computational fluid dynamics (CFD) problems for general polygonal meshes with fixed connectivity. Main components of the method are: (1) a Lagrangian scheme, (2) a Reference Rezone Jacobian Strategy, and (3) a Remapping method. In the Lagrangian scheme each polygon is split into subcells. The compatible Lagrangian hydrodynamics equations are solved during one time step and the mesh is moved according to the fluid velocity (see Refs. 1, 2, 3).

The Reference Rezone Jacobian Strategy improves the quality of the untangled mesh and, at the same time, requires the new mesh to be close to the original untangled grid (from Step 2) and preserves interfaces between materials (see Ref. 4). An Untangling process ensures the validity of the mesh, if the mesh was tangled as a result of the Lagrangian step. The method finds an untangled mesh which is as close as possible to the previous Lagrangian grid (see Refs. 5, 6).

The Remapping method gives the linear and bound preserving remapped hydrodynamics variables on the new mesh (see Refs. 7, 8).

These three steps have been adapted to the subcell description of the scheme and the polygonal meshes. The Untangling and the reference rezone Jacobian processes deal now with general polygonal meshes and preserve the interfaces between materials. The remapping step is performed from a

subcell point of view and the accuracy of the remapping stage has been improved with new techniques from [9].

ALE INC. can be used as a purely Lagrangian code (only Step 1 is used), an ALE one (x Lagrangian steps are performed then Steps 2, 3 are activated) or as an Eulerian one (Steps 1 and 3 are used and the remapping is done on the same initial grid). Moreover the code can be used in Cartesian or cylindrical coordinates.

Fig. 1 is the simulation of the Guderley problem: a unit disk ($\rho = 1$, $p = 0$) at rest is compressed by a cylindrical shock wave. The initial mesh is polygonal (either symmetric or with a false center of convergence, located at $(-0.5, 0)$ as in [1]). Time $t = 0$, $t = 0.6$, $t = 1.0$ are printed showing the cylindrical symmetry preservation with or without an initial symmetric polygonal mesh.

- [1] E.J. Caramana and M. Shashkov, "Elimination of Artificial Grid Distortion and Hourglass-Type Motions by Means of Lagrangian Subzonal Masses and Pressures," *J. Comp. Phys.* **142** (1998), 521–561.
- [2] E.J. Caramana, et al., "The Construction of Compatible Hydrodynamics Algorithms Utilizing Conservation of Total Energy," *J. Comp. Phys.* **146** (1998), 227–262.
- [3] J. Campbell, M. Shashkov, "A Tensor Artificial Viscosity using a Mimetic Finite Difference Algorithm," *J. Comp. Phys.* **172** (2001), 739–765.
- [4] P. Knupp, L.G. Margolin, M.J. Shashkov, "Reference Jacobian Optimization-Based Rezone Strategies for Arbitrary Lagrangian Eulerian Methods," *J. Comp. Phys.* **176** (2002), 93–128.
- [5] P. Vachal, M. Shashkov, R. Garimella, "Untangling of 2D Meshes in ALE Simulations, submitted to *J. Comp. Phys.*
- [6] P. Knupp, "Hexaedral and Tetrahedral Mesh Untangling," *Eng. Comput.* **17** (2001), 261–268.
- [7] L.G. Margolin, M.J. Shashkov, "Second-Order Sign-Preserving Conservative Interpolation (Remapping) on General Grid," *J. Comp. Phys.* **184** (2003), 266–298.
- [8] M. Kucharik, M.J. Shashkov, B. Wendroff, "An Efficient Linearity and Bound-Preserving Remapping Method," to be published in *J. Comp. Phys.*

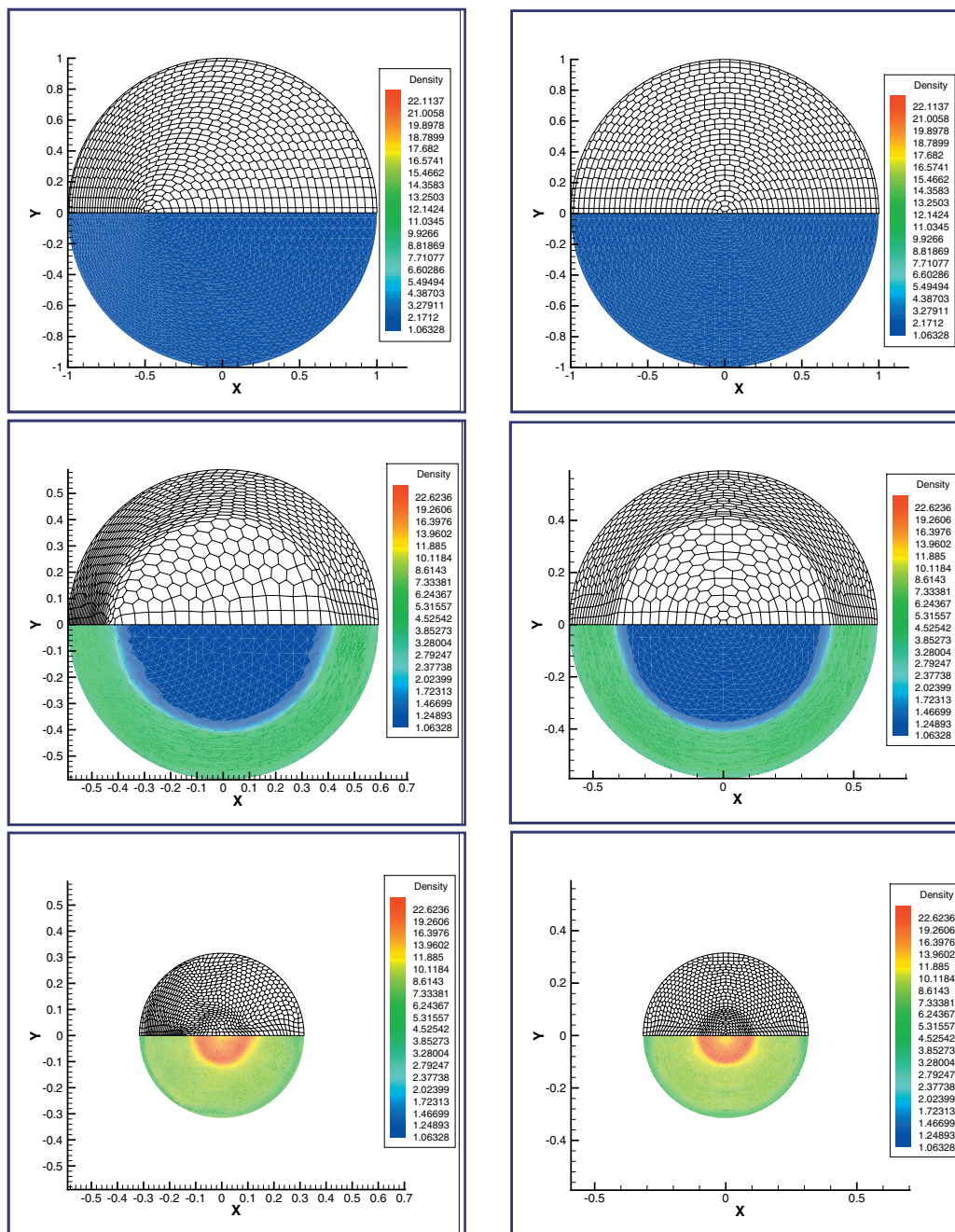


Figure 1—
Guderley problem
nonsymmetric (left)
and symmetric (right)
polygonal mesh—Top:
 $t = 0.0$, Middle: $t = 0.6$,
and Bottom: $t = 1.0$.

[9] R. Loubere, M. Shashkov, “A Subcell Remapping Method on Staggered Polygonal Grids for Arbitrary-Lagrangian-Eulerian Methods,” Los Alamos National Laboratory report LA-UR-04-6692 (September 2004), submitted to *J. Comp. Phys.*

For more information, contact
Raphaël Loubère (loubere@lanl.gov).

Acknowledgements

We would like to acknowledge NNSA's Advanced Simulation and Computing (ASC), Advanced Applications Program, for financial support.

A Subcell Remapping Method on Staggered Polygonal Grids for Arbitrary-Lagrangian-Eulerian Methods

*Raphaël Loubère and
Mikhail Shashkov (T-7)*

In this work we have constructed a full 2D remapping method to be used on a staggered polygonal mesh. This technique has been implemented into an Arbitrary-Lagrangian-Eulerian (ALE) code. It combines and generalizes previous work on the Lagrangian and rezoning phases including this new remapping algorithm [1]. In the Lagrangian phase of the ALE method we use compatible methods to derive the discretizations [2, 3]. We assume a staggered grid where velocity is defined at the nodes, and where density and internal energy are defined at cell centers. In addition to nodal and cell-centered quantities, our discretization employs subcell masses that serve to introduce special forces that prevent artificial grid distortion (hourglass-type motions) [4]. This kind of numerical scheme adds an additional requirement to the remap phase: that the subcell densities (corresponding to subcell masses) have to be conservatively interpolated in addition to nodal velocities and cell-centered densities and internal energy. In the remap phase, we assume that the rezone algorithm produces a mesh that is “close” to the Lagrangian mesh so that a local remapping algorithm (i.e., where mass and other conserved quantities are only exchanged between neighboring cells) can be used.

Our new remapping algorithm consists of three stages.

- A gathering stage, where we define momentum, internal energy, and kinetic energy in the subcells in a conservative way such that the corresponding total quantities in the cell are the same as at the end of the Lagrangian phase.
- A subcell remapping stage, where we conservatively remap mass, momentum, internal, and kinetic energy from the subcells of the Lagrangian mesh to the subcells of the new rezoned mesh.
- A scattering stage, where we conservatively recover the primary variables: subcell density, nodal velocity, and cell-centered specific internal energy on the new rezoned mesh.

We have proved that our new remapping algorithm is conservative (in mass, momentum, and total energy), reversible (if the old and new meshes are identical then the primitive variables are kept unchanged), at least positive (density and specific internal energy are kept positive thanks to a repair method, at most, preserving a maximum principle), and satisfies the DeBar consistency condition (if a body has a uniform velocity and spatially varying density, then the remapping process should exactly reproduce a uniform velocity). We have also demonstrated computationally that our new remapping method is robust and accurate for a series of test problems in one and two dimensions. Figure 1 presents the results of the Sedov blastwave in 2D Cartesian coordinates for a polygonal mesh in ALE regime: a cylindrical shock wave is initiated at the origin and at $t = 1.0$ its exact location is $r = 1$. In this run the rezone strategy improves the mesh quality and the remapping technique preserves the accuracy of the Lagrangian scheme without the its pathological behaviors.

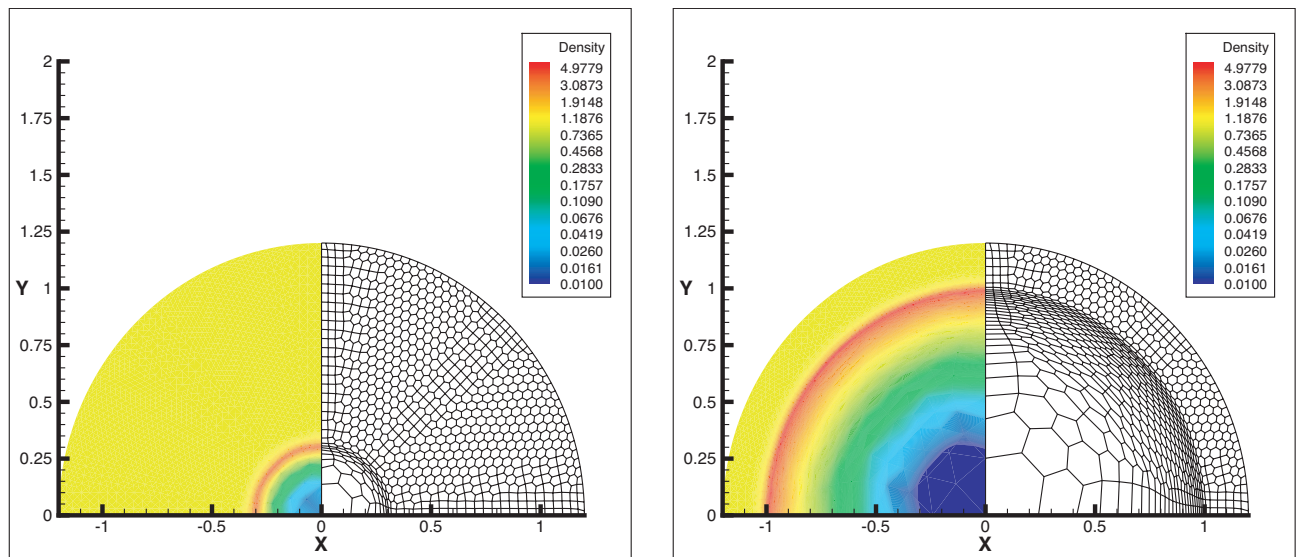


Figure 1—

Sedov blastwave on a polygonal mesh (1325 nodes and 775 cells)—ALE-10—regime-mesh and density contours (exponential scale) at $t = 0.1$, and $t = 1.0$.

- [1] R. Loubere, M. Shashkov, "A Subcell Remapping Method on Staggered Polygonal Grids for Arbitrary-Lagrangian-Eulerian Methods," Los Alamos National Laboratory report LA-UR-04-6692 (September 2004), submitted to *J. Comp. Phys.*
- [2] J. Campbell and M. Shashkov, "A Compatible Lagrangian Hydrodynamics Algorithm for Unstructured Grids," *Selcuk J. Appl. Math.*, **4** (2003), pp. 53–70; report version can be found at (<http://cnls.lanl.gov/~shashkov>).
- [3] J. Campbell, M. Shashkov, "A Tensor Artificial Viscosity using a Mimetic Finite Difference Algorithm," *J. Comp. Phys.*, **172** (2001), pp. 739–765.
- [4] E. J. Caramana and M. J. Shashkov, "Elimination of Artificial Grid Distortion and Hourglass-Type Motions by means of Lagrangian Subzonal Masses and Pressures," *J. Comp. Phys.*, **142** (1998), pp. 521–561.

**For more information, contact
Raphaël Loubère (loubere@lanl.gov).**

Acknowledgements

We would like to acknowledge NNSA's Advanced Simulation and Computing (ASC), Advanced Applications Program, for financial support.

The Repair Paradigm: New Algorithms and Applications to Compressible Flow

*Raphaël Loubère, Martin Staley, and
Burton Wendroff (T-7)*

A critical part of Lagrangian-based methods for Computational Fluid Dynamics (CFD) is the ability to remap or interpolate data from one computational mesh to another. This is the case for the popular ALE schemes that perform Lagrangian steps followed by remaps to fixed grids. Remapping is also essential for pure Lagrangian methods, since they can lead to tangled grids that must then be untangled with a concomitant remap step. Even if the basic scheme produces only physically meaningful quantities, a remapping method can create out-of-bounds quantities such as negative densities or pressures. In some CFD codes, the offending values are simply set to a small positive number when this occurs, at which point mass or total energy is no longer conserved. Although in most instances the error thereby created is negligible, we have shown that in at least one example the error is significant.

By taking great care with the remapping in the CFD context, it is possible to maintain positive mass density. This is done by first extending the given mean densities in each original cell to the whole domain so that the new distribution is everywhere positive, and then computing new mean values by exact integration over the cells of the new grid. Total energy can be remapped in this way, but then there is no guarantee that internal energy will be positive. Furthermore, in more than one dimension, exact integration is computationally intensive.

Another context in which nonphysical data can occur is in divergence-free advection of a concentration that must retain values between zero and one. High quality advection

schemes, some of which are based on remapping ideas [1, 2], unavoidably have this fault [3].

The goal in this work is to improve upon and apply the repair idea introduced in [4, 5]. A repair method can be viewed as a way to correct values on a discrete mesh by redistributing the conserved quantity so that conservation and a maximum principle are preserved. The maximum principle is that new values should obey certain upper and lower bounds obtained from old values. In this way not only are nonphysical quantities eliminated, but oscillations are reduced (albeit not necessarily eliminated). We therefore seek repair algorithms that can be applied to CFD problems, advection problems, or other situations where values of a discrete variable must be placed in bounds without violating a conservation law and without introducing significant errors into the dynamics.

Repair methods can be used for many kinds of variables, including density, velocity, energy, pressure, and concentration, but we will henceforth call our variable to be repaired a density ρ , or equivalently, a mass m . If we denote old cells by c and new cell by \tilde{c} , then the quantity to be conserved is the total mass $m = \sum_c m(c) = \sum_c \rho(c) V(c)$, where $m(c)$, $\rho(c)$, and $V(c)$ denote the mass, density, and volume, respectively, of cell c .

Consider an old mesh M with cell-averaged densities (called old densities), and a new mesh \tilde{M} with remapped cell-averaged densities (called new densities). The connectivity is the same for the old and new grids.

Typically the new mesh is a small perturbation of the old grid. If we define the *bound* neighborhood $N(c)$ of a cell c as a patch of surrounding cells, we can define maximum and minimum density bounds as $\rho_+(c) = \max_{s \in N(c)} \rho(s)$ and $\rho_-(c) = \min_{s \in N(c)} \rho(s)$. (There are, of course, other reasonable ways to define density bounds.) No matter how the bounds are defined, there is a feasibility condition for repair to work at all.

FEASIBILITY: The total mass m must not exceed (resp. be below) the total upper bound mass (resp. the total lower bound mass), that

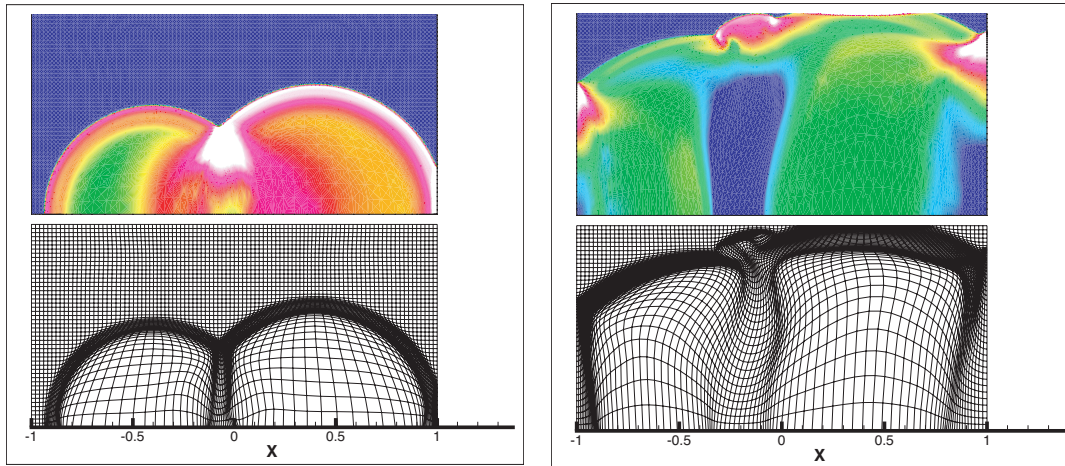


Figure 1—
Interaction of two blastwaves in a box. Initially, two half disks centered at $x = (\pm 0.5, 0)$ have a high energy compared to the interior of the box— $t = 0.3$ and $t = 0.8$.

is, the total mass if each new cell were at its upper (resp. lower) bound.

If a remapping process produces negative densities $\rho(\tilde{c})$, or more generally produces out-of-bounds densities, then a repair step must be done to make these densities obey their bounds. The properties to be fulfilled by a repair method are:

Conservation:

$$\begin{aligned}\Sigma_c m(c) &= \Sigma_c \rho(c) V(c) = \Sigma_c \rho(\tilde{c}) V(\tilde{c}) \\ &= \Sigma_c m(\tilde{c}).\end{aligned}$$

Maximum principle:

$$\forall c, \rho_-(c) \leq \rho(\tilde{c}) \leq \rho_+(c).$$

In this work we first reviewed a local repair method [5] which repairs out-of-bounds values and distributes the mass discrepancies locally. This method can produce different results depending on the order in which cells are visited, and it is therefore called order-dependent. Next we reviewed a simple global repair process [4] which repairs out-of-bounds values and distributes the resulting mass discrepancy across the entire grid. Then, we introduced two order-independent local methods, only one of which is well suited for parallelization. The idea of this method is to repair as many cells as possible with a local treatment: first the upper bounds, then the lower bounds, with an iterative process.

Then, if some cells are still out-of-bounds, a global treatment is provided to fix them.

Numerical tests were performed to show the effects of such methods on advection and hydrodynamics problems like the double nonsymmetric blastwave solved with the ALE INC. code (see the article “An Arbitrary-Lagrangian-Eulerian Code for Polygonal Mesh: ALE INC(ubator)” in this volume on page 118) where the repair method [6] is necessary for the code to produce a physically meaningful solution (see Fig. 1).

- [1] P. Colella, *J. Comp. Phys.*, **87** (1990) 171–200.
- [2] J.K. Dukowicz and J.R. Baumgardner, *J. Comp. Phys.*, **160** (2000), 318–335.
- [3] A. Oliveira and A.B. Fortunato, *J. Comp. Phys.*, **183** (2002), 142–164.
- [4] M. Shashkov and B. Wendroff, *J. Comp. Phys.*, **198** (2004) 265–277.
- [5] M. Kucharich, M. Shashkov, and B. Wendroff, *J. Comp. Phys.*, **188** (2003) 462–471.
- [6] R. Loubere, M. Staley, and B. Wendroff, “The Repair Paradigm: New Algorithms and Applications to Compressible Flow, Los Alamos National Laboratory report LA-UR-04-7095 (October 2004), submitted to *J. Comp. Phys.*

For more information, contact
Raphaël Loubère (loubere@lanl.gov).

Acknowledgements

We would like to acknowledge NNSA’s Advanced Simulation and Computing (ASC), Advanced Applications Program, for financial support.

CORE: Conservative Remapper

Martin Staley and Mikhail Shashkov (T-7)

Conservative Remapper, or CORE, is a C++ language software library for remapping cell masses and cell-averaged densities on unstructured two-dimensional grids, maintaining conservation of total mass in the process. CORE contains implementations of two remapping algorithms: a new, efficient “swept-region” algorithm and a more traditional algorithm based on the computation of cell intersections. Grids may be Cartesian or cylindrical, and cells may have three or more vertices, with no upper limit. CORE can run in serial and in parallel, but in order to achieve wide applicability, CORE uses no particular parallel communication library. Instead, it achieves parallel communication through strategically placed, user-defined callbacks. Users can also provide callbacks to redefine different parts, or subcomponents, of the remapping process. CORE allows the use of different data types, e.g., single, double, and quadruple precision floating-point numbers, through the use of C++ templates. Using CORE is simple and requires no configuration scripts or makefiles.

The swept-region remapping algorithm [1] achieves its goal by performing three steps: density reconstruction, mass exchange, and mass repair. This algorithm performs well if the new grid is a small perturbation of the old grid, and it is faster than the exact-intersection algorithm.

For the density reconstruction step, consider that the mean cell densities obey some underlying, theoretical density function ρ . For the reconstruction step, we assume ρ is piecewise linear—one piece per cell—and then use our discrete mean densities to reconstruct ρ .

For the mass exchange step, consider that each edge has two adjacent cells. For a given edge, we identify which of these cells the edge “moves into” more when we go from the old grid to the new grid. We then integrate the cell’s reconstructed density function over the entire region swept by the edge’s motion. This gives us a mass, which is then removed from this cell and added to the cell on the other side of the edge.

Consider Fig. 1, where the old grid is drawn with dotted lines and the new grid with solid lines. When the edge illustrated in the figure moves from its original position to its final position, it sweeps the shaded region. So, we integrate Cell 5’s reconstructed linear density function over this region, giving a mass which is subtracted from Cell 5 and added to Cell 4.

For the mass repair step we recognize that the earlier, mass exchange step involved inexact integration, in that only one cell’s piece of the reconstructed density function (Cell 5’s piece in the figure) was considered, even though portions of the swept region intersect with other cells. Because of inexact integration, new masses in individual cells can conceivably violate local bounds. For example, a mass might be negative. The repair step fixes out-of-bounds masses, while conserving the total mass over the entire grid.

Figure 1—
Swept-region remapping.

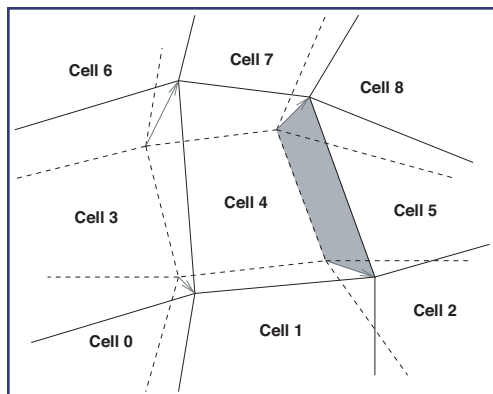
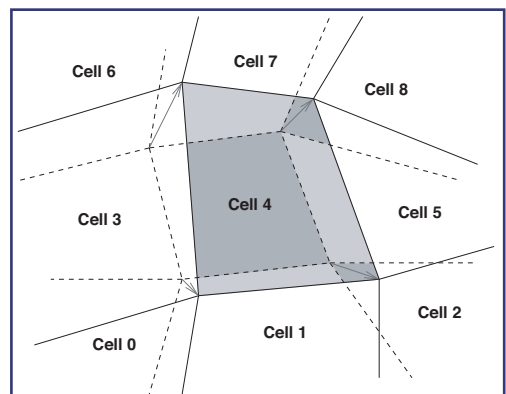


Figure 2—
Exact-intersection remapping.



The exact-intersection remapping algorithm [2] begins with the same density reconstruction step used in the swept-region algorithm. However, the mass exchange step is now quite different. Consider Fig. 2, in which Cell 4 moves from its position on the old grid (dotted lines) to its position on the new grid (solid lines) as shown by the arrows. Exact-intersection remapping examines each of the grid's cells. Cell 4 on the new grid intersects with Cells 1, 2, 4, 5, 7, and 8 on the old grid, as shown by the shaded regions in the figure. So, the algorithm computes Cell 4's new mass by summing the integral of Cell 1's reconstructed density function over Cell 4's intersection with old Cell 1, the integral of Cell 2's reconstructed density function over Cell 4's intersection with old Cell 2, etc.

Although this algorithm no longer involves inexact integration, as the swept-region algorithm did, it still allows for a mass repair step in the event that masses fall outside user-defined bounds.

The exact-intersection algorithm does not require that the new grid is a small perturbation of the old grid. Moreover, it allows the two grids to have different connectivities, whereas the swept-region algorithm only makes sense when the grids have the same connectivity. Figures 3 and 4 illustrate this fact with a remap from a coarser grid to a much finer grid. Notice how the original grid's relative coarseness is still visible in the remapped values on the finer grid.

[1] M. Kucharik, M. Shashkov, and B. Wendroff, "An Efficient Linearity-and-Bound-Preserving Remapping Method," *J. Comp. Phys.*, **188** (2003) pp. 462–471.

[2] L. Margolin and M. Shashkov, "Second-Order Sign-Preserving Conservative Interpolation (Remapping) on General Grids," *J. Comp. Phys.*, **184** (2003) pp. 266–298.

For more information, contact Martin Staley (mstaley@lanl.gov).

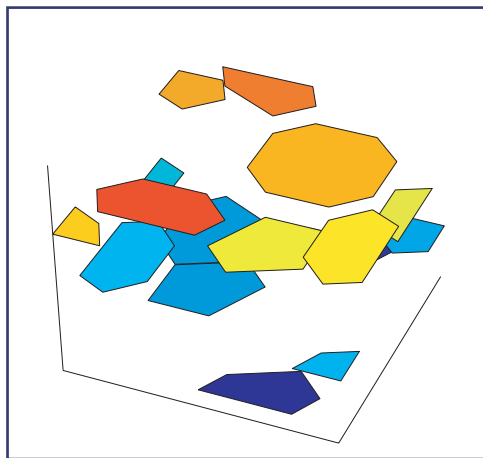


Figure 3—
Densities on the original, coarser grid.

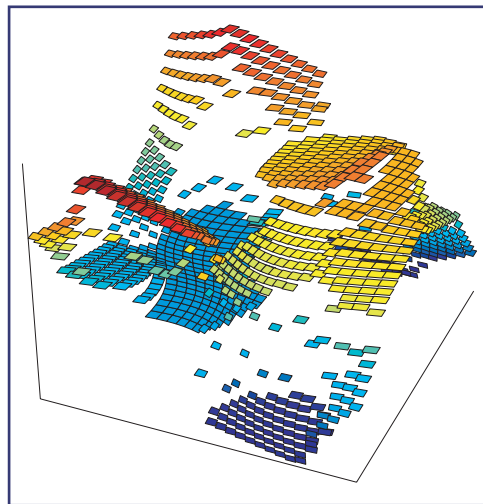
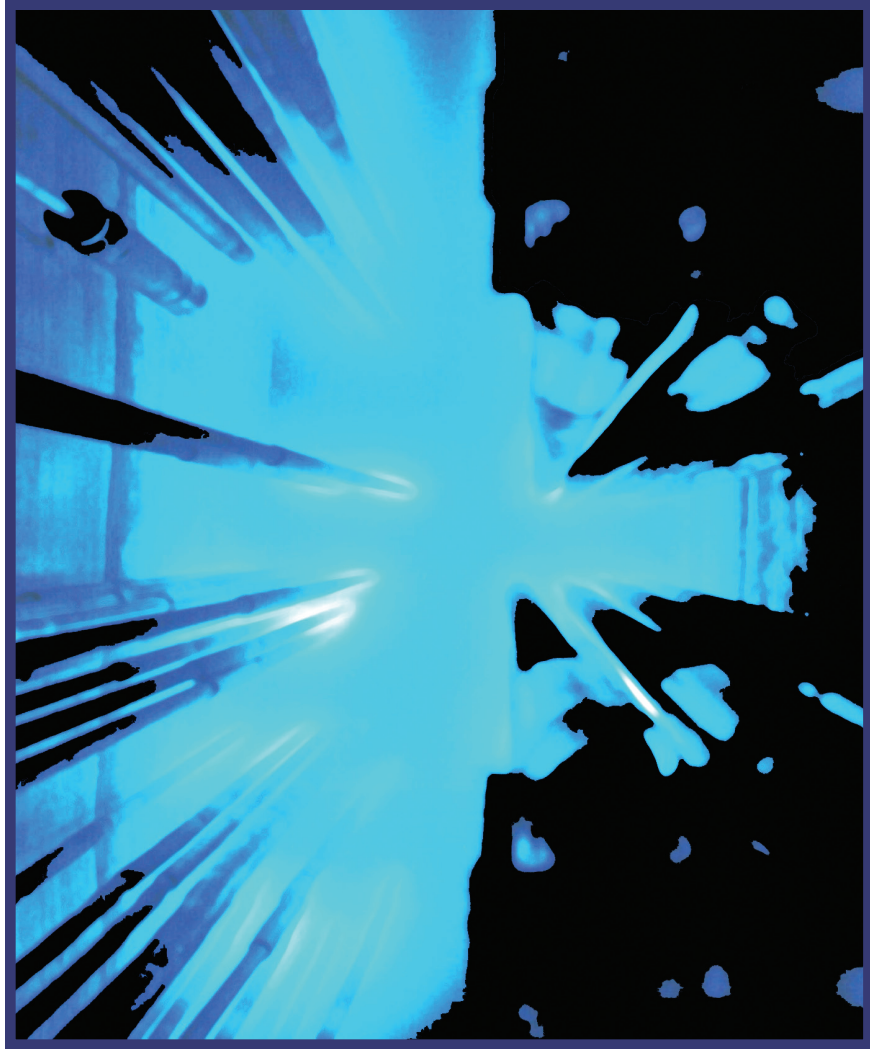


Figure 4—
Remapped densities on the new, finer grid.

Acknowledgements

We would like to acknowledge NNSA's Advanced Simulation and Computing (ASC), Advanced Applications Program, for financial support.

NUCLEAR PHYSICS



Attribution for Nuclear Devices Based on Reactor Grade Fuel

Anna C. Hayes, Patrick Goda, Jack Hills, and Gerard Jungman (T-6); and John Richter (X-4)

There are presently 439 reactor power plants and 264 research reactors in operation, and 33 reactors under construction around the world (Fig. 1). These reactors are producing 35,000 kg of plutonium (Pu) per year. This is to be compared with the critical mass of reactor grade Pu of 8 kg, as used by the International Atomic Energy Agency. It is unclassified that the U.S. fielded a successful nuclear test of a device based on reactor grade Pu, and reactor grade Pu is known to work as a nuclear weapon fuel. In this project we have been combining nuclear physics, radiochemistry, and weapons design to develop the tools needed for attribution of a nuclear attack on the U.S. using a device based on reactor grade fuel.

The key difference between weapons grade fuel and reactor grade fuel is the ratio of the Pu isotopes that each contains. Reactor grade fuel typically contains 60% ^{239}Pu , 20% ^{240}Pu , 14% ^{241}Pu , and 5% ^{242}Pu . This is to be compared with 93% ^{239}Pu , 6.5% ^{240}Pu , and 0.5% ^{241}Pu in weapons grade Pu. The even isotopes of Pu (240 and 242) have high spontaneous fission rates, which leads to an increased probability of preinitiation. We are deriving improved models of preinitiation and examining the restrictions on feasible designs arising from the high spontaneous fission rates. In this way we can provide a distribution of probable yield distribution for a class of possible designs.

Detailed analysis of the Pu isotopics determines: (1) the type of reactor used to generate the fuel, (2) the burn time of the fuel in the reactor, and (3) the sophistication of the nuclear device. Because ^{241}Pu decays to ^{241}Am , the ^{241}Am -content of the fuel can be used to age the fuel (see Fig. 2). We are presently developing a set of tools to allow a determination of the predetonation isotopics from postdetonation radiochemical debris analysis. This will allow attribution in the event of a domestic nuclear attack from a device that uses reactor grade Pu.

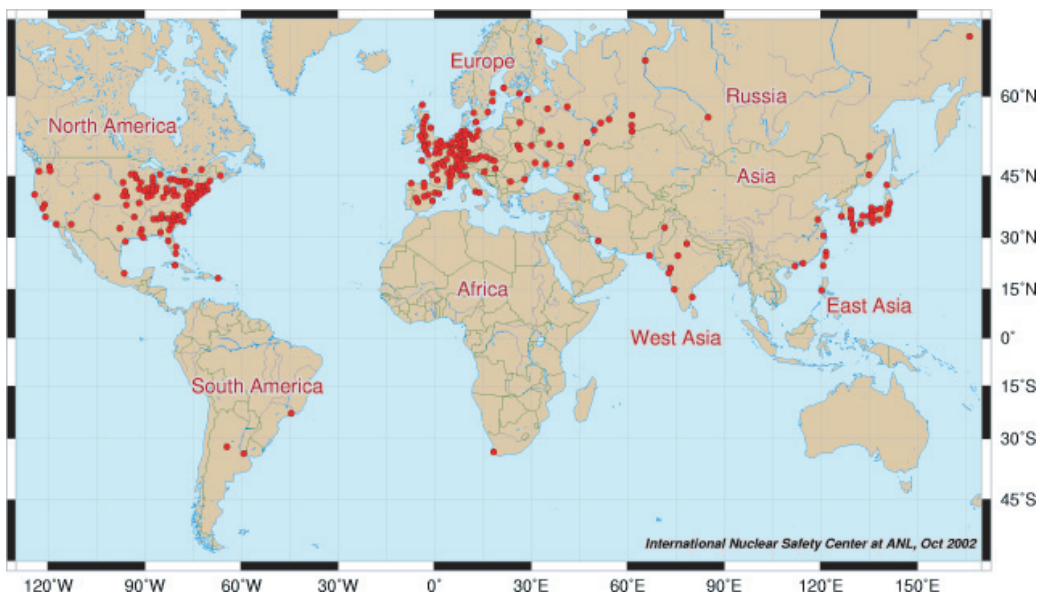


*Figure 1—
Reactor locations
around the world.*

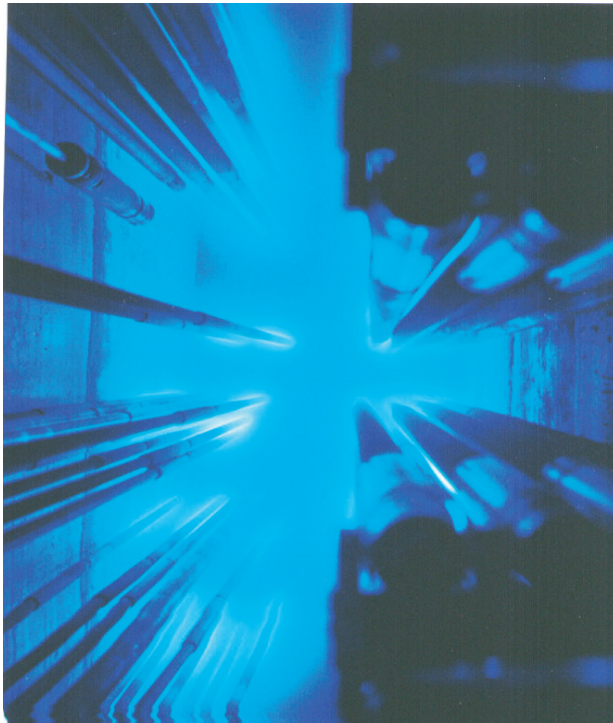


*Figure 2—
As fuel rods cool ^{241}Am
grows in ^{241}Am deter-
mines age of fuel.*

*For more information, contact
Anna C. Hayes (anna_hayes@lanl.gov).*

Acknowledgements

We would like to acknowledge DOE Office of Research and Engineering (NA-22) for financial support.

Implications of the Uncertainties in the $n + \text{Li}$ Cross Sections

Anna C. Hayes (T-6), Gerald Hale (T-16), Steven Howe (LANSCE-DO), Andrew S. Johnson (X-2), Britton A. Girard (X-4), Thomas J. Gorman (X-3), and Robert C. Little (X-5)

The most important reaction for breeding tritium is the ${}^6\text{Li}(n,t)\alpha$ reaction. This together with the neutron inelastic three-body breakup of Li, ${}^6\text{Li}(n,n')d\alpha$, are the most important neutron reactions on ${}^6\text{Li}$ at neutron energies up to about 20 MeV. However, the tritium breeding reaction is uncertain by about 25% for all neutron energies above 0.5 MeV. Similarly, the three-body reaction

is uncertain for neutron energies above 3 MeV. Indeed, the Los Alamos and Lawrence Livermore National Laboratories' cross-section libraries for these two reactions are quite different at these neutron energy regions. In this project, we have been examining the implications of these uncertainties in weapons simulations for systems currently in the nation's nuclear stockpile.

The uncertainty in the ENDF/B-VI ${}^6\text{Li}(n,t)$ cross section at energies below 1 MeV (the "standards" region) was based on scaling up the uncertainty given by propagating the covariances of the R-matrix parameters to account for the fact that chi-square per degree of freedom for the fit exceeded unity. At higher energies for the ${}^6\text{Li}(n,t)$ cross section, and also for the ${}^6\text{Li}(n,n')$ cross section, the uncertainties were estimated from the scatter in the experimental data and from the deviation from other evaluations. It is interesting to note that a new R-matrix analysis of the ${}^7\text{Li}$ system is giving ${}^6\text{Li}(n,t)$ cross sections very similar to those of ENDF/B-VI at energies below 4 MeV.

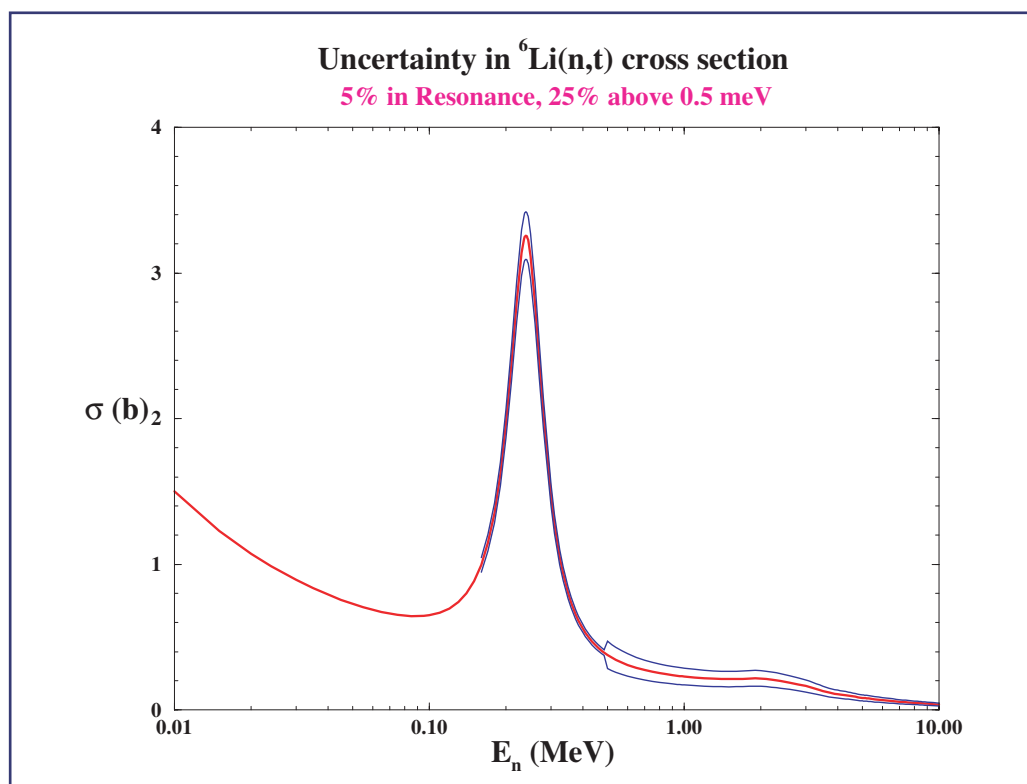


Figure 1—
Uncertainty in ${}^6\text{Li}(n,t)$
cross section.

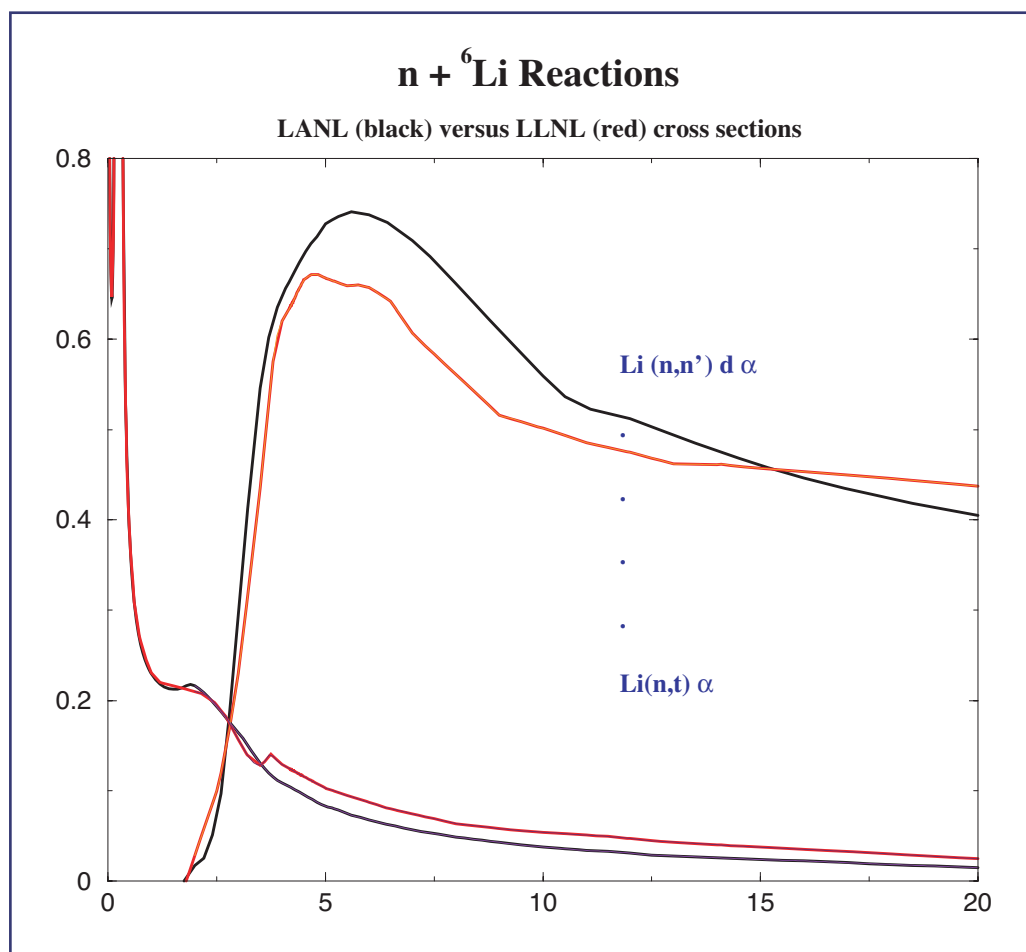


Figure 2—
 $n + {}^6\text{Li}$ reactions.

The Nuclear Data Interface (NDI) allows straightforward manipulation of the nuclear cross section and neutron transport scattering matrices for the present sensitivity studies. We carried out a series of simulations testing the sensitivity to the Los Alamos and Lawrence Livermore National Laboratories' Li cross-section libraries and the sensitivity to the total uncertainty in the cross sections. We also examined the tritium production as a function of neutron energy. These calculations show some unexpected but important results.

From these studies we concluded that there is a need for a high-accuracy measurement of the tritium breed cross section at neutron energies above 0.5 MeV. Experimental feasibility studies suggest that a 5% measurement is possible at the Los Alamos Neutron Science Center.

*For more information, contact
Anna C. Hayes (anna_hayes@lanl.gov).*

Acknowledgements

We would like to acknowledge NNSA's Advanced Simulation and Computing (ASC), Materials and Physics Program; and Campaign 4, Secondary Certification and Nuclear Systems, for financial support.

New Antineutrino Spectra for Plutonium and Uranium

Anna C. Hayes and
Corinne M. Teeter (T-6),
William B. Wilson (T-16), and
Michael Martin Nieto (T-8)

There is considerable interest by the International Atomic Energy Agency in determining the feasibility of using antineutrino monitoring of the plutonium (Pu) content of reactors. In the present project we have improved antineutrino spectra from thermal fission of ^{235}U and ^{239}Pu needed for these feasibility studies.

The total beta spectrum seen in fission arises from thousands of beta end-points from over 1000 fission product nuclei. Here beta spectra for Pu and U were calculated using the appropriate individual spectra data

from ENDFB-VI, as updated by Katakura and England. In these data, beta spectra are represented using known end-point energies and supplemental by continuous spectra from the gross theory of beta decay. All available beta spectra have been processed to 14.9 MeV using 158 energy bins. These spectra were then combined with the ENDFB-VI updated cumulative fission yields to calculate equilibrium fission product beta spectra for the two fission systems Pu and U. Each of these was fitted using 48 fictitious end-point energies with high precision. The antineutrino spectra associated with the calculated beta spectra could then be calculated from the fitted 48 end points.

Figure 1 compares the aggregate calculated beta and neutrino spectrum for ^{235}U with the experimentally determined spectrum of Keyser and the equilibrium spectrum calculated by Vogel. The agreement between the measured and calculated beta spectra is exceptional. Figure 2 shows the corresponding beta and antineutrino spectrum for ^{239}Pu . These newly calculated spectra for ^{235}U and ^{239}Pu are the first available spectra out to such large energies (15 MeV), and they span 8 orders of magnitude.

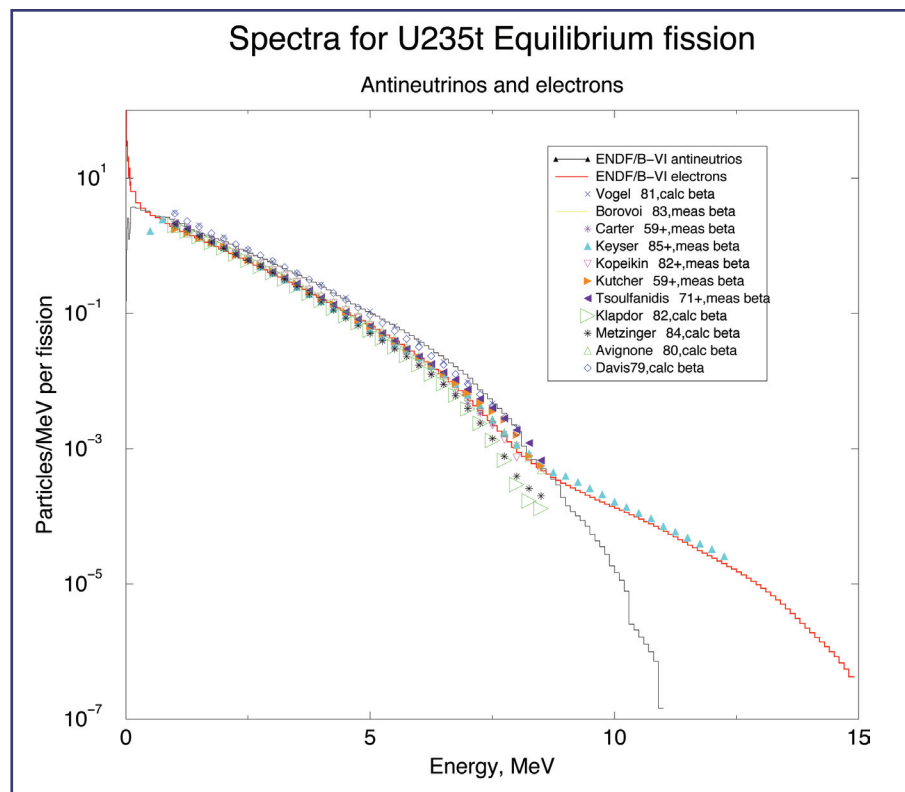


Figure 1—
Spectra for U235t
Equilibrium fission.

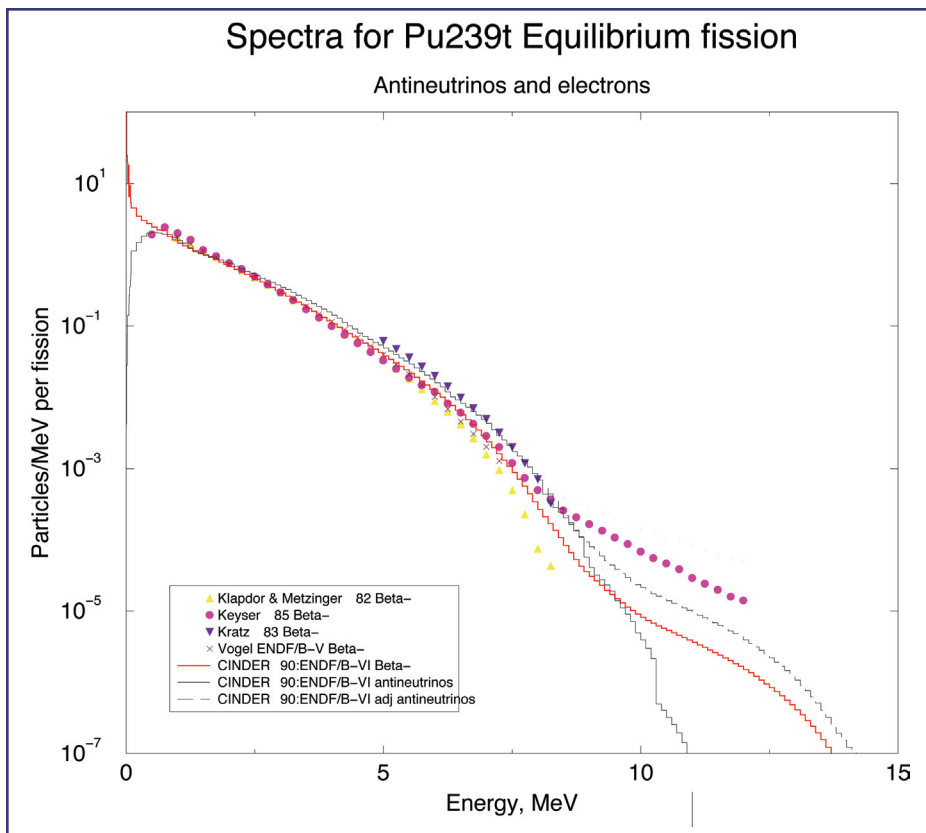


Figure 2—
Spectra for Pu239t
Equilibrium fission.

For more information, contact
Anna C. Hayes (anna_hayes@lanl.gov).

Acknowledgements

We would like to acknowledge the Laboratory
Directed Research and Development Program for
financial support.

Nuclear Isomers

*Anna C. Hayes and
Gerard Jungman (T-6), Eric Lynn (T-16),
and Britt Girard (X-4)*

A nuclear isomer is a nuclear state that is energetically above the ground state but which is typically long-lived compared to other excited states due to selection rules for nuclear transitions. Since an isomeric state and the ground state have different nuclear structure, they differ in many properties. In particular, the cross sections for neutron reactions such as (n,n') , (n,γ) and $(n,2n)$ differ. We have studied these reactions in detail for the interesting 77 eV isomer of ^{235}U , which has a 26-minute half-life. Differences in cross sections between the ground state and the isomeric state can be significant [1].

Isomeric states are produced in the thermonuclear environment. Because of the differences in cross sections, their presence can change some aspects of the reaction kinetics (Fig. 1). It is important to understand what effect such changes will have on other physical processes. Self-consistent weapons simulations have been conducted in order to assess the effect of the isomer [2, 3]. This work is done in close collaboration with members of the Applied Physics Division (X-2 and X-4) at Los Alamos National Laboratory, and results have been presented at the 2003 Nuclear Explosives Design Physics Conference [3].

[1] J.E. Lynn and A.C. Hayes, "Theoretical Evaluations of the Fission Cross Section of the 77 eV Isomer of U^{235} ," *Phys. Rev. C* **67**, 014607 (2003).

[2] A.C. Hayes, G. Jungman, J.E. Lynn, J.C. Solem, G. Girard, S.M. Sterbenz, "The Effects of 77eV Isomer of ^{235}U ," Los Alamos National Laboratory report LA-CP-04-0170 (2004).

[3] Anna C. Hayes, "Effect of 26 Minute Isomer of ^{235}U ," Los Alamos National Laboratory report LA-CP-04-1017 (2004).

For more information, contact
Anna C. Hayes (anna_hayes@lanl.gov).

Acknowledgements

We would like to acknowledge NNSA's Advanced Simulation and Computing (ASC), Reactivity and Compression Program; and Campaign 4, Secondary Certification and Nuclear Systems, for financial support.

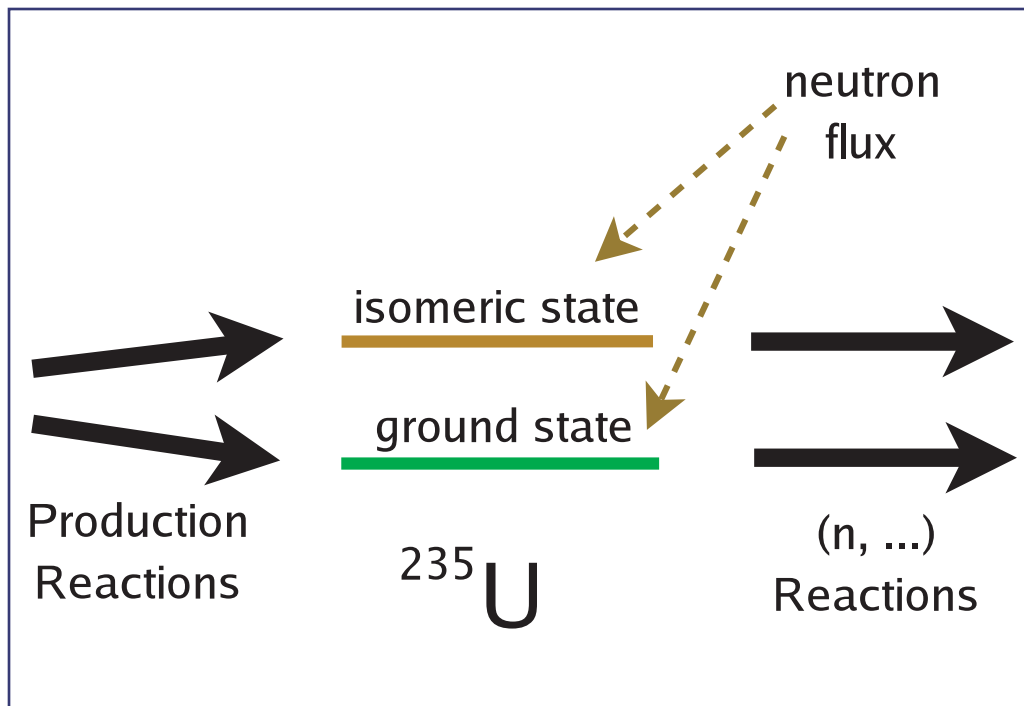


Figure 1—
In a high neutron fluence environment the isomer of ^{235}U is strongly populated. The cross sections for subsequent neutron reactions, including fission, on the isomer are different than those for the ground state. Thus, the isomer can play an important role in a nuclear explosion involving ^{235}U .



Radiochemical Detectors Probe Physical Processes

Gerard Jungman and Anna C. Hayes (T-6)

Neutron reactions on radiochemical detector isotopes provide a key diagnostic for fusion yields and thus for the interpretation of Nevada Test Site data; for example, see Ref. [1, 2]. Our work focuses on the theoretical interpretation of radiochemical data and its role in the analysis of device performance. This includes sensitivity studies for nuclear data and the interaction between nuclear processes and other physical processes. As we have demonstrated previously [2, 3], radiochemical reactions provide a generic probe of neutron physics in the thermonuclear environment.

The main reactions of interest for diagnosing the high energy part of the neutron spectrum are $(n,2n)$ reactions on detector isotopes such as yttrium and thulium. Because different detector isotopes have different thresholds for $(n,2n)$ reactions, it is possible to obtain differential spectral information for the neutron energy distribution. Physical processes that lead to softening of the neutron spectrum are therefore open to investigation through comparison of isotopic yields in detector isotope chains. We are currently engaged in more detailed studies to parameterize the time-development of the neutron spectrum. A cartoon of the softening is shown in Fig. 1.

[1] Anna C. Hayes and Gerard Jungman, "Weapons Sensitivity Studies for Nuclear Physics (U)," Los Alamos National Laboratory internal memo (2004).

[2] Anna C. Hayes and Gerard Jungman, "Yttrium Equivalences in Weapons Radiochemistry and Fusion Yields," in *T-Division Activities in Support of the Nuclear Weapons Program: 2002/2003*, LA-UR-03-0001 (2003).

[3] Gerard Jungman, "The Physics of Yttrium Equivalence (U)," LA-CP-03-0538. Presented at the 2003 Nuclear Explosives Design Physics Conference.

For more information, contact
Gerard Jungman (jungman@lanl.gov).

Acknowledgements

We would like to acknowledge NNSA's Advanced Simulation and Computing (ASC), Materials and Physics Program; and Campaign 4, Secondary Certification and Nuclear Systems, for financial support.

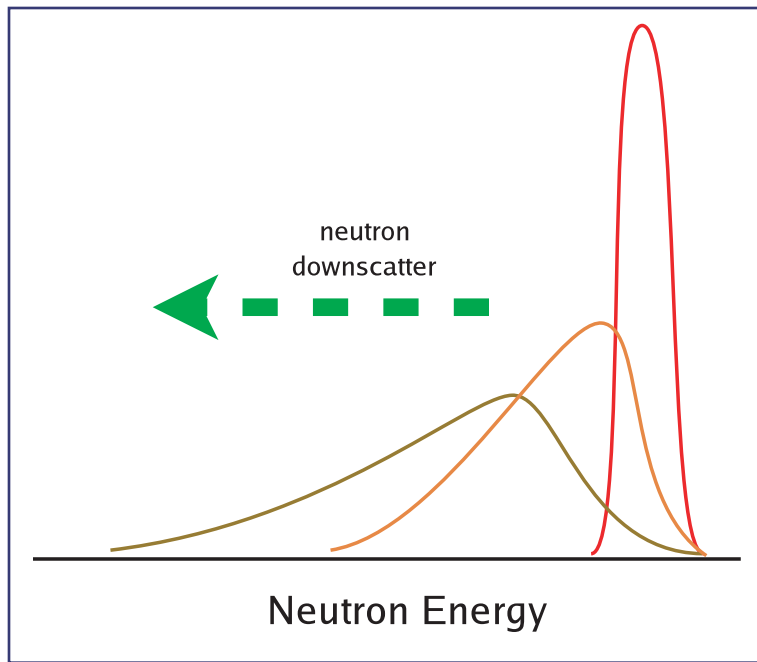


Figure 1—
The cartoon shows the softening of a neutron spectrum due to elastic scattering in an ambient material. Neutron interactions with radiochemical detector nuclides provide a window into the structure of the neutron spectrum in the thermonuclear environment.

Prompt Beta Spectroscopy as a Diagnostic for Mix in Ignited NIF Capsules

*Anna C. Hayes and Gerard Jungman (T-6),
Johndale C. Solem (T-DO),
Paul A. Bradley (X-2), and
Robert S. Rundberg (C-INC)*

The National Ignition Facility (NIF) technology is designed to drive deuterium-tritium (DT) internal confinement fusion (ICF) targets to ignition using indirect radiation from laser beam energy captured in a hohlraum. Hydrodynamical instabilities at interfaces in the ICF capsule leading to mixing between the DT fuel and the ablator shell material are of fundamental physical interest and can affect the performance characteristics of the capsule. In this project we have been examining a new radiochemical diagnostics for mix processes in ICF capsules with plastic or Be (0.9% Cu) ablator shells.

A microscopic understanding of mixing remains one of the key issues for ICF. We examined the possibility of studying mix of the ablator shell into the DT fuel by measuring the number of interactions of tritons with the shell material. The promising reactions emit high-energy betas, and we have proposed prompt beta spectroscopy as a new probe of mix. For the plastic ablator shells we considered the $^{18}\text{O}(t,n)^{20}\text{F}(\beta^-)$, and $^{13}\text{C}(t,\alpha)^{12}\text{B}(\beta^-)$ reactions, and for the Be ablator shells the $^9\text{Be}(t,\alpha)^8\text{Li}(\beta^-)$ and $^9\text{Be}(t,p)^{11}\text{Be}(\beta^-)$ reactions.

The energetic tritons in the above reactions are produced by collisions with high-energy neutrons from the central DT burn.

The number of knock-on tritons scales with the high-energy neutron production. Some of these energetic tritons go on to fuse with deuterium, some will escape, but a significant fraction will react with detector nuclei in the shell. Stopping of these energetic tritons reduces the probability of reaction with nuclei in the shell. If the shell material is intimately mixed with the fuel, the reaction yields are enhanced by the ratio of the mixing length (the thickness of the mixed region) to the triton stopping length in the unmixed fuel. Therefore, the total number of reactions of knock-on tritons with shell material is a measure of the mixing.

We carried out a detailed analysis of the effects of mixing processes on the $t + \text{shell}$ reactions and found that atomic mix gives rise to an order of magnitude enhancement in the reaction yield. Thus, triton-induced reactions leading to prompt high-energy beta-decay signals can provide an important diagnostic for mixing in ICF capsules. The predicted number of such reactions, at the yields and neutron fluences expected at the NIF facility, is sufficient for a detectable radiochemical signature of mixing processes. Our estimates for the interaction of high-energy knock-on tritons with shell material suggest that an adequate number of beta-emitters are produced to provide a unique prompt diagnostic for mix between the fuel region and the shell material. The reaction yields for the $t + \text{shell}$ reactions of interest are enhanced by the ratio of the mixing length to the triton stopping length, and this leads to increased reaction yields of more than an order of magnitude over the no-mix situation. Table 1 lists and summarizes our estimated $t + ^9\text{Be}$, $t + ^{18}\text{O}$ and $t + ^{13}\text{C}$ reaction yields for the different mix scenarios.

For more information, contact
Anna C. Hayes (anna_hayes@lanl.gov).



| Expected Reaction Yields | | | | | | | |
|---------------------------------------------|-----------|----------------------------------------------------------------------------|--------------------------|----------------|----------------------|----------------------|----------------------|
| Reaction | Q-value | β energy | Half-life | σ_0 | No Mix | Chunk Mix | Atomic Mix |
| ${}^9\text{Be}(t, \alpha){}^8\text{Li}$ | 2.93 MeV | 13.0 MeV | 840 ms | 200 mb | 1.4×10^{12} | 2.8×10^{12} | 9.3×10^{13} |
| ${}^9\text{Be}(t, p){}^{11}\text{Be}$ | -1.17 MeV | 11.5 MeV 9.4 MeV (+2.13 MeV γ) 5.3 MeV (+1.63 MeV γ) | 54.7% 13.8 s 31.4% | 13.8 s 1 mb | 4.0×10^9 | 8.2×10^9 | 3.6×10^{11} |
| ${}^{18}\text{O}(t, n){}^{20}\text{F}$ | 6.10 MeV | 5.3 MeV (+1.63 MeV γ) | 11.0 s | 100 mb | 1.4×10^8 | 2.8×10^8 | 9.3×10^9 |
| ${}^{13}\text{C}(t, \alpha){}^{12}\text{B}$ | 2.28 MeV | 13.37 MeV | 20 ms | 100 mb | 5.4×10^9 | 1.1×10^{10} | 3.5×10^{11} |

Table 1—
A summary of our estimated $t + {}^9\text{Be}$, $t + {}^{18}\text{O}$ and $t + {}^{13}\text{C}$ reaction yields for the different mix scenarios.

Intrinsic Decay of Quantum Many-Body Systems

George E. Cragg and Arthur K. Kerman
(Massachusetts Institute of Technology)

We present a novel many-body decay mechanism inherent in low-density bosonic systems at zero temperature. Exemplified by atomic Bose-Einstein condensates, such systems can be produced experimentally, thereby providing a natural test bed for theoretical models. Specifically, we explore the physics of atom-molecule condensates, coupled through a Feshbach resonance. Using a variational procedure on the corresponding Hamiltonian, an equation of state is found revealing a two-piece collapsing ground state in which only a molecular condensate component is present up to some critical density. Although the usual low-density atomic condensate energy per particle dependence is found in an excited state, it is associated with a complex-valued chemical potential, where the imaginary part quantifies the underlying decay of this state. (A more detailed analysis of this problem is given in Ref. [1].) Using the random phase approximation (RPA), the excited state is seen to decay into collective phonon excitations of the ground state.

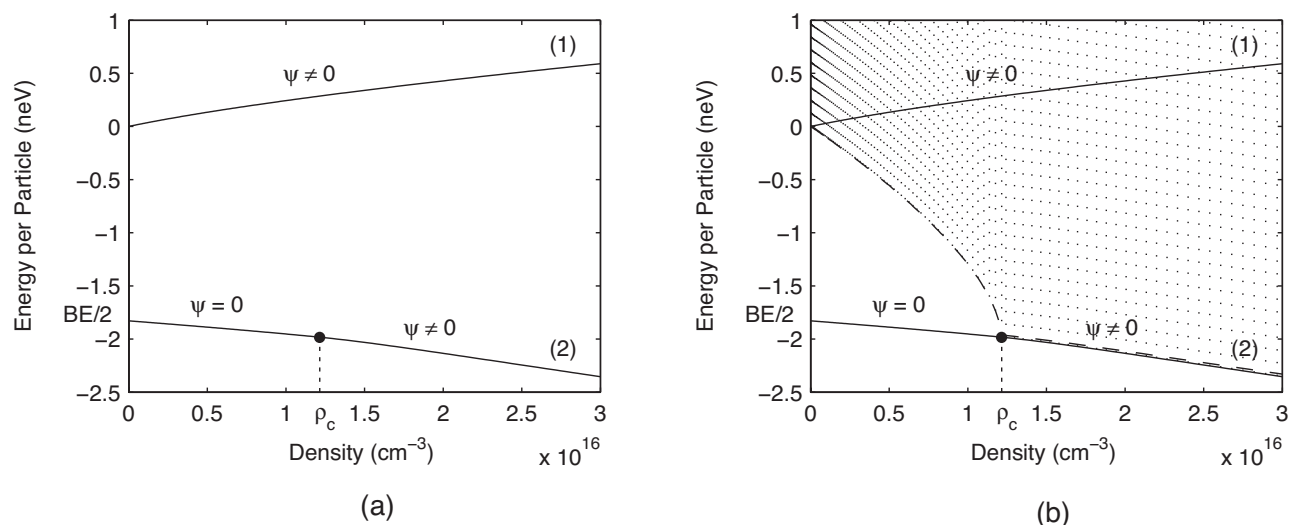
Since the production of Bose-Einstein condensates in the laboratory, many schemes have been proposed to control the interatomic interactions in these gases. One such scheme relies on the Feshbach resonance, a phenomenon in which two atoms combine to form an intermediate molecular state. Since the electronic spin configurations of the atoms in this quasi-bound state is different from the initial configurations of the constituent atoms, these two states have an energy difference that can be tuned by an external magnetic field using the Zeeman effect. Consequently, when the binding energy is brought close to the energy of the colliding atoms, the appearance of this molecular state increases

thereby modifying the scattering physics of the interaction. Near zero energy, the atomic interactions are described by a single parameter, the s-wave scattering length, a , which is positive for repulsive interactions, but negative for attractive interactions. Thus, by controlling the sign and magnitude of the scattering length, a Feshbach resonance can be used to tune the effective interparticle interactions. Specifically, we treat the case of ^{85}Rb , which has a large, negative background scattering length, $a_{bg} = -450a_0$ ($a_0 = \text{Bohr radius}$), indicating a collapsing condensate. By exploiting the Feshbach resonance at a magnetic field of approximately 155 G, the scattering length can be tuned to positive values yielding a stable condensate as verified by experiment [2].

A variational analysis of the uniform Hamiltonian reveals much richer physics than expected from simple scattering length arguments. In spite of being in the positive scattering length regime, there is still a collapsing ground state in the system. Moreover, this ground state has a unique two-piece structure, which is best described by the atomic order parameter, ψ , or the mean density of the atomic condensate, ψ^2 . Containing no atomic condensate ($\psi = 0$), the first piece of the ground state is composed of only a molecular condensate and correlated atom pairs. Starting at half the molecular binding energy, this section continues down to some critical density ρ_c where it terminates, as shown in Fig. 1(a). At this critical point, the second piece begins where the atomic order parameter, starting from zero, grows with increasing density. Because there is a marked difference in the density dependence of the energy per particle, this solution is of a fundamentally distinct nature from that of ordinary collapsing condensates. In particular, there is a quantum phase transition at the critical density since the compressibility is discontinuous at this point.

In addition to the collapsing ground state, the “stable” solution seen in experiments is associated with a complex-valued chemical potential, μ , that has the density expansion

$$\frac{2m}{\hbar^2} \mu = 8\pi a \rho - i \frac{\sqrt{\pi}}{3} 256 a^{5/2} \rho^{3/2} + \dots$$



Relating μ to the energy per particle,

$$e(\rho) = (1/\rho) \int_0^\rho \mu(\rho') d\rho', \text{ obtains}$$

the observed low-density dependence of $e \sim 4\pi a\rho$. Since the chemical potential plays the role of phase of the atomic field, its imaginary part has a natural interpretation as

$$\text{a decay rate, } \Gamma = (256\sqrt{\pi}\hbar/3m)a^{5/2}\rho^{3/2}.$$

Using the ^{85}Rb parameters of the experiment at $B = 162.3$ G, a decay time of approximately 14 s is obtained, which is in qualitative agreement with the observed time of 10 s [2]. Since particle number is conserved, this decay represents a flux of particles from the excited state into phonon modes of the ground state. Quantitatively, this is confirmed by an RPA analysis where the spectrum of excitations is found by expanding all quantities around the stationary ground state solution. The results of this analysis are shown in Fig. 1(b).

Finally, typical losses in atomic condensates are attributed to two- and three-body mechanisms described using semi-classical arguments. As opposed to these phenomenological loss pictures, we have found that there is an intrinsic decay in these coupled systems, accounted for in the many-body physics of the problem.

Most importantly, the predicted dependencies on density and on scattering length can be measured in experimental tests of this theory.

This work was supported by the Massachusetts Institute of Technology-Los Alamos National Laboratory Collaborative Research Grant to Develop an Understanding of Bose-Einstein Condensates, contract number 19442-001-99-35.

[1] G.E. Cragg and A.K. Kerman, "A Complex Chemical Potential: Signature of Decay in a Bose-Einstein Condensate," *Phys. Rev. Lett.* (submitted).

[2] S.L. Cornish et al. "Stable ^{85}Rb Bose-Einstein Condensates with Widely Tunable Interactions," *Phys. Rev. Lett.* **85**, 1795 (2000).

For more information, contact
George E. Cragg (cragg@mit.edu).

Acknowledgements

We would like to acknowledge the MIT-Los Alamos Collaborative Research Grant to Develop an Understanding of Bose-Einstein Condensates, contract number 19442-001-99-35.

Figure 1—
(a) The real part of the excited state (1) and the collapsing ground state (2) are evaluated at a magnetic field of $B = 162.3$ G with the parameters given in Ref. [2].
(b) The same figure as in (a) with the shaded region showing the continuum of excitations of the ground state solution. This spectrum not only contains the excited state, but also exhibits an energy gap along the first piece of the ground state.

Neutron Cross Sections for Reactions on ${}^6\text{Li}$ and ${}^9\text{Be}$

Gerald M. Hale (T-16)

Neutron cross sections on light elements are used in many applications of interest to the laboratory. The ${}^6\text{Li}(n,t){}^4\text{He}$ reaction, for example, is widely used as a neutron standard at low energies and as a means of breeding tritium with fission-spectrum neutrons. Beryllium is often used as a reflector material in integral assemblies and as a neutron multiplier because of the relatively low threshold of the $(n,2n)$ reaction on ${}^9\text{Be}$.

We have been studying the ${}^6\text{Li}(n,t){}^4\text{He}$ reaction within a broader R-matrix analysis of reactions in the ${}^7\text{Li}$ system for a number of years. Some recent results for the reaction cross section from this analysis are shown

in Fig. 1. The calculated curve is compared in the resonance region with measurements of Drosg and of Macklin. Also shown is the evaluation from Lawrence Livermore National Laboratory's Evaluated Nuclear Data (ENDL) library. The differences between the curves in region above about 800 keV may be important for understanding integral assemblies, and they are being investigated further.

Part of our work on the reactions in the $A = 10$ systems involved analyzing the ${}^{10}\text{Be}$ system in order to determine the structure of the isospin-1 part of these systems. Figure 2 shows a comparison of the measured $n + {}^9\text{Be}$ total cross sections with the calculation, and with the present ENDF/B-VI evaluation. The level structure found in this analysis differs somewhat from that usually given for ${}^{10}\text{Be}$. The noticeable difference between the evaluated curves at low energies may have practical significance in studies done with integral assemblies having beryllium reflectors. A systematic bias with beryllium thickness has been found in those studies indicating that the ENDF/B-VI scattering cross sections for ${}^9\text{Be}$ are too high at low energies.

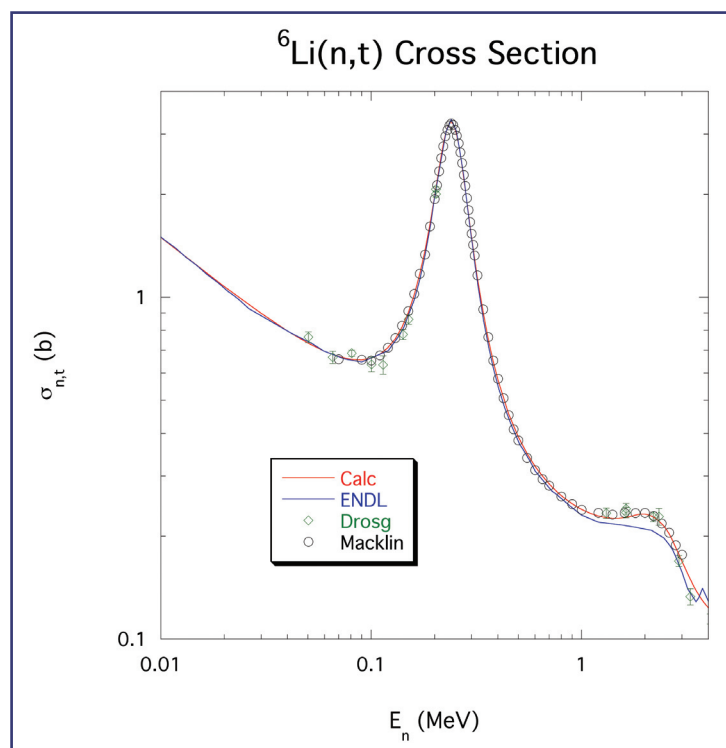


Figure 1—
R-matrix calculation
(red curve) compared to
measurements by Drosg
(green triangles) and by
Macklin (black circles),
and to the ENDL eval-
uation (blue curve).

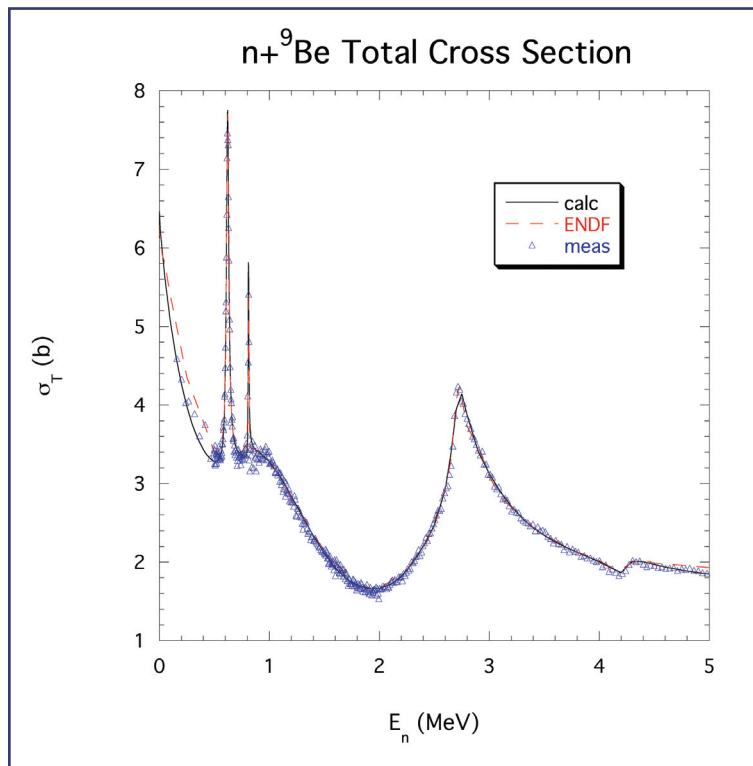


Figure 2—
Calculated total cross sections (black curve) for neutrons on ^9Be , compared with experimental measurements (blue triangles) and with the ENDF/B-VI evaluation (dashed red curve).

For more information, contact Gerald Hale (ghale@lanl.gov).

Acknowledgements

We would like to acknowledge NNSA's Advanced Simulation and Computing (ASC), Materials and Physics Program for financial support.

Combining Differential and Integral Cross Sections to Improve Nuclear Data for Fission Applications

*Toshihiko Kawano (T-16),
Kenneth M. Hanson (CCS-2/T-16),
Stephanie C. Frankle (X-5), Patrick Talou
and Mark B. Chadwick (T-16), and
Robert C. Little (X-5)*

Since high accuracy is required for fission cross sections of uranium and plutonium isotopes in neutron transport calculations, improvement of fission cross-section data in the evaluated nuclear data libraries has very high priority in a nuclear data study. The fission cross-section data (differential data, as a function of neutron energies) have been measured in various laboratories in the past. However, we still see discrepancies among different experimental data sets, which leads to an inaccurate prediction of neutron multiplication.

The critical assembly experiments at Los Alamos National Laboratory (LANL) such as Godiva and Jezebel, which are relatively simple, well characterized, and highly accurate, have been used for data testing and validation. We have utilized those integral measurements to constrain the differential fission cross sections by using a Bayesian technique. With this method, we can reduce uncertainties in the fission cross sections, and the combined differential/integral data can predict the neutron multiplication within the accuracy of LANL critical assembly experiments, which are typically less than 0.5%.

The fission cross section of Pu-239 was evaluated based on the differential experimental data, and those uncertainties (variance/covariance) were estimated from those experiments, which are shown by the red line in Fig. 1 (variance) and Fig. 2 (correlation matrix). We performed the neutron transport calculations for Jezebel, and sensitivity coefficients of cross sections to the neutron multiplicity were obtained. Then the fission cross sections were adjusted to the Jezebel experiment with the Bayesian method. The combined uncertainties are shown in Fig. 1 by the blue line. The change in the fission cross sections are usually very small. However, the uncertainties become smaller and negative correlations appear as shown in Fig. 3.

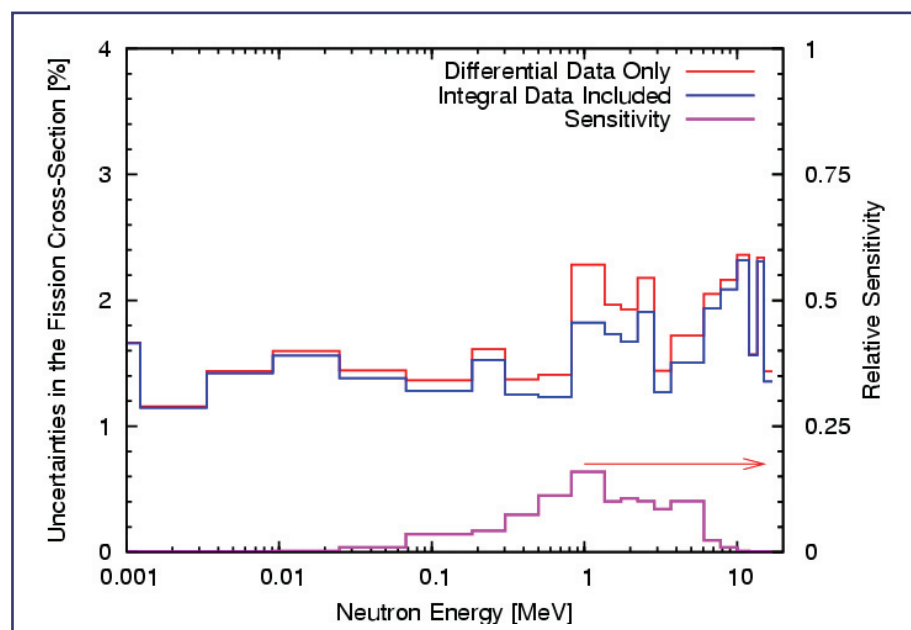


*Figure 1—
Estimated uncertainties
in the Pu-239 fission
cross sections.*

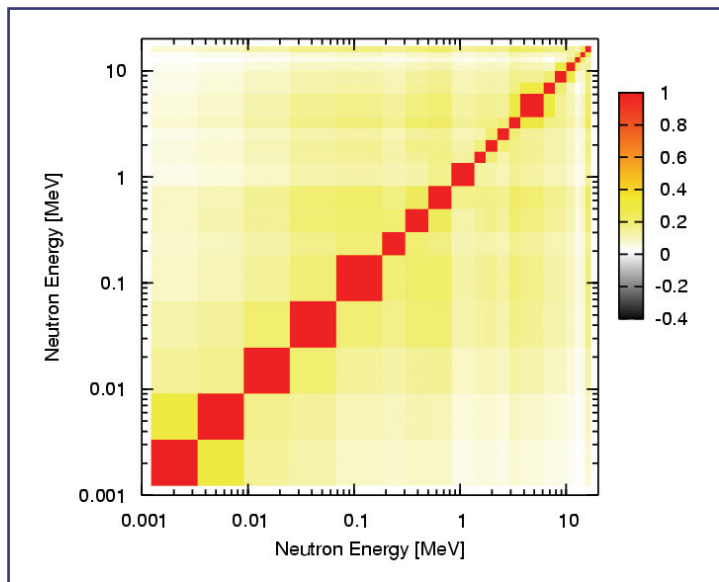


Figure 2—
Correlation matrix
for the Pu-239 fission
cross sections. The dif-
ferential data are only
included.

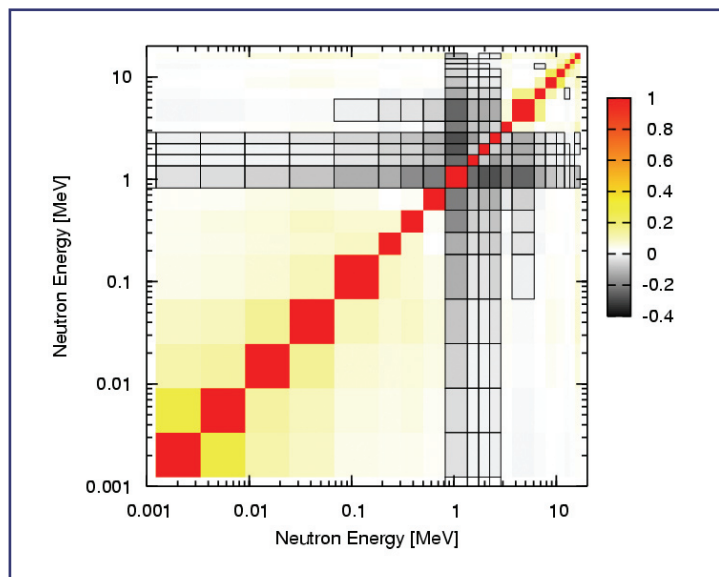


Figure 3—
Correlation matrix for
the Pu-239 fission cross
sections. The integral
data are combined with
the differential data.

These negative correlations constrain the fission cross sections to keep the integral quantities constant. If we generate randomly sampled fission cross section ensembles in accordance with this covariance, the calculated neutron multiplicities for Jezebel form a Gaussian distribution of 0.2% uncertainty.

*For more information, contact
Toshihiko Kawano (kawano@lanl.gov).*

Acknowledgements

We would like to acknowledge NNSA's Advanced Simulation and Computing (ASC), Verification and Validation Program for financial support.

Correlated Neutron Emission in Fission

Sebastien Lemaire, Patrick Talou, Toshihiko Kawano, Mark B. Chadwick, and David G. Madland (T-16)

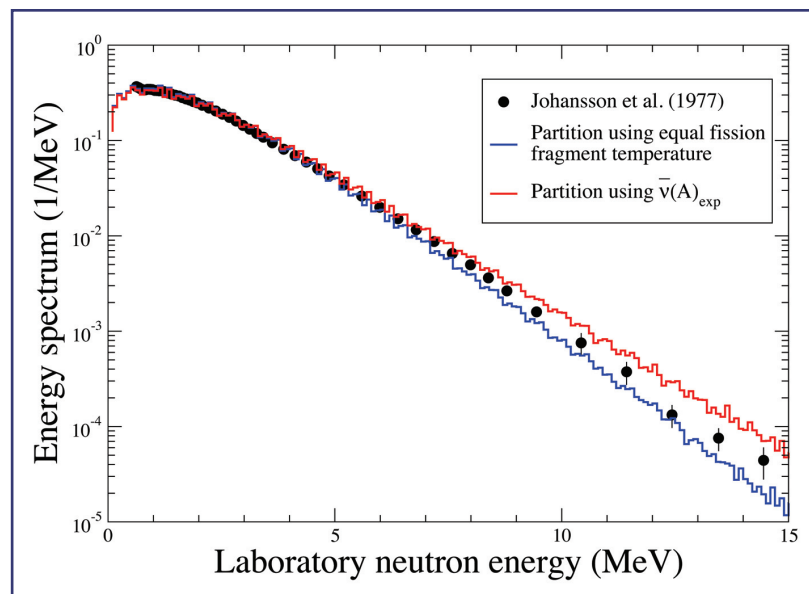
We have developed a new and powerful tool to study the process of sequential neutron emission from fission fragments (FF). We have implemented a Monte Carlo simulation of this decay process that allows us to infer important physical quantities that could not be assessed otherwise, for instance, within the original Los Alamos model framework. In particular, the multiplicity distribution of prompt neutrons $P(\nu)$, the distribution of ν as a function of the FF mass number, and neutron-neutron correlations can all be inferred from the present work.

This research is motivated in part by the needs of detecting correlated neutrons from a fission chain, for active and passive detection of special nuclear materials for nonproliferation applications.

Within this approach, we calculate both the center-of-mass and laboratory frame prompt neutron energy spectra, the prompt neutron multiplicity distribution $P(\nu)$, and the average total number of emitted neutrons as a function of the mass of the fission fragment $\bar{\nu}(A)$. Two assumptions for partitioning the total available excitation energy among the light and heavy fragments are considered. One assumption is that the temperatures in the light and heavy fragments are equal (an hypothesis identical to the one made in the Los Alamos model [1]) at the instant of scission. In the alternative hypothesis, the experimental $\bar{\nu}(A)$ is used to infer the initial excitation of each fragment. Preliminary results for the neutron-induced fission of ^{235}U (at 0.53 MeV neutron energy) and for the spontaneous fission of ^{252}Cf have been obtained.

For the neutron-induced reaction on ^{235}U , the neutron energy spectrum in the laboratory frame is shown in Fig. 1, as calculated using the two different hypotheses for distributing the total available excitation energy among the FF. Also shown for comparison are the experimental data points by Johansson and Holmqvist [2]. The spectrum obtained by assuming equal nuclear temperatures in both FF at scission is shown to be too soft when compared with experimental data, while the spectrum obtained by splitting the energy according to $\bar{\nu}_{\text{exp}}(A)$ is too hard.

Figure 1— Neutron energy spectrum for $n(0.53 \text{ MeV}) + ^{235}\text{U}$ reaction. The red line is the Monte Carlo calculation result assuming partitioning of the FF total excitation energy as a function of $\bar{\nu}(A)$ and the blue line is the result obtained under the assumption of an equal temperature of complementary FF. The experimental points are from Johansson and Holmqvist [2].



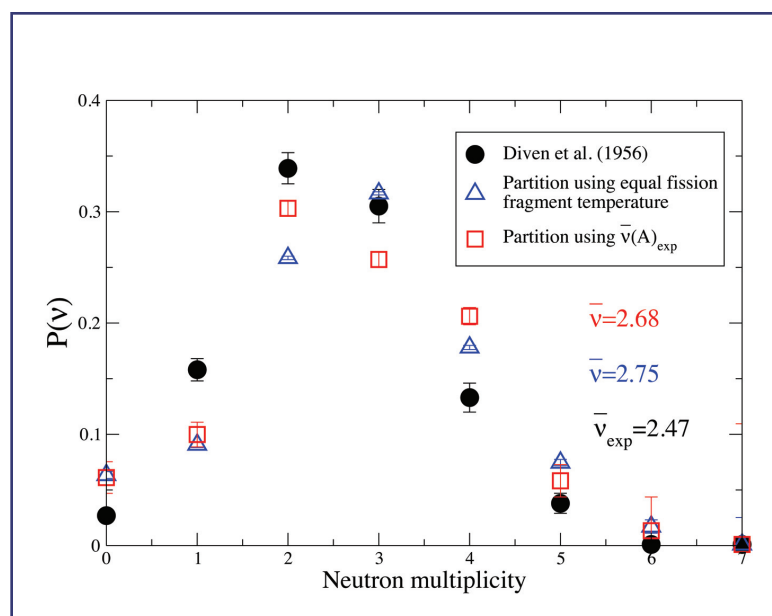


Figure 2— Neutron multiplicity distribution for $n(0.53 \text{ MeV}) + {}^{235}\text{U}$ reaction. Open square symbols \square are from our Monte Carlo calculation assuming partitioning of FF total excitation energy as a function of $\bar{\nu}(A)$, triangles Δ are the result obtained under the assumption of an equal temperature of complementary FF. The full points are experimental data from Diven et al. [3].

The calculated neutron multiplicity distribution $P(\nu)$ is compared to the experimental distribution by Diven et al. [3] in Fig. 2. In both calculated cases, the average $\bar{\nu}$ of the distribution is larger than the experimental value ($\bar{\nu}_{\text{exp}} = 2.47$, Diven et al. [3]). We found $\bar{\nu} = 2.75$ in the case of equal nuclear temperature for both FF and $\bar{\nu} = 2.68$ in the other case. In the case of ${}^{252}\text{Cf}$ spontaneous fission, similar qualitative conclusions can be drawn. More details can be found in [4].

Acknowledgements

We would like to acknowledge NNSA's Advanced Simulation and Computing (ASC), Materials and Physics Program for financial support.

- [1] D.G. Madland and J.R. Nix, *Nucl. Sci. Eng.* **81**, 213 (1982).
- [2] P.I. Johansson and B. Holmqvist, *Nucl. Sci. Eng.* **62**, 695 (1977).
- [3] B.C. Diven, et al., *Phys. Rev.* **101**, 1012 (1956).
- [4] S. Lemaire, et al., in *Proceedings of International Conference on Nuclear Data for Science & Technology, ND2004, Santa Fe, Sept. 26-Oct. 1, 2004* (AIP, Melville, NY, 2005), in press.

For more information, contact
Sebastien Lemaire (lemaire@lanl.gov).

Importance of Proton-Nucleus Strong Interaction to Proton-Radiography Simulation

Lon-Chang Liu (T-16)

The use of high-energy protons (20–50 GeV) to probe the internal structure of thick objects has added a new dimension to radiographic studies. One may mention [1], among other studies:

1. The mean free path λ of high-energy protons is much longer than that of x-rays. The huge difference in the mean free paths has an important consequence. For example, the beam attenuation factor (N_0/N) of high-energy protons in C, Fe, Pb with a thickness 200 g/cm² are 28, 11, and 6, respectively, while those of 15-MeV x-rays are 30, 518, and 66910. In other words, high-energy protons penetrate much deeper into materials.
2. The proton is a charged particle. It, therefore, interacts with material through both the electromagnetic and strong nuclear interactions, thus providing

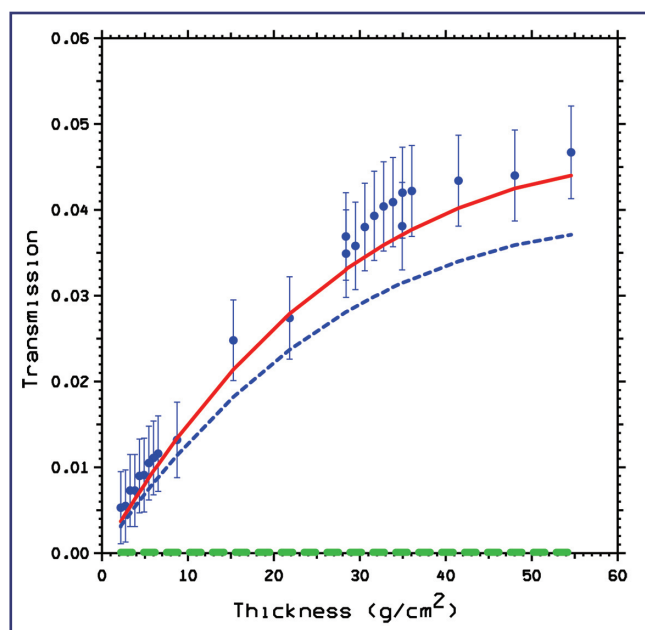
valuable information on the material compositions, such as the ratio Z/A , of the targets.

There is a coordinated effort at Physics (P), Applied Physics (X), Los Alamos Neutron Science Center (LANSCE) and Theoretical divisions in understanding the proton-radiography technologies. While the multiple p-nucleus electromagnetic interaction can be calculated with the aid of multiple Coulomb scattering theories [2], any Monte Carlo type simulation of multiple nuclear scattering in a thick object needs proton-nucleus differential cross sections as the basic input. However, in the literature there are only sparse data available at proton-radiography energies.

We have developed an eikonal optical model for proton-nucleus scattering and provided differential cross sections for 18 nuclei/isotopes ranging from $A = 3$ (triton) to $A = 239$ (plutonium) at a fine incoming proton momentum interval between 1 and 50 GeV/c. Our model predictions agree well with the data available in the open literature. They also agree with the results given by the Glauber model for nuclei having $A \leq 12$.

Our cross sections have been used by the Diagnostic Methods Group (X-5) in their MCNP code and have since been used by LANSCE in their simulations. One example of the important effect of p-nucleus elastic scattering is shown in Fig. 1 [3]. In this

Figure 1—
Comparison of a PRAD simulation by Neri and Walstrom [3] with Carbon step-wedge data measured at incident proton momentum 23 GeV/c. The data are given in blue with error bars attached. The simulations given by using MCS alone, using MCS together with elastic nuclear scattering, and using MCS, elastic nuclear scattering, quasielastic nuclear scattering are represented, respectively, by the green, blue, and red curves.



figure, the data are from Experiment EA955 performed at Brookhaven National Laboratory with a proton beam of incident momentum 23 GeV/c. The figure gives the dependence of the transmission coefficient as a function of target thickness. In this particular measurement in order to enhance the contrast of proton radiographic image, an anti-collimator was used to block the outgoing protons at angles between 0 and 4.56 mrad. As we can see, if only the multiple Coulomb scattering (MCS) is considered in the simulation, the predicted transmissions will be nearly zero (the green line), which clearly disagree with the data. However, when the p-¹²C elastic differential cross sections provided by T-16 are taken into account, the blue curve is obtained. This curve illustrates the dramatic effect of nuclear scattering. A further improvement has been noted when p-nucleus quasielastic (QEL) scattering is also taken into account (the red curve).

To understand the result in Fig. 1, I present in Fig. 2 the p-¹²C Coulomb and nuclear elastic scattering, separately. As we can see, the Coulomb scattering is dominant only within a very small solid angle which is almost completely blocked by the collimator. What were observed are, in fact, almost entirely due to nuclear scattering beyond the collimator cutoff angles.

The QEL scattering cross sections used for generating the red curve in Fig. 1 were modeled in Ref. [3], where one assumed

$$(d\sigma/d\Omega)_{pA}^{q.el.} = A_{eff} \times (d\sigma/d\Omega)_{pp}^{el.}$$

with A_{eff} being a parameter. Here, the subscripts pA and pp refer, respectively, to proton-nucleus and proton-proton. This class of model has also been extensively used by other research groups. However, it can underestimate the QEL contribution because the model uses essentially the 2-body pp kinematics. As high-energy protons easily fragment the nucleus, we are currently developing a QEL model which takes into consideration the many-body aspect of the kinematics and dynamics. Preliminary results indicate that our model gives bigger QEL contributions.

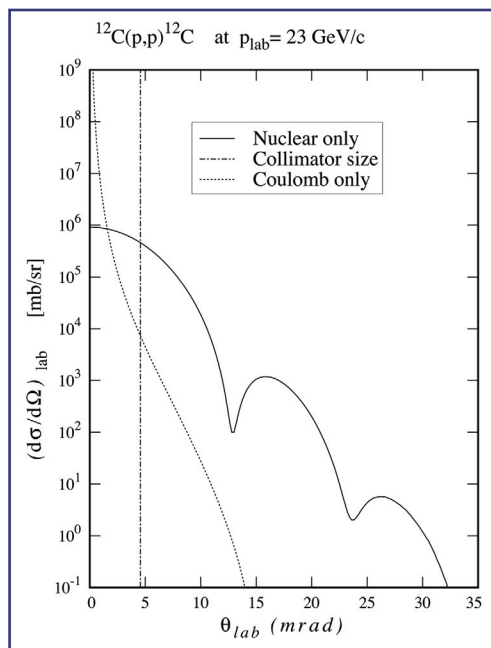


Figure 2—
Calculated proton-¹²C Coulomb and elastic differential cross sections for incident proton momentum 23 GeV/c. The anticollimator blocks the beam scattered into angles between 0 and 4.56 milliradians.

In summary, it has been demonstrated that proton-nucleus elastic and quasielastic scatterings play a significant role in proton radiography. We are currently developing a refined model for quasielastic scattering. We will also model diffractive production, another important p-nucleus strong interaction channel that has not been fully studied. We are confident that a precise simulation of proton radiographic process will soon be available.

- [1] Communication from Physics Division.
- [2] G. Molière, *Z. Naturforsch.*, **3a**, 78 (1948); an English version of the theory can be found in H.A. Bethe, *Phys. Rev.* **89**, 1256 (1953).
- [3] F. Neri and P.L. Walstrom, "A Simple Empirical Forward Model for Combined Nuclear and Multiple Coulomb Scattering in Proton Radiography of Thick Objects," Los Alamos National Laboratory report LA-UR-03-9011 (December 2003).

For more information, contact
Lon-Chang Liu (liu@lanl.gov).

Acknowledgements

I would like to acknowledge NNSA's Advanced Simulation and Computing (ASC), Verification and Validation Program for financial support.

Critical Assembly Data Testing for Nuclear Cross Sections

*Robert E. MacFarlane and
Mark B. Chadwick (T-16),
Michael MacInnes (X-2), and
Robert C. Little (X-5)*

The fast critical assemblies at the Los Alamos Critical Experiment Facility (LACEF) represent a unique capability within the DOE/NSA complex for studying nuclear criticality. Measurements over the last 50 years at LACEF have provided integral data that provide important tests of fundamental nuclear cross sections that Group T-16 develops for applications in nuclear technology. It is widely known that measurements of the criticality (“k-eff”) of a system, can be used to test certain aspects of the fundamental nuclear data quantities such as the fission cross section play a key role here. In this article we discuss a less well-known use of critical assemblies, where they have been used to measure reaction rates of certain important nuclear processes within the neutron spectrum provided by the assembly in order to provide important integral tests of the underlying nuclear cross section databases that we develop.

Many different critical assemblies have been developed over the years: Godiva is a bare sphere of highly enriched uranium (HEU); Jezebel is a bare sphere of plutonium; Jezebel-23 is a bare sphere of ^{233}U . The Flattop experiments involved spherical cores of HEU or plutonium surrounded by ^{238}U reflector material to make the composite systems critical. These different systems all produce neutron spectra within them that are “fast,” i.e., the neutrons are predominantly of energies in the 100 keV – few MeV region, but the exact spectra vary from system to system. Holes were drilled into the critical assemblies to allow foils of different materials to be placed such that they are exposed to different neutron spectra depending upon their location. An assembly with a softer neutron spectrum is BigTen whose core was made up of interleaved plates of ^{235}U and ^{238}U so as to have a lower effective enrichment than the fast assemblies.

The neutron spectrum gets softer as one moves out from the center of the assembly, thereby giving additional information about the quality of the cross-section data. An example of radiochemical ratio data as taken in traverses of the Flattop-25 and Topsy assemblies is shown in Fig. 1. The calculations were done using multigroup methods based on MATXS cross sections from NJOY formatted with TRANSX for PARTISN. A very fine group structure was used for high accuracy. The multigroup results were checked by tallying in several 1-cm shells using MCNP5, and good agreement was obtained.

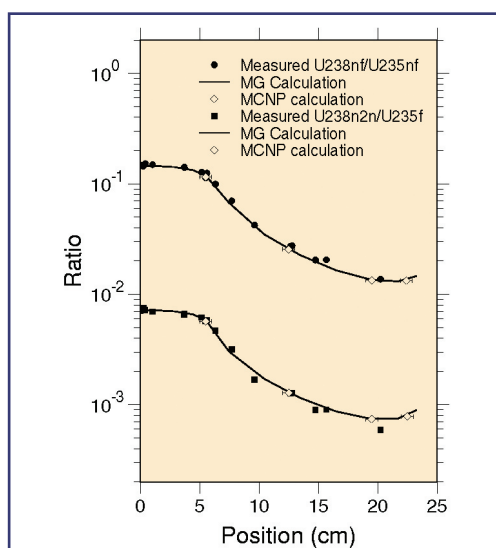


Figure 1—
Traverse data and
calculations.

Figure 2 shows a different presentation of these data in a form often used by radiochemists. The abscissa is a measure of the hardness of the spectrum, and this kind of plot often allows data from different assemblies to be compared on a common basis. This is demonstrated here using data from Flattop-25 and Topsy. Note how the calculated central ratio for BigTen also fits into this kind of plot. These comparisons of prediction with experiment provide some confidence in the quality of the $^{238}\text{U}(n,2n)$ cross section—both its magnitude and its energy-dependence.

In Fig. 3 we show a calculation compared with experimental values for ^{238}U neutron capture. Good agreement is found for most of the critical assembly measurements, though for harder-spectrum systems (large values of 238-fission/235-fission) there is an indication of an underprediction of the data by 5–10%. This is valuable information as it tells us that a new study of ^{238}U neutron capture in the ~ 1 MeV region is needed. Furthermore, for this reaction and many other similar capture reactions, there is a lack of fundamental capture cross-section data measurements in this energy region, so the integral critical assembly information is particularly useful.

Neutron capture on ^{241}Am is shown in Fig. 4 for different critical assembly spectra. In this reaction, the capture can lead to both an isomeric and ground state in ^{242}Am .

It is the ground state that then beta decays relatively quickly to make ^{242}Cm , which is then measured by radiochemists. Again, we see good agreement between the calculations and the measurements, except for the harder-spectrum systems where the measurements appear to be underpredicted by up to 15%. This tells us that the ^{241}Am capture cross section to the ground state may be too low in our current evaluation in the MeV region—something that we will be studying using theory and experiment in a new LDRD/DR on americium that is now starting.

Finally, in Fig. 5, we show two important reaction rates for iridium: the $^{193}\text{Ir}(n,n')$ cross section for creating the isomer, and the $^{191}\text{Ir}(n,g)$ cross section. Iridium plays an important role as a radiochemical detector

in weapons diagnostics. A new evaluation for the iridium cross sections has been recently completed, representing collaborations between T-16 and T-6 theorists, Los Alamos Neutron Science Center and Chemistry Division experimentalists, and Applied Physics Division. The good integral testing performance shown in this figure provides some confidence in the accuracy of the new iridium cross sections. Again, the fact that the calculation predicts reasonably well the shape of the (n,n') isomer reaction provides confidence in the energy-dependence obtained from the recent T/LANSCE cross-section evaluation.

For more information, contact
Robert E. MacFarlane (ryxm@lanl.gov).

Acknowledgements

We would like to acknowledge NNSA's Advanced Simulation and Computing (ASC), Materials and Physics Program, for financial support.

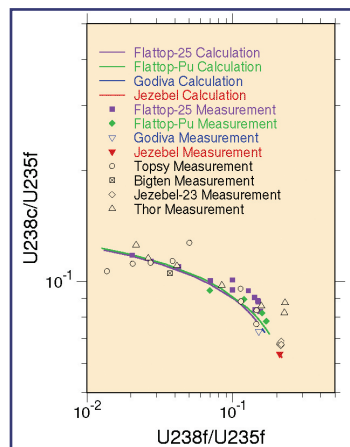
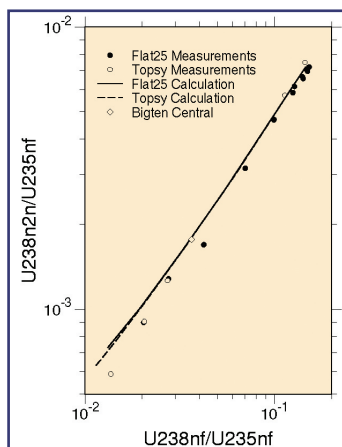


Figure 2—
Radiochemical plot
from traverse.

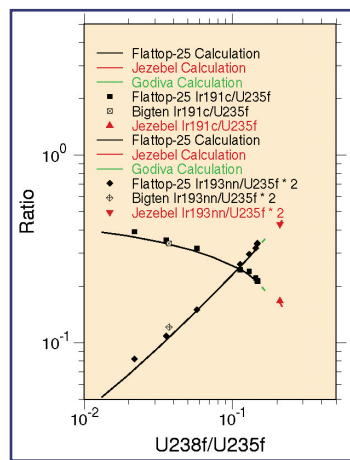
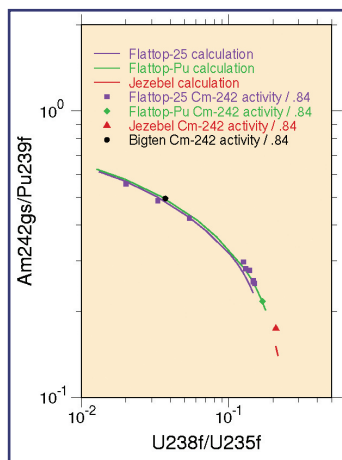


Figure 3—
Radiochemical plot for
 $^{238}\text{U}(n,g)$.

Figure 4—
Radiochemical plot for
 $^{241}\text{Am}(n,g)$.

Figure 5—
Radiochemical plot for
iridium.



Global Calculation of Nuclear Shape Isomers

Peter Möller (T-16), Ragnar Bengtsson and Peter Olivius (Lund University, Sweden)

Nuclear isomer states are long-lived states that often significantly impact various reaction rates in weapons environments.

The reaction rates on isomers are often challenging to measure. As a result many important rates are insufficiently known from experimental work; modeling them is therefore an important task.

We have previously reported that we have enhanced our model for calculating the potential energy of nuclei as a function of shape to also allow the study of axially asymmetric shapes. This is important both for modeling fission barriers of actinide nuclei and for modeling the structure of the nuclear ground state.

We report here on our use of the enhanced model for systematic, global calculations of the potential energy in the vicinity of the nuclear ground state for 7206 nuclei from ^{16}O to $A = 290$ from very proton-rich nuclei to very neutron-rich nuclei, for the following 3D grid of nuclear shapes: $\epsilon_2 = 0.0(0.025)0.45$, $\epsilon_4 = -0.12(0.02)0.12$, and $\gamma = 0(2.5)60$. In Fig. 1 we show as an example the calculated results for 12 different even-even nuclei. As is customary we display the calculated potential energy as a function of ϵ_2 and γ with ϵ_2 varying in the radial direction and γ in the angular direction. In each point the energy has been minimized with respect to the third shape-degree of freedom, ϵ_4 . In general this procedure will not yield a 2D surface that correctly describes the significant structures of the higher-dimensional space. However, we have found, by employing an imaginary water-immersion technique to analyze the full 3D space, that the saddles and minima in the 2D surfaces presented here correctly reflects the 3D structure. Our deformation coordinates are such that $\gamma = 0$ represents prolate nuclei and $\gamma = 60$ represents oblate nuclei. The tip of the “pie” corresponds to spherical shape. The energy is plotted in MeV, with $\dots -1, 0, 1, \dots$ MeV given by thick lines. The spacing between the thin lines is 0.2 MeV.

Table 1—
Table of potential-energy minima for nuclei for which at least two minima are found. The higher minima are shape-isomers. The optimal saddle points between all pairs of minima are also tabulated, as well as the values of the three shape coordinates associated with the minima and saddle points. Here we list a small section of the complete results of the global calculation, which is about 60 pages. The right column, labeled S.H., gives the saddle point height relative to the higher of the pair of minima tabulated on this line.

| Nucleus | | Minimum | | | | Saddle | | | | Minimum | | | | S.H. |
|--------------------|-----|--------------|--------------|----------|---------|--------------|--------------|----------|---------|--------------|--------------|----------|---------|------------------------|
| N | A | ϵ_2 | ϵ_4 | γ | E (MeV) | ϵ_2 | ϵ_4 | γ | E (MeV) | ϵ_2 | ϵ_4 | γ | E (MeV) | E_{sad} (MeV) |
| Z = 39 (Y) | | | | | | | | | | | | | | |
| 44 | 83 | 0.225 | 0.06 | 50.0 | 3.23 | 0.100 | 0.02 | 60.0 | 3.51 | 0.000 | 0.00 | 0.0 | 3.18 | 0.28 |
| 60 | 99 | 0.275 | -0.02 | 60.0 | 4.56 | 0.275 | 0.00 | 45.0 | 4.82 | 0.325 | 0.00 | 0.0 | 2.28 | 0.26 |
| 68 | 107 | 0.250 | 0.06 | 60.0 | 3.99 | 0.300 | 0.06 | 45.0 | 4.21 | 0.325 | 0.06 | 0.0 | 1.93 | 0.22 |
| 72 | 111 | 0.225 | 0.06 | 52.5 | 2.90 | 0.225 | 0.04 | 32.5 | 3.16 | 0.300 | 0.08 | 0.0 | 2.19 | 0.25 |
| 73 | 112 | 0.200 | 0.06 | 45.0 | 2.55 | 0.250 | 0.06 | 12.5 | 2.75 | 0.325 | 0.06 | 0.0 | 2.34 | 0.20 |
| 91 | 130 | 0.225 | -0.06 | 0.0 | 1.62 | 0.200 | -0.04 | 17.5 | 1.94 | 0.100 | -0.02 | 30.0 | 1.49 | 0.32 |
| | | 0.225 | -0.06 | 0.0 | 1.62 | 0.200 | -0.04 | 17.5 | 1.94 | 0.150 | -0.02 | 52.5 | 1.48 | 0.32 |
| | | 0.100 | -0.02 | 30.0 | 1.49 | 0.125 | -0.02 | 32.5 | 1.72 | 0.150 | -0.02 | 52.5 | 1.48 | 0.24 |
| Z = 40 (Zr) | | | | | | | | | | | | | | |
| 33 | 73 | 0.250 | 0.04 | 50.0 | 2.91 | 0.300 | 0.04 | 27.5 | 3.19 | 0.300 | 0.06 | 0.0 | 2.91 | 0.28 |
| 34 | 74 | 0.250 | 0.04 | 60.0 | 3.13 | 0.325 | 0.04 | 30.0 | 3.50 | 0.325 | 0.08 | 0.0 | 2.96 | 0.38 |
| 35 | 75 | 0.275 | 0.04 | 57.5 | 3.54 | 0.300 | 0.06 | 32.5 | 4.04 | 0.325 | 0.06 | 0.0 | 3.03 | 0.50 |
| 36 | 76 | 0.275 | 0.06 | 60.0 | 3.79 | 0.325 | 0.04 | 35.0 | 4.25 | 0.350 | 0.06 | 0.0 | 2.68 | 0.46 |
| 37 | 77 | 0.200 | 0.06 | 60.0 | 4.07 | 0.325 | 0.04 | 37.5 | 4.54 | 0.350 | 0.06 | 0.0 | 2.42 | 0.46 |
| 38 | 78 | 0.200 | 0.06 | 60.0 | 4.01 | 0.300 | 0.06 | 37.5 | 4.52 | 0.375 | 0.08 | 0.0 | 1.95 | 0.51 |
| 39 | 79 | 0.200 | 0.06 | 60.0 | 4.06 | 0.300 | 0.06 | 37.5 | 4.58 | 0.375 | 0.08 | 0.0 | 1.83 | 0.52 |
| 40 | 80 | 0.000 | 0.00 | 0.0 | 4.55 | 0.075 | 0.02 | 60.0 | 4.77 | 0.200 | 0.06 | 60.0 | 3.81 | 0.22 |
| | | 0.000 | 0.00 | 0.0 | 4.55 | 0.075 | 0.02 | 60.0 | 4.77 | 0.375 | 0.08 | 0.0 | 2.00 | 0.22 |
| | | 0.200 | 0.06 | 60.0 | 3.81 | 0.300 | 0.06 | 37.5 | 4.38 | 0.375 | 0.08 | 0.0 | 2.00 | 0.57 |
| 41 | 81 | 0.200 | 0.06 | 60.0 | 3.79 | 0.275 | 0.06 | 40.0 | 4.25 | 0.400 | 0.08 | 0.0 | 2.51 | 0.46 |
| 42 | 82 | 0.000 | 0.00 | 0.0 | 4.02 | 0.075 | 0.00 | 60.0 | 4.34 | 0.225 | 0.08 | 60.0 | 3.44 | 0.32 |
| | | 0.000 | 0.00 | 0.0 | 4.02 | 0.075 | 0.00 | 60.0 | 4.34 | 0.375 | 0.08 | 0.0 | 2.98 | 0.32 |
| | | 0.225 | 0.08 | 60.0 | 3.44 | 0.275 | 0.06 | 37.5 | 3.88 | 0.375 | 0.08 | 0.0 | 2.98 | 0.43 |
| 43 | 83 | 0.025 | 0.00 | 47.5 | 3.99 | 0.100 | 0.02 | 60.0 | 4.21 | 0.375 | 0.08 | 0.0 | 3.51 | 0.23 |
| | | 0.025 | 0.00 | 47.5 | 3.99 | 0.100 | 0.02 | 60.0 | 4.21 | 0.225 | 0.08 | 57.5 | 3.35 | 0.23 |
| | | 0.375 | 0.08 | 0.0 | 3.51 | 0.350 | 0.06 | 7.5 | 3.79 | 0.225 | 0.08 | 57.5 | 3.35 | 0.29 |
| 44 | 84 | 0.000 | 0.00 | 0.0 | 3.09 | 0.100 | 0.02 | 60.0 | 3.40 | 0.225 | 0.08 | 60.0 | 2.97 | 0.32 |
| 45 | 85 | 0.225 | 0.08 | 60.0 | 2.76 | 0.100 | 0.02 | 60.0 | 3.00 | 0.000 | 0.00 | 0.0 | 2.72 | 0.24 |

Several of the calculated potential-energy surfaces exhibit more than one minimum. In such surfaces we have indicated the minima with a dot and saddle points between all combinations of minima with crossed lines. For such nuclei we also tabulate pairwise all minima and the optimal saddle point between all pairs of minima and the associated shape parameters. A section of the global table is shown in Table 1. We plan to make the complete set of results, namely all contour surfaces, and a computer-readable version of the full table available on the T-16 web site.

Many nuclear properties are affected if shape isomers are present in nuclei. For example, in nuclear β -decay the decay can proceed both

to states in the lowest minimum, the nuclear ground state, and to states in the shape isomer. In neutron-induced reactions the reaction rates can be affected by the presence of a shape isomer. The availability of our global, calculated data base of shape-isomer properties is highly useful in developing models that take into account the isomer influence on reaction rates.

For more information, contact Peter Möller (moller@lanl.gov).

Acknowledgements

We would like to acknowledge NNSA's Advanced Simulation and Computing (ASC), Materials and Physics Program for financial support.

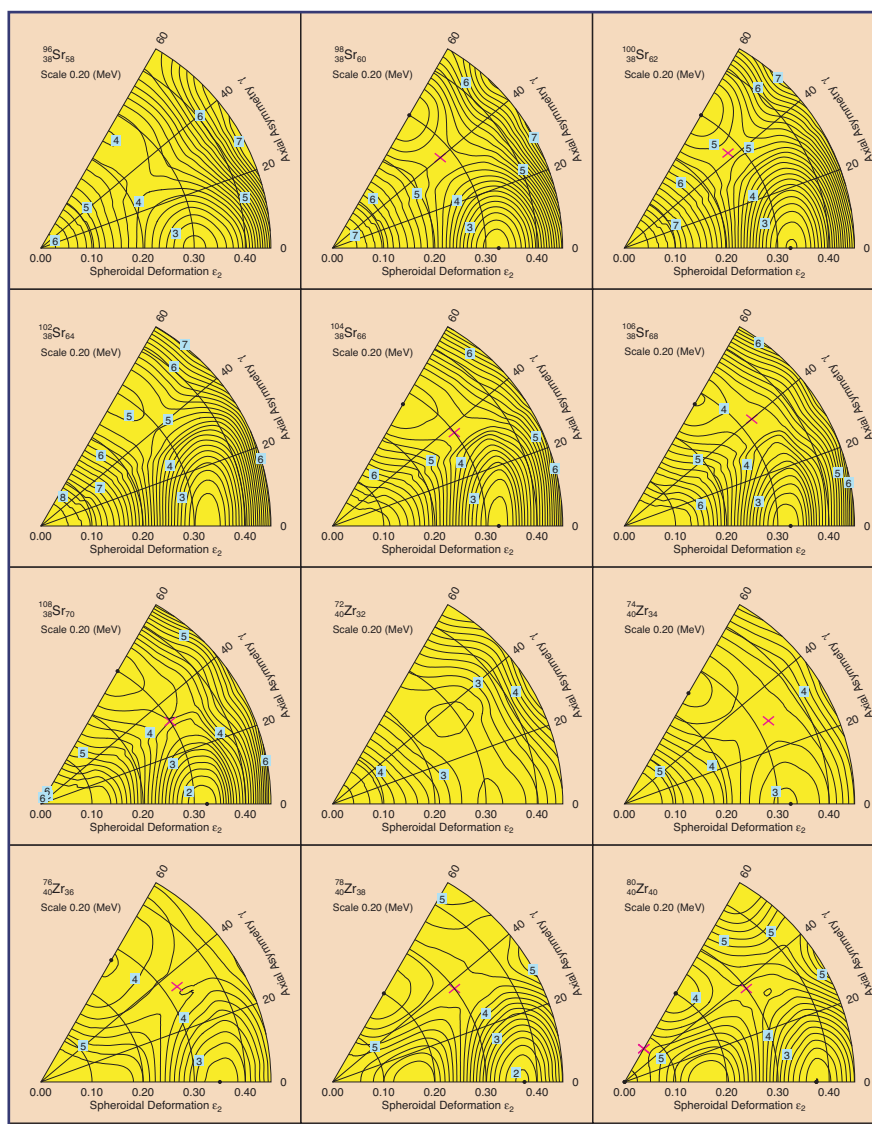


Figure 1—
Twelve calculated potential energy surfaces. Nine of the nuclei plotted have more than one minimum. The nucleus $^{80}_{40}\text{Zr}_{40}$ has one spherical minimum, one prolate minimum and one oblate minimum. Only minima deeper than 0.2 MeV are indicated.

Testing the Predictive Power of Nuclear-Structure Models Against New Experimental Data

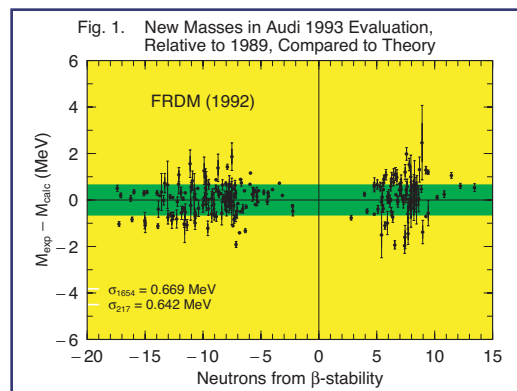
Peter Möller (T-16)

Figure 1—
Reliability of the FRDM (1992) in new regions of nuclei. The FRDM (1992) was adjusted to 1654 masses known in 1989. The figure shows the deviations between experimental and calculated masses for 217 new nuclei whose masses were measured between 1989 and 1993. The error is 4% smaller in the new region compared with that in the region where the model constants were adjusted. There are no systematic effects visible in the figure.

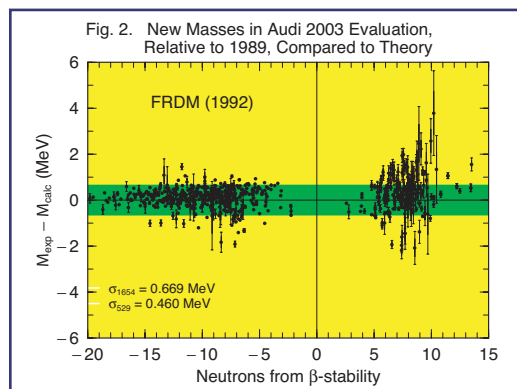
Figure 2—
Reliability of the FRDM (1992) in new regions of nuclei. The figure shows the deviations between experimental and calculated masses for 529 new nuclei whose masses were measured between 1989 and 2003. The error is 30% smaller in the new region compared with that in the region where the model constants were adjusted. There are no systematic effects visible in the figure.

The mass of a nucleus is one of its most primary properties. Nuclear masses are tabulated in many databases, for example ENDF.

In nuclear reaction-rate calculations the Q-value of the reaction is obtained from the nuclear masses of the reaction participants.



In α -decay the half-life of the decay may in many cases be determined to within a factor of 2 or 3 from the decay Q-value alone. At Los Alamos National Laboratory (LANL), nuclear mass models have been developed and refined over a period of about 30 years,



starting in the early 1970s. In these models the energy as a function of nuclear shape is calculated as a sum of a macroscopic liquid-drop model energy plus microscopic effects obtained from a deformed single-particle model. Reliable mass models are of paramount importance to provide masses to nuclear databases for nuclei for which no experimental masses are available. A key question is: Are the masses calculated for nuclei where no measurements are available reliable? Or, do the models diverge, as is often assumed, outside the data set to which the model parameters were adjusted? To address this question it is customary to compare published masses obtained from the models of interest to masses that are measured after the publication of the calculations. We argue that in addition one needs to address (1) if the basis of the model is sound, (2) if it is general enough to provide additional nuclear structure quantities, not just nuclear masses, and (3) if the model is global so that it is possible to calculate these properties for any or almost any nucleus with proton number Z and neutron number N . The LANL mass model fulfills these three conditions. The latest version, designated FRDM (1992), was finalized and provided to a limited community in September 1992, submitted for publication in 1993, and published in 1995 [1].

The FRDM (1992) model parameters were adjusted to a 1989 interim evaluation of experimental masses by Audi et al. In 1997 we compared the FRDM (1992) masses to 217 masses in a 1993 mass evaluation by Audi et al. that were not present in the 1989 set to which the model was adjusted. Figure 1 shows this comparison; specifically the model error remains constant in this region of new masses. Very recently a new experimental mass evaluation, the Audi 2003 evaluation, became available. This evaluation contains 529 new masses relative to the 1989 evaluation. We show in Fig. 2 the difference between these experimental masses and the corresponding calculated masses. The FRDM (1992) model error in this region of new masses is significantly lower than in the region where the model parameters were determined. Also there is no evidence of any systematic increase in model error with distance from stability. Furthermore we noticed that on the proton-rich side of

β stability (negative values of “neutrons from stability”) many of the points with the largest deviations in Fig. 1 are not present in Fig. 2! This means that on further evaluation these experimental data points were found incorrect and excluded from the 2003 evaluation!

It has been assumed by some that models that go beyond the single-particle model of the LANL mass model, for example self-consistent Hartree-Fock models based on two-body (Skyrme) interactions, would by nature of their added complexity lead to much better mass models. However, this expectation has so far not been fulfilled. The largest effort in this area is the work by the Brussels group. We compare in Fig. 3 their latest published calculated masses from 2001 (the HFB2 model [2]) to the same set of experimental masses as considered in Fig. 2. The HFB2 model discrepancy with data is much larger than the FRDM (1992) model, *despite* that this 2001 model was *adjusted* to more than 90% of the nuclei in this data set!

The Duflo-Zuker mass model of 1995 [3] is considered by some to show considerable promise. The reason is that the deviation between calculated masses and the 286 new masses measured since the model was presented is only 0.364 MeV, considerably smaller than the FRDM (1992) model error. Also, in their presentation the authors claim it is a “shell model.” However, in the end what they do is to fit the parameters of a simple function to data. Consequently one needs to be cautious about its reliability. Moreover it does not fulfill conditions 1 and 2 above.

It is instructive to compare the FRDM (1992), the HFB2, and the Duflo-Zuker mass models to additional experimental quantities. For lack of space we limit our additional comparisons here to the α -decay chain of the new element $^{278}_{113}\text{X}$ which was recently observed at RIKEN [4]. It is clear that only the FRDM model shows the characteristic change in slope around $Z = 107$ – 109 , an indication of a deformed stabilizing shell gap

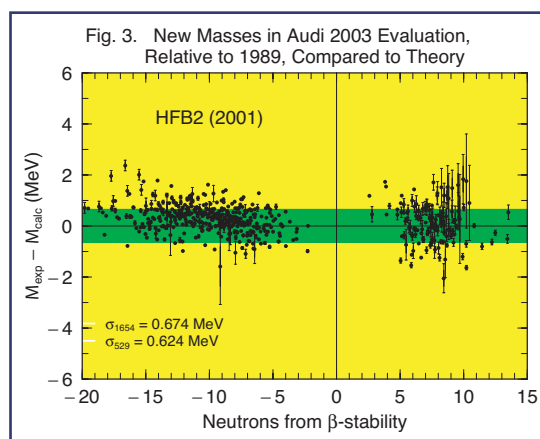


Figure 3—
Comparison of the HFB2 model calculated masses to the same experimental data set considered in Figs. 1–2. Although the HFB2 model was adjusted to more than 90% of the data in this figure [and just as the FRDM (1992) to more than 1600 additional masses known previously] the HFB2 model error is 35% larger than the FRDM (1992) model error in this region.

here. The deviations between data and the Duflo-Zuker model are all of the same sign. This means that the error of this mass model for element $Z = 113$ has grown to 5 MeV.

In summary we have tested the FRDM (1992) mass model and other models against a recently substantially expanded experimental database. In contrast to other models, the FRDM (1992) exhibits extraordinary reliability in the regions of new data. We therefore feel that with considerable confidence we can use this model in LANL databases to provide masses where experimental data are currently unavailable.

- [1] P. Möller, et al., *Atomic Data Nucl. Data Tables* **59**, 185 (1995).
- [2] S. Gorieli, et al., *Phys. Rev. C* **66**, 024326 (2002).
- [3] J. Duflo and A.P. Zuker, *Phys. Rev. C* **52**, R23 (1995).
- [4] Kosuke Morita, et al., *J. Phys. Soc. Jpn.*, **73**, 2593 (2004).

For more information, contact Peter Möller (moller@lanl.gov).

Acknowledgements

We would like to acknowledge NNSA's Advanced Simulation and Computing (ASC), Materials and Physics Program for financial support.

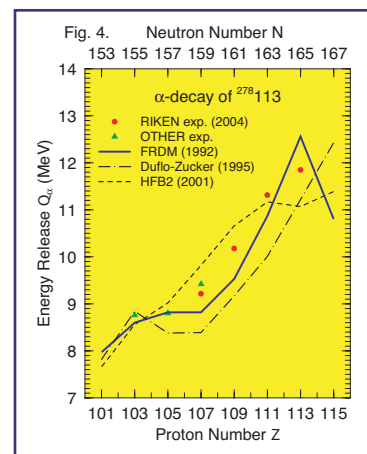


Figure 4—
Observed element $^{278}_{113}\text{X}$ α -decay chain compared with three models. The FRDM (1992) best reproduces the characteristic trends in the data that are due to microscopic shell effects.

Detection of Antineutrinos for Nonproliferation

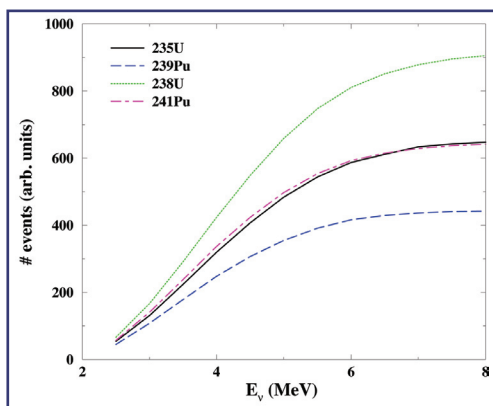
Michael Martin Nieto (T-8),
Anna C. Hayes, and Corinne M. Teeter
(T-6), William B. Wilson (T-16) and
William D. Stanbro (N-4)

It is widely reported that India obtained its weapons-grade plutonium (Pu) by running its unsafeguarded CANDU reactors to produce Pu. In this project we have been examining the feasibility of monitoring the Pu content of reactor fuel from the antineutrinos emitted. When a uranium ^{235}U or ^{239}Pu nucleus undergoes fission, the unstable fission products beta-decay, thus emitting antineutrinos.

However, the fact that reactor monitoring is a steady-state measurement means that time variation is not an issue. The energy spectrum of the antineutrinos ranges from zero to about 15 MeV and peaks at about 3 MeV. However, only a very small fraction of the antineutrinos emitted have energies above 8 MeV. The differences in the fission products produced in the fissioning of U versus Pu leads to a significant difference in the magnitude and shape of the respective antineutrino spectra. These differences and the fact that the emitted antineutrinos cannot be shielded are key to the concept of monitoring the core fuel.

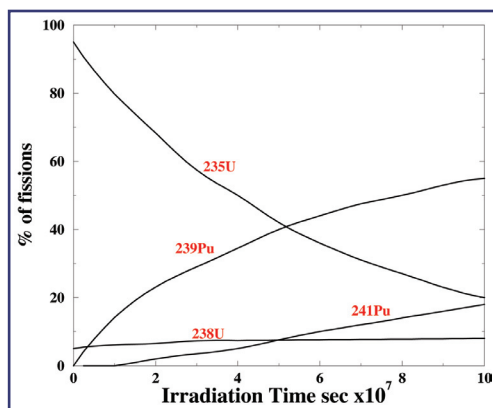
In the present work we restricted our studies to a Pressurized Water Reactor (PWR) similar to the San Onofre reactor in California. We examine the predicted time-dependent antineutrino spectra for a 2.7%-enriched PRW reactor. To test the sensitivity of the expected signals to the initial U enrichment we also examined a 4.2%-enriched PRW.

Figure 1—
The absolute magnitude of the detected antineutrino spectrum for ^{235}U is larger than for ^{239}Pu , so that the total number of antineutrinos detected changes with the relative fissioning fraction of the two isotopes in the reactor core.



On average, about five antineutrinos are emitted per fission. These antineutrinos are emitted over a period of up to minutes.

Figure 2—
The fission history for the 2.7% enriched (97.3% ^{238}U , 2.7% ^{235}U) reactor. As can be seen, the percentage of the total fission from ^{235}U steadily drops as a function of time, while that from ^{239}Pu steadily increases.



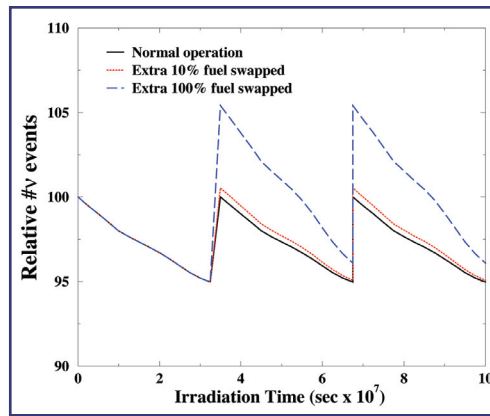
A 3.4 GW power reactor emits on the order of 10^{26} antineutrinos per day. The absolute magnitude of the detected antineutrino spectrum for ^{235}U is larger than for ^{239}Pu (Fig. 1), so that the total number of antineutrinos detected changes with the relative fissioning fraction of the two isotopes in the reactor core. Thus, for a fixed reactor power, the number of detected antineutrinos is a reflection of the core burn-up. The shape of the spectrum is also a measure of the core burn-up. As shown in Fig. 1, the cumulative number of antineutrinos (when folded over the detection cross section) as a function of antineutrino energy is different for the two species. By comparing the number of antineutrinos with energies up to 3 MeV with the number up to 6 MeV, pure ^{235}U and ^{239}Pu are easily distinguishable.

In Fig. 2 we show the fission history for the 2.7% enriched (97.3% ^{238}U , 2.7% ^{235}U) reactor. As can be seen, the percentage of the total fission from ^{235}U steadily drops as a function of time, while that from ^{239}Pu steadily increases. After about 3 years burning (30 GWd/MTU) the fuel has an isotopic composition of (95% ^{238}U , 1% ^{235}U , 1% ^{239}Pu , 3% high-level radioactive waste including $^{240,241}\text{Pu}$).

A large pressurized light water reactor has about 240 fuel assemblies, of which 80 are replaced at the same time every year, and the assembled are then shuffled in their location. When the reactor is running in equilibrium, at the beginning of each fuel cycle one-third of the fuel is fresh enriched U, one-third has been irradiated for 1 year and one-third for 2 years. At the end of the cycle one-third of the fuel has been irradiated for 3 years and is removed and replaced with fresh fuel. Each fuel assembly typically contains one-half ton of fuel. Therefore, in 3 years about 5 kg of Pu will be produced in each assembly of normal fuel.

Typical diversion scenarios would likely involve the diversion of an entire fuel assembly and replacement with fresh fuel. In principle, a single assembly would contain enough plutonium to make a nuclear weapon. An unannounced removal of 1–2 additional fuel assembly at the same time that other scheduled work was being carried out would require an accuracy in the antineutrino detection rate of better than 1%. The detection of this type of change would be a much more difficult task than observing the 5% change in the magnitude of the spectrum over one fuel cycle.

In Fig. 3 we compare the expected time-dependent antineutrino count rate under normal operation of a 2.7% PWR with that expected for a significant fuel diversion. In this latter case we have assumed that an additional unannounced 10% of the fuel was replaced during a scheduled fuel cycle management. The solid curve shows the relative change in the number of events on normal fuel management, i.e., at the end of the fuel cycle the 3-year exposed fuel is removed and at the start of the next cycle the core consists of 1/3 fresh 2.7% U fuel, 1/3 fuel irradiated for 1 year, and 1/3 irradiated for 2 years. The dotted curve shows a realistic and significant violation of the nonproliferation treaty in which an additional unreported 10% of the 2-year irradiated fuel has been replaced with fresh fuel. In this case the start of the new cycle involves a core with 37% fresh 2.7%



enriched U, 33% 1-year irradiated fuel, and 30% 2-year irradiated fuel.

In contrast to the above 10% diversion of the fuel scenario, gross diversions of fuel or gross deviations in the reactor operation from that announced would likely lead to quite detectable changes from the expected antineutrino spectrum. The long-dashed curve in Fig. 3 represents the expected number of antineutrino in the case that 2/3 (as opposed to the regular 1/3) of the irradiated fuel is replaced at the end of a 1-year cycle. In this scenario the start of the new cycle the core would consist of involves 2/3 fresh 2.7% U and 1/3 1-year irradiated fuel. This gross misuse of the reactor would lead to a 10% shift in the antineutrino count rate, to be compared with the 5% change expected under normal fuel-cycle management.

Thus, we conclude that antineutrino monitoring of reactors could be used to detect gross misuse of reactor for proliferation purposes. However, more subtle diversion of Pu, such as the diversion of a critical mass of Pu, would be very difficult.

For more information, contact
Michael Martin Nieto (mmn@lanl.gov).

Acknowledgements

We would like to acknowledge the Laboratory Directed Research and Development Program for financial support.

Figure 3—
Comparison of the expected time-dependent antineutrino count rate under normal operation of a 2.7% PWR with that expected for a significant fuel diversion. The solid curve shows the relative change in the number of events on normal fuel management. The dotted curve shows a realistic and significant violation of the nonproliferation treaty in which an additional unreported 10% of the 2-year irradiated fuel has been replaced with fresh fuel.

^8Be Nuclear Data Evaluation

Philip R. Page and Gerald M. Hale (T-16)

A reanalysis of two-body strong reactions leading to the ^8Be intermediate state was motivated by large discrepancies between various evaluations (Fig. 1).

An R-matrix analysis of experimental nuclear data on the reactions $^4\text{He}(\alpha,\alpha)$, $^4\text{He}(\alpha,p)$, $^4\text{He}(\alpha,d)$, $^7\text{Li}(p,\alpha)$, $^7\text{Li}(p,p)$, $^7\text{Li}(p,n)$, $^7\text{Be}(n,p)$, $^6\text{Li}(d,\alpha)$, $^6\text{Li}(d,p)$, $^6\text{Li}(d,n)$, and $^6\text{Li}(d,d)$, leading to the ^8Be intermediate state, has been completed in the last 2 years. About 4700 data points from 69 experimental references are included. The excitation energy above the ^8Be ground state is 25–26 MeV for all reactions except $^4\text{He}(\alpha,\alpha)$ and $^7\text{Be}(n,p)$. The data for the reactions $^4\text{He}(\alpha,\alpha)$ and $^6\text{Li}(d,d)$ do not fit well, but the other reactions fit with a $\chi^2/(\text{point})$ of less than the overall value of 7.9. Most of the 19 resonances found in the R-matrix analysis correspond to resonances formerly known

from experiment. Evaluated cross-section and angular dependence files in ENDF format were prepared for the twelve reactions $p^7\text{Li}$, $n^7\text{Be}$, $d^6\text{Li} \rightarrow \alpha^4\text{He}$, $p^7\text{Li}$, $n^7\text{Be}$, $d^6\text{Li}$. Maxwellian averaged temperature-dependent cross-sections in nuclear data interface (NDI) format were prepared for the six reactions $^7\text{Li}(p,\alpha)$, $^7\text{Li}(p,n)$, $^7\text{Be}(n,p)$, $^6\text{Li}(d,\alpha)$, $^6\text{Li}(d,p)$, and $^6\text{Li}(d,n)$.

Figure 2 indicates the $^6\text{Li}(d,p)$ cross-section obtained in the 2004 R-matrix analysis. Figure 2 should be compared with the former situation depicted in Fig. 1. Figure 3 shows the $^6\text{Li}(d,\alpha)$ reaction. Details of the 2004 analysis are available in [1].

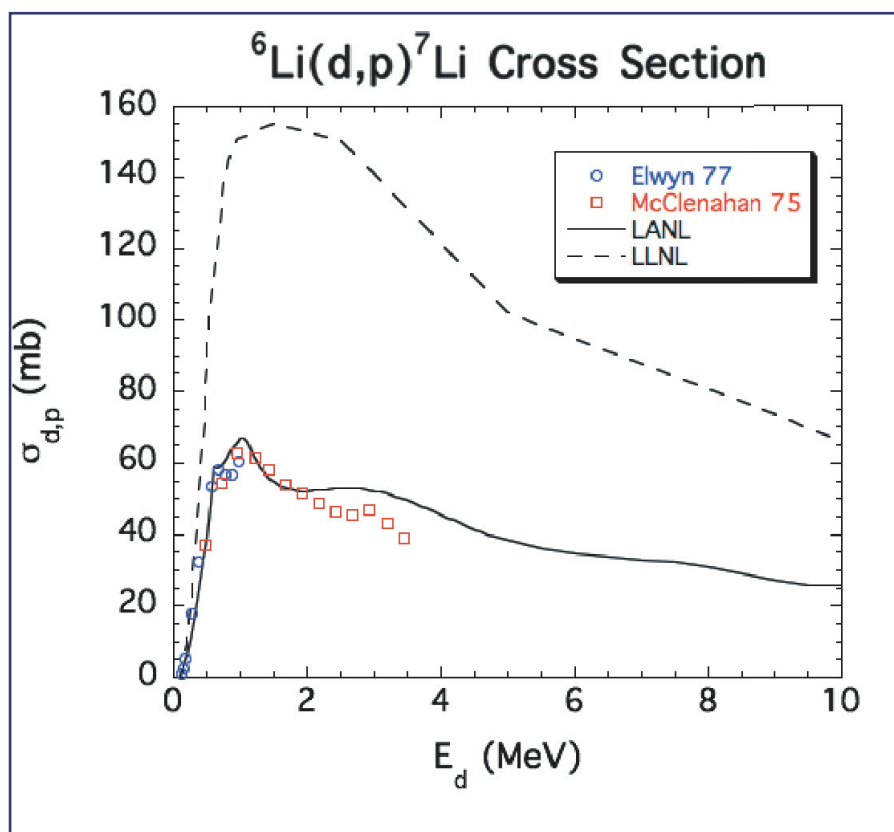
[1] P.R. Page, “ ^8Be Nuclear Data Evaluation,” Los Alamos National Laboratory report LA-UR-04-7172 (October 2004).

For more information, contact Philip R. Page (prp@lanl.gov).

Acknowledgements

We would like to acknowledge NNSA's Advanced Simulation and Computing (ASC), Materials and Physics Program for financial support.

Figure 1— Comparison of Los Alamos National Laboratory (LANL) and Lawrence Livermore National Laboratory (LLNL) $^6\text{Li}(d,p)$ cross-sections before the current analysis was started and two sets of experimental data. The cross-section is in millibarns up to a deuteron laboratory energy E_d of 10 MeV.



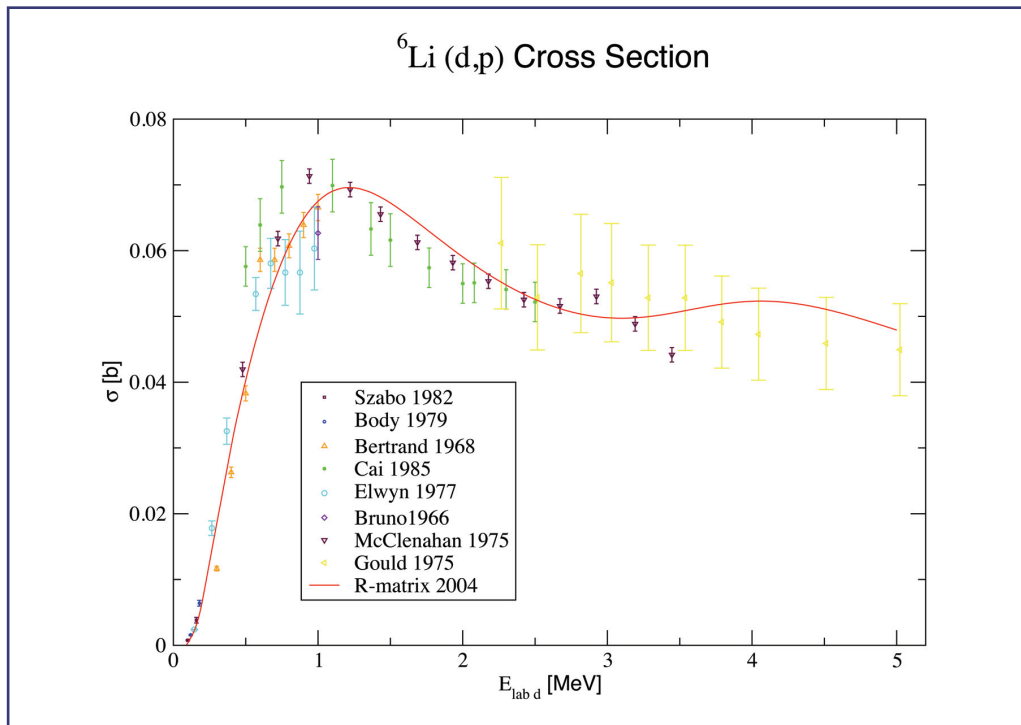


Figure 2—
The 2004 R-matrix analysis cross-section in barns for the ${}^6\text{Li}(d,p)$ reaction up to a deuteron laboratory energy $E_{\text{lab } d}$ of 5 MeV, corresponding to the excitation energy of this analysis, with eight of the sets of experimental data entered in the analysis.

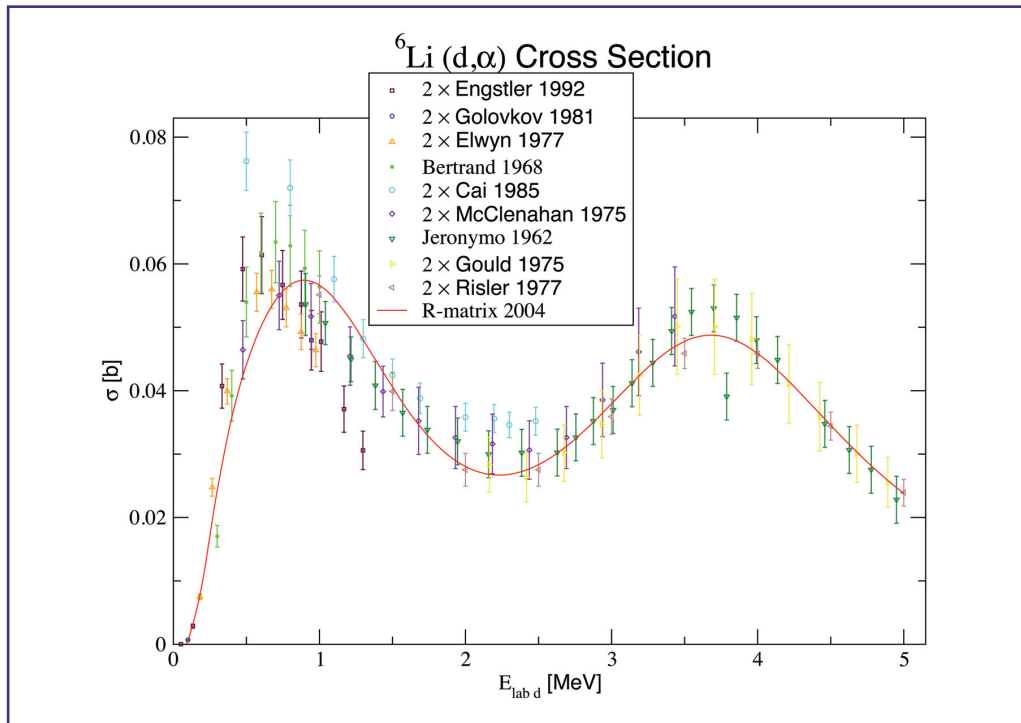


Figure 3—
Same as Fig. 2, except that this is for the ${}^6\text{Li}(d,\alpha)$ reaction. This cross-section should be divided by 2 to obtain a reaction cross-section, since there are identical final α particles.



The Nuclear Reaction Code McGNASH

*Patrick Talou, Mark B. Chadwick,
Phillip G. Young, and
Toshihiko Kawano (T-16)*

We are developing a modern version of the GNASH nuclear reaction code [1], which has been used successfully over the years to compute neutron-, proton-, and photon-induced reactions cross sections on a variety of nuclei targets, and for incident particle energies from tens of keV up to 150–200 MeV. This code has been instrumental in producing numerous nuclear data evaluation files for various ENDF (Evaluated Nuclear Data Files) libraries around the world, and in particular the ENDF/B-VI and pre-ENDF/B-VII libraries in the U.S. More recently, GNASH was used extensively for the creation of the LA150 library [2], containing data on neutron- and proton-induced reactions up to 150 MeV incident energy.

Written in old FORTRAN, the GNASH code was born in the early seventies and was continuously improved since then to incorporate new physics models. However, in doing so, the structure of the code has become very complicated and somewhat cumbersome to upgrade or even simply maintain. The advent of the modern FORTRAN 90/95 scientific language has opened the path toward modern and higher-level programming techniques that can be implemented efficiently to create a modern and more powerful version of the GNASH code.

This new code is called McGNASH and is being written in FORTRAN 95. It uses the concept of modular programming extensively. In fact, the McGNASH code is really a collection of such FORTRAN modules, each dealing with a specific (and often independent) part of the nuclear reaction sequence calculation. These modules are always written with the ideas of robustness

and capacity to evolve in mind. The coding in McGNASH is strongly influenced by the notion of object-oriented programming, though it does not make use of some specific characteristics of this type of programming.

McGNASH is also being written with the user in mind. While a default GNASH input can be cumbersome to read or/and build for the nonexpert, a McGNASH input has been reduced to a very simple and compact form, which can be easily tuned to any user's needs. We hope that this move will encourage the broad use of McGNASH outside its developer base community. Of course, simplicity and compactness come at a price. The same parameters appearing explicitly in a GNASH input are now “hidden” as default parameters in a McGNASH calculation. For simple and default calculations (or for producing large amounts of data over a large portion of the nuclear landscape), this last solution is certainly the best. However, in case the physics at hand is only poorly known, a default calculation might easily lead to relatively wrong answers, which only an expert-eye can detect. Hence, a word of caution may be worthwhile here.

In order to get default calculations running for the most common nuclear reaction data needs, it is necessary to provide the code with default input data (e.g., discrete level schemes, optical model parameters, etc.). To do so, we have chosen to link the RIPL-2 database [3] directly to McGNASH, hence providing default data for many nuclei and nuclear reactions.

For evaluation work, performing a nuclear reaction calculation is just not enough. The extraction and formatting of the pertinent results in a ENDF-type file is required. To achieve this task, GNASH uses an auxiliary code called GSCAN, which needs to be run independently of GNASH. With McGNASH, this feature will be automatically available.

The basic physics models that constitute the backbone of the GNASH code are also present in McGNASH. A neutron- or proton-induced reaction on a heavy target leads to the formation of a compound nucleus in statistical equilibrium, which then decays by emitting gamma-rays, neutron or light-charged particles, until a stable ground- or

isomeric-state is reached. The assumption of a compound nucleus in equilibrium breaks down at low- (very few open channels) and high- (emission of pre-equilibrium high energy particles) incident energies. Both the coding and the physics models used to calculate the needed corrections to the statistical picture represent a great improvement in McGNASH with respect to GNASH.

At low-incident energies, the so-called width fluctuation correction factors are calculated within three models: HRTW, Moldauer, and exact Gaussian Orthogonal Ensemble (GOE). The two first models represent only approximations to the exact GOE calculation, which however takes significantly longer to compute. Figure 1 provides an overview of the domain of validity of both HRTW's and Moldauer's methods.

At high-incident energies, the DDHMS Monte Carlo code by Chadwick is used within McGNASH, implementing the Hybrid Monte Carlo model by Blann and Chadwick [4].

This model has several important advantages over the exciton model, implemented in the GNASH code. In particular, the DDHMS approach can be used to predict the residual spin distribution of the excited nucleus after the emission of pre-equilibrium nucleons. This distribution can differ significantly from the Hauser-Feshbach compound nucleus spin distribution, depending on the number and energy of the pre-equilibrium ejectiles. In applications particularly sensitive to the conservation of angular momentum (e.g., branching ratios to spin isomers, or precise determination of γ -ray lines in a gamma-cascade), it is important to calculate this residual spin distribution accurately. An example of such calculated residual spins distributions after pre-equilibrium emission is shown in Fig. 2 for protons (160 MeV) on ^{90}Zr .

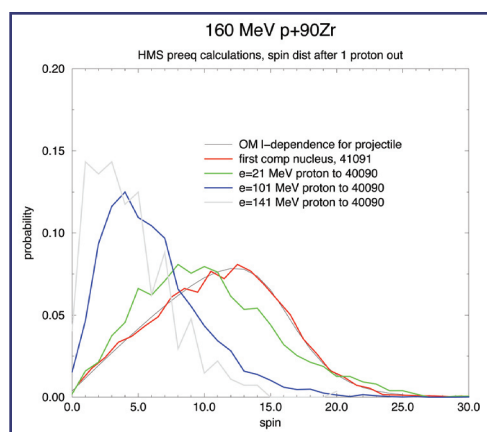


Figure 1—
Study of the validity of Moldauer's and HRTW's approximations to the exact Gaussian Orthogonal Ensemble (GOE) calculations for the width fluctuation correction factors that modify the simple statistical picture of the compound nucleus decay at low-incident energies.

HRTW / Moldauer vs. GOE

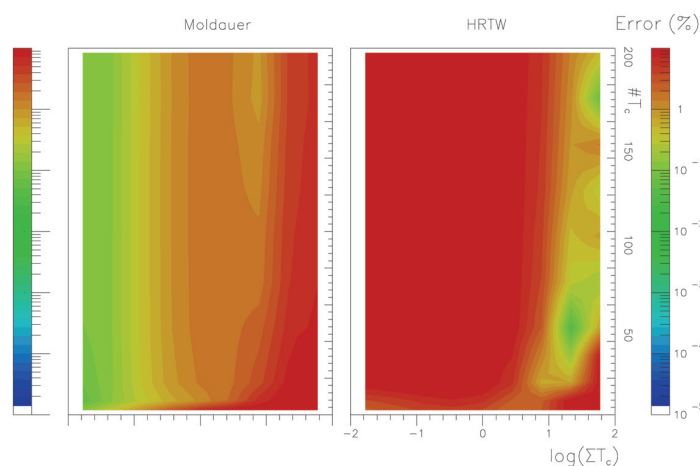


Figure 2—
Proton-induced reaction on ^{90}Zr with $E_p = 160$ MeV: residual spin distributions after the emission of a pre-equilibrium proton, as calculated with the DDHMS code and compared to the compound nucleus spin distribution.

A first version of McGNASH is expected to be released by the end of 2005.

- [1] P.G. Young, E.D. Arthur, and M.B. Chadwick, Proc. Workshop on *Nuclear Reaction Data and Nuclear Reactors*, ICTP Trieste, Italy, April 15–May 17, 1996 (World Sci. Publ. Co., Singapore, 1998), pp. 227–404.
- [2] M.B. Chadwick, et al., *Nucl. Sci. Eng.* **131**, 293 (1999).
- [3] "Reference Input Parameter Library RIPL-2," <http://www-nds.iaea.org>.
- [4] M. Blann and M.B. Chadwick, *Phys. Rev. C* **57**, 233 (1998).

For more information, contact Patrick Talou (talou@lanl.gov).

Acknowledgements

We would like to acknowledge NNSA's Advanced Simulation and Computing (ASC), Materials and Physics Program for financial support.

Neutron Emission Spectra from Actinides

Phillip G. Young and
Robert E. MacFarlane (T-16),
Mark B. Chadwick (PADNWP), and
Stephanie C. Frankle (X-5)

We have carried out a systematic analysis of the nuclear reaction data for all isotopes of uranium. In the course of this work, we have addressed a long-standing problem in adequately describing neutron emission spectra emanating from neutron-induced reactions on actinides. The problem is manifested in our failure to adequately calculate measurements of neutron leakage as a function of time-of-flight following the introduction of 14-MeV neutron pulses into the center of uranium or plutonium spheres [1]. Additionally, this problem is seen in attempting to reproduce measurements of neutron emission spectra [2].

This problem is illustrated in Fig. 1, where we show angle-integrated neutron emission

spectra from a ^{238}U target bombarded by 14.05-MeV neutrons. The red dashed curve (“Maslov, 2003”) is a calculation that includes compound nucleus and pre-equilibrium theory contributions, as well as direct reactions to known low-lying states in ^{238}U below an excitation energy of 1 MeV. The problem that occurs between emission neutron energies 9 and 13 MeV results from the omission of direct reaction contributions to collective states at excitation energies 1–4 MeV that have not been measured but are known to exist from theoretical considerations [3]. A similar problem occurs to a lesser extent in the ENDF/B-VI curve (blue short dashes), in which these missing states have been only partially taken into account.

To solve this problem, we postulate the existence of a set of states at excitation energies between 1 and 4 MeV having spin and parity 3^- and 2^+ that approximate the unmeasured collective states. We perform coupled-channels optical model calculations with the code ECIS96 [4] for each of the assumed states and use the Baba data [2] to determine the spin, parity, and deformation parameters of each assumed state. With these parameters assigned, we then can calculate cross sections and angular distributions for these states for any incident neutron energies and outgoing emission angles. The results

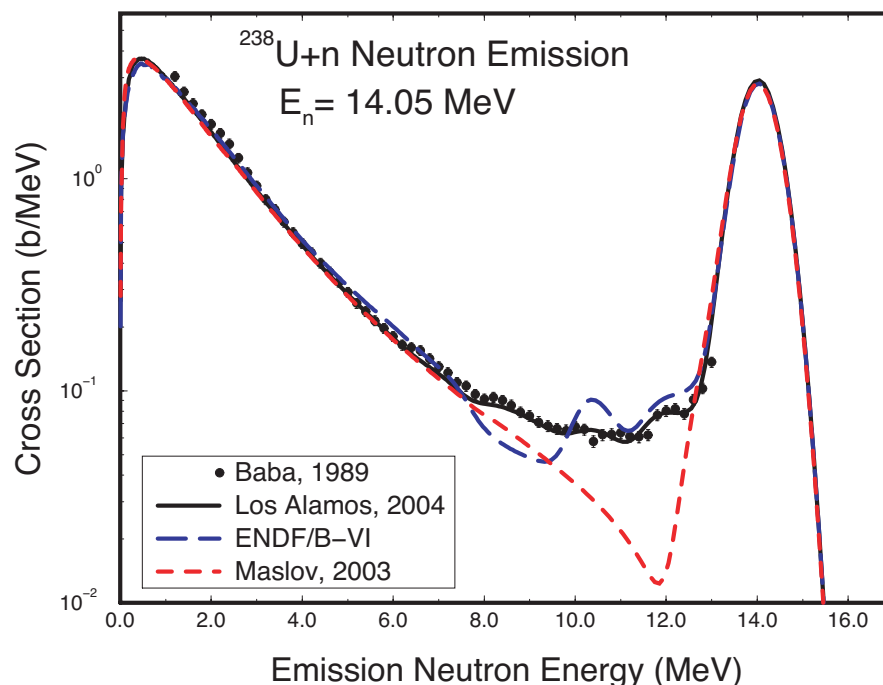


Figure 1—
Angle-integrated
neutron emission
spectra from 14-MeV
neutron reactions
on ^{238}U .

of our calculations for ^{238}U at 14 MeV are shown by the black solid curve in Fig. 1 (“Los Alamos, 2004”), which essentially coincides with the experimental data. These assumptions lead to significantly improved calculations of neutron emission spectra from ^{238}U at all incident neutron energies and emission angles.

To address the problem of poor simulations of time-of-flight neutron distributions from pulsed-sphere measurements, we applied these same ideas to calculations of neutron emission from a ^{239}Pu target by assuming similar states in this nucleus. While there are no direct measurements of neutron emission cross-sections from ^{239}Pu , we compare the results of our calculations for ^{239}Pu (black solid curve) with the Baba ^{238}U measurements [2] and prior evaluation (red dashed curve) in Fig. 2. These results are encouraging, but to directly test the new analysis, we simulated the 14-MeV time-of-flight neutron emission measurements from a ^{239}Pu sphere with the MCNP Monte Carlo code using our ^{239}Pu evaluation. The results are compared in Fig. 3, where the black solid curve represents the experimental data, the red short-dashed curve is the MCNP simulation with the previous evaluation, and the blue long-dashed curve is our new result. The improvement in reproduction of the measurements is significant, and we plan to broaden our analysis in the future to cover all important actinides.

- [1] L.F. Hansen, C. Wong, T.T. Komoto, B.A. Pohl, E. Goldberg, R.J. Howerton, and W.W. Webster, *Nucl. Sci. Eng.* **72**, 35 (1979).
- [2] M. Baba, H. Wakabayashi, N. Itoh, K. Maeda, and N. Hirakawa, Japanese Atomic Energy Research Institute report JAERI-M-89-143 [INDC(JPN)-129] (1989).

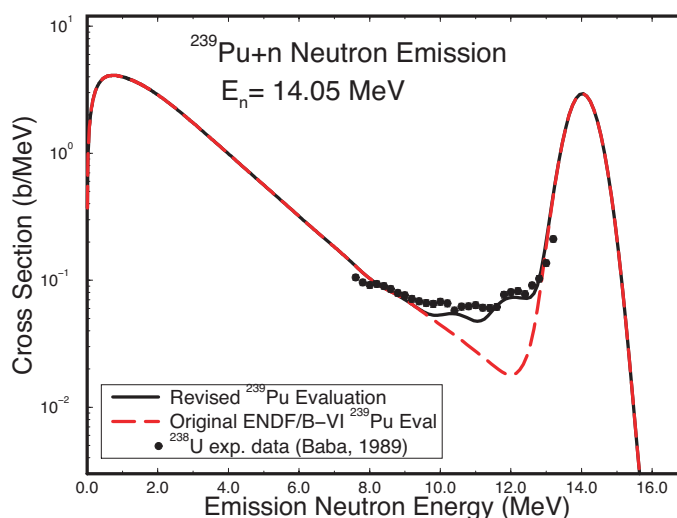


Figure 2—
Angle-integrated
neutron emission
spectra from 14-MeV
neutron reactions on
 ^{239}Pu .

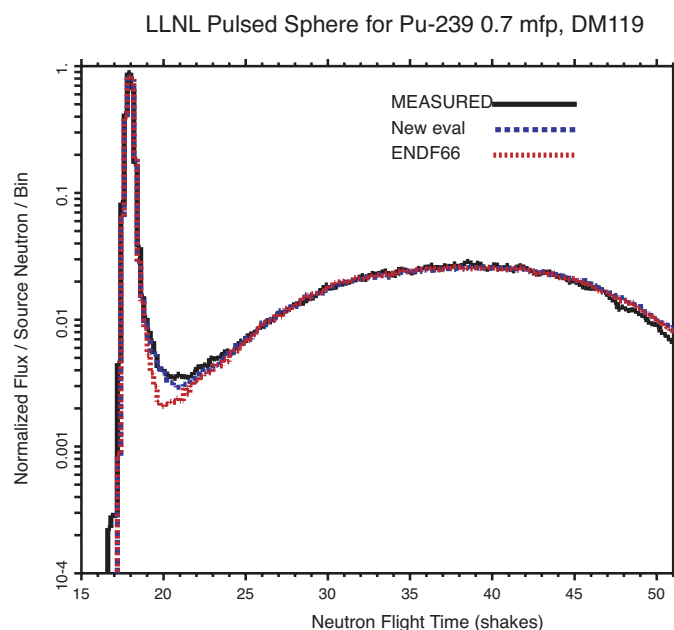


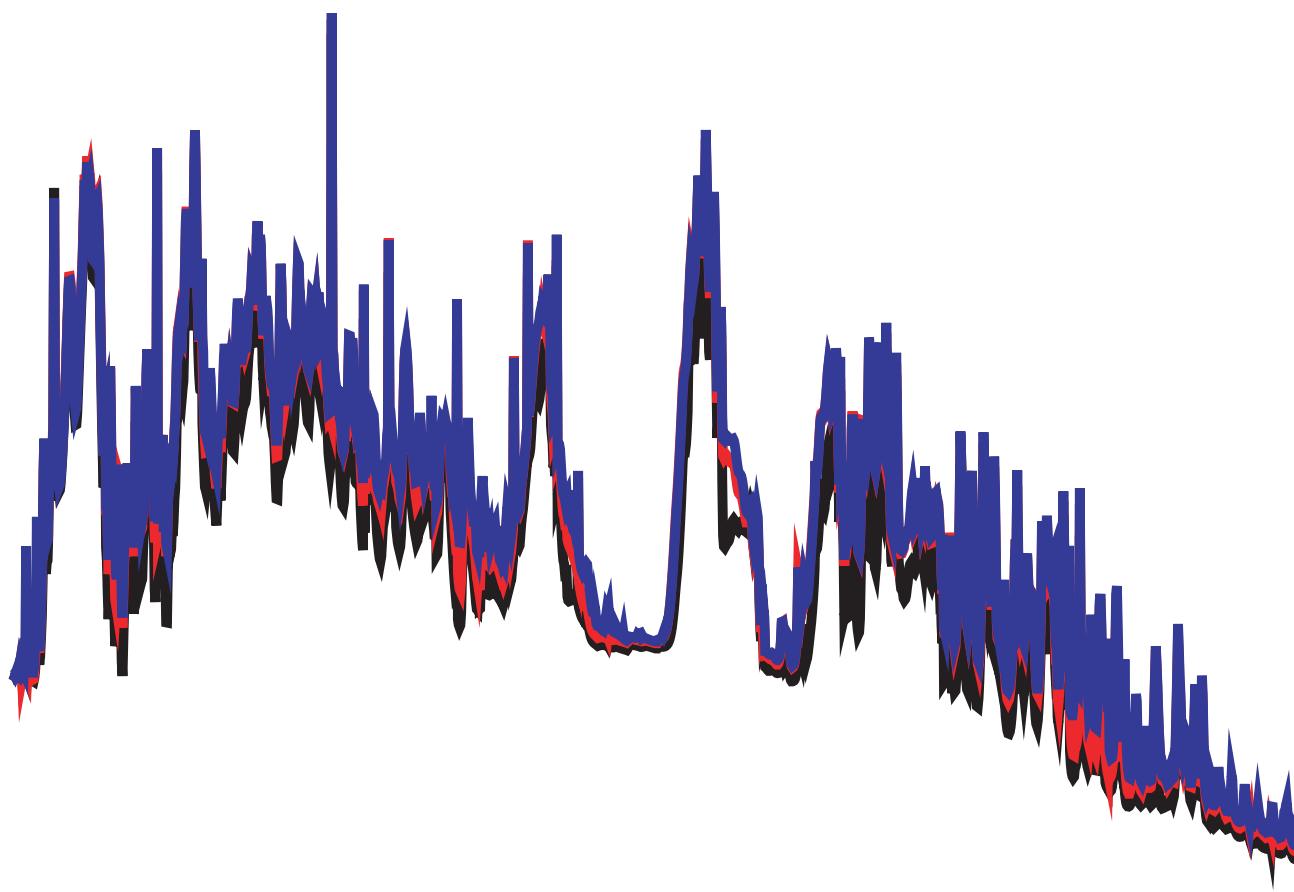
Figure 3—
Time-of-flight spectrum
of leakage neutrons
from a sphere of ^{239}Pu
pulsed with 14-MeV
neutrons at its center.

- [3] A. Marcinkowski, P. Demetriou, and P.E. Hodgson, *J. Phys. G [Nucl. & Part. Phys.]* **22**, 1219 (1996).
- [4] J. Raynal, “Notes on ECIS94,” Centre d’Etudes Nucleaires (Saclay) report CEA-N-2772 (1994).

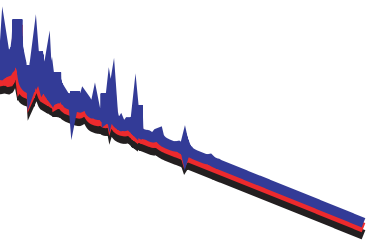
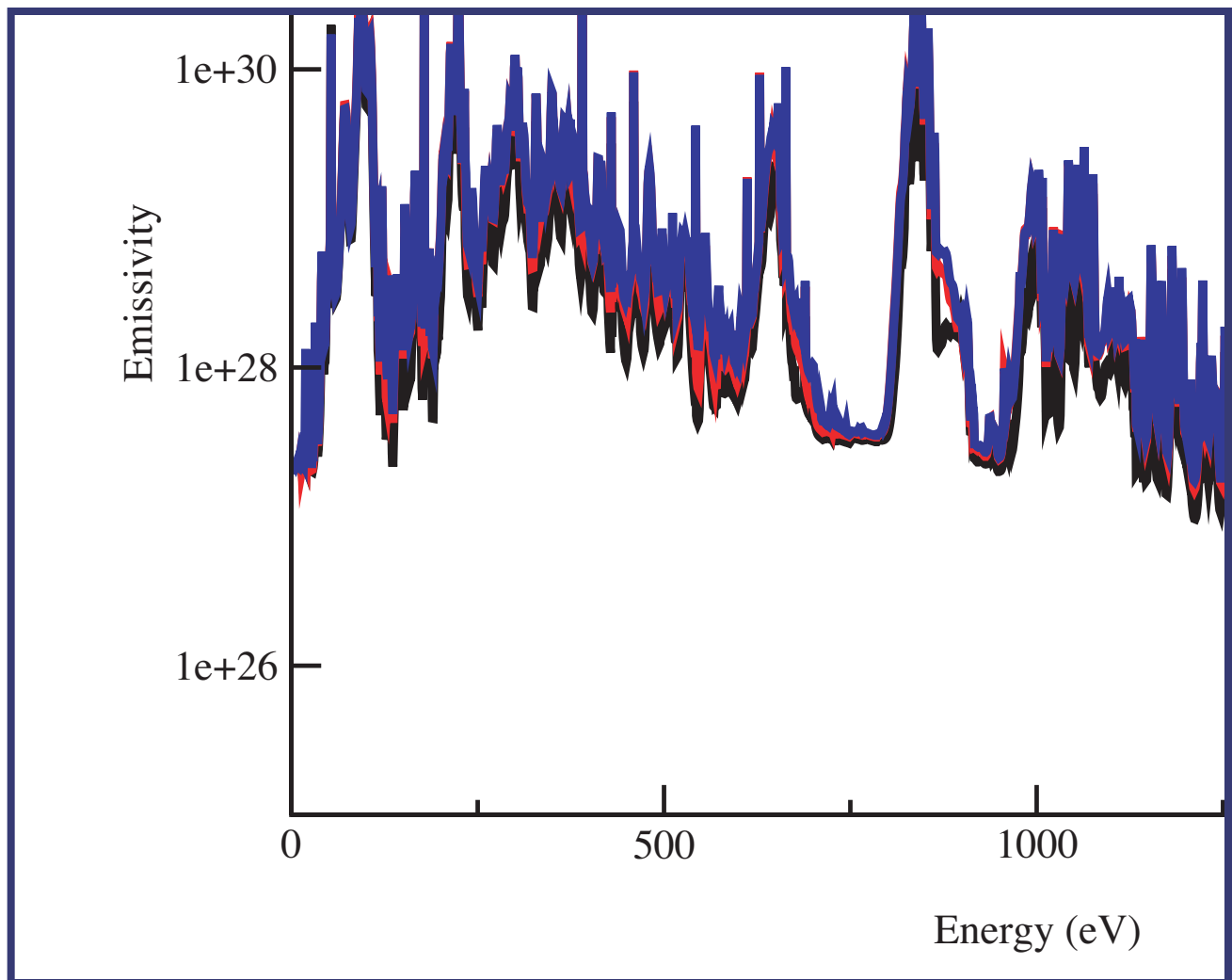
For more information, contact
Phillip G. Young (pgy@lanl.gov).

Acknowledgements

We would like to acknowledge NNSA’s Advanced Simulation and Computing (ASC), Materials and Physics Program for financial support.



ATOMIC PHYSICS



Line-Edge Blending in ATOMIC

*Joseph Abdallah, Jr., Peter Hakel,
David P. Kilcrease, Norman H. Magee, Jr.,
Stephane Mazevet, and Manolo Sherrill
(T-4)*

A line-edge blending algorithm was introduced into ATOMIC to eliminate an erroneous gap in absorption spectra and to provide a smooth transition into higher density where continuum lowering and the disappearance of spectral lines occur. The erroneous absorption gap occurs in the region where the calculated atomic physics data ends for a Rydberg series of photo-excitations, usually determined by a principal quantum number cut-off, and where the photo-ionization edge begins at the binding energy of the ionizing electron. Line-edge blending can have a significant effect on the calculated opacity.

The first step to accomplish this scheme is to extend the bound-free cross section to photon energies below the photo-ionization edge. Software was developed to identify the Rydberg series of spectral lines leading up to each edge. Then using the Rydberg series oscillator strengths, a table of extended cross sections is built internally with photon energies corresponding to the particular final n state leading up to that edge. Thus, the entire procedure is automated. For the present time only edges with initial states of $n \leq 3$ are considered.

For a given density and temperature, the EOS computation provides occupation probabilities, ϕ for every level that is included in the calculation. The occupation probability is the probability that a particular state has not disappeared due to density effects. Therefore the intensity of spectral lines must be decreased by the factor ϕ and the corresponding extrapolated bound-free cross section is multiplied with the factor $(1-\phi)$ in order to conserve total oscillator strength.

At low densities the occupation probabilities are near unity. As density increases, the values for ϕ decrease with the most highly excited levels decreasing the fastest.

An interpolation table is constructed to calculate the bound-free cross section for each density, temperature, and edge combination. It consists of the photo-ionization cross section for energies at and above the edge and the bound-free extension scaled by $(1-\phi)$ for energies below the tabulated limit, usually $n = 10$. An additional point is included at 25% of the distance between the tabulated series energy limit and the ionization edge to ensure the gap fills in smoothly.

Figure 1 illustrates line-edge blending computed by ATOMIC for different plasma ion densities for the Lyman Rydberg series of hydrogen-like oxygen. The electron temperature is held fixed at 60 eV for each calculation. The curve labeled NB corresponds to the calculation at an ion density of 10^{18} ions per cubic centimeter without line-edge blending. The gap in the calculation from the last $n = 10$ line in the data (863 eV) to the photo-ionization edge (872 eV) is evident. Note that the gap is filled in for the calculation at the same density including line-edge blending. Also note that as the ion density is increased the lines become broader with decreased magnitude. At an ion density of 10^{20} spectral lines below $n = 10$ start to disappear and by a density of 10^{22} the entire series from $n = 3$ to $n = 10$ has sunk into the continuum.

**For more information, contact
Joseph Abdallah (abd@lanl.gov).**

Acknowledgements

We would like to acknowledge NNSA's Advanced Simulation and Computing (ASC), Materials and Physics Program for financial support.

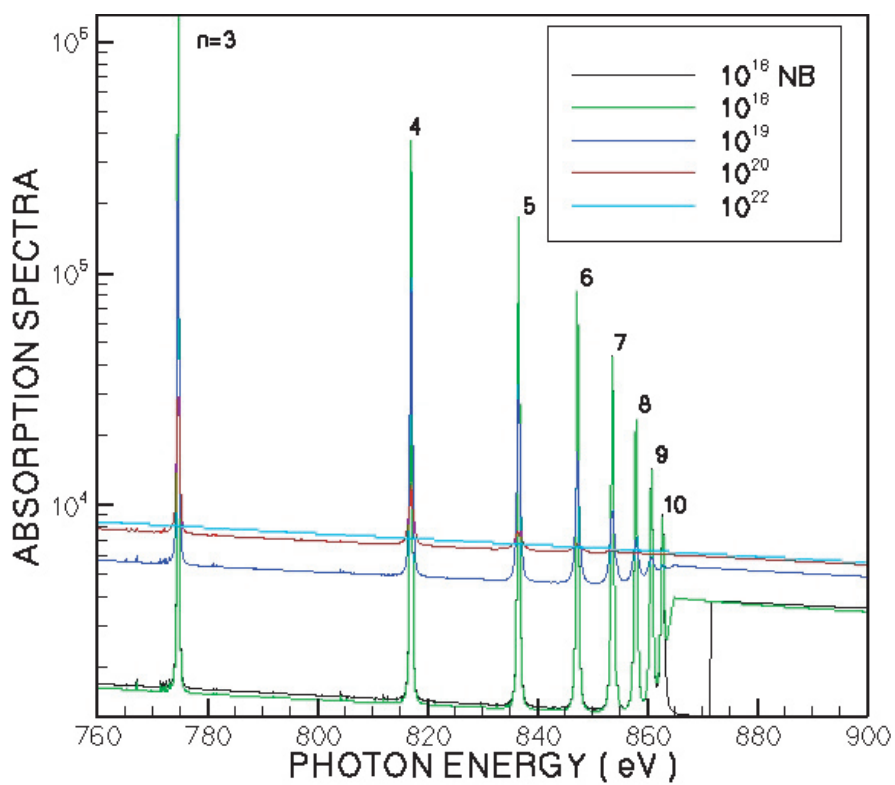


Figure 1—
Line-edge blending
computed by ATOMIC
for different plasma
ion densities for the
Lyman Rydberg series of
hydrogen-like oxygen.

New Methods for Spectral Generation in ATOMIC

Joseph Abdallah, Jr., Manolo Sherrill, Stephane Mazevet, Norman H. Magee, Jr., David P. Kilcrease, and Peter Hakel (T-4)

In opacity calculations, the spectral line generation for the bound-bound contribution is by far the most time-consuming operation. In intermediate coupling, hundreds of millions of lines can contribute and an individual line-by-line treatment over the entire photon energy range can take hundreds of hours of computer time on an SGI Origin 200 for a single density-temperature point. This would make opacity calculations over the entire OPLIB density-temperature grid, which consists of several thousand points, unfeasible. The purpose of this paper is to briefly describe two methods that have been developed to overcome this problem.

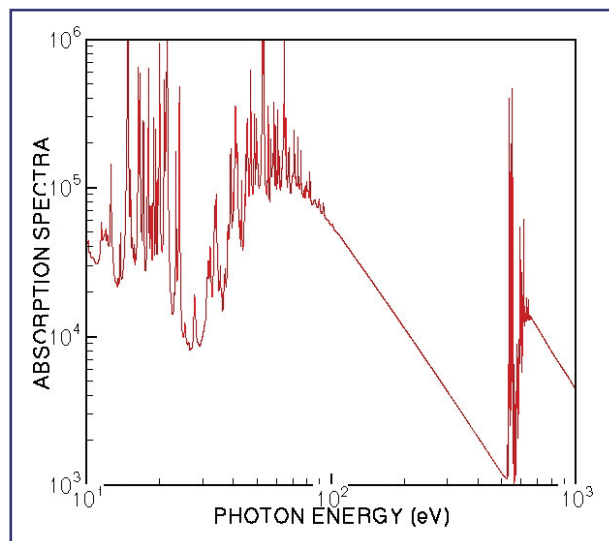
Zoning is the first method that is discussed. The entire photon energy grid to be considered is divided into a series of twenty or so zones. The zones are chosen so they are plentiful in regions where spectral lines are expected to occur, and relatively few zones in regions in other regions. A given spectral line is only calculated in those zones where its relative intensity is greater than some

input tolerance. It turns out that a majority of the spectral lines need to be evaluated in only very few zones resulting in substantial savings over the full line-by-line treatment. The results obtained with the zoning approach are exactly the line-by-line limit as the tolerance is lowered.

A more elaborate method using histograms was also developed. Here photon energy space is divided into bins, much finer than the output photon energy grid, on the order of a million. The strength of all spectral lines is summed into the bins corresponding to their line centers. The average and the inverse average of all the line widths are also computed for each energy bin. These line widths are used as criteria for determining narrow lines and broad lines. Then for each energy bin in the histogram, two spectral lines are generated on the output photon energy grid; one with line strength corresponding to narrow lines, and one with line strength corresponding to broad lines. Thus the technique reduces the number of line evaluations from several hundred million to two times the histogram grid, which is on the order of a few million. A further reduction is obtained because many bins will have zero line strength and are therefore not calculated.

Figure 1 shows a plot of the absorption spectra using the histogram method for oxygen at a density of 10^{20} ions/cm³ and a temperature of 10 eV. The results for the zoning method show no difference to this result on the scale shown. The calculated

Figure 1—
A plot of the absorption spectra using the histogram method for oxygen at a density of 10^{20} ions/cm³ and a temperature of 10 eV.



Rosseland mean differed by less than a tenth of a percent for the two methods. The zoning calculation took a little more than 5 hours using about 30 zones while the histogram calculation took less than an hour. A total of one hundred million spectral lines were included in each calculation. The full line-by-line calculation would have taken well over one hundred hours.

*For more information, contact
Joseph Abdallah (abd@lanl.gov).*

Acknowledgements

We would like to acknowledge NNSA's Advanced Simulation and Computing (ASC), Materials and Physics Program for financial support.

Parallel Rate Matrix Solvers in the ATOMIC Code

James Colgan and Joseph Abdallah (T-4), Christopher J. Fontes and H. L. Zhang (X-5)

The need to solve large systems of equations in order to model non-Local Thermodynamic Equilibrium (non-LTE) plasmas is becoming increasingly important. Los Alamos National Laboratory (LANL) data were submitted to the recent NLTE-3 workshop in Gaithersburg, Maryland, where comparisons were carried out among a number of international modeling efforts [1]. In some of the test cases the largest models predicted significantly different plasma behavior when compared to results from smaller models. Another use of non-LTE data involves the attempt to create an in-line, rad-hydro algorithm for computing non-LTE atomic spectra via the effective rate method [2], which requires tables of accurate atomic data. For LTE plasmas, the tabular data approach has been in use for many years. However, the concept is relatively unexplored for non-LTE modeling for a number of reasons, as discussed in [2]. One of the reasons for this disparity is the need to solve a system of coupled rate equations in order to obtain the atomic level populations in the non-LTE case. For LTE plasmas the populations can be obtained from the much simpler Saha equation.

For heavy elements, the LANL suite of codes regularly calculates models containing on the order of 100,000 relativistic configurations. However, in order to move beyond models of this size a more efficient method of solving the rate equations is needed because the amount of computing time and memory quickly becomes prohibitive as the number of configurations is increased.

Currently the LANL code ATOMIC contains two rate matrix solvers, which are only able to run in a serial manner. The first (direct) solver performs the solution using standard

LU decomposition techniques designed for a general matrix. This solver is typically very stable; however, the time to run the solver scales as around n^3 (n being the number of configurations), and also the memory required to store the rate matrix quickly becomes prohibitively large. Therefore this solver has only been used for relatively small problem sizes to date. The second rate matrix solver in ATOMIC is an incomplete LU iterative sparse solver. This solver has been found to run very quickly for larger problems. Problems containing up to around 300,000 configurations have already been solved using this method. However, the stability of more ill-conditioned problems (e.g., those containing neutral ion stages) is sometimes uncertain. Also, in order to move to larger configuration data sets, the memory required to hold the data becomes progressively larger and needs to be distributed over several processors to fit on current machines.

Although three different types of parallel rate matrix solvers were considered, here we focus on the LAMG solver, developed at LANL. This package has been the subject of a previous LANL memo [3]. This code has previously been demonstrated to give scalable performance on shared and distributed-memory parallel platforms.

At the present time, this code has solved problems on the order of 1.2 million configurations [4]. The solver scales well for up to 128 processors on the LANL QSC machine. The run-time requirements of the solver, when 128 processors are used, are comparable to the iterative sparse serial solver. The code has been checked and modified where necessary to ensure that as little memory as possible is used throughout the code. This becomes very important, since the input data sets which generate up to 1 million or more configurations typically require arrays which use greater than 10.0 Gb of RAM memory. Figure 1 shows three different emissivity calculations for a Xe spectrum, where models containing different numbers of configurations are shown. For this electron temperature (200 eV) and density ($1.1 \times 10^{20}/\text{cm}^3$) we find that the spectrum appears to be reasonably well converged with respect to the number of configurations included in the model. Also, the radiative power loss from the largest

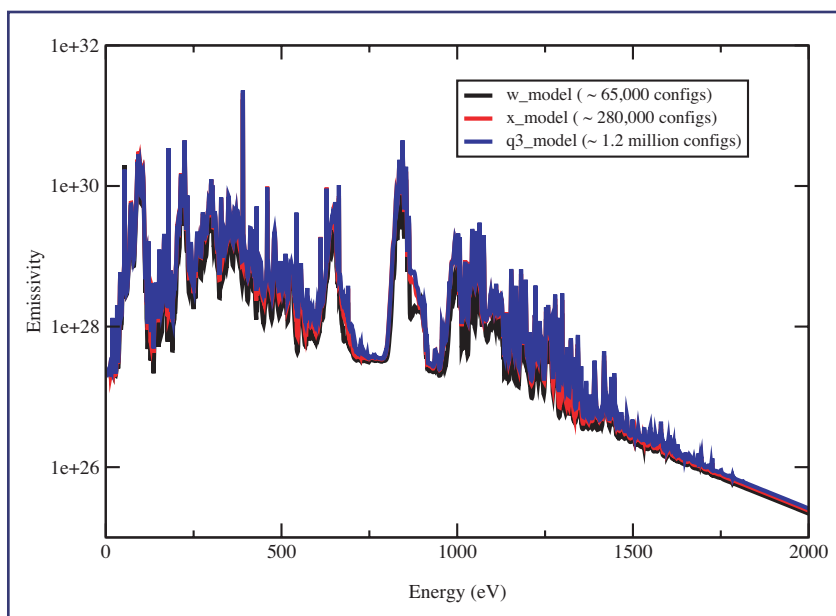


Figure 1—
Xenon emissivities for three ATOMIC models at an electron temperature of 200 eV and an electron density of $1.1 \times 10^{20}/\text{cm}^3$.

model is within 4% of the smaller model. Further efforts are underway to compare such spectra to experimental results.

We find that parallel rate matrix solvers have been demonstrated to extend the size of the rate matrices that can be calculated by the ATOMIC code. We have demonstrated that the current parallel iterative sparse rate matrix solvers can solve systems containing on the order of 1 million configurations. This work, along with other advances in the ATOMIC package, should make significant progress towards the goals of non-LTE atomic data table generation and improved agreement when comparing with experimental data.

- [1] C.J. Fontes, et al., “LANL Data Submissions to the NLTE-3 Workshop,” Los Alamos National Laboratory memorandum X-5:04-49 (U) (June 2004).
- [2] C.J. Fontes, et al., *J. Quant. Spectros. Rad. Transfer* **65**, 223 (2000).
- [3] “LAMG: Los Alamos Multigrid Code Reference Manual,” Los Alamos National Laboratory report LA-UR-03-6183 (December 2003).

- [4] J. Colgan and C.J. Fontes, “Parallel Rate Matrix Solvers in the ATOMIC code,” Los Alamos National Laboratory memorandum X-5:04-48 (U) (July 2004)

For more information, contact James Colgan
(jcolgan@lanl.gov).

Acknowledgements

We would like to acknowledge NNSA’s Advanced Simulation and Computing (ASC), Materials and Physics Program for financial support.

Time-Dependent Studies of Photoionization of Light Systems: Beyond Two-Electron Systems

James Colgan (T-4)

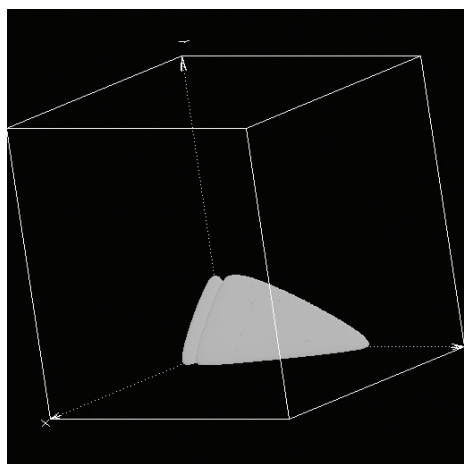
In the last 10–15 years, significant progress has been made in solving, by a variety of powerful theoretical methods, the Coulomb three-body problem inherent in the double photoionization of a two-electron atom ($\gamma, 2e$), or in the electron-impact ionization of a one-electron system ($e, 2e$). These problems are found in their most basic form in the double photoionization of helium and the electron-impact ionization of hydrogen. Recently, as many as four distinct methods have found great success when applied to the full solution of these problems. These include the convergent close-coupling [1], the exterior complex-scaling [2], the hyperspherical R-matrix with semiclassical outgoing waves [3], and the time-dependent close-coupling methods [4]. Total, single, double, and triple differential cross sections have been calculated for these systems for a variety of different dynamical situations and, in general, very good agreement has been found with recent experimental measurements of these quantities.

It has therefore become natural to consider problems beyond this level of complexity. In particular, Coulomb four-body problems have recently been of interest due to experimental measurements of the triple photoionization of lithium and many measurements of cross sections associated with the double photoionization of the hydrogen molecule, H_2 . The triple photoionization of lithium involves three charged particles moving away

from a charged nucleus, and the double photoionization of H_2 entails two electrons being ejected from a diatomic molecule (which itself can then fragment).

Recently, the time-dependent close-coupling technique has been used to numerically investigate these problems. The time-dependent method was extended to treat equally three outgoing electrons moving in the field of a nucleus by propagating in time a 9D wave function according to the Schrödinger equation [5]. The three radial dimensions were represented on a lattice and a coupled channels expansion represented the remaining six angular dimensions. After propagation in time, double photoionization (with excitation) and triple photoionization cross sections for lithium were obtained by projection onto fully antisymmetric spatial and spin functions. In Fig. 1, we show on the left the radial part of the ground state of lithium on a 3D lattice. This ground state represents the starting point for the real time propagation. On the right we show the double photoionization cross sections as compared with recent experiments. The agreement with experiment is very good and we are also able to distinguish in which final state the Li^{2+} ion is left. It is hoped that planned experiments will also be able to measure these double photoionization (with excitation) cross sections. Triple photoionization cross sections have also been calculated and are in good agreement with other experimental measurements.

The time-dependent calculations as applied to molecular systems started with a preliminary investigation of single- and multi-photoionization of the one-electron system H_2^+ [6]. These calculations were made in an effort to test our new computer programs against previous theoretical work. In this case, the radial and one angular dimension of the electron were represented on a lattice for each value of the remaining angular dimension. For the time being, the internuclear separation is held fixed in these calculations. The single-, two- and three-photon ionization rates were found to be in good agreement with previous calculations made using time-independent techniques.



This work allowed us then to pursue calculations on the two-electron H_2 system [7]. Double photoionization calculations of H_2 were now made by representing two radial and two angular dimensions on a lattice and propagating in time this coupled wave function according to the Schrödinger equation. As before, photoionization cross sections are obtained by projecting onto suitably antisymmetrized functions. In this case, the double photoionization cross sections were in good agreement with experimental measurements. We now are applying our methods to look at angular differential cross sections, as well as examining the role of nuclear motion in these molecular calculations.

- [1] I. Bray and A.T. Stelbovics, *Phys. Rev. Lett.* **70**, 746 (1993).
- [2] C.W. McCurdy, M. Baertschy, and T.N. Rescigno, *J. Phys. B* **37**, R137 (2004).
- [3] L. Malegat, P. Selles, and A.K. Kazansky, *Phys. Rev. Lett.* **85**, 4450 (2000).
- [4] M.S. Pindzola and F. Robicheaux, *Phys. Rev. A* **54**, 2142 (1996); J. Colgan, M.S. Pindzola, and F. Robicheaux, *J. Phys. B* **43**, L457 (2001).

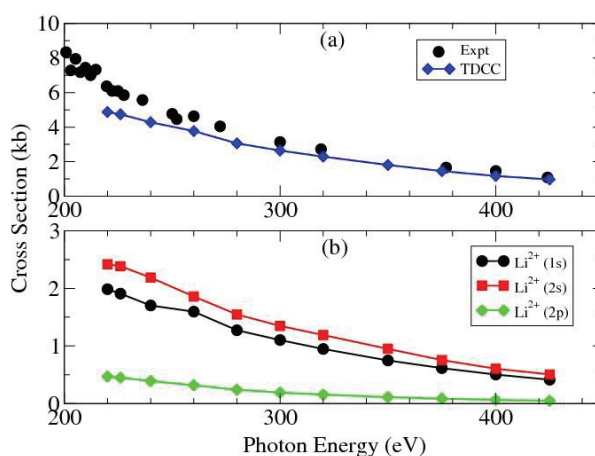


Figure 1—
On the left we show the radial part of the ground state of lithium on a 3D lattice. This ground state represents the starting point for the real time propagation. On the right we show the double photoionization cross sections as compared with recent experiments. The agreement with experiment is very good and we are also able to distinguish in which final state the Li^{2+} ion is left. It is hoped that planned experiments will also be able to measure these double photoionization (with excitation) cross sections.

- [5] J. Colgan, M.S. Pindzola, and F. Robicheaux, *Phys. Rev. Lett.* **93**, 053201 (2004).
- [6] J. Colgan, M.S. Pindzola, and F. Robicheaux, *Phys. Rev. A* **68**, 063413 (2003).
- [7] J. Colgan, M.S. Pindzola, and F. Robicheaux, *J. Phys. B*, **37**, L377 (2004).

For more information, contact James Colgan
(jcolgan@lanl.gov).

Acknowledgements

We would like to acknowledge NNSA's Advanced Simulation and Computing (ASC), Materials and Physics Program for financial support.

The ATOMIC Equation of State

Stephane Mazevet, Joseph Abdallah, Peter Hakel, David P. Kilcrease, Norman H. Magee, Jr., and Manolo Sherrill (T-4)

We report on meeting a major deliverable for the development of ATOMIC, a code designed to compute opacities under both local thermodynamic equilibrium (LTE) and non-LTE conditions for a large range of elements. ATOMIC will become the successor of the T-4 opacity code LEDCOP. The calculations shown here demonstrate that all the equation of state (EOS) capabilities have been successfully implemented into ATOMIC and are robust enough to calculate opacity tables over a wide range of temperatures and densities and for various atomic systems.

The basis of ATOMIC is the FORTRAN 90 reconstruction of the FINE nonequilibrium spectral modeling code, to which physics packages extracted from LEDCOP have been added. ATOMIC provides improved atomic physics data, a user-friendly interface, modularity to facilitate code improvements, platform independence, and less

manipulation of the atomic physics databases than is currently necessary for LEDCOP. The development of ATOMIC in FORTRAN 90 also provides a platform for parallelization of both the LTE and non-LTE calculations.

A complete opacity table contains on average about 2,000 density-temperature points. To keep the production time tractable, we developed a parallel scheme where density-temperature point calculations are distributed over the set of processors used in the calculation. The parallel scheme makes use of a simple queuing system where the next density-temperature point is sent to the first processor that has completed the calculation at a previously given condition. This scheme allows for an efficient use of the parallel resource and its performance is independent of the number of processors used.

ATOMIC makes use of a new model to calculate the EOS. The model is based on the chemical picture, which aims at minimizing the Helmholtz free energy. The plasma is represented as an ensemble of various species corresponding to the electrons and the different ion stages. Plasma and density effects are included within the framework of the occupation probability formalism as developed by Mihalas and coworkers [1, 2]. A package has been developed, implemented in ATOMIC, and tested for hydrogen, helium, and oxygen over the whole density-temperature conditions needed for the production of an opacity table.

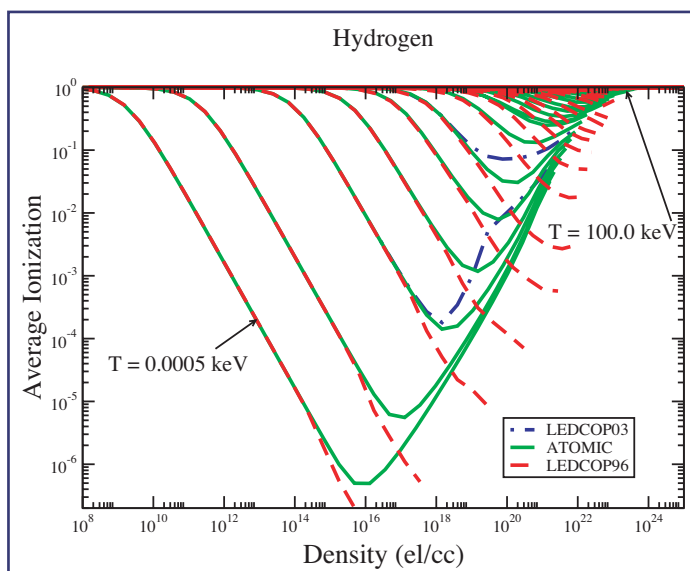


Figure 1—
Hydrogen ionization
fraction calculated by
ATOMIC and LEDCOP.

Figure 1 shows a comparison of the hydrogen effective ionization fraction, Z , calculated with ATOMIC and LEDCOP. Figure 1 shows a significant improvement for the calculation of the hydrogen EOS, particularly in the region where pressure ionization is important, i.e., for electron densities greater than 10^{20} elec./ cm^3 . One sees in Fig. 1 that the EOS implemented in LEDCOP tends to fail dramatically when pressure ionization becomes important. In contrast, the new EOS provides a smooth transition along each isotherm when density effects lead to an increase in the ionization fraction.

This result indicates that the new EOS developed for ATOMIC will allow to extend current opacity tables to higher densities.

The calculation of the EOS for a more complicated system such as oxygen is not straightforward in the current formalism as the number of ion stages of the species under consideration translates into an equivalent number of coupled nonlinear equations to be solved. In addition, the various density and plasma terms entering the set of nonlinear equations vary rather drastically as a function of density and, as such, the number of nonlinear equations to be solved also varies along a given isotherm. To keep the calculation time sufficiently low to enable the production of a complete opacity table and independent of the species involved, we developed a computational scheme that only uses a restricted number of ion stages. The ion stages needed at a given density-temperature condition are selected by first finding the four ion stages that minimize the free energy using the average configuration properties. This calculation is followed by a second minimization of the free energy where two additional ion stages are included and, this time, using the fine structure level properties. This scheme has been implemented and tested for oxygen for the whole density-temperature conditions needed for the production of an opacity table. Figure 2 shows the result of this calculation for the oxygen pressure and along the complete opacity table.

In conclusion, we have developed, tested, and implemented in ATOMIC a new scheme to calculate the EOS. This new model indicates that the physics models included provide a better description of the density and plasma effects than in the previous opacity code

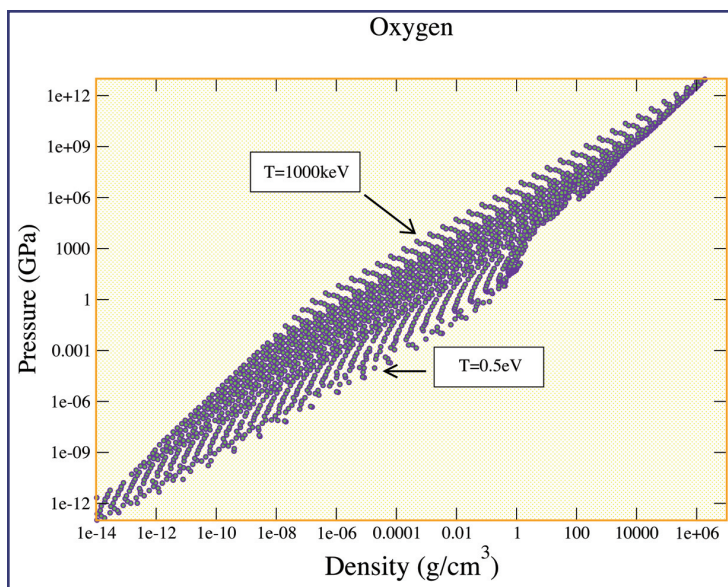


Figure 2—
Variation of the oxygen pressure as a function of density and temperature.

LED COP. We have also demonstrated that the model implemented is also efficient to calculate the EOS of more complex systems by calculating the oxygen EOS for all the density-temperature conditions needed for an opacity table production. Finally, as the computational scheme implemented only uses a fixed number of ion stages, we anticipate that the model implemented can be readily applied to elements with higher atomic number without a significant increase in computational time.

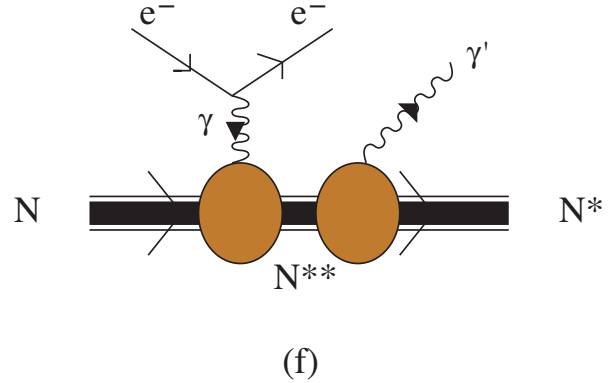
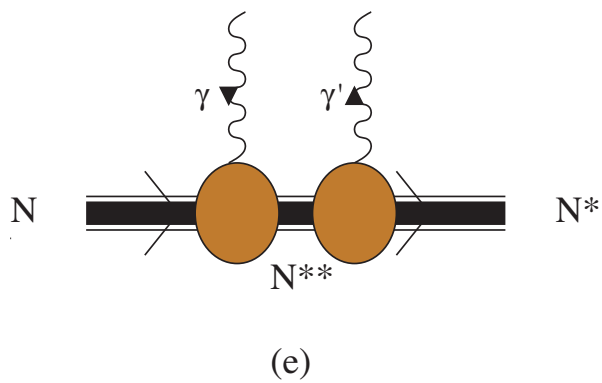
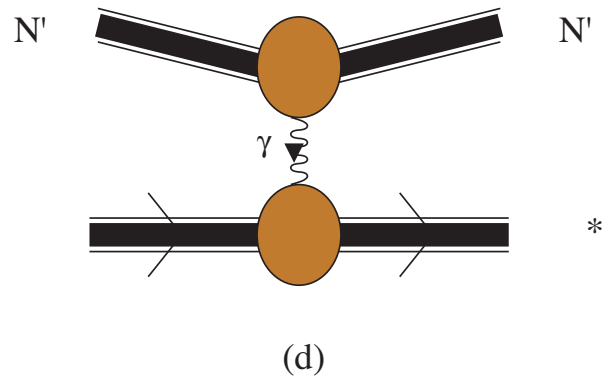
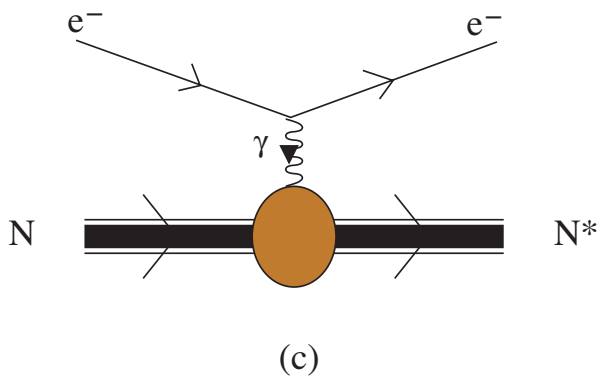
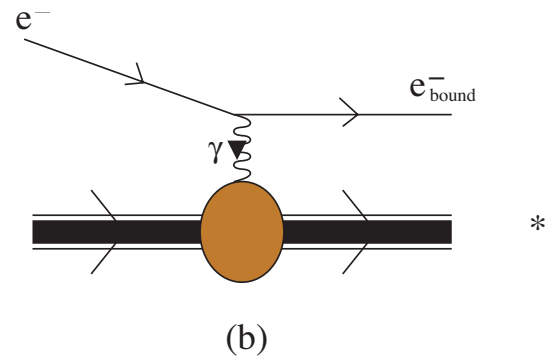
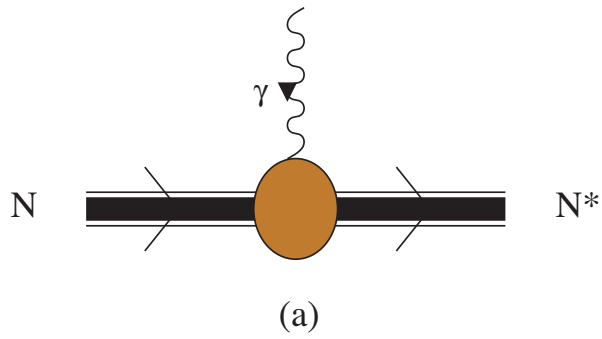
- [1] W. Dappen, L. Anderson, and D. Mihalas, *Ap. J.* **319**, 195 (1987).
- [2] D. Saumon and G. Chabrier, *Phys. Rev A* **44**, 5122 (1991).

For more information, contact
Stephane Mazevet (smazevet@lanl.gov).

Acknowledgements

We would like to acknowledge NNSA's Advanced Simulation and Computing (ASC), Materials and Physics Program for financial support.

PLASMA PHYSICS



Recent Developments in High Energy-Density Plasma Physics

Michael S. Murillo and Jon Weisheit
(T-15)

High energy-density physics (HEDP) is one of the five technical pillars of the Stockpile Stewardship Program, and it is now recognized as an important, multidisciplinary area of research to be emphasized at the national level [1]. Conventionally, HEDP is defined as the study of matter under extreme pressures, in excess of one megabar. As Fig. 1 notes, HEDP science also is relevant to astrophysics and fusion energy research.

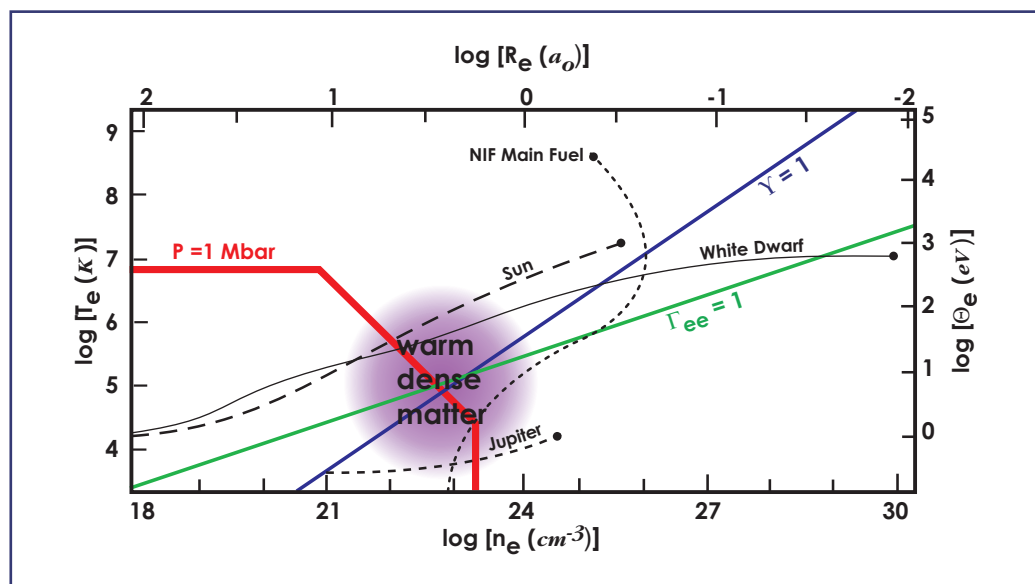
A plasma's ionic charge states, and the many-body correlations among its particles, influence its equation of state, its transport coefficients, and its radiation spectrum, so it is useful to illustrate HEDP effects on these basic quantities. Figure 2 reveals that even a "simple" issue like ionization balance can be difficult to treat accurately in dense plasmas: the Saha equation (appropriate at low densities)

predicts mean charge states $\langle Z \rangle$ that differ substantially from the values of $\langle Z \rangle$ predicted by the Thomas-Fermi equation (appropriate at high densities). Moreover, both of these prescriptions incorporate simplifying assumptions that, at best, are questionable under HEDP conditions, and neither is valid for nonequilibrium plasmas. Further, the Saha equation yields charge state fractions—essential for spectroscopy—but the Thomas-Fermi equation yields just $\langle Z \rangle$.

A second example of HEDP effects is shown in Fig. 3, which plots radial distribution functions $g(r) = n_i(r)/n_i$ in a one component plasma of ions (charge Ze) embedded in a uniform density background of electrons ($n_e = Zn_i$), for different values of the Coulomb coupling parameter $\Gamma = (Ze)^2/a\Theta$, where Θ is the temperature in energy units and $a = (3/4\pi n_i)^{1/3}$ is the mean inter-ion spacing. Radial distribution functions for the larger Γ -values exhibit peaks that indicate substantial short-range order in the plasma.

Within the past year, we reviewed many of the concepts and methodologies (from hydrodynamics, condensed matter, statistical, plasma, and atomic physics) that underlie the field of HEDP [2, 3]. Novel ideas and experiments are needed to better understand and model matter that may be far from equilibrium, strongly coupled by Coulomb interactions, and/or involve degenerate electrons, so one goal of our work was to

Figure 1—
The HEDP regime in the temperature-density plane. Above and to the right of the dark red line, the pressure of matter plus radiation exceeds 1 Mbar. Plasmas below the line $\Gamma_{ee} = 1$ are strongly coupled, and those below the line $Y_e = 1$ are degenerate. The tracks shown mark conditions within the Sun, Jupiter, a white dwarf star, and an imploding ICF capsule.



identify challenging problems in this subject that are important generally to the Nuclear Weapons Program and that could be tackled effectively with present Los Alamos National Laboratory capabilities.

Due to particular Theoretical (T) Division strengths and interests in theory and simulation, three important HEDP subjects have now been identified for emphasis:

Quantum simulation methods (our essential enabling “technologies”—quantum Monte Carlo, quantum molecular dynamics, and wavepacket molecular dynamics); *Radiation Hydrodynamics* (equation of state for mixtures, opacities of inhomogeneous media, turbulence effects, astrophysical and fusion applications); and *Nonequilibrium Phenomena* (relaxation, particle transport, nuclear reactions, laser-plasma interactions, intense magnetic fields).

At last count, more than a dozen specific projects within these areas are already underway or are being organized. These T-Division efforts involve partnerships with both theoretical (e.g., Applied Physics and Computer and Computational Sciences) and experimental (e.g., Physics, Materials Science and Technology, and the Los Alamos Neutron Science Center) divisions at LANL, as well as external laboratories and universities.

- [1] “Frontiers in High Energy Density Physics,” National Research Council, 2003.
- [2] M.S. Murillo, “Strongly Coupled Plasma Physics and High Energy-Density Matter,” *Phys. Plasmas* **11**, 2964 (2004).
- [3] J. Weisheit and M.S. Murillo, “Atoms in Dense Plasmas,” in *AIP Handbook of Atomic Molecular and Optical Physics*, 2nd ed. (Springer, New York, in press).

For more information, contact
Michael S. Murillo (murillo@lanl.gov).

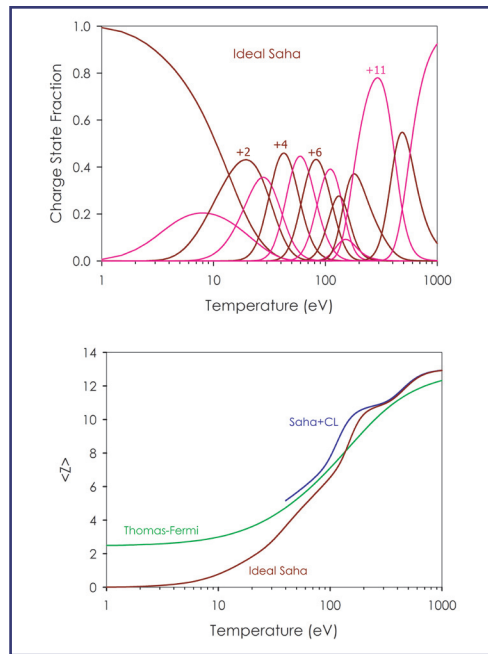


Figure 2—
The variation of mean charge state $\langle Z \rangle$ with temperature in an aluminum plasma at solid density (2.70 g/cm^3), as predicted by the Saha and Thomas-Fermi equations (lower panel). Corresponding Saha charge state fractions (upper panel).

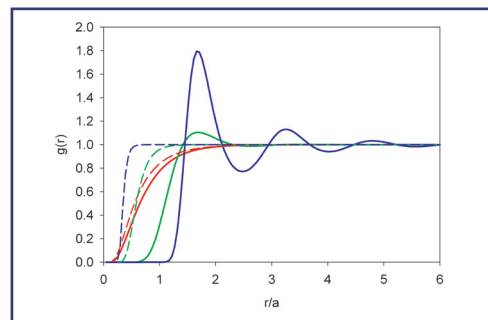


Figure 3—
Radial distribution functions $g(r)$, which measure the expected density of ions neighboring one at the origin, are plotted versus scaled distance r/a , for $\Gamma = 1$ (red), $\Gamma = 10$ (green), and $\Gamma = 100$ (blue). Solid lines: hypernetted-chain theory. Dashed lines: analytic model using Debye potential of mean force.

Acknowledgements

We would like to acknowledge NNSA's Advanced Simulation and Computing (ASC), Materials and Physics Program; and Campaign 1, Primary Certification, for financial support.

Electromagnetic Excitation Rates for Nuclear Isomers in a Hot Dense Plasma

*Thomas C. Luu and Anna C. Hayes (T-6),
and James L. Friar (T-16)*

Nuclear isomers play an important role in the nucleosynthesis of isotopes in weapons and stellar explosions. At the high temperatures and densities available in the hot dense plasmas of interest to both weapons physics and astrophysics there is the possibility of populating nuclear isomers electromagnetically. In this project we examined the rates for electromagnetic excitation of the isotopes of several isomers of interest both in astrophysics and applied physics. We consider six possible electromagnetic processes, namely, photo-absorption, inverse internal conversion, inelastic electron scattering, Coulomb excitation, (γ, γ) , and $(e, e'\gamma)$ reactions.

The electromagnetic excitation rates for all of these processes depend on the temperature of the plasma, the excitation energy of the isomer, and the lifetime of the isomer. To simplify calculations, we assumed that nuclei are completely stripped of their electrons in the plasma. We derived expressions for these electromagnetic processes and examined the rates for several nuclear isomers. Of particular interest for applied physics are the low-lying isomers of ^{235}U , ^{193}Ir , ^{87}Y , ^{88}Y . The half-lives of these isomers range from 0.3 msec to years and their excitation energies from $\sim 77\text{ eV} - 2.5\text{ MeV}$.

The Feynman diagrams representing the electromagnetic processes considered are shown in Fig. 1. We find that for plasma temperatures of $kT \sim 1 - 10\text{ keV}$ the reaction rates for electromagnetic populations are negligible. Thus, these isomers can only be populated by neutron excitation in the explosive environments of interest. Thus, we conclude that weapons radiochemical calculations of the nucleosynthesis of unstable nuclei need not include electromagnetic excitation of isomers.

For more information, contact
Thomas C. Luu (tluu@lanl.gov).

Acknowledgements

We would like to acknowledge NNSA's Advanced Simulation and Computing (ASC), Materials and Physics Program; and Campaign 4, Secondary Certification and Nuclear Systems, for financial support.

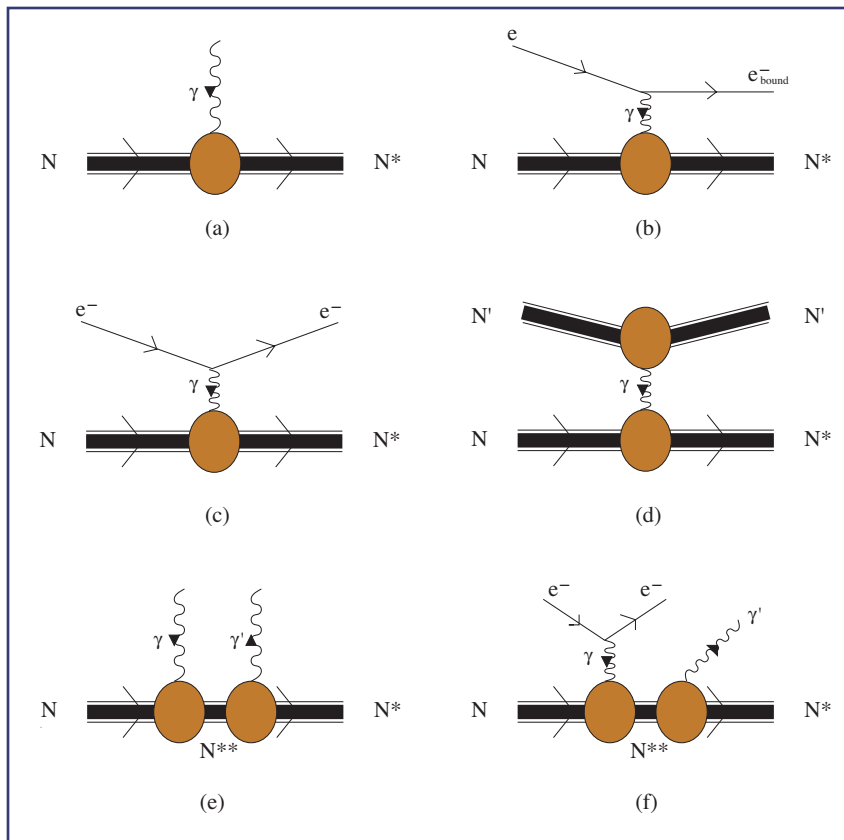


Figure 1—
Feynman diagrams representing the electromagnetic processes considered in this paper. Plot (a) represents photoexcitation. Plot (b) represents inverse internal conversion, where the final electron is bound. Plot (c) shows electron scattering, where the final electron belongs to the continuum. Plot (d) shows ion-excitation, where N' is another ion. Plot (e) shows γ, γ' excitation. Finally, Plot (f) shows $e, e' \gamma$ excitation.

Self-Focusing of Plasma Waves and the Control of Laser-Plasma-Instability

Harvey A. Rose (T-13)

The high-energy-density/inertial confinement fusion HED/ICF program utilizes powerful laser beams, as at the National Ignition Facility (NIF) facility currently under construction at Lawrence Livermore National Laboratory, to create a high-temperature plasma relevant to nuclear weapons research. Design tools, however, do not see the microscopic (submicron length and subpicosecond time scale) interaction between the beams and plasma waves. This interaction may lead to plasma turbulence. Although this is well known, experimental data has become available only in the last few years with sufficient detail to distinguish different regimes of laser-plasma-instability (LPI) relevant to NIF. If these instabilities are too energetic, then design code predictions become less reliable. This aspect of design codes, however, has no direct weapons relevance. Work on LPI has been unclassified since its inception 40 years ago.

There has been recent theoretical progress in Theoretical (T) Division on basic LPI issues. One is the nonlinear saturation of stimulated scatter, whose linear theory was worked out by a retired T-Division staff member [1]. Stimulated scatter is when the following coupled processes become an unstable loop as shown in Fig. 1.

If the plasma wave is a high frequency electron oscillation, or a Langmuir wave, the instability is known as stimulated Raman scatter (SRS). At the high temperatures and low densities of NIF ignition plasma, it is possible that the Langmuir wave's propagation is distorted by self-induced changes in its index of refraction. Technically this arises because a finite fraction of electron orbits are trapped by the wave, reducing its frequency, and then in analogy with propagation of an intense laser beam, the Langmuir wave self-focuses, spraying itself incoherently out of the instability loop, thereby controlling the energy diverted by SRS [2].

Comparison of theory [2] with experimental data [3] shows qualitative agreement in the transition between the coherent SRS, and incoherent self-focusing regimes. A Langmuir wave's amplitude may be characterized by an electron's escape speed, which is inferred from experimental data. Its uncertainty is represented by the length of the black bar in the Fig. 2. By positioning that bar horizontally so as to span both regimes, the theoretical boundary between the two regimes is crossed at a plasma temperature, T_e , of 6.5 million degrees (K), while experimentally the actual transition is closer to 7 million degrees.

Further comparison between LPI theory and experimental data is in progress as part of an ongoing process to arrive at LPI predictive capability.

[1] D.F. DuBois and M.V. Goldman, *Phys. Rev. Lett.* **14**, 544 (1965).

[2] H.A. Rose, "Langmuir Wave Self-Focusing versus Decay Instability," *Phys. Plasmas* **12**, 012318 (2005).

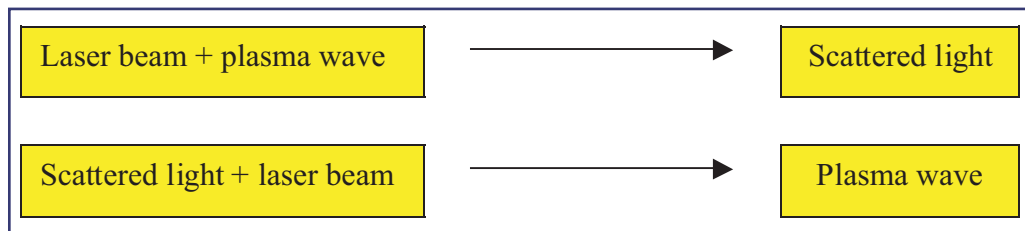


Figure 1—
Stimulated scatter is when these coupled processes become an unstable loop.

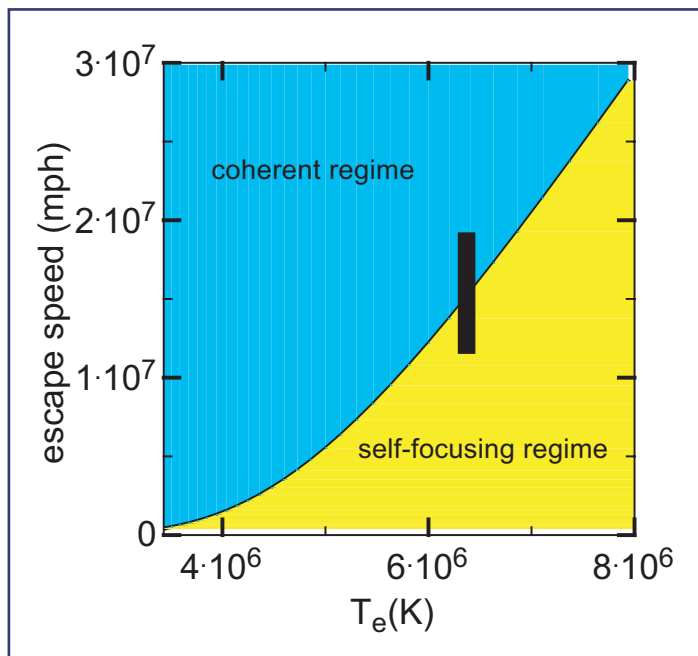


Figure 2—
A Langmuir wave's uncertainty is represented by the length of the black bar.

[3] J.L. Kline and D. Montgomery,
“Observation of a Transition from Fluid to
Kinetic Nonlinearities for Langmuir Waves
Driven by Stimulated Raman Backscatter,”
to be published in *Phys. Rev. Lett.*

For more information, contact Harvey Rose
(har@lanl.gov).

Acknowledgements

We would like to acknowledge NNSA's Advanced
Simulation and Computing (ASC), Materials
and Physics Program; and Campaign 10, Inertial
Confinement Fusion Ignition, for financial
support.

Extended Thomas-Fermi Models for Equations of State of Dense, High Energy-Density Matter

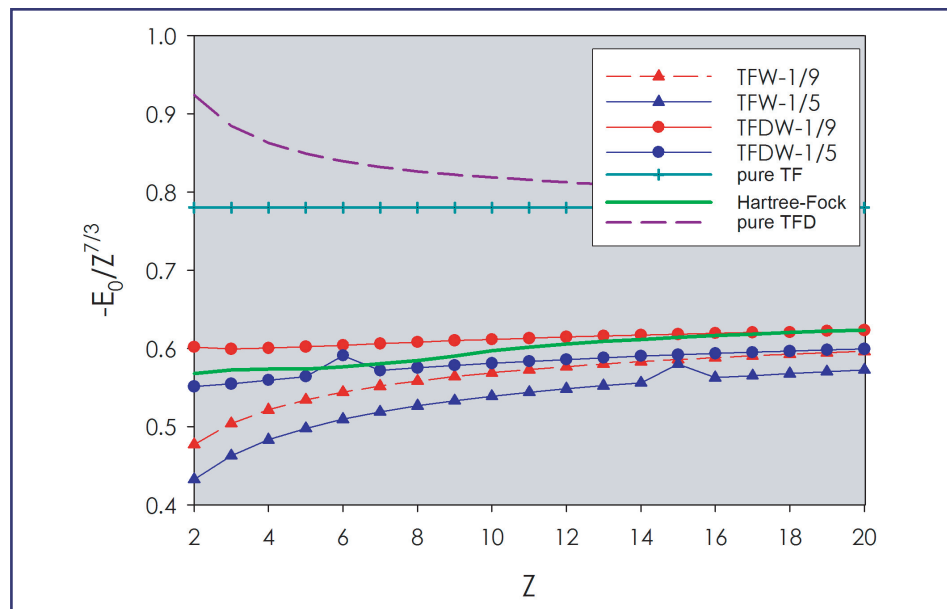
George Csanak (T-4), Jérôme Daligault and Michael S. Murillo (T-15)

Our goal is to develop an equation of state model for dense, high energy-density matter—which has densities near solid and pressures exceeding one megabar—that spans temperatures from tens of electron volts to several kilovolts. Density functional theory (DFT) is our starting point, since it is formally exact and therefore allows us to construct rigorous, self-consistent models of wide applicability. In the high-density and/or high-temperature limit, we know that DFT tends toward the so-called Thomas-Fermi (TF) model; unfortunately, solid density is too low for this limit to be of use. Moreover, there is evidence that the first obvious

correction to basic TF theory, which adds an exchange term to the free energy and carries the name “Thomas-Fermi-Dirac” (TFD), can actually be worse [1, 2]. It is also generally recognized [2] that the most important correction to TF theory is the inclusion of the cusp condition near a nucleus, which makes the electronic density finite there. The cusp arises from a gradient correction term known as the “Weizsäcker” (TFDW) correction, which occurs with various coefficients λ . To understand these issues we are working to develop a *rigorous* formulation of extended Thomas-Fermi theory that is an all-electron theory, does not employ ad hoc scaling factors λ of the gradient terms, and does not assume that various physical effects (e.g., kinetic energy and exchange) enter in an additive manner; that is, our formulation will be internally self-consistent.

To understand the main features that we wish to keep in our formulation, we have first studied various forms of extended TF theory. Specifically, we have studied cold, neutral atoms because (1) we can study variations with nuclear charge, (2) it is possible to compare with very accurate experimental and theoretical results, and (3) the low temperature regime represents a difficult limit of our intended high-temperature regime of interest. As we are also interested in a computationally efficient method, we also use the simple case of atomic systems to develop a variational method to

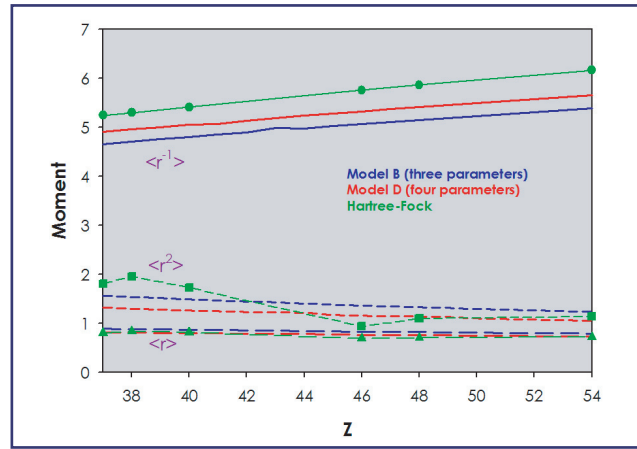
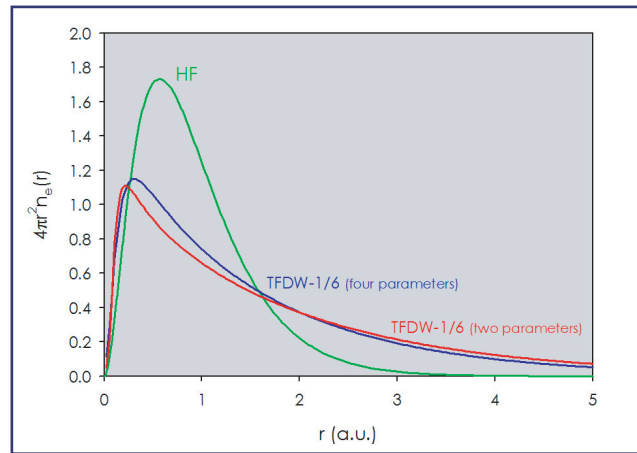
Figure 1—
This figure shows the ground state energy of atoms, in terms of $-E_0/Z^{7/3}$, versus nuclear charge Z as computed with several models. The most important extension is the gradient correction (TFDW). The fractions following the TFDW results are the values of the coefficient λ . The Dirac (exchange) (TFD) correction to TF degrades the result.



find the electronic density. In addition to computational efficiency, our variational method employs an electronic density that has desirable behaviors, such as a finite value near the nucleus. We choose various forms for the parameterization to ensure convergence. In practice, we construct forms for the free energy that correspond to different extended TF theories, all of which depend only on the density, and perform a minimization with respect to the parameters of the density subject to normalization of the density. We have used two different methods for performing the minimization, and we report results in this paper that use the Powell method.

We display some of our results in Figs. 1–3. In the first figure we show the ground state energy of atoms with nuclear charges $Z = 2 - 20$ as computed from various models, including the accurate Hartree-Fock (HF) theory. We plot $-E_0/Z^{7/3}$, where E_0 is the actual ground state energy, because this quantity is constant in pure TF theory. Our results confirm that TF is not very accurate, TFD is worse, and models with gradient correction that are consistent with the cusp condition are quite good with about 10% agreement with HF. Figure 2 shows the actual density for the case of helium ($Z = 2$) and poor agreement is found, as expected for a low- Z element. This indicates that other quantities might be more or less sensitive to the result depending on how they weight the density variations. To quantify the density variations we compare density moments in Fig. 3 between HF and our parameterized density versus nuclear charge. For higher- Z elements, the moments are quite well described with extended TF models.

In conclusion, we feel that an extended TF model will yield accurate equations of state for hot, dense matter provided exchange (“Dirac”) and gradient terms are included rigorously and self-consistently. Although other contributions, such as correlation corrections beyond the mean-field, may be important at high temperatures [3], we



feel that we will be able to obtain extremely accurate equations of state. For dense matter we will develop our “high temperature-DFT” first in a spherical cell and then in a macrocell consisting of many—possibly different—nuclei. We have made considerable progress in developing such a formulation from DFT, and this will be reported in the future.

- [1] J.F. Barnes and R.D. Cowan, *Phys. Rev.* **132**, 236 (1963).
- [2] R.G. Parr and W. Yang, *Density-Functional Theory of Atoms and Molecules* (Oxford University Press, Oxford, 1994).
- [3] U. Gupta and A.K. Rajagopal, *Phys. Reports* **87**, 259 (1982).

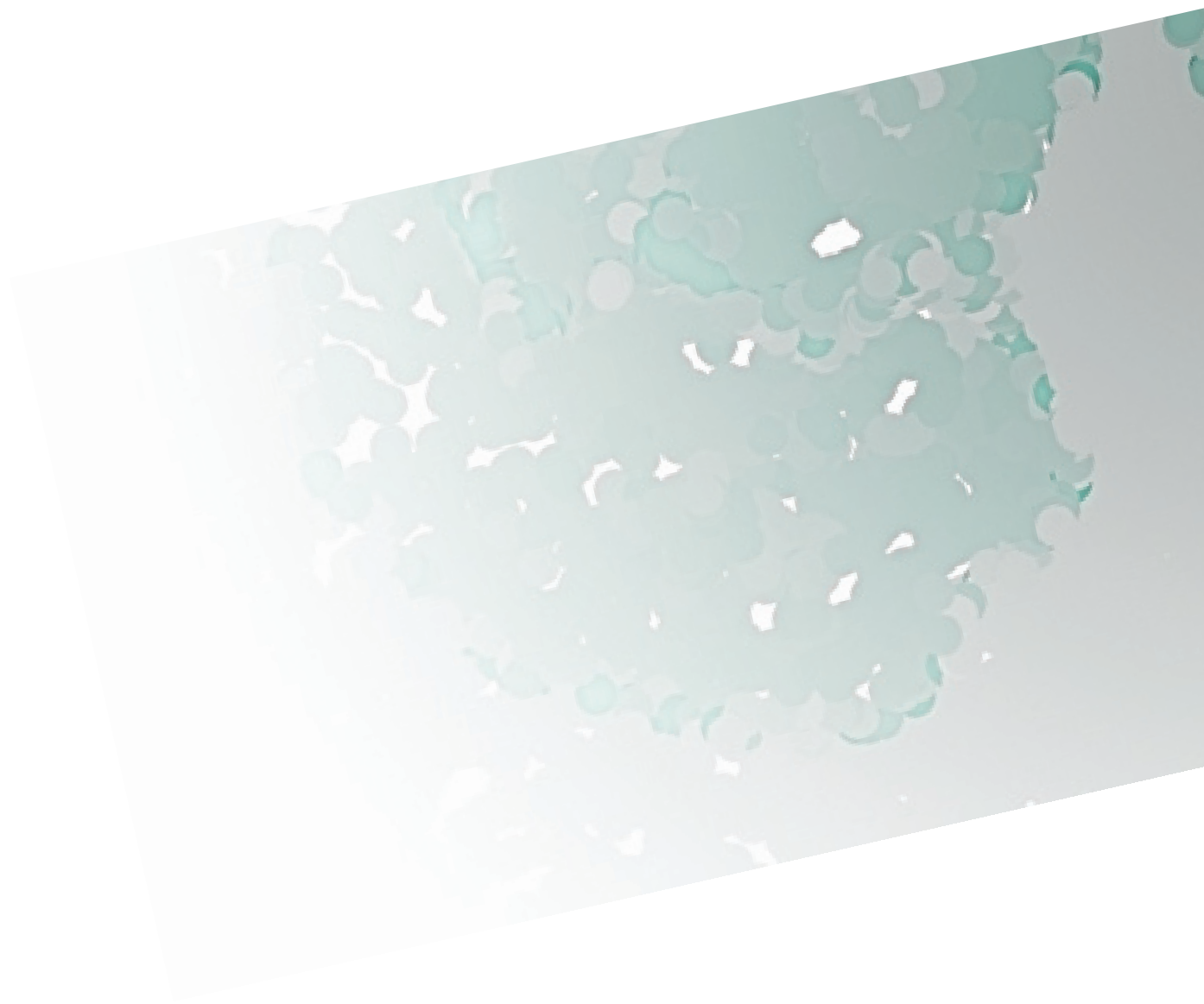
For more information, contact
Michael S. Murillo (murillo@lanl.gov).

Acknowledgements

We would like to acknowledge NNSA’s Advanced Simulation and Computing (ASC), Materials and Physics Program for financial support.

Figure 2—
Here we show the radial density $4\pi r^2 n(r)$ for helium from three models: green (HF), red (our TFDW-1/6 with two parameter minimization), and blue (same as red with four parameters). The agreement is poor, as expected for a low- Z element.

Figure 3—
Moments of the density are shown versus nuclear charge from several models: green (HF), blue (three parameter TFDW), and red (four parameter TFDW). Overall agreement between extended TF and HF is good and convergence with respect to the number of parameters is seen.



ASTROPHYSICS



Theoretical Prediction of an Observed Solar g-Mode

Arthur N. Cox (T-6) and
Joyce A. Guzik (X-2)

Since the beginnings of nuclear weapons research at Los Alamos National Laboratory, there has been an interest in the conditions in stars with similar high temperatures, densities, and pressures. This interest has grown to full-time efforts of a few astrophysicists to become part of worldwide research on stellar astrophysics. This report covers very recent results for the pulsational stability of the sun that have been obtained to interpret just-published [1], line-of-sight radial velocity data of the solar surface. Periods of solar pulsations from these Lagrange point satellite observations indicate global oscillation modes. Here we discuss a single mode that seems to be confirmed as being pulsationally unstable. Our result showing that only a very few of all possible long-period modes should be pulsationally unstable has just been published in a recent *Astrophysical Journal Letters* paper.

For most of 30 years, periods of the observed shorter global oscillation periods have been known to ever-increasing accuracy, and their theoretical prediction at Los Alamos and elsewhere reveals accurate details of the outer solar layers [2, 3]. The new, finally reliable, longer periods of about 1 hour, are for pulsation modes with large amplitudes only very near to the solar center. These extremely difficult to observe modes (called nonradial g-modes) are of great interest, because matching the mode periods reveals information about the solar center temperature and density where solar neutrinos originate. Further, the observed splitting of these mode periods reveals the central rotation velocity. These conditions are found to smoothly match those found from the shorter periods (called nonradial p-modes).

The figure shows the radial and horizontal motion amplitudes (eigenvectors), plus the period weight for the detected $\ell = 2$, g_3 mode. Note the determination of the period, its weight, depends almost entirely on conditions deeper than about 0.2 of the solar radius (near where the gravity acceleration peaks), but not at the very center.

Also shown are the deep radiative damping (dips at shells 415, 500, and 650), the radiation luminosity blocking [4], and hydrogen opacity effect driving of this eigensolution. Damping is due almost entirely to radial motions at these low spherical harmonic ℓ values. Transverse motions are found to be very small in our linear nonradial nonadiabatic calculations. One can see that where the radiation fraction goes to zero at the convection zone bottom, the driving also goes to zero. The near-surface hydrogen ionization driving actually occurs inside the convection zone upper boundary with some radiation still available for opacity blocking to occur anyway.

Across the top of Fig. 1 is a band of data showing the coordinates for the mass depth, the fractional radii, the temperature in units of millions of kelvin, and the helium mass fraction composition Y for various Lagrange shells.

- [1] S. Turck-Chieze, et al., "Looking for Gravity-Mode Multiplets with the GOLF Experiment aboard SOHO," *Ap. J. L.* **604**, 1 (March 2004), p. 455.
- [2] J.A. Guzik and F.J. Swenson, *Ap. J.* **491**, 967 (1997).
- [3] C. Neuforge-Verheecke et al., *Ap. J.* **550**, 493 (2001)
- [4] A.N. Cox, *Solar Physics* **128**, 123 (1990).

For more information, contact Arthur Cox (anc@lanl.gov).

Acknowledgements

We would like to acknowledge NNSA's Advanced Simulation and Computing (ASC), Verification and Validation Program for financial support.

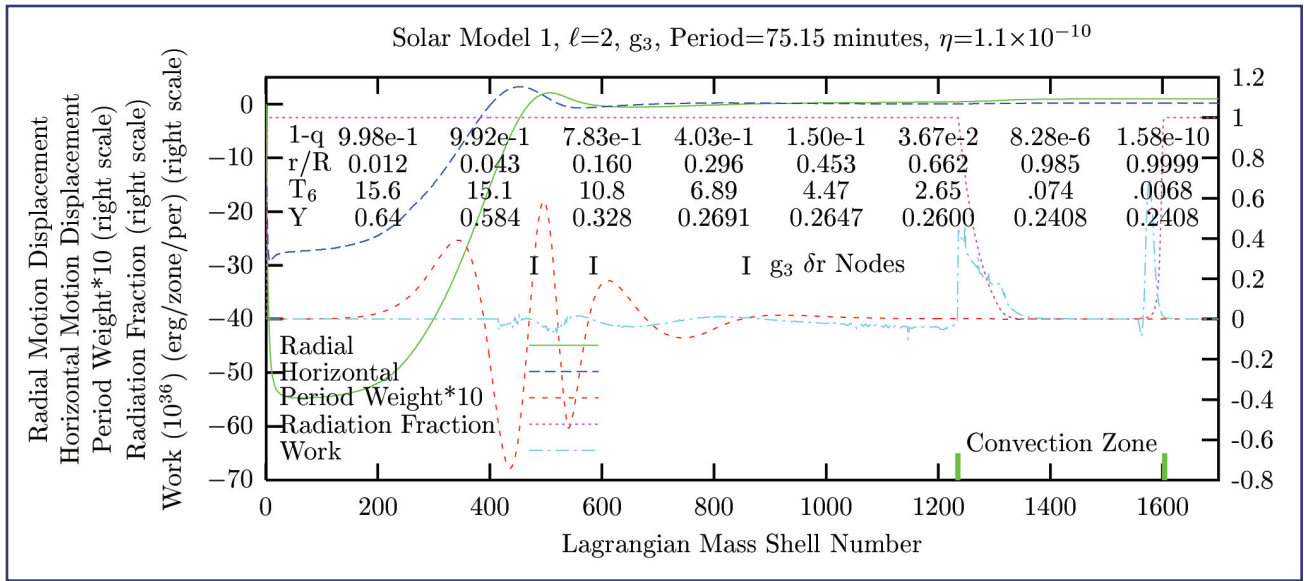


Figure 1—

The radial and horizontal displacement eigenvectors, normalized to the standard $\delta r/r = 1$ at the 1700 mass shells model surface, are plotted versus the zone number with the solar model center at the left and the surface at the right. The work done at each linear pulsation cycle is also plotted, showing pulsation driving at the bottom of the convection zone and at the convection zone surface by hydrogen κ effect. The fraction of the solar luminosity due to radiation inside and outside the convection zone is also indicated.

Modeling Supernova Explosions

*Chris Fryer and Gabe Rockefeller (T-6),
Kim New (X-2), and Aimee Hungerford
(CCS-4)*

Supernovae are one of the biggest explosions in the universe. Their ejecta plow through the Milky Way, producing spherically shaped “remnants” composed of supernova debris mixed with dust in our Galaxy. The shocks produced by this motion heat the debris, causing it to radiate. Astronomers detect this radiation and use their observations to study both the supernova explosion and the interstellar matter through which the supernova plows.

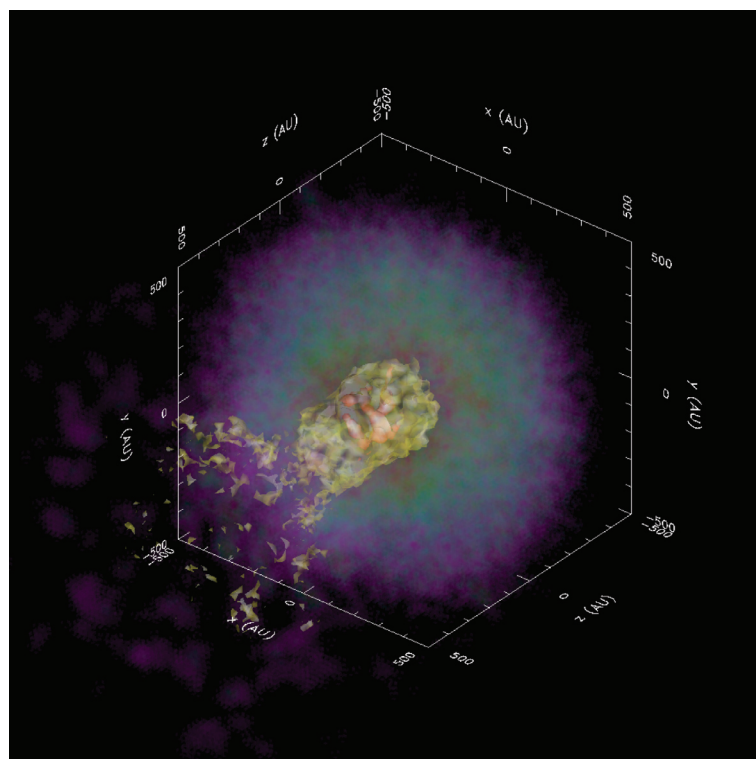
A few nearby supernova remnants have been studied in space, time, and composition. We can use these observations to not only study supernova explosions, but also to study hydrodynamics and test the ability of our numerical codes to model the detailed mixing in the explosive phenomena. The wealth of observational data, from the time evolution

of specific knots in the ejecta to detailed composition measurements, provides a number of checks, allowing us to overcome the uncertainties in the initial explosion and, ultimately, to test our hydrodynamic codes.

This project, currently at its initial stages, is set to model the propagation of the supernova explosion, paying particular attention to the turbulence and elemental mixing that occurs in this ejecta. Figure 1 shows an isosurface of the abundance of a radioactive isotope of nickel (^{56}Ni) within the explosion ejecta (shading) from an asymmetric explosion using the three-dimensional (3D) Smooth Particle Hydrodynamics code (SNSPH) developed in T-6 [1]. The asymmetry in the explosion mixes the ^{56}Ni well out into the outer layers of the ejecta and the amount of mixing provides an ideal diagnostic of the supernova explosion.

But our modeling of this mixing is very sensitive to the hydrodynamic algorithm. To test these calculations, we have begun detailed comparison calculations between the SNSPH and RAGE [2] codes. In our first suite of comparison calculations, we compare 1D simulations using a 1D Lagrangian code [3] to RAGE. Figure 2 (top) shows a comparison of the velocity profiles

Figure 1—
An isosurface of the abundance of a radioactive isotope of nickel (^{56}Ni) within the explosion ejecta (shading) from an asymmetric explosion using the 3D Smooth Particle Hydrodynamics code (SNSPH) developed in T-6 [1].



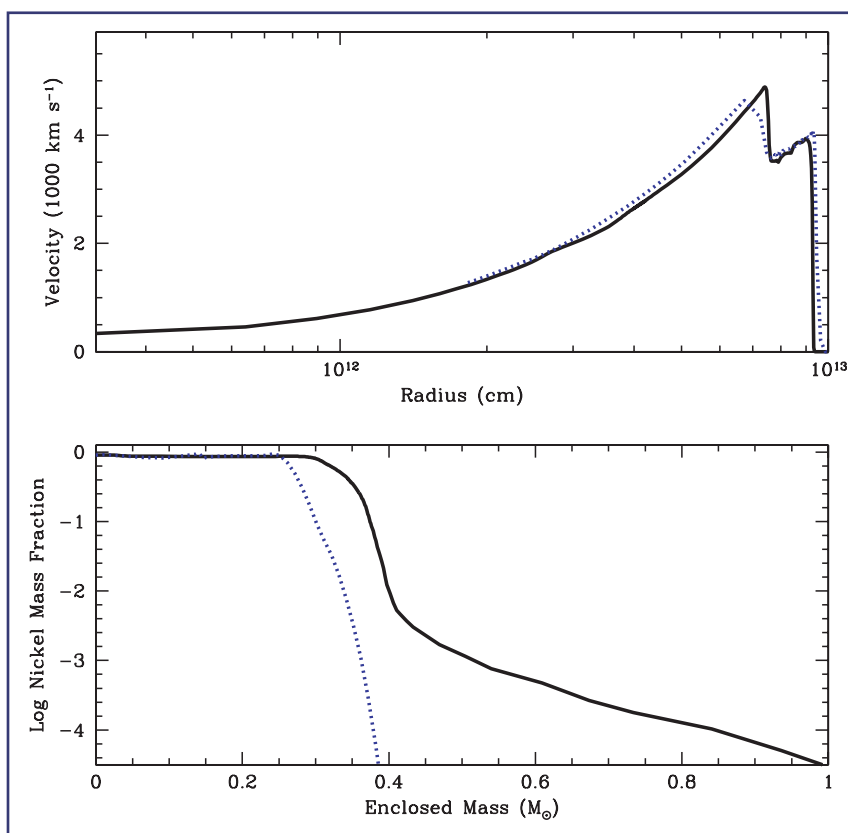


Figure 2—
 (top) A comparison of the velocity profiles of the ejecta at two different times during the explosion.
 (bottom) The nickel abundance distribution vs enclosed mass for these codes for these same two time slices plus one final time slice as the shock breaks out of the star.

of the ejecta at the end of our simulation. Such an explosion is a slight variant over the standard Sedov test used to calibrate codes. It differs by including a complex equation of state and a nonpower-law density profile. It provides a much more rigorous test of these hydrodynamics codes. Figure 2 (bottom) shows the nickel abundance distribution versus enclosed mass for these codes for this same time. Both simulations are using extremely low resolution (roughly 200 zones in the Lagrangian simulation and 500 zones in the RAGE calculation). This resolution is what we will be able to achieve in our 3D calculations. In the Lagrangian calculation, the ^{56}Ni distribution does not change with time. The spreading of the ^{56}Ni in the RAGE calculations is due to numerical diffusion. It is this artificial diffusion that we must understand and constrain to successfully complete this validation experiment.

- [1] C.L. Fryer and M.S. Warren, “Modeling Core-Collapse Supernovae in Three Dimensions,” *Ap. J.* **574**, L65 (2002).
- [2] R.L. Holmes, et al. “Richtmyer-Meshkov Instability Growth: Experiment, Simulation and Theory,” *J. Fluid Mech.* **389**, 55 (1999).
- [3] M. Herant, et al., “Inside the Supernova: A Powerful Convective Engine,” *Ap. J.* **435**, 339b (1994).

For more information, contact Chris Fryer
 (fryer@lanl.gov).

Acknowledgements

We would like to acknowledge NNSA’s Advanced Simulation and Computing (ASC), Verification and Validation Program for financial support.

Stellar Burning and Mixing

Falk Herwig, Alexander Heger, and Frank Timmes (T-6); and Rob Hueckstaedt and Rob Coker (X-2)

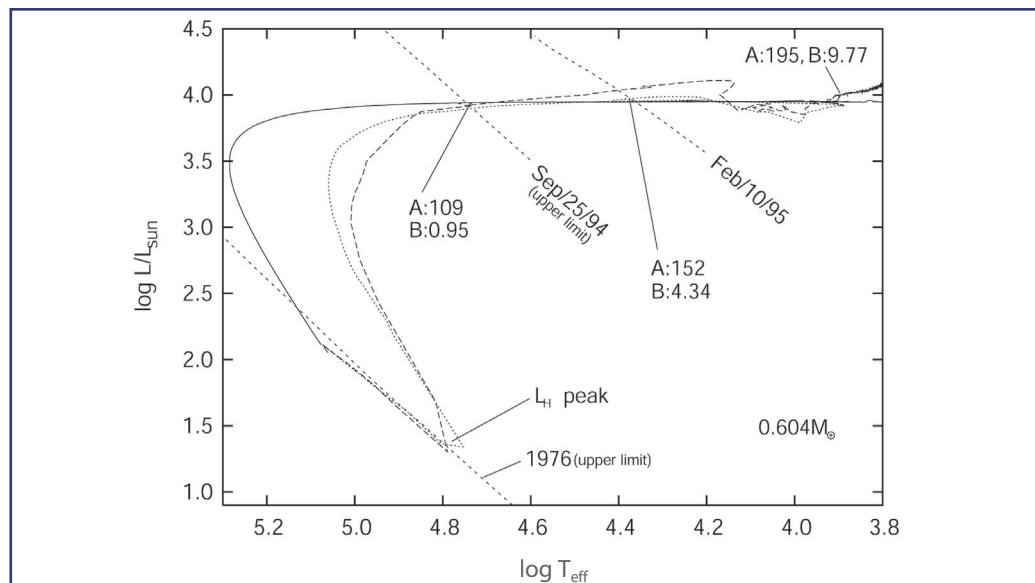
During most phases of stellar evolution, nuclear burning and convective mixing operate on largely different time scales. However, 1D astrophysical modeling of stars has been able over the past years to tie several important observational peculiarities in stars to rapid nuclear burning in convective regions in which mixing and nuclear energy release proceeds on comparable time scales.

We have identified one type of object—the born-again giants—that provide astrophysical observables in the form of light curves and elemental surface abundances that are especially well suited to test how nuclear burning may affect the inherently multidimensional mixing process of convection [1]. In these objects, a thermonuclear runaway of the helium shell on top of an electron-degenerate core (a young White Dwarf) causes a rapid expansion of the outer layers, and the star evolves back to high luminosity and low surface temperature—an evolutionary state from which it just descended (Fig. 1).

Using 1D calculations we find a link between the turbulent diffusion coefficient in the He-shell flash driven by the convection zone and the observable time scale of the change of stellar parameters (Fig. 2) [2]. In these astrophysical objects, mixing may be less efficient because convection brings hydrogen into the very hot carbon-rich helium-burning layer. This is a very volatile mixture that burns on the convective time scale, adding buoyancy to blobs in which hydrogen and carbon were mixed together.

An outstanding scientific puzzle concerns the mechanisms by which the first significant amounts of nitrogen were produced in the universe. Processes similar to those given above may play a role in the helium burning and nitrogen production of the first generation of stars. In these stars, a convective helium-burning carbon-rich region comes into contact with a hydrogen-rich layer. Also here, a convective helium-burning carbon-rich region gets in contact with a hydrogen-rich layer. The key questions are (1) how much mixing occurs before rising entropy gradients due to burning eventually shuts off further mixing, (2) how much nitrogen is being produced, and (3) how many protons are mixed into the center of the star. The degree of proton mixing has implications for the production of neutron-rich elements.

Figure 1—
A thermonuclear runaway of the helium shell on top of an electron-degenerate core (a young White Dwarf) causes a rapid expansion of the outer stellar layers, which leads the star back to high luminosity and low surface temperature—an evolutionary state from which it just descended.



We have started a project using RAGE and FLASH to model the effect of rapid nuclear energy release on turbulent flow patterns in convection. We are currently setting up Rayleigh-Bernard-like test problems of convection (Fig. 3) to serve as a starting point for developing simulations that represent stellar conditions. We will include a stellar equation of state as well as thermonuclear burning (TN burn) into RAGE. By comparing simulations with and without TN burn we aim to recover the averaged effect of burning on the mixing suggested by astrophysical observables.

This project takes RAGE into a new application regime. Complementary 1D astrophysical modeling allows us to access specific observables from the astrophysical context to probe the RAGE behavior with regard to burning and mixing. This verification problem is innovative because it utilizes a certain class of astrophysical observational data for the first time.

- [1] M. Hajduk et al., “The Real-Time Stellar Evolution of Sakurai’s Object,” *Science* **8**, 308, 231–233 (April 2005).
- [2] F. Herwig, “The Evolutionary Timescale of Sakurai’s Object: A Test of Convection Theory?” *ApJ Lett.* **554**, 74 (2001).

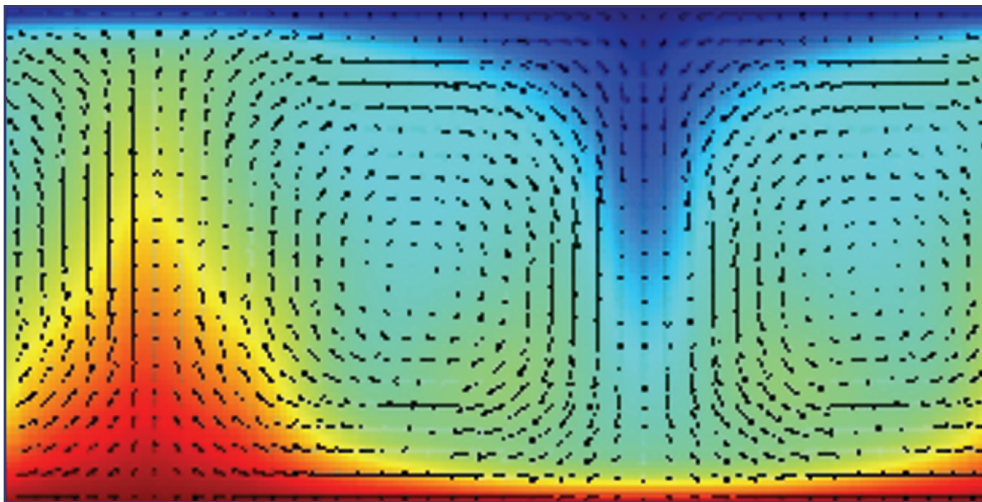
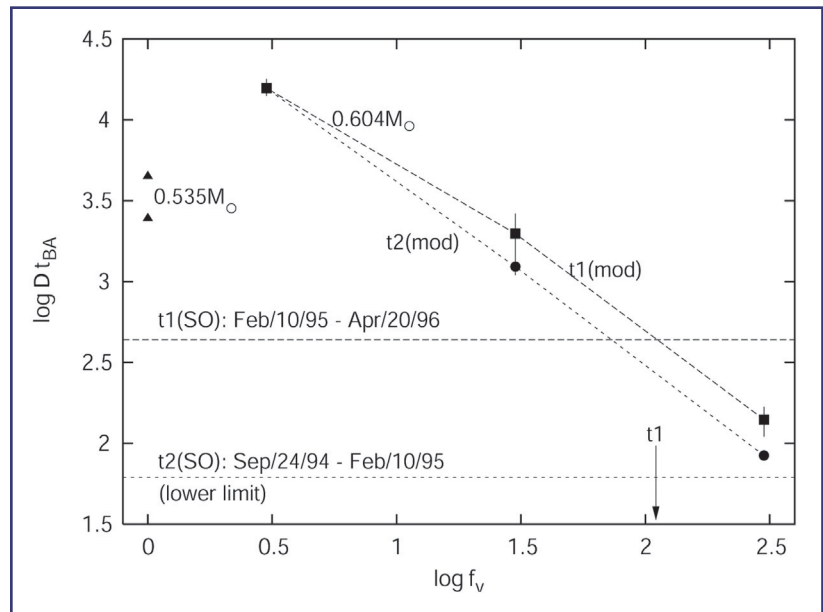


Figure 2—
A link between the mixing velocity in the He-shell flash driven convection zone and the observable time scale of the change of stellar parameters. This case implies that nuclear burning may reduce mixing by a factor ~ 100 .



For more information, contact Falk Herwig
(pherwig@lanl.gov).

Acknowledgements

We would like to acknowledge NNSA’s Advanced Simulation and Computing (ASC), Verification and Validation Program for financial support.

Figure 3—
Snapshot of temperature of 2D simulation box for Rayleigh-Bernard-like test problem with RAGE.

Fission Neutron Multiplicity Functions for Preinitiation Calculations

*Thomas C. Luu, Jack Hills,
Gerard Jungman, and
Anna C. Hayes (T-6)*

The vast majority of the world's plutonium (Pu) comes in the form of reactor-grade Pu as opposed to weapons-grade Pu. For this reason, the threat of a nuclear attack on the U.S. from a device based on reactor-grade Pu must be taken very seriously. The most important difference between weapons-grade and reactor-grade fuel is the high content of ^{240}Pu in the latter. Plutonium-240 has a high spontaneous fission rate and this in turn leads to a greatly increased probability of device preinitiation. In this project we have been examining the fission neutron multiplicities associated with spontaneous fission of the Pu isotopes found in reactor-grade Pu.

The probability of obtaining a divergent fission chain from a neutron emitted in spontaneous fission depends on neutron multiplicity probabilities $p(n)$. The neutron multiplicity probabilities determine the probability of obtaining n neutrons given that the average number of neutrons emitted per fission is $\bar{\nu}$. In the transport codes used to calculate preinitiation probabilities, these neutron multiplicities appear directly in the total multiplicity functions C_n , which determine the number of ways of obtaining n neutrons given $\bar{\nu}$. The neutron multiplicity probabilities $p(n)$'s are well described in terms of a Gaussian distribution around the average number, $\bar{\nu}$, as first calculated by Terrell in 1957. Terrell evaluated the available neutron multiplicity data and found that a single Gaussian distribution with a global variance $\sigma = 1.08$ provided a good description of data.

However, there have been numerous experiments since then. In the present work we have compiled all the data measured since the mid 1950s and examined whether or not a global variance still satisfactorily describes all experimental data. In doing so, we have obtained improved descriptions of fission neutron multiplicities.

Our analysis of the more modern and expanded data for neutron multiplicities showed that the variance of the Gaussian distribution around the average neutron number increased from Terrell's global value of 1.08 to 1.14 for the Pu isotopes. This in turn implied a 33% increase in the probability of emitting four neutrons from the fission of ^{239}Pu .

We also found that the data sets showed a systematic dependence on the variance, $\bar{\nu}$ which varies with the mass and charge of the nucleus. Our analysis suggests that an overall weighted average for $\bar{\nu}$ is not physically justified. We have proposed that the transport codes be extended to include a nucleus and $\bar{\nu}$ dependent σ . Figure 1 shows how the total multiplicity functions C_n change when such a dependence is used.

For more information, contact
Thomas C. Luu (tluu@lanl.gov).

Acknowledgements

We would like to acknowledge DOE Office of Research and Engineering (NA-22) for financial support.

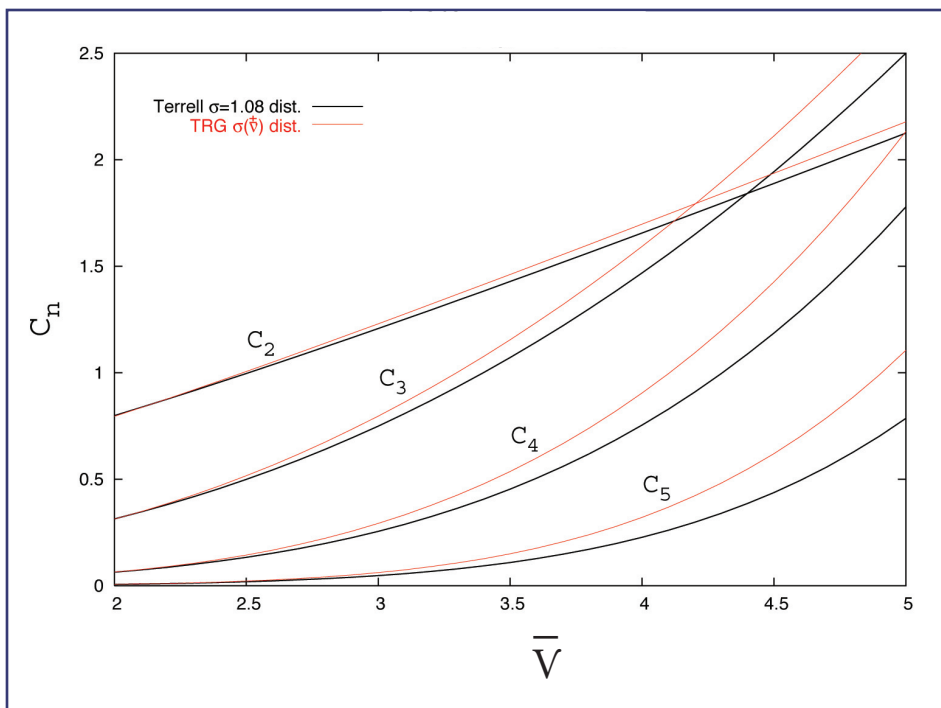


Figure 1—
The figure shows how
the total multiplicity
functions C_n change.

On Variations in the Peak Luminosity of Type Ia Supernovae

Frank X. Timmes (T-6), Edward F. Brown (Michigan State University), and J. W. Truran (University of Chicago)

We explore the idea that the observed variations in the peak luminosities of Type Ia supernovae originate in part from a scatter in metallicity of the main-sequence stars that become white dwarfs. Previous, numerical, studies have not self-consistently explored metallicities greater than solar. One-dimensional Chandrasekhar mass models of Type Ia supernovae produce most of their radioactive nickel in a thermonuclear burn to nuclear statistical equilibrium between where the electron to nucleon ratio is constant. We show analytically that, under these conditions, charge and mass conservation constrain the mass of nickel produced to depend linearly on the original metallicity of the white dwarf progenitor. This curious result is independent of any complicated hydrodynamics or flame propagation microphysics, and 3-dimensional (3D) explosion models confirm this linear dependence. The observed factor of three scatter in the metallicity of solar neighborhood stars is enough to induce a 25% variation in the mass of nickel ejected by Type Ia supernova, which is enough to vary the peak luminosity of Type Ia events by about 0.2 magnitudes in the visual band. We argue that this intrinsic scatter in the peak luminosity is present in spirals and elliptical

galaxies out to the limiting redshifts of current observations.

Nearly all 1D Chandrasekhar mass models of Type Ia supernova produce most of their ^{56}Ni in a burn to nuclear statistical equilibrium between the mass shells $0.2 M_{\odot}$ and $0.8 M_{\odot}$. In this region, unlike in the innermost $0.2 M_{\odot}$, weak interactions operate on timescales longer than the time for the thermonuclear burning front to disrupt the white dwarf. Following this rapid burn to nuclear statistical equilibrium, most of the mass is in the iron-peak nuclei ^{56}Ni , ^{58}Ni , and ^{54}Fe . First consider the case when ^{56}Ni and ^{58}Ni are the only two competing species. Mass and charge conservation,

$$\sum_{i=1}^n X_i = 1, \sum_{i=1}^n \frac{Z_i}{A_i} X_i = Y_e$$

imply that the mass fraction of ^{56}Ni depends linearly on Y_e ,

$$X(^{56}\text{Ni}) = 58Y_e - 28,$$

where isotope i has Z_i protons, A_i nucleons (protons + neutrons), and a mass fraction X_i . The aggregate ensemble has a proton to nucleon ratio of Y_e .

In the white dwarf progenitors of Type Ia supernovae, the surplus neutrons come from ^{22}Ne formed from the original CNO of the progenitor main-sequence star, and from the original ^{56}Fe . Using this to compute only unknown, Y_e , we find

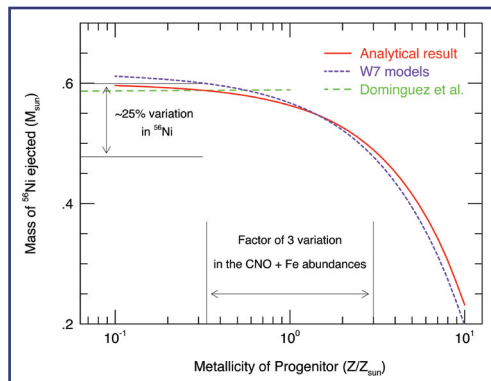
$$X(^{56}\text{Ni}) = \left(1 - 0.057 \frac{Z}{Z_{\odot}}\right).$$

The total mass of ^{56}Ni ejected is then

$$M(^{56}\text{Ni}) \approx 0.6 \left(1 - 0.057 \frac{Z}{Z_{\odot}}\right) M_{\odot}.$$

This linear relation is shown by the red line in Fig. 1 along with the results of our post-processing calculation (purple dashed line) of a standard one-dimensional model of Type Ia supernovae (courtesy F. Brachwitz and F. Thielemann). Our analytical result [1] and postprocessing result are in good agreement with those of Refs. [2, 3] and (green dotted line) where the calculations overlap in metallicity. Our findings disagree, however, with those of [4], who found only a 4% variation in $M(^{56}\text{Ni})$ over an even larger range of Z (0.1 to 10 times solar).

Figure 1— Mass of ^{56}Ni ejected by Type Ia Supernovae as a function of the initial metallicity Z . Shown is the linear relation (red curve; the curvature is from the logarithmic abscissa), and two popular 1-dimensional models (purple and green curves). As indicated by the arrows, a scatter in the abundances with which a low mass star is born leads to a variation of about 25% of ^{56}Ni ejected if the metals are uniformly distributed within the remnant white dwarf. A factor of seven scatter about the mean in the initial metallicity corresponds to a factor of 2 variation in $M(^{56}\text{Ni})$.



The Max-Planck group in Germany [5], and the ASC/Alliance Center at the University of Chicago [6] have recently explored the dependence of the $M(^{56}\text{Ni})$ abundance on the initial metallicity, as reflected in $X(^{22}\text{Ne})$, with 2D and 3D calculations. The temperature field of our 2D calculations is shown in the impressionistic Seurat-like pointillism of Fig. 2. Both of these groups substantially reproduce the analytic result (Fig. 3).

The general trend among field stars is that the metallicity rises rapidly and then increases gradually over the last 10 Gyr corresponding to redshifts $z \lesssim 1$. The scatter in the abundances is roughly from 1/3 to 3 times solar at all ages, and this scatter in the material from which stars are born is sufficient to induce a 25% variation ($0.13 M_{\odot}$) in the mass of $M(^{56}\text{Ni})$ ejected. The minimum peak brightness variations caused by this variation in ^{56}Ni mass are $\Delta M_v \sim 0.2$.

For the nearby Type Ia supernovae with Cepheid determined distances, the overall dispersion in the peak magnitude is rather small, about 0.5 magnitude in the B and V bands [7, 8]. When the sample is enlarged to include more distant supernovae, there are several subluminal events that broaden the variation to about 1 magnitude in B [9, 10], but the bulk of the Type Ia sample lies within 0.5 magnitude in B. While the magnitude of analytic effect that we have identified cannot account for all of the observed variation in peak luminosity of local Type Ia supernovae, it is probably the largest contributor [11].

- [1] Timmes et al., *Ap. J. L.*, **590**, L83 (2003).
- [2] Iwamoto et al., *Ap. J. S.*, **125**, 439 (1999).
- [3] Domínguez, et al., "Constraints on the Progenitors of Type Ia Supernovae and Implications for the Cosmological Equation of State," *Astrophys. J.* **557**, 279–291 (2001).
- [4] Höflich et al., *Astrophys. J. S.* **495**, 617 (1998).
- [5] Travaglio et al., *A&A* **425**, 1029 (2004).
- [6] Brown et al., to be published in *Nucl. Phys. A*, 2005.

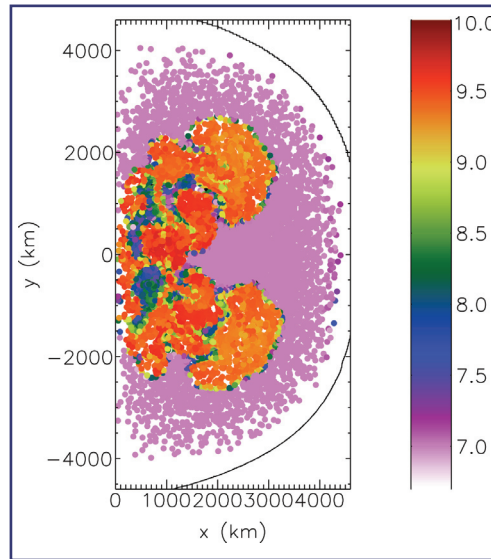


Figure 2—
Nickel mass from a two-dimensional calculation performed at the ASC Alliance Center the University of Chicago [6]. The strong 45° symmetry in the Seurat-like image is due to artificial symmetries present in the initial conditions.

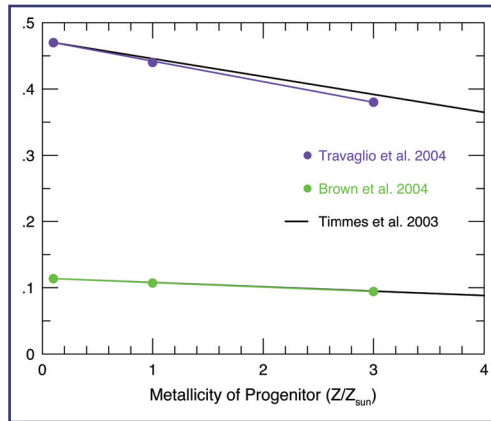


Figure 3—
Nickel mass from three-dimensional (purple curve) and two-dimensional (green curve) simulations. The linear relationship of the analytical formula (black curve) is largely reproduced. The difference between the 3D and 2D results has less to do with the dimensionality of the calculation and more to do with how the burning front is modeled.

- [7] Saha et al., *Ap. J.*, **522**, 802 (1999).
- [8] Gibson et al., *Ap. J.* **529**, 723 (2000).
- [9] Hamuy et al., *Astron. J.* **112**, 2438 (2004).
- [10] Riess et al., *A.J.* **106**, 1009 (2004).
- [11] F.K. Roepke and W. Hillebrandt, *A&A* **420**, L1 (2004).

For more information, contact
Francis Timmes (timmes@lanl.gov).

Acknowledgements

We would like to acknowledge NNSA's Advanced Simulation and Computing (ASC), Verification and Validation Program and Alliance Center Program for financial support.

Physical Properties of White Dwarf Atmospheres

Stephane Mazevet (T-4), Piotr Kowalski and Didier Saumon (X-7)

With the advance of wide field sky surveys, such as the Sloan Digital Sky Survey and the SuperCOSMOS survey, the sample of known white dwarf stars is growing rapidly (Fig. 1). Because they represent the end stage of the life of the vast majority of stars—essentially a stellar graveyard—they can be used as “cosmochronometers” to answer various cosmological questions such as the age of the disk of the galaxy, of the surrounding globular clusters, and the first generation of halo stars. To bring this approach to its full potential requires an increased understanding in white dwarfs cooling rates.

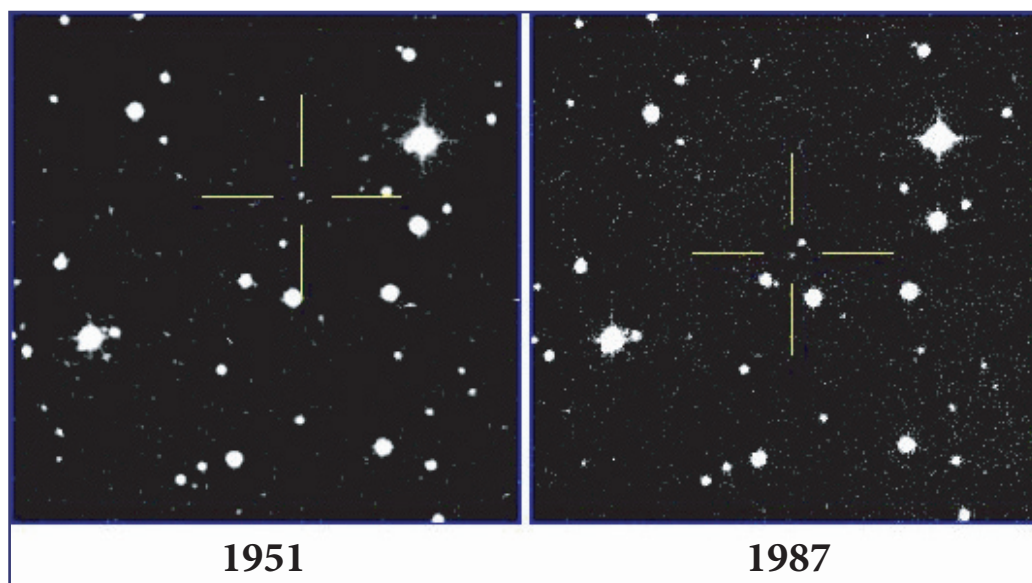
In current white dwarfs models, the largest uncertainties currently reside in the modeling of the outer atmosphere which, in turn, requires accurate dynamical and optical properties of hydrogen, helium, and hydrogen-helium mixtures in the difficult physical regime of low temperature and high density where conventional opacity

calculations fail. To address this issue, we performed Quantum Molecular Dynamics (QMD) simulations of the dynamical, electrical, and optical properties of helium for densities ranging from 0.35 to 10 g/cm³ and temperatures less than 10,000 K. This work is further motivated by the fact that the various helium equations of state currently in use in astrophysics as well as in the SESAME tables are all adjusted to reproduce the same four experimental Hugoniot points measured below 1 g/cm³.

QMD simulations are particularly well suited to study the physical properties of helium relevant to white dwarf atmospheres as the method provides a consistent set of dynamical electrical and optical properties from the same simulations. The physical properties are obtained within the theoretical framework of Density Functional Theory (DFT) and the electric and optical properties from the linear response theory.

In Fig. 2, we show a sample result of this study where we compare the QMD index of refraction and absorption coefficients calculated at two different temperatures and densities with the result of the latest opacity calculations developed for white dwarf atmospheres [1]. The latter model is developed within the framework of a standard opacity calculation where the classical free-free contribution is corrected for density effects. The free electron density is obtained from a chemical EOS [2, 3].

Figure 1—
The motion of the very cool white dwarf WD0346+248 against the backdrop of distant stars between 1951 and 1987. WD0346 has a surface temperature of perhaps less than 3500 K and a surface composition of He/H $\sim 10^3$.



For the temperatures and densities shown in Fig. 2, we find a good agreement between the QMD and a virial expansion for the index of refraction. The largest difference between the two calculations appears at 2 g/cm^3 and $T = 2000 \text{ K}$ where the virial expansion shows a stronger temperature and density dependence than the QMD calculation.

On the other hand, the absorption coefficients differ by several orders of magnitude between the two calculations. At a temperature of $T = 2000 \text{ K}$, the opacity model indicates that Rayleigh scattering dominates the opacity down to a photon energy of 0.5 eV essentially due to the very low ionization fraction. While this effect is described classically in the opacity model, further study is required to ascertain to which extent it is accounted for in the QMD calculations. At $T = 6000 \text{ K}$, the opacity is dominated by free-free processes and is proportional to the ionization fraction in the chemical model. At 0.5 g/cm^3 , the chemical model underestimates the ionization fraction by ~ 3 orders of magnitude. It then rises very rapidly with density to be ~ 10 times larger than the simulations imply. This indicates that the pressure ionization is too abrupt in the chemical model calculation. We further note that a very good agreement between the two equations of state is found in that regime. Using the QMD calculations as reference, this comparison suggests that, in this regime of extremely low ionization fraction where the free electron density does not contribute significantly to the total pressure and energy, it may be very difficult to calculate a conventional opacity based on a free energy minimization technique as in the EOS of Bergeron et al.

Preliminary models of very cool white dwarf atmospheres of pure helium composition based on the new QMD opacities show significant departures from previous generations of models. The increased opacity results in lower atmospheric densities by factors of about 20–30. This reduces the role of density effects in the models, returning to a regime that is perhaps easier to model. The flatter frequency dependence of the opacity affects the emergent spectrum of

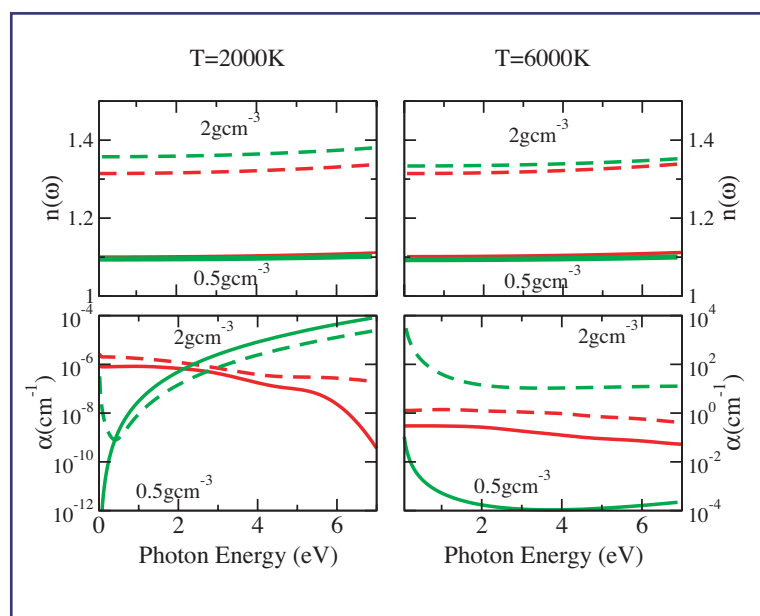


Figure 2—
Comparison between the absorption coefficient and index of refraction obtained using QMD and the results of [1]: (red) QMD; (green) Iglesias et al.; (solid) 0.5 g/cm^3 ; (dashed) 2 g/cm^3 .

the models. This would have immediate astrophysical consequences. First, the temperatures of the coolest helium-rich white dwarfs known would be reduced by over 10%, lengthening their cooling age. Second, none of the very cool white dwarfs would fall on the pure helium sequence, implying that they all have at least traces of hydrogen mixed in. This bears directly on ideas of the physical processes that are responsible for the evolution of the surface composition of very cool white dwarfs as they age. Finally, these new opacities are a first step toward modeling peculiar white dwarfs discovered recently that have so far defied all attempts to fit their spectral energy distributions. Those stars, such as WD0346+248, LHS 3250, and SDSS1337 are obviously very cool and apparently of mixed hydrogen/helium composition.

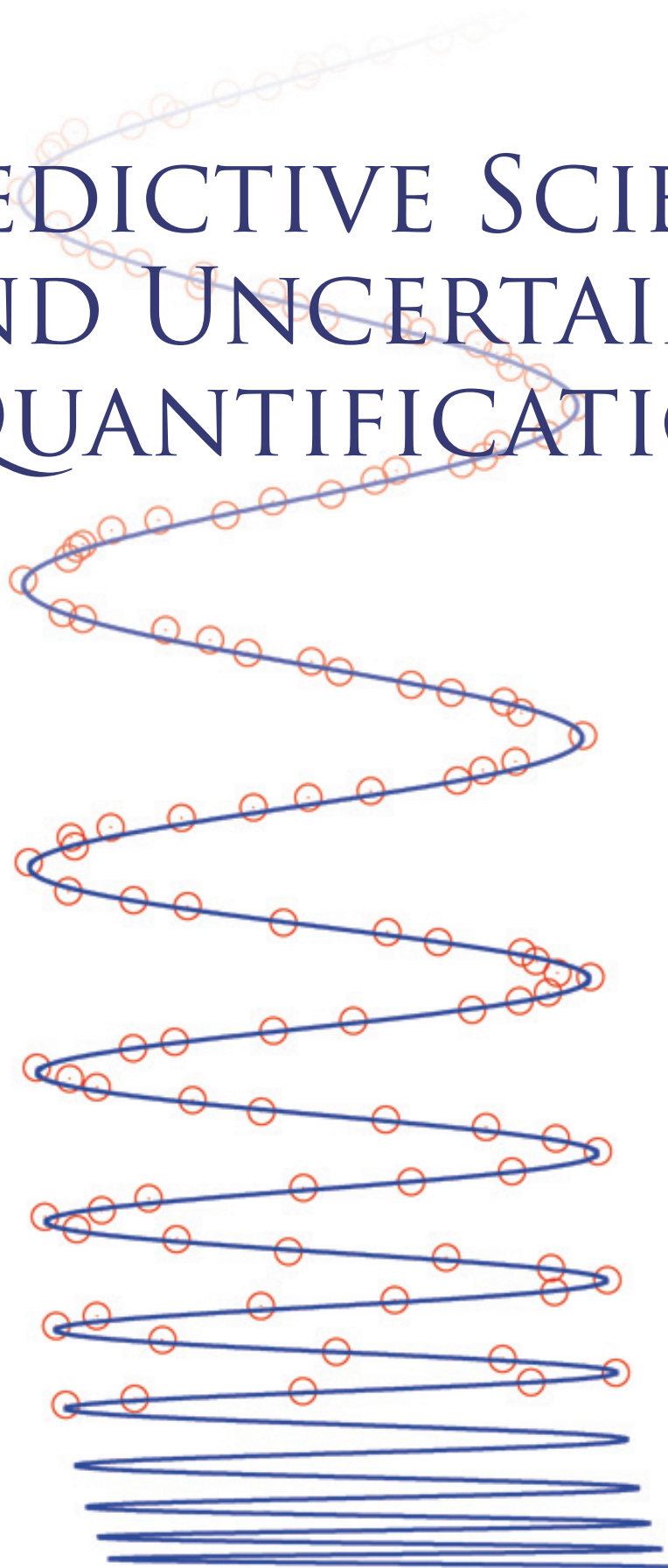
- [1] C. Iglesias, F. Rogers, and D. Saumon, *Astrophys. J. Lett.* **569**, L111 (2002).
- [2] D. Saumon, G. Chabrier, H.M. van Horn, *Astrophys. J. Supp.* **99**, 713–41 (1995).
- [3] P. Bergeron, D. Saumon, F. Wesemael, *Astrophys. J.* **443**, 764–779 (1995).

For more information, contact
Stephane Mazevet (smazevet@lanl.gov).

Acknowledgements

We would like to acknowledge NNSA's Advanced Simulation and Computing (ARC), Materials and Physics Program for financial support.

PREDICTIVE SCIENCE AND UNCERTAINTY QUANTIFICATION



The Use of Smoothing Splines to Assess Uncertainties in Alpha Curves

Timothy C. Wallstrom (T-13)

The degree of criticality of a nuclear assembly is quantified by α , the logarithmic derivative of the neutron flux. The evolution of the criticality in time is called the “ α -curve.” Measurements of the α -curve are one of the most useful sources of information about the performance of a nuclear device.

The measurement of the α -curve is complicated by the extreme physical conditions and short time scales of the nuclear reaction. Ingenious methods of measuring the α -curve have been developed for use in nuclear testing. Chief among these is a technique introduced by the astrophysicist Bruno Rossi which enables the α -curve to be inferred from the trace of a suitably configured oscilloscope. An extraordinary amount of effort has been expended in recording and analyzing Rossi trace data generated by nuclear tests. These measurements, however, have uncertainties,

which have not been fully quantified. In order to make full use of the measured data, and to understand which inferences are or are not justified from the data, the uncertainty in the α -curve needs to be quantified. The purpose of the present work is to show how the method of smoothing splines, as developed by Wahba and others [1], can be used to quantify the measurement error in α -curves inferred from Rossi traces. The use of splines to analyze Rossi traces was first introduced by Hanson and Booker [2]. The use of Wahba’s formalism was suggested by David Sharp.

The raw data is provided in the form of a Rossi trace, as recorded on photographic film or some similar medium. A synthetic trace is shown in Fig. 1. The film is placed in a reader, and a large number of individual points of the trace are measured. There are two primary sources of error: random measurement uncertainty and systematic distortions due to imperfections in the electronics. Here we restrict our attention to the measurement uncertainty.

The method of smoothing splines can be interpreted in terms of a probabilistic model for noisy measurements of an unknown function f . In our case, $f(t)$ is the signal flux, as a function of time. The prior measure on the space of functions f is chosen to be $(m - 1)$ -fold integrated Wiener measure [3], which is essentially the m -fold integral of white noise. The likelihood is that corresponding to independent measurements y_i of $f(t_i)$ with variances σ_i^2 . With these assumptions, it can be shown that the Bayes’ estimate is the solution to the following minimization problem: Choose f to minimize

$$\sum_i w_i [y_i - f(t_i)]^2 + p \int [f^{(m)}(u)]^2 du,$$

where w_i are appropriate weights, and p is determined from the data [1]. This is exactly the type of minimization problem that arises in the variational approach to splines, and indeed, the solution is a natural spline of order m , with knots at the measurement points.

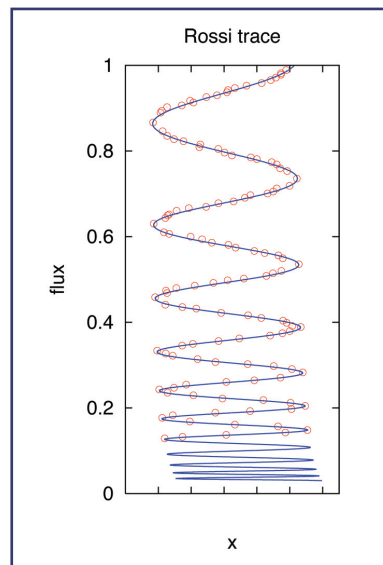


Figure 1—
A synthetic Rossi trace.

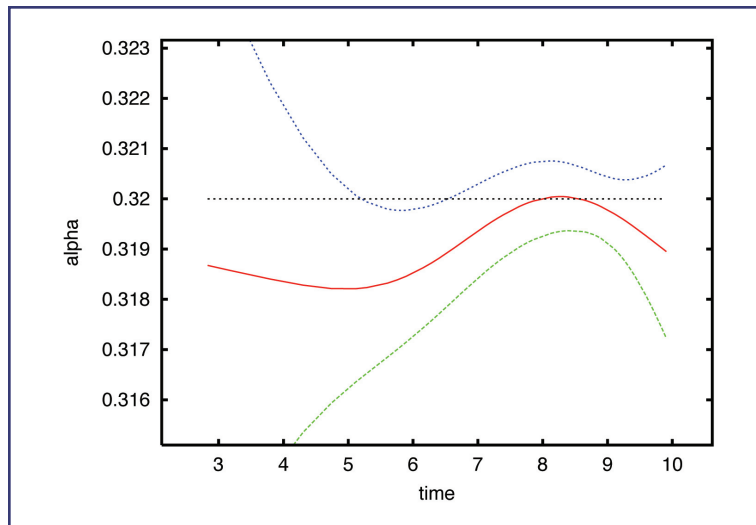


Figure 2—
This figure shows a typical estimate of the α -curve and its uncertainty, using the method of the text.

The probabilistic model provides the necessary foundation for estimating f as the posterior mean (Bayes' estimate), and also for determining the uncertainty in f and its derivatives. In particular, it enables us to compute uncertainties in α , which is the logarithmic derivative of f .

Figure 1 shows a synthetically generated Rossi trace, in arbitrary units, with both random and systematic errors. For this data, α is assumed constant, so the flux rises exponentially. The vertical axis is the signal flux. The horizontal trace varies like $\cos \omega t$, so that $x(t)$ encodes the time. An initial step, not discussed here, is to recover the time from x . The output of this step is a set of noisy flux measurements. The flux curve, the alpha curve, and its uncertainties can be estimated from this data.

The estimate of the α -curve and its uncertainty corresponding to Fig. 1 is shown in Fig. 2. I emphasize that the result shown here should be regarded as an example of the technique, and not an assessment of the true uncertainty in experimental α -curves. The latter requires accurate estimates of the uncertainties in the measured data.

- [1] Grace Wahba, *Spline Models for Observational Data* **59** in CBMS-NSF Regional Conference Series in Applied Mathematics (SIAM, Philadelphia, 1990).
- [2] Kenneth M. Hanson and Jane M. Booker, "Inference from Rossi Traces," in A. Mohammad-Djafari, Ed., *Bayesian Inference and Maximum Entropy Methods in Science and Engineering* **568** (AIP Conf. Proc., Melville, NY, 2001) p. 604.
- [3] L. Shepp, "Radon-Nikodym Derivatives of Gaussian Measures," *Ann. Math. Statist.*, **37**, 321–354 (1966).

For more information, contact
Timothy Wallstrom (tcw@lanl.gov).

Acknowledgements

I would like to acknowledge NNSA's Advanced Simulation and Computing (ASC), Verification and Validation Program, for financial support.

Physics Package Confidence: “ONE” vs “1.0”

*David H. Sharp (T-13 and X-DO),
Timothy C. Wallstrom (T-13), and
Merri Wood-Schultz (X-2)*

The “reliability” of the nuclear explosive package of a stockpiled nuclear weapon has historically been stated to be “ONE,” with the intent to convey very high confidence that a device that was properly constructed and that had been properly handled would perform as expected on receipt of the appropriate arming, fusing, and firing signals. We report on recent work clarifying the basis for assertions of confidence when applied to high consequence systems in the context of Quantified Metrics and Uncertainty (QMU) [1]. Previous work on QMU has used a conservative approximation that assigns a confidence of “ONE” or “Not ONE” for nuclear weapons. We extend QMU to a fully probabilistic setting, in which confidence in performance can be assigned a probability between zero and one. We use this more general formulation to examine the assumptions underlying the more conservative model.

The approach to confidence that has been taken historically is based on conservative bounds on uncertainty, grounded in nuclear test results, and supplemented by scientific judgment. This has led to a binary assessment of confidence as “ONE” (we have high enough confidence that the weapon will work properly to allow certification) or “Not ONE” (we do not have sufficient confidence for certification). A confidence assessment of “ONE” is thus not an assertion that the probability of some event (successful operation of a nuclear weapon) is 1.0. It is rather a statement that the balance of evidence is sufficient to support certification.

The questions that must be answered to maintain confidence in the stockpile include assessments of weapons’ behavior in

circumstances where (1) aging, engineering flaws, or manufacturing defects result in stockpile devices that fail to meet original specifications, or (2) nuclear design flaws, apparent or suspected, come to light. In addition, certification of new designs and/or new applications of existing devices could be desired if deemed necessary for national security. Under a comprehensive test ban, the design laboratories must attempt to answer this range of questions without further nuclear tests. It seems likely that this can be done with the requisite confidence for some questions but not for others. To push the envelope of what can be reliably certified without nuclear testing as far as possible requires advances in predictive science across a broad front including experimental, modeling, and simulation capabilities.

The most crucial role of any certification methodology is to clarify the choices and judgments made in deciding whether or not to certify a device at all. The determination that a device fully meets the weapon system military characteristics, and the predictions of the range of its performance are qualitatively different products of the certification process. Thus, while reliability and performance are both important, they are not the same thing for a nuclear weapon system.

Because of the potential consequences of a weapon failure, a policy of strict conservatism is usually adopted. This is implemented in part by requiring that a certification be based on persuasive evidence that the device will work, as well as on the absence of significant evidence that it might not work. Note that conservatism requires judgment in its application. Both excessive and insufficient conservatism have their costs. The QMU method has been introduced to provide a systematic and explicit framework for explaining the scientific basis for confidence in assessments of the performance, safety, and reliability of nuclear weapons. QMU is built on salient characteristics of a weapon’s performance, each of which is known as a metric, derived from an analysis of experimental data and computer simulations. Requirements for robust operation for the metrics are termed “gates,” and the margins of interest to QMU are the amounts by which the metrics exceeds the requirements

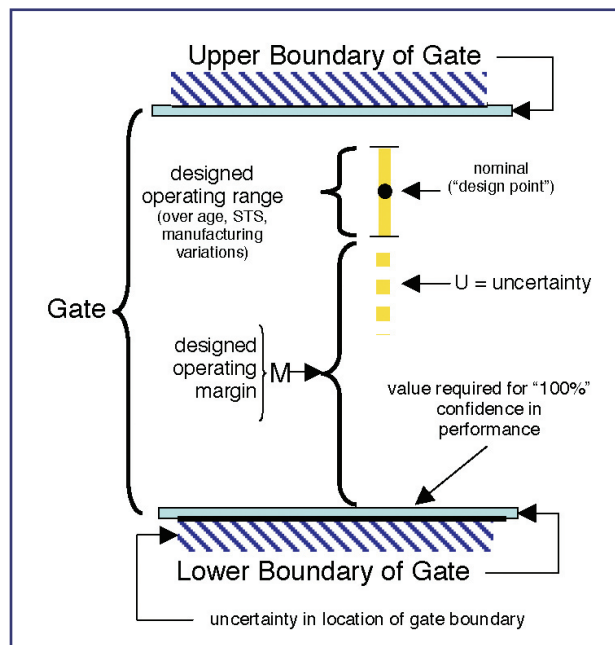


Figure 1—
The main features of
a performance gate.

(see Fig. 1). Gates and margins are well suited to inform the binary decision of whether or not to certify a weapon.

In our full paper [1], we present two ways of formulating QMU that we have termed “Interval” and “Full.” The use of either formulation requires approximations and scientific judgment. However, fully probabilistic analyses require knowledge of uncertainties that will usually be difficult to obtain.

“ONE/Not ONE” estimates of reliability are consistent with historical practice. Both approaches are a response to the very limited availability of detailed uncertainty information. Extending this class of estimates to current and future stockpile questions is itself a significant challenge.

The U.S. nuclear weapons community is just beginning to explore where QMU can be useful. The emphasis in QMU on characterization of uncertainties is essential for determining which stockpile questions can be answered with confidence using the data and simulation capabilities that are

available at any given time. Improvements in predictive science may allow improved estimates of uncertainties, and potentially may also allow them to be reduced. This would affect the scope of questions that can be dealt with successfully, but significant limitations are expected to remain. Identifying these limits is an important task of the nuclear weapons program.

We submit that when carefully applied, QMU can improve our basis for assessing the reliability of stockpile decisions.

[1] D.H. Sharp, T.C. Wallstrom, and M.M. Wood-Schultz, “Physics Package Confidence: ‘ONE’ vs ‘1.0’” Los Alamos National Laboratory report LA-UR-04-0496 (January 2004); presented as a poster at NEDPC 2003.

For more information, contact
Timothy C. Wallstrom (tcw@lanl.gov).

Acknowledgements

We would like to acknowledge NNSA’s Advanced Simulation and Computing (ASC), Verification and Validation Program for financial support.

AUTHOR INDEX

A

Abdallah, Jr., Joseph 166, 168, 170, 174
Addressio, Francis L. 4, 26, 30, 32, 34
Ahluwalia, Rajeev 38, 40
Albers, Robert C. 44
Alder, Berni 104
Andrews, M.J. 96
Austin, Travis 88, 110

B

Bannerjee, S. 40
Bardenhagen, Scott 36, 66
Baskes, Michael I. 72
Bedrov, Dmitry 70
Bengtsson, Ragnar 152
Berndt, Markus 88, 110, 112
Bock, Nicolas 2, 6
Borodin, Oleg 70
Bouchet, Johann 44
Bradley, Paul A. 138
Bronkhorst, Curt A. 28, 90
Brown, Edward F. 196
Brydon, Andrew 36, 66
Burakovsky, Leonid 8

C

Cerreta, Ellen K. 90
Chadwick, Mark B. 144, 146, 150, 160, 162
Challacombe, Matt 24, 70
Cherne, Frank J. 72
Chisolm, Eric 2, 10
Chitanvis, Shirish M. 68
Clements, Brad E. 14, 20, 26
Cline, Michael C. 92
Coffey, D. 6
Coker, Rob 192
Colgan, James 170, 172
Collins, Lee A. 54
Cox, Arthur N. 188
Cragg, George E. 140
Crockett, Scott 2, 10
Csanak, George 184

D

Daligault, Jérôme 184
Davande, Hemali 70
De Lorenzi-Venneri, Giulia 2, 12
Dienes, John K. 34
Dimonte, Guy 96, 104
Dotson, Paul J. iii
Dwivedi, V. 40

E

F

Fontes, Christopher J. 170
Frankle, Stephanie C. 144, 162
Friar, James L. 180
Fryer, Chris 190

G

Gan, Chee Kwan 70
Garimella, Rao V. 114
George, Denise C. 2, 14
Germann, Timothy C. 48, 72, 104
Ghoniem, Nasr 22
Girard, Briton 130, 134
Goda, Patrick 128
Gore, Robert 64
Gorman, Thomas 130
Gray, III, George T. 4, 90
Greeff, Carl 2, 4, 30
Guzik, Joyce A. 188

H

Hadjiconstantinou, Nicolas G. 104
Hakel, Peter 166, 168, 174
Hale, Gerald M. 130, 142, 158
Hall, David 42
Han, Si-ping 50
Hanson, David 52
Hanson, Kenneth M. 144
Harlow, Francis H. 32, 64
Harstad, Eric 4, 30, 100
Hayes, Anna C. 128, 130, 132, 134, 136, 138, 156, 180, 194
Heger, Alexander 192
Heim, Andrew J. 74
Hennig, Richard G. 44
Herwig, Falk 192
Hills, Jack 128, 194

Hixson, Rob 4
Holian, Brad Lee 56, 72, 80, 104
Howe, Steven 130
Hubbard, Margaret S. 92
Hueckstaedt, Rob 192
Hull, Larry M. 84
Hungerford, Aimee 190

I

J

Jaramillo, Eugenio 70
Johnson, Andrew S. 130
Johnson, J.D. 2, 6
Jungman, Gerard 128, 134, 136, 138, 194

K

Kadau, Kai 48, 72, 104
Kawano, Toshihiko 144, 146, 160
Kerman, Arthur K. 140
Kilcrease, David P. 166, 168, 174
Knudson, Marcus 4
Kober, Edward 42, 46, 74
Kowalski, Piotr 198
Kress, Joel D. 54, 58
Kuprat, Andrew P. 108
Kuznetsov, Yuri 116

L

Lemaire, Sebastien 146
LeSar, Richard 22
Lipnikov, Konstantin 116
Little, Robert C. 130, 144, 150
Liu, Cheng 28
Liu, Lon-Chang 148
Lomdahl, Peter S. 48, 72, 104
Lookman, Turab 38, 40, 42, 46
Loubère, Raphaël 118, 120, 122
Luo, Sheng-Nian 78
Luu, Thomas C. 180, 194
Lynn, Eric 134

M

Mace, Jon 62
MacFarlane, Robert E. 150, 162
MacInnes, Michael R. 150
Madland, David G. 146
Magee, Jr., Norman H. 166, 168, 174
Maniadis, Panagiotis 46
Mas, Eric M. 14, 20, 26, 62, 100
Mason, Thomas A. 90, 100

Maudlin, Paul J. 20, 62, 84, 90, 100
Mazevet, Stephane 166, 168, 174, 198
Möller, Peter 152, 154
Moulton, J. David 88, 110, 112
Murillo, Michael S. 178, 184

N

New, Kim 190
Nieto, Michael Martin 132, 156
Niklasson, Anders M.N. 24

O

O'Rourke, Peter J. 92
Olivius, Peter 152

P

Padial-Collins, Nely T. 94, 102
Page, Philip R. 158
Pauler, Denise K. 58
Plohr, Bradley J. 82
Plohr, JeeYeon N. 82
Preston, Dean L. 8

Q

R

Ramaprabhu, Praveen 96
Rasmussen, Kim Ø. 46
Rauenzahn, Rick M. 32, 64, 98
Ravelo, Ramon J. 72
Richter, John 128
Rigg, Paulo 4
Rockefeller, Gabe 190
Rose, Harvey A. 182
Rudin, Sven 2, 4
Rundberg, Robert S. 138

S

Sahota, Manjit S. 32, 64, 92, 98, 100
Saumon, Didier 198
Saxena, Avadh 38, 40
Sewell, Thomas D. 70
Sharp, David H. 204
Shashkov, Mikhail 88, 114, 116, 118, 120, 124
Shaw, M. Sam 76

Sherrill, Manolo 166, 168, 174
Smith, Grant D. 70
Solem, Johndale C. 138
Sportsman, Scott 94
Srinivasan, Srivilliputhur G. 44
Staley, Martin 122, 124
Stanbro, William D. 156
Steinkamp, Michael 64
Strachan, Alejandro 50, 56, 78, 80
Swartz, Blair K. 114

T

Talou, Patrick 144, 146, 160
Teeter, Corrine M. 132, 156
Thompson, Darla G. 28
Timmes, Frank 192, 196
Torres, David J. 92
Trinkle, Dallas R. 44
Truran, J.W. 196
Tymczak, Christopher J. 76

U

V

VanderHeyden, W.B. 94, 98, 102

W

Wallace, Duane 2, 6, 10, 12
Wallstrom, Timothy C. 202, 204
Wang, Zhiqiang 22
Weber, Valéry 24
Weisheit, Jon 64, 178
Wendroff, Burton 122
Wilkins, John W. 44
Williams, Todd O. 26, 28, 30
Wilson, William B. 132, 156
Wood-Schultz, Merri M. 98, 204

X

Y

Young, Phillip G. 160, 162

Z

Zhang, Duan Z. 94, 102
Zhang, H.L. 170
Zhang, Jianzhong 4
Zhao, Yusheng 4
Zou, Qisu 94, 102
Zuo, Q. Ken 30, 34, 84

LA-UR-05-0000 June 2005

Los Alamos National Laboratory, an affirmative action/ equal opportunity employer, is operated by the University of California for the U.S. Department of Energy under contract W-7405-ENG-36. By acceptance of this article, the publisher recognizes that the U.S. Government retains a nonexclusive, royalty-free license to publish or reproduce the published form of this contribution, or to allow others to do so, for U.S. Government purposes. Los Alamos National Laboratory requests that the publisher identify this article as work performed under the auspices of the U.S. Department of Energy. Los Alamos National Laboratory strongly supports academic freedom and a researcher's right to publish; as an institution, however, the Laboratory does not endorse the viewpoint of a publication or guarantee its technical correctness.

This document was produced for the Theoretical Division, Los Alamos National Laboratory, June 2005.



